Optical Tweezers in Viscoelastic Media

Ph.D. Thesis

submitted to the

Niels Bohr Institute

Faculty of Science

University of Copenhagen

Denmark

October 2007

presented by

Mario Fischer

born in Magdeburg

Thesis Author:
Dipl.-Phys. Mario Fischer, University of Copenhagen, Faculty of Science, Niels Bohr Institute, Denmark, email: mfischer@nbi.dk

Thesis Advisors:
Prof. Kirstine Berg-Sørensen, Technical University of Denmark, Department of Physics, Denmark

Prof. Lene Oddershede, University of Copenhagen, Faculty of Science, Niels Bohr Institute, Denmark

Thesis Submission Date: 22.10.2007

Thesis Defense Date: 04.12.2007

Abstract:

With optical tweezers, a tracer particle of nano- to micrometer size is caught in the focus of a laser trap. Within the last years optical tweezers have become an important tool in biophysics and are nowadays used in many experiments. A recent application of optical tweezers are studies in viscoelastic media like the cytoplasm of a living cell or a filament solution. So far, in none of these studies, optical tweezers could be used for quantifying the applied forces. The reason is that there is no method for measuring forces in viscoelastic media *in situ*, as *ex situ* calibrations cannot be applied. Indeed, there is considerable interest in such force measurements. A force calibration is in particular important for investigating how forces are generated inside the cell.
In this work, I present a novel force calibration method for optical tweezers inside viscoelastic media. The method is based on the validity of the fluctuation-dissipation theorem. Knowledge about the trapped particle or the medium is not required for the application of the method, except for the medium's temperature. In this thesis, the complete theoretical framework of the method is derived. Simulations and experiments are presented, which have been performed in order to test the method.
Furthermore, within this thesis, two investigations on the viscoelasticity of biological systems on the subcellular scale are presented, which employ microrheological and simulation techniques.

Contents

1 Introduction

A biological cell is fulfilling various tasks by the interaction of many different molecular species. Within a living cell, the reactions between these molecular agents have been observed with numerous biochemical and bio-molecular methods. With such methods, the influence of important physical quantities like time, temperature, dimension, space, concentrations and force is mostly not assessable. Hence, with non-physical methods, a profound understanding of how cellular components interact in order to make the whole cell work, can not be established.

Nowadays, biophysicists seek to gain quantitative insight by the application of physical methods to the investigation of biological systems. Optical tweezers are a relatively young technique which allows the examination of distances, durations and forces on very small scales. In *in vitro* experiments, this technique has already been successfully applied to the exploration of biomolecules like molecular motors [1]. Furthermore, in a small number of in vivo cell experiments with optical tweezers, biological processes have been investigated. For example the tweezers have been used to track the motion of a trapped bead under its incorporation by a macrophage [2].

The next step would be to apply optical tweezers in order to investigate how forces are generated inside the living cell. These intracellular forces are generated by a complicated interplay of biomolecules, filaments and organelles like molecular motors, microtubuli and the cell nucleus. An understanding of how these components are mechanically acting together inside the living cell would deliver new insight into complex life processes like cell division and nuclear positioning.

So far, it has not been possible to use optical tweezers to measure or to exert forces quantitatively in the cell. The reason for this is that no method is available for the *in situ* calibration of the tweezers inside the cell. The main objective of this thesis is to develop such a method and to test it (chapters 3-8). Furthermore, within this thesis I have worked on the viscoelasticity of biological systems on the subcellular scale by microrheological (chapter 9) and simulation (chapter 10) approaches.

In chapter 2, an introduction to optical tweezers and to viscoelasticity is given. A formal description of a particle which is trapped with the optical tweezers and which performs Brownian motion within a viscoelastic medium is introduced in chapter 3. Systems in which the trapped particle in the viscoelastic medium is additionally exposed to an external perturbation are described in chapter 4. In chapter 5, the situation of a trapped particle bound to a biological structure is discussed. Furthermore, bio-active systems will be discussed in which the medium is not only viscoelastic, but also contains biological processes that can alter the motion of the trapped particle. The novel FDT method for the calibration of optical tweezers in viscoelastic media is presented in chapter 6. The central assumption of the FDT method is the validity of the fluctuation-dissipation theorem (FDT) which gives the method its name. The method demonstrates that by performing two simple measurements, basically all linear properties of the system can be found. This involves that the FDT method includes a novel microrheology approach to the investigation of viscoelastic properties of the medium. In chapter 7, it is explained how to perturb the system in the active part of the FDT method. Furthermore, simulations that allow testing the method are presented. Experiments, which have been performed in water in

order to test the FDT method beyond the simulations, are shown in chapter 8. In chapter 9, an investigation of the frictional force, which is exerted on a trapped bead close to a phagocyte cell membrane, is presented. The underlying biological question of this microrheological study is, how the viscoelastic properties of the medium close to the phagocyte membrane are altered to enable an efficient binding of nearby particles. Finally, in chapter 10, work on the microscopic origin of viscoelasticity is shown. The non-linear shear strain response of a semiflexible network has been investigated by simulations of shear cell experiments.

2 Optical tweezers and viscoelastic media

As described in the introduction, this work focuses on calibration of optical tweezers in viscoelastic media. In this chapter some requisite basics of both optical tweezers and viscoelasticity are presented. This is fundamental for the subsequent chapters.

2.1 Optical tweezers

In this section an introduction to the method of optical tweezers is given. Optical tweezers are a sophisticated technique with many different features. I will only give a basic outline of this technique here, a more comprehensive description can be found in the review by Neuman and Block [3].

2.1.1 History, principle and forces of optical tweezers

The concept and the technique of optical tweezers was developed by Arthur Ashkin during the 1970s and 1980s and the first stable laser trap was presented by him and his coworkers in 1986 [4]. Today *single beam optical tweezers* are a well established and valuable tool in biophysics from the single molecule level up to the cellular scale. Optical tweezing is performed by a laser beam which is tightly focused with an objective lens of high numerical aperture. A sketch of the experimental setup of the optical tweezers at the Niels Bohr Institute in Copenhagen is shown in Fig. 2.1. The steep gradient of the electro-magnetic field in the proximity of the laser focus

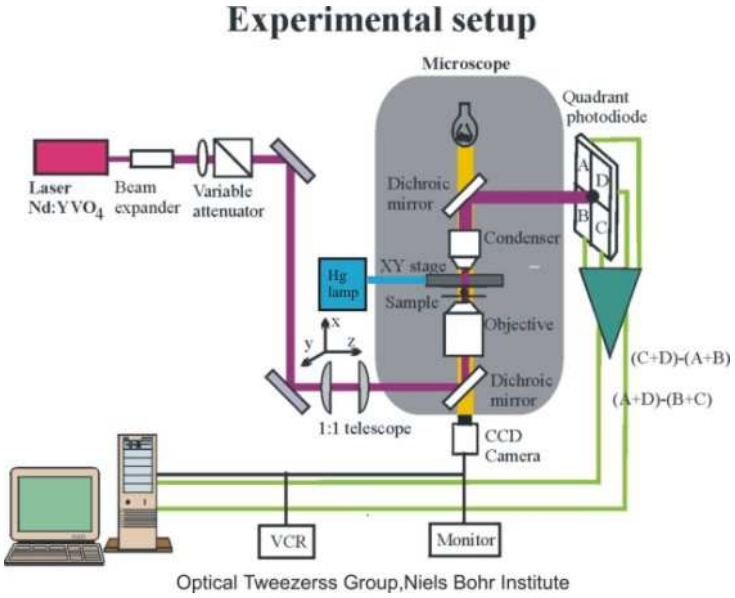

Figure 2.1: Sketch of the experimental setup of optical tweezers at the Niels Bohr Institute in Copenhagen, by courtesy of Prof. Lene Oddershede.

results in a *gradient force* on a microscopic or nanoscopic dielectric particle. If that particle has

a refractive index which is higher than that of the surrounding medium, the gradient force is directed towards the focus. If that force balances the *scattering force* which also acts on the trapped particle and tends to push it into the direction of light propagation, the particle will stay close to the focus, i.e, the particle will be trapped.

Theoretically, the forces that are acting on the dielectric particle can be described for two limiting cases. When the particle radius is much larger than the wavelength of the trapping laser, the optical forces can be computed from *ray optics*. Here, the force on the particle is given by the rate of momentum change of the light and it is proportional to the light intensity, see Fig. 2.2. In cases where the radius of the trapped particle is significantly smaller than the wavelength of

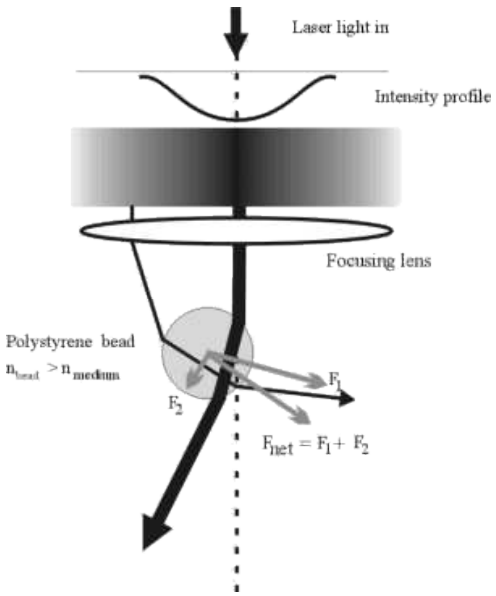

Figure 2.2: Principle sketch of optical trapping in the ray optics picture, by courtesy of Prof. Lene Oddershede. A particle encountering the laserbeam will be pushed towards the center of the beam, if the particle's index of refraction is higher than that of the surrounding medium. As the light is deflected in the particle, a gradient force results that pushes the particle vertically to the propagation of the laserbeam, towards the largest intensity of light. By focussing the light, the gradient force pushes the particle backwards as well. If this force overcomes the propagation force of the laserbeam, the particle is trapped. The forces exerted on the dielectric sphere have been calculated by Ashkin [5].

the light, the conditions for *Rayleigh scattering* are satisfied and the particle can be treated as a point dipole in an inhomogeneous electromagnetic field. The gradient force $\mathbf{F}_{\mathrm{grad}}$ applied on such a dipole in an electromagnetic field is then simply given by the *Lorentz force* which is the force exerted on a charged particle in an electromagnetic field. This force is proportional to the light intensity gradient and one has for a sphere of radius R [3]

$$\mathbf{F}_{\mathrm{grad}} = \frac{2\pi\alpha}{cn_{\mathrm{m}}^2}\nabla I_0, \tag{2.1}$$

where I_0 is the intensity of the incident light, c is the speed of light in vacuum, and the polariz-

ability α of the sphere is given by

$$\alpha = n_{\mathrm{m}}^2 R^3 \left(\frac{m^2 - 1}{m^2 + 2} \right), \tag{2.2}$$

with m being the ratio of the index of refraction of the particle to the index of the medium $n_{\mathrm{p}}/n_{\mathrm{m}}$. For the scattering force one has

$$\mathbf{F}_{\mathrm{scatt}} = \frac{\langle \mathbf{P} \rangle \sigma n_{\mathrm{m}}}{c}, \tag{2.3}$$

where $\langle \mathbf{P} \rangle$ is the time-averaged Poynting vector and the scattering cross section σ of the sphere is given by

$$\sigma = \frac{128\pi^5 R^6}{3\lambda^4} \left(\frac{m^2 - 1}{m^2 + 2} \right)^2. \tag{2.4}$$

The scattering force is in the direction of propagation of the incident light and is proportional to the intensity.

2.1.2 Optical tweezers as a Hookean spring and calibration

For small displacements, the gradient force is proportional to the distance from the equilibrium position. This means that the optical trap acts like a Hookean spring which has a characteristic stiffness that is proportional to the light intensity. Such a harmonic force description of the trapping force is a very good approximation within a spatial extension of about 300 nm [3] and it even holds for gold particles with a radius as small as $R = 20\,\mathrm{nm}$ which are trapped with a laser power of 270 mW [6]. Throughout this work I describe the action of the optical tweezers on the trapped particle solely as a harmonic force. This is necessary for the description in terms of linear response theory. The validity of the harmonic force assumption can be tested by, e.g., optical potential analysis which is described in paragraph 6.1.3.

The stiffness constant of the optical trap will be denoted throughout this work as κ. In principle κ can be found from computation of the electromagnetic forces which are acting on the trapped particle. In practice, those forces depend on experimental parameters which are difficult to determine, and a quantitative agreement between calculated and measured forces can only be obtained for relatively simple situations [7]. In general one has to *calibrate* the trap stiffness.

In quantitative experiments employing optical tweezers, the motion of the trapped particle has to be tracked. That motion can be recorded with high sampling rates by quadrant photo diode position detection systems. Here one typically measures voltages which have to be converted into positions by *positional calibration* which is another essential part of the calibration of optical tweezers. The calibration of optical tweezers is the major concern of this work.

2.1.3 Experiments with optical tweezers

Biophysical experiments with optical tweezers can be divided into two general classes. The first class are experiments where mechanical properties of a biological material are investigated by

observing the motion of a trapped micron-sized bead made of polystyrene or latex. The bead is *not* chemically *bound* to any structure and performs Brownian motion in the harmonic trap potential and interacts hydrodynamically with the surrounding medium. From the observed bead motion the mechanical properties of the medium can be derived. This technique, which is called microrheology, is explained in more detail in section 2.3. The materials examined by microrheology can be membrane-like structures [8,9] or gels and filament solutions [10–13] or the cytoplasm of living cells [14]. The force calibration method presented in this work allows for a simultaneous determination of the mechanical properties in viscoelastic media corresponding to one-point microrheology.

Experiments of the second class are those where the trapped particle is chemically *bound* to a biological structure like a single molecule, a filament [15], an organelle [16] or a cell [17]. In most cases those structures can not be trapped themselves by the optical tweezers with sufficient force. Therefore an artificial bead has to be chemically attached to such a structure and that bead is then used as a handle which couples the trap force to the biological structure. This enables the manipulation of the biological structure by the optical tweezers. If the tweezers have been calibrated, one can manipulate with quantitatively known forces, and forces can be measured quantitatively. In that way optical tweezers have been successfully applied since the 1990s to the characterization of single molecules like molecular motors [1,18] or RNA polymerase [19,20]. Optical tweezers have allowed biophysicists to observe the forces and dynamics of those molecules. *Optical trap force-spectroscopy* has led to greater understanding of the stochastic nature of such molecules. The novel force calibration formalism portrayed within this work suggests a way of how to obtain force spectra more directly.

Most experiments of both classes have so far been performed *in vitro*. This means for microrheological measurements on the one hand, that it is not measured within living matter but rather on polymer solutions which contain purified ingredients. For measurements on molecules or filaments on the other hand, *in vitro* experiments typically involve taking the molecule or filament out of its biological context, diminishing the number of unknown parameters, and getting it to work in an artificial environment, typically in a sample chamber [21]. Some other experiments with optical tweezers have already been performed on living systems and an increasing effort towards such *in vivo* experiments over the past couple of years can be observed. I will discuss *in vivo* experiments in more detail in section 2.4. The novel method presented in this work aims at a calibration of optical tweezers inside *in vivo* systems.

2.2 Viscoelasticity

The term *viscoelasticity* describes materials that exhibit both viscous and elastic characteristics. This means that those materials behave both fluid-like and solid-like with respect to their response to stresses. Classical solids, which are purely elastic materials, strain instantaneously when stretched and return to their original state once the stress is removed. Fluids on the other hand, which are viscous materials, resist shear flow and strain linearly with time when a stress is applied, but they do not return to their original, undeformed state.

Viscoelasticity is exhibited by different material classes like glasses, metals, rubbers and polymers. Within biophysics we are typically confronted with viscoelasticity of polymers or polymer solutions. The book of Ferry gives a comprehensive survey of the viscoelasticity of such materials and its microscopic origin [22].

Whereas elasticity is usually the result of bond stretching along crystallographic planes in an ordered solid, the microscopic origin of viscoelasticity is of statistical nature. Generally, viscoelasticity is the result of the diffusion of atoms or molecules inside of an amorphous material. This involves that the response of the material to stress is characterized by one or several typical time scales. Equivalently, one observes a certain time-dependence of stress response to a deformation. One has [23]

$$\sigma_{xy}(t) = \int_{-\infty}^{t} dt' G(t-t') \frac{\partial u_{xy}(t')}{\partial t'}, \tag{2.5}$$

where $\partial u_{xy}(t')/\partial t'$ is the velocity of shear deformation, $\sigma_{xy}(t)$ is the resulting stress and $G(t)$ is the *viscoelastic shear function* which is a material property[1]. Its Fourier transformed, the *viscoelastic dynamic shear modulus* $G(\omega)$ is composed of the real part $G'(\omega)$ which accounts for elastic processes and is called *storage modulus* and of the imaginary part $G''(\omega)$ which accounts for dissipative processes and which is called *loss modulus*.

2.3 Microrheology

The investigation of viscoelastic properties of materials is the concern of the research field of *rheology*. The traditional approach to determine viscoelastic properties experimentally is called *macrorheology* at which stresses or strains are applied on bulk samples of the medium. This involves that external forces are exerted on the surface of the sample. A more recent approach is *microrheology* where only minute amounts of the material to be investigated are required. Either a known external force or the thermal force arising from fluctuations within the medium acts on microscopic spherical particles that are immersed in the material. These particles interact hydrodynamically with the medium. By measuring trajectories of the immersed particles, viscoelastic properties of the medium can be extracted. Comparisons of the elastic moduli obtained by microrheology have yielded good agreement with results from macrorheology. A technique to perform microrheological experiments is optical tweezers.

[1] $u_{xy}(t)$ and $\sigma_{xy}(t)$ are off-diagonal components of the strain and stress tensor, respectively.

An approach to microrheology is to link $G(\omega)$ to a quantity which describes the frictional interaction between the medium and the microscopic bead moving in the medium. This quantity is the so-called *friction retardation spectrum* $\tilde{\gamma}(\omega)$ and for incompressible media it can be related to $G(\omega)$ with the *generalized Stokes-Einstein relation*, [10, 24–26]

$$\tilde{\gamma}(\omega) = 6\pi \frac{G(\omega)}{\mathrm{i}\omega} R. \tag{2.6}$$

In Eq. (2.6) the expression $G(\omega)/(\mathrm{i}\omega)$ plays the role of a frequency-dependent viscosity. Eq. (2.6) represents one of the two basic equations of *one-point microrheology*[2]. It is derived by solving the equation of elastic equilibrium $\partial\sigma_{ij}/\partial x_i = 0$ for u_{ij} with no-slip boundary conditions on a rigid spherical surface [10][3]. Eq. (2.6) is written in a Fourier-transform notation which is convenient if the *power spectrum* is used as a measurable quantity for the determination of $\tilde{\gamma}(\omega)$, as proposed by Schnurr et al. [10] and Gittes et al. [11]. More details on that approach are given in section 9.1. Mason, Weitz and Gang proposed another approach which makes use of the mean square displacement for the determination of the friction retardation spectrum $\hat{\gamma}(s)$ [24, 27]. In this case one has to apply a description which uses the Laplace transform with complex frequency s instead of the Fourier transform with real frequency ω. Both approaches are widely-used in microrheology. Microrheology measurements have been applied in many different viscoelastic media including living cells [14, 28–32].

Based on experimental rheology results, viscoelastic media have been modelled for a long time as systems of springs and dashpots [33]. Many viscoelastic media can be described by a limited number of springs and dashpots and therewith by a limited number of time scales. In the cytoplasm which can be considered as an viscoelastic medium in first approximation, one has found that this description with a limit number of springs and dashpots does not longer apply. One finds rather a continuum of time scales [30, 34]. By a description of the bead-medium interaction through the *continuous* frequency-dependent function $\tilde{\gamma}(\omega)$, it can be accounted for such a continuum of time scales. In this work I use such a description and apply it to the calibration of optical tweezers.

2.4 Quantitative force measurements in living cells with optical tweezers

Several biological processes inside the cytoplasm of a living cell have already been investigated by means of optical tweezers. For example, the subdiffusion of a natural lipid granule in a yeast cell [14] and the motion of a trapped bead during its incorporation by a phagocyte [2] have been tracked with optical tweezers.

In none of these experiments optical tweezers could be used for measuring forces inside the cell. The reason is that no method for calibrating and measuring forces *in situ* inside viscoelastic media was available. Indeed, there is considerable interest in such force measurements, especially

[2] A second equation, the *Fluctuation-dissipation theorem*, is used to relate the friction retardation spectrum to a measurable quantity, see section 4.4.

[3] For viscoelastic media which are composed of a filament network and a solvent, the condition of incompressibility would be given for high enough frequencies, when the filament network and the incompressible solvent are moving as one.

for the elucidation of the intracellular mechanics of the cell. Several research groups aim at investigating how biomolecules, filaments and organelles like molecular motors, microtubuli and the cell nucleus are mechanically acting together inside the living cell in order to perform complex life processes. For example, nuclear positioning in yeast cells is a process which takes place in the cell interphase. During that process, polymerizing and depolymerizing microtubli that are associated to bundles and linked to the nucleus are perpetually positioning the nucleus in the center of the cell [35]. Experiments and computer simulations suggest that several motor proteins and crosslinker proteins must play a roll in this process [36]. Force measurements could reveal crucial information about the interaction of the individual components. Cell division is another example for a complex process where microtubuli and many different proteins act together. Initially a mitotic spindle is formed which segregates the chromosomes to the daughter cells and in the end of the process the cell body divides. Many details of cell division are far from understood. Also in this case, force measurements could help to understand that complex and dynamic system. With a proper force calibration, optical tweezers could be used here as a *force-scope*.

More basic force measurements with optical tweezers in living cells would aim at the determination of mechanical properties of the individual components, like the bending stiffness of microtubuli or the force exerted by molecular motor proteins. It would be very interesting to compare the results to *in vitro* studies, since it is not straightforward that the mechanical behavior of the components is the same for different environments. For example, thermal bending modes of microtubuli which are typically present in water could be suppressed or altered in the more dense and viscoelastic cytoplasm, which might result in diminishing of entropic contributions to the total microtubule spring constant.

3 The trapped particle in a viscoelastic medium

In section 2.3 it has already been shortly explained how optical tweezers can be used to investigate mechanical properties of viscoelastic media. For a deeper understanding of how a particle which is trapped by optical tweezers behaves in a viscoelastic medium, it is necessary to start from the equation of motion. In the first section of this chapter the equation of motion will be derived as a linear differential equation of second order for the system at thermal equilibrium where no external forces are present. The interaction between the trapped particle and the medium is characterized by the friction relaxation spectrum $\tilde{\gamma}(\omega)$ which is introduced and portrayed by means of several examples in section 3.2. In section 3.3, the behavior of the random force $F_{\mathrm{R}}(t)$, which is not white noise, is described. Finally, in section 3.4 the power spectrum which is an important measurable quantity is introduced.

3.1 Equation of motion in linear response theory

In this chapter only closed thermodynamic systems in equilibrium are considered. This implies that no external forces F_{ext} are present and the system is denoted as being *undriven*. Further, any heating effect due to the optical trap is neglected. In the following, a continuous, homogeneous medium is assumed in which the motion of the trapped object is described by three independent degrees of freedom, the coordinates x, y, z. Here, one of these coordinates $x(t)$ is described without loss of generality. In linear response theory, terms of higher than first order in x or in the derivatives $\dot{x}$, $\ddot{x}$ do not appear. In the most general form, the equation of motion describing the bead dynamics at time t is then given by the differential equation

$$0 = f_0\left[x(t-\tau)\right] + f_1\left[\dot{x}(t-\tau)\right] + f_2\left[\ddot{x}(t-\tau)\right] + F_{\mathrm{int}}(t) \quad \text{with} \quad \tau > 0, \tag{3.1}$$

where $f_{0/1/2}$ are functions which are linear in $x(t-\tau)$, $\dot{x}(t-\tau)$ and $\ddot{x}(t-\tau)$, respectively. Note that $t-\tau$ indicates the whole range of past times, because in general the present particle motion at time t can depend on its whole history, due to causality. One can be more specific about the functions $f_{0/2}$ since it is clear that there must be a harmonic trapping force term $-\kappa x(t)$ and an inertia term $m\ddot{x}(t)$, where κ and m denote the optical tweezer's stiffness and the trapped particle's mass, respectively. Technically, the linearity of $f_{0/1/2}$ in positions, velocities and accelerations over a whole range of times can be described with integrals. One has

$$f_0\left[x(t-\tau)\right] = -\int_0^\infty \underbrace{\gamma_0(\tau)}_{=0,\,\text{homogeneity}} x(t-\tau)d\tau - \kappa x(t), \tag{3.2}$$

$$f_1\left[\dot{x}(t-\tau)\right] = -\int_0^\infty \gamma_1(\tau)\dot{x}(t-\tau)d\tau, \tag{3.3}$$

$$f_2\left[\ddot{x}(t-\tau)\right] = -\int_0^\infty \gamma_2(\tau)\ddot{x}(t-\tau)d\tau - m\ddot{x}(t), \tag{3.4}$$

with the memory functions $\gamma_{0/1/2}(\tau)$[‡]. In Eqs. (3.2) to (3.4) it is integrated over all positive time lags τ[§]. The memory functions $\gamma_{0/1/2}(\tau)$ are position-independent since the medium is assumed homogeneous[1]. Moreover, homogeneity of the medium implicates that one does not need to include a position memory term in Eq. (3.2)[2], i.e., $\gamma_0(\tau) = 0$. The only position dependence is then due to the optical trap. Further, the internal force $F_{\mathrm{int}}(t)$ is given by the random thermal force $F_{\mathrm{R}}(t)$ which originates from molecules of the medium which incessantly hit the trapped particle due to their thermal motion, see section 3.3. From these general arguments, Eq. (3.1) can be rewritten as general integro-differential equation

$$\underbrace{m\ddot{x}(t)}_{\text{inertia}} = \underbrace{-\int_0^\infty \gamma_1(\tau)\dot{x}(t-\tau)d\tau}_{\text{velocity memory}} \underbrace{-\int_0^\infty \gamma_2(\tau)\ddot{x}(t-\tau)d\tau}_{\text{acceleration memory}} \underbrace{-\kappa x(t)}_{\text{trapping force}} + \underbrace{F_{\mathrm{R}}(t)}_{\text{random thermal force}}, \tag{3.5}$$

where the interaction of the trapped object with the medium is specified by the velocity and acceleration memory terms. Eq. (3.5) represents an extension of the *generalized Langevin equation* [37] by a trapping force term and an acceleration memory term which accounts for inertial forces on the bead due to the backlash of displaced fluid. The generalized Langevin equation has been extensively applied in microrheology in non-biological [24] as well as in biological [30, 31] materials. Furthermore, the extension of the equation by acceleration memory has been used to describe the Brownian motion of a sphere in an incompressible fluid [38].

3.2 The complex friction retardation spectrum

In this section I switch to a frequency-dependent description of the problem attained by means of Fourier and Fourier-Laplace transforms. The complex frequency dependent *friction retardation spectrum* $\tilde{\gamma}(\omega)$ is introduced which accounts for all viscous and elastic processes in the interaction between particle and medium. Thereafter some physical examples which are relevant for experiments with optical tweezers are given.

3.2.1 Fourier transform of the equation of motion and definition of the friction retardation spectrum

A Fourier decomposition (see appendix A.2, page 139) of Eq. (3.5) gives

$$-\omega^2 m\tilde{x}(\omega) = \underbrace{-\mathrm{i}\omega\tilde{\gamma}(\omega)\tilde{x}(\omega)}_{\text{friction force } \tilde{F}_{\mathrm{fric}}(\omega)} - \kappa\tilde{x}(\omega) + \tilde{F}_{\mathrm{R}}(\omega), \tag{3.6}$$

[‡]Mathematically, $\gamma_{0/1/2}(\tau)$ can be understood as weighting functions which embody the importance of position/velocity/acceleration at past time $t-\tau$ for the present motion. The physical meaning of the functions $\gamma_{1/2}(\tau)$ is frictional or hydrodynamic memory. This is discussed in more detail in section 3.2.

[§]In the literature mostly another parameterization of the memory integral $-\int_0^\infty \gamma_1(\tau)\dot{x}(t-\tau)d\tau$ is used [27,37], where the integration range is $(-\infty, t)$. To avoid the present time t being an integral boundary and because it appears more intuitive, a parameterization with integral boundaries $(0, \infty)$ will be used. See appendix A.1.

[1]Note that position independence of $\gamma_1(\tau)$ and $\gamma_2(\tau)$ are a requirement for linearity.

[2]In other words, it is not important for the present motion of the particle where it was in the past.

with the *friction retardation spectrum*,

$$\tilde{\gamma}(\omega) \equiv \tilde{\gamma}_1(\omega) + \mathrm{i}\omega\tilde{\gamma}_2(\omega), \tag{3.7}$$

in which the real part accounts for dissipative processes, whereas the imaginary part accounts for elastic processes.

3.2.2 Simple viscous friction

Simple viscous friction is instantaneous and only coupled to the velocity of the particle,

$$\begin{aligned} \gamma_1(t) &= \gamma_0\delta(t), \\ \gamma_2(t) &= 0. \end{aligned} \tag{3.8}$$

Here, γ_0 represents the constant *friction coefficient*. For a spherical particle of radius R which is immersed in a viscous liquid of viscosity η it is given by the *Stokes law*,

$$\gamma_0 = 6\pi\eta R. \tag{3.9}$$

From the Fourier-Laplace transform of Eq. (3.8) one obtains a *frequency-independent* friction retardation spectrum,

$$\tilde{\gamma}(\omega) = \gamma_0. \tag{3.10}$$

3.2.3 Hydrodynamic interactions between a microsphere and a simple viscous medium

In this section, also the acceleration memory term in Eq. (3.5) has is taken into account. This term corresponds physically to an inertial force from entrained fluid. The acceleration memory term has not been included explicitly in the approaches for microrheology mentioned in section 3.2.4, though one should expect that it is non-zero in general viscoelastic media. It is straightforward to extend those approaches for the presence of acceleration memory. In fact, the mathematical description in these approaches will not change at all, one only has to understand the friction retardation spectrum $\tilde{\gamma}(\omega)$ as the full expression, Eq. (3.7). In the following, I present two examples from the literature where the friction retardation spectrum becomes frequency-dependent because of hydrodynamic interactions.

Stokes friction for a sphere in harmonic rectilinear motion in an incompressible fluid

In 1851 Stokes considered the hydrodynamics of an incompressible fluid surrounding a sphere of radius R that performs rectilinear harmonic motion with no-slip boundary condition, at vanishing Reynolds number, and with the fluid at rest at infinity [38,39]. Stokes found an expression for the frequency-dependent frictional force which gives the friction retardation spectrum

$$\tilde{\gamma}_{\mathrm{Stokes}}(\omega) = \gamma_0 \left(1 + (1-\mathrm{i})\frac{R}{d(\omega)} - \mathrm{i}\frac{2R^2}{9d(\omega)^2}\right). \tag{3.11}$$

Here, $d(\omega)$ is the *penetration depth* which characterizes the exponential decrease of the fluids velocity field as a function of the distance from the oscillating sphere. It is given by

$$d(\omega) = \left(\frac{2\nu}{\omega}\right)^{1/2}. \tag{3.12}$$

From a Fourier back transform of the corresponding frictional force which is exerted on a particle following an arbitrary trajectory $x(t)$, one gets the memory functions ([37, 38] and references therein)

$$\begin{aligned} \tilde{\gamma}_1(\tau) &= \gamma_0\delta(\tau), \\ \tilde{\gamma}_2(\tau) &= \frac{2}{3}\pi R^3\delta(\tau) + 6\pi\rho R^3 f_\nu^{1/2}\tau^{-1/2}. \end{aligned} \tag{3.13}$$

Here, $f_\nu = \nu/(\pi R^2)$ represents a ratio between the kinematic friction ν and the cross sectional area of the sphere. Since during its *past* motion the particle was displacing fluid, the *present* motion of the fluid is affected. One has *backflow effects* which cause that the present friction between particle and fluid depends on the past motion of the particle. The memory functions in Eq. (3.13) describe quantitatively how the interaction force between body and fluid depends on the body's past motion.

Proximity of a hard wall

Many applications of optical tweezers require that the trapped microsphere is close to the microscope coverslip which can be considered as a *hard wall*. Consequently one must include the hydrodynamic interaction between the microsphere and the essentially infinite surface of the coverslip [40]. For a sphere undergoing linear oscillating motion parallel to a plane, one finds the friction retardation spectrum,

$$\begin{aligned} \tilde{\gamma}_{\mathrm{hw},R/l}(\omega) = \tilde{\gamma}_{\mathrm{Stokes}}(\omega) \quad & \left\{1 + \frac{9}{16}\frac{R}{l}\times \right. \\ & \left[1 - \frac{1-\mathrm{i}}{3}\frac{R}{d(\omega)} + \frac{2\mathrm{i}}{9}\left(\frac{R}{d(\omega)}\right)^2 \right. \\ & \left.\left. + \frac{4}{3}\left\{1 - \exp\left[-(1-\mathrm{i})(2l+R)/d(\omega)\right]\right\}\right]\right\}, \end{aligned} \tag{3.14}$$

where l is the distance from the sphere's center to the coverslip plane.

3.2.4 Viscoelastic media

Incompressible viscoelastic media and one-point microrheology

For viscoelastic incompressible one-component media, the friction retardation spectrum $\tilde{\gamma}(\omega)$ is related to the viscoelastic shear modulus $G(\omega)$. One has a simple relationship between these quantities which is the generalized Stokes law, Eq. (2.6).

Viscoelastic two-fluid medium

Levine and Lubensky calculated the response function[3] $\alpha(\omega) \equiv 1/(\mathrm{i}\omega\tilde{\gamma}(\omega))$ of a sphere in a viscoelastic *two*-fluid medium which consists of an elastic network permeated by a viscous fluid [41]. The dynamic shear modulus of the medium is assumed to be given by $G(\omega) = \mu(\omega) - i\omega\eta$ where η represents the viscosity of the background solvent and $\mu(\omega)$ is the *complex*, frequency-dependent shear modulus of the network. From Levine and Lubensky's result one obtains for the friction retardation spectrum

$$\tilde{\gamma}(\omega) = 6\pi\frac{G(\omega)}{\mathrm{i}\omega}R\left\{1 + J(\omega) + \frac{1}{1 - X(\omega)}\frac{G(\omega)}{4\mu + 2\lambda}H\left[\frac{\omega}{\omega_\mathrm{B}}\right]\right\}^{-1}. \tag{3.15}$$

Here, $J(\omega)$ and $X(\omega)$ are terms which contain corrections to the response function coming from the inertia of the two-fluid medium and from the difference in the stresses in the background fluid and in the viscoelastic network, respectively. λ is the Lame coefficient of the network which may in general be a complex function of frequency[4]. The *crossover frequency* ω_B is characterized by the decay time of the network compression mode at the length scale of the bead. Thus the function $H\left[\frac{\omega}{\omega_\mathrm{B}}\right]$ controls the cross-over from compressible network dynamics to an incompressible network.

Obviously, Eq. (3.15) represents an extension of the generalized Stokes law, Eq. (2.6), for two-fluid media that accounts for the interaction processes between background fluid and viscoelastic network which are happening when a microsphere is moving in the medium. Eq. (3.15) demonstrates that it is difficult to obtain a correct expression for the friction retardation spectrum $\tilde{\gamma}(\omega)$ even if one has a good model for the viscoelastic modulus $G(\omega)$ of the network. The other way around, because it is difficult to determine the correction terms, it is difficult to obtain the correct modulus $G(\omega)$ from a measured friction retardation spectrum $\tilde{\gamma}(\omega)$, i.e., microrheology as described in section 3.2.4 is of limited use here. The solution to this problem is to measure the correlation in the motion of *two* microspheres [42]. This technique is called *two-point microrheology* and it yields clearer information about the network modulus $\mu(\omega)$. Two-point microrheology has been applied extensively during the past years in bulk media [25, 31, 43–46], and for particles embedded in membranes [47] .

Crosslinked actin networks

From the viscoelastic modulus theoretically derived by Gittes and MacKintosh [48], Mizuno et al. calculated the response function $\alpha(\omega)$ for a bead inside a cross-linked actin network [49]. From that result which agrees well with experimental data for frequencies higher than $\sim 100\,\mathrm{Hz}$ [49] one obtains for the friction retardation spectrum

$$\tilde{\gamma}(\omega) = \frac{1}{\mathrm{i}\omega}\left(\frac{5}{2\pi R\rho_\mathrm{actin}l_\mathrm{c}}\frac{1}{k_\mathrm{B}Tq_1^4l_\mathrm{p}}\sum_{n=1}^{\infty}\frac{1}{n^4 - \mathrm{i}\omega/2\omega_1}\right)^{-1} - \mathrm{i}\omega m. \tag{3.16}$$

Here, R is the bead radius, ρ_actin is the length density of actin filaments per unit volume, l_c it the mean distance between crosslinks, $q_1 = \pi/l_\mathrm{c}$, $l_\mathrm{p} = \kappa_\mathrm{bend}/(k_\mathrm{B}T)$ is the persistence length and

[3] The response function will be introduced in chapter 4.

[4] λ and μ together define the compression modulus, $K_\mathrm{V} = \lambda + 2\mu/3$.

$\omega_1 = (\kappa_{\rm bend}/\zeta)q_1^4$. Further, $\kappa_{\rm bend}$ is the bending modulus of the individual actin filaments and ζ is the transverse friction coefficient per unit length of a filament. Eq. (3.16) describes the response of a bead in an actin network in the *absence of tension*. That model has been generalized for the presence of a tension σ. The generalized model has been found to be consistent with data from a bead within an actin-myosin solution where the actin network is under tension due to the activity of myosin motors [49].

Viscoelastic liquids and solids

According to Qian [50], viscoelastic media can be subdivided into two classes: viscoelastic liquids and viscoelastic solids. *Viscoelastic liquids* exhibit only transient elasticity which means that the memory function $\gamma_1(t)$ is approaching 0 for $t \to \infty$. In other words, in viscoelastic liquids the diffusion of the particle will only be confined by the optical trap potential. *Viscoelastic solids* on the other hand involve a contribution to $\gamma_1(t)$ which is constant over time. Consequently one obtains a simple elasticity term of the same structure like the trapping force term which corresponds to persistent elasticity. An example for a viscoelastic solid is a medium in which the particle remains trapped within a strong network of filaments. Thus the particle feels two traps, the optical trap and the trap generated by filaments. Both traps will affect the long-time limit of diffusion.

3.3 Random force

After the consideration of the friction retardation spectrum $\tilde{\gamma}(\omega)$ in the last section, I will turn now to another important and complicated quantity which shows up in Eq. (3.5). This quantity is the random force $F_{\rm R}(t)$. The Fourier transformed of the random force $\tilde{F}_{\rm R}(\omega)$ is characterized by a correlation function which is given by the *fluctuation-dissipation theorem of second kind* (Ref. [51], pages 268-270 and Ref. [37], pages 33-37),

$$\langle \tilde{F}_{\rm R}(\omega)\tilde{F}_{\rm R}^*(\omega')\rangle = 2k_{\rm B}T{\rm Re}\left\{\tilde{\gamma}(\omega)\delta(\omega-\omega')\right\}. \tag{3.17}$$

Note that the delta function on the left hand side of Eq. (3.17) does not imply that one has white noise. Eq. (3.17) gives rather the colour of the noise by modulating the delta function with the the friction retardation spectrum $\tilde{\gamma}(\omega)$. Thus Eq. (3.17) represents a general expression for the correlation function of the random force *in the frequency domain*, but it can be formulated equivalently in the time-domain. By applying the Fourier back transform twice one obtains

$$\begin{aligned}
\langle F_{\rm R}(t_1)F_{\rm R}(t_2)\rangle &= \int_{-\infty}^{\infty}d\omega\int_{-\infty}^{\infty}d\omega'\left\langle F_{\rm R}(\omega)\tilde{F}_{\rm R}^*(\omega')\right\rangle\exp\{{\rm i}\omega t_1\}\exp\{-{\rm i}\omega' t_2\}\\
&= 2k_{\rm B}T\int_{-\infty}^{\infty}d\omega{\rm Re}\left\{\tilde{\gamma}(\omega)\right\}\exp\{{\rm i}\omega(t_1-t_2)\}\\
&= 2k_{\rm B}T\int_{-\infty}^{\infty}d\omega\frac{1}{2}\int_{-\infty}^{\infty}dt\left\{\gamma_{1,{\rm s}}(t)+\dot{\gamma}_{2,{\rm s}}(t)\right\}\exp\{-{\rm i}\omega t\}\exp\{{\rm i}\omega(t_1-t_2)\}\\
&= k_{\rm B}T\left\{\gamma_{1,{\rm s}}(t_1-t_2)+\dot{\gamma}_{2,{\rm s}}(t_1-t_2)\right\}.
\end{aligned} \tag{3.18}$$

Here, it has been used that the real part of the friction retardation spectrum is given by

$$\mathrm{Re}\{\tilde{\gamma}(\omega)\} = \frac{1}{2}\int_{-\infty}^{\infty} dt\,\{\gamma_{1,\mathrm{s}}(t) + \dot{\gamma}_{2,\mathrm{s}}(t)\}\exp\{-\mathrm{i}\omega t\}, \tag{3.19}$$

with the symmetrized functions $\gamma_{1,\mathrm{s}}(t)$ and $\dot{\gamma}_{2,\mathrm{s}}(t)$[5]. The fluctuation-dissipation theorem of second kind, Eq. (3.17) can be regarded as a consequence of the fluctuation-dissipation theorem of first kind which will be introduced in chapter 4, but it can also be obtained from relating the correlation function of the random force to the correlation function of the random stress tensor [52]. Eqs. (3.17) and (3.18) both state that if one has frequency-*in*dependent friction, $\tilde{\gamma}(\omega) = \text{const.}$, which corresponds to that $\gamma_{1,\mathrm{s}}(t)$ and $\dot{\gamma}_{2,\mathrm{s}}(t)$ are both proportional to $\delta(t)$, there will be no correlations in the random force[6]. This is the case for simple viscous friction (see paragraph 3.2.2) and one refers to the random force as *white noise*. If on the other hand one does *not* only have such instantaneous friction, one will have correlations in the random force. This follows automatically from the frequency-dependence of $\tilde{\gamma}(\omega)$ in Eq. (3.17). Accordingly, in that case the random force can not longer be designated as white noise, it must rather be addressed as *coloured noise*. Coloured noise arises in all cases which are described in sections 3.2.3 and 3.2.4[7]. In some cases the colouring of the noise will be only observable at very high frequencies, however.

With Eq. (3.17), the thermal force can be written as

$$\tilde{F}_{\mathrm{R}}(\omega) = \sqrt{2k_{\mathrm{B}}T\mathrm{Re}\{\tilde{\gamma}(\omega)\}}\tilde{\eta}(\omega), \tag{3.20}$$

where $\tilde{\eta}(\omega)$ is an uncorrelated Gaussian process with

$$\langle\tilde{\eta}(\omega)\tilde{\eta}^*(\omega')\rangle = \delta(\omega - \omega'). \tag{3.21}$$

3.4 Power spectrum

In experiments, the trajectory is measured for a finite measuring time T_{m} and one may expand the trajectory into a Fourier series with discrete frequencies $\omega_k = 2\pi k/T_{\mathrm{m}}$ $(k = 0, \pm1, \pm2, ...)$ (see appendix A.4, page 140). As an approximation for the delta-function on the right-hand sides of Eqs. (3.17) and (3.21) which is continuous in the frequency ω, one may write

$$\lim_{T_{\mathrm{m}}\to\infty}\frac{T_{\mathrm{m}}}{2\pi}\delta_{k,k'} = \delta(\omega_k - \omega_{k'}). \tag{3.22}$$

The *power spectrum* is proportional to the average intensity of the Fourier expansion coefficients[8]. From the Fourier transform of the equation of motion, Eq. (3.6), and from Eq. (3.17) one obtains

[5] In the literature one often forgets about the subscript s for the symmetrized function. It is included here for mathematical correctness as done in the book of Kubo [37].

[6] Note that $\dot{\gamma}_{2,\mathrm{s}}(t) \propto \delta(t)$ and symmetry of $\gamma_{2,\mathrm{s}}(t)$ together require $\gamma_{2,\mathrm{s}}(t)$ to be zero, since $\dot{\theta}(t) = \delta(t)$. This implies that *any* non-zero acceleration-dependence of the friction causes colored noise.

[7] An experiment in which the noise coloring due to the hydrodynamic interactions described in paragraph 3.2.3 is directly observed is suggested in Ref. [53].

[8] The physical meaning of the power spectrum can be illustrated in the following way: If $x(t)$ would be the noise produced between two terminals of an electrical network, $P(\omega)$ would be the intensity of the noise heard by filtering frequencies to a narrow bandwidth $\Delta\omega$ around ω.

for the power spectrum at frequency $\omega = \omega_k$

$$P(\omega) \equiv \lim_{T_\mathrm{m}\to\infty} \frac{\langle|\hat{x}_k|^2\rangle}{T_\mathrm{m}} = \frac{2k_\mathrm{B}T\mathrm{Re}\left\{\tilde{\gamma}(\omega)\right\}}{|\kappa + \mathrm{i}\omega\tilde{\gamma}(\omega) - \omega^2 m|^2}, \tag{3.23}$$

by approximating the Fourier transform by a Fourier series with $T_\mathrm{m} \to \infty$ and by using Eq. (3.22).

4 The trapped particle in a viscoelastic medium under external perturbation

In this chapter, I describe systems out of equilibrium where a time-dependent external perturbation is added to the undriven system of the last chapter. These systems are denoted as *driven systems*. The perturbation is taken into account as an external force in section 4.1. Average positions of the trapped particle are linked to this external force via the response function which is introduced in section 4.2. In section 4.3 the Kramers-Kronig relations are presented which relate the real and imaginary part of the response function to each other. The fluctuation-dissipation theorem which connects equilibrium systems from chapter 3 to perturbed systems is introduced in section 4.4. Two practical options to perturb the system are relocation of the trap position and relocation of the piezo stage position as portrayed in sections 4.5 and 4.6, respectively. A convenient measurable quantity related to these options of driving the system is the active spectrum which is introduced in section 4.7.

4.1 Equation of motion with external force

A time-dependent external force $F_{\mathrm{ext}}(t)$ is added to the equation of motion of the undriven system, Eq. (3.5). Thus one has

$$\underbrace{m\ddot{x}(t)}_{\text{inertia}} = \underbrace{-\int_0^\infty \gamma_1(\tau)\dot{x}(t-\tau)d\tau}_{\text{velocity memory}} \underbrace{-\int_0^\infty \gamma_2(\tau)\ddot{x}(t-\tau)d\tau}_{\text{acceleration memory}} \underbrace{-\kappa x(t)}_{\text{trapping force}} + \underbrace{F_{\mathrm{R}}(t)}_{\text{R thermal force}} + F_{\mathrm{ext}}(t). \tag{4.1}$$

4.2 The response function

Under a perturbation, the average value $\langle x\rangle$ is in general different from zero while in equilibrium one has $\langle\tilde{x}\rangle = 0$. For a small time-dependent perturbation, a linear relationship between the Fourier components of the external force and the Fourier components of the response exists [54],

$$\langle\tilde{x}(\omega)\rangle = \chi(\omega)\tilde{F}_{\mathrm{ext}}(\omega). \tag{4.2}$$

$\chi(\omega)$ is called *response function* or generalized susceptibility. Whereas the real part of the response function describes the reactive response which is in-phase with the driving force, the imaginary part of the response function describes how the system dissipates energy, since it is out of phase with the driving force. A Fourier decomposition of Eq. (4.1) gives

$$-\omega^2 m\tilde{x}(\omega) = -\mathrm{i}\omega\tilde{\gamma}(\omega)\tilde{x}(\omega) - \kappa\tilde{x}(\omega) + \tilde{F}_{\mathrm{R}}(\omega) + \tilde{F}_{\mathrm{ext}}(\omega). \tag{4.3}$$

From averaging and taking into account that the random force is zero in average, $\langle\tilde{F}_{\mathrm{R}}(\omega)\rangle = 0$, one obtains

$$\chi(\omega) = \frac{1}{\kappa + \mathrm{i}\omega\tilde{\gamma}(\omega) - \omega^2 m}. \tag{4.4}$$

The response function $\chi(\omega)$ describes the response of a system where the particle is caught by a static harmonic trap of stiffness κ which is centered at position $x_{\mathrm{L}} = 0$ to a time-dependent external force. In the literature, one often uses the response function of the system which does not comprise the static optical trap,

$$\alpha(\omega) = \frac{1}{\mathrm{i}\omega\tilde{\gamma}(\omega) - \omega^2 m}. \tag{4.5}$$

From

$$\langle\tilde{x}(\omega)\rangle = \alpha(\omega)\left[-\kappa\langle\tilde{x}(\omega)\rangle + \tilde{F}_{\mathrm{ext}}(\omega)\right] = \chi(\omega)\tilde{F}_{\mathrm{ext}}(\omega) \tag{4.6}$$

one obtains a relationship between $\chi(\omega)$ and $\alpha(\omega)$ [25],

$$\chi(\omega) = \frac{1}{1/\alpha(\omega) + \kappa}. \tag{4.7}$$

4.3 The Kramers-Kronig relations

The *Kramers-Kronig relations* are mathematical properties which connect the real and imaginary parts of any complex function analytic in the upper half plane. These relations are often used to relate the real and imaginary parts of response functions in physical systems because causality implies that the analyticity condition is satisfied and conversely.

The real part of the response function, $\chi'(\omega)$, is related to the imaginary part $\chi''(\omega)$ by the Kramers-Kronig relation (KKR) [10, 11, 25, 54]

$$\chi'(\omega) = \frac{2}{\pi}\mathcal{P}\int_0^\infty d\zeta \frac{\zeta\chi''(\zeta)}{\zeta^2 - \omega^2} \tag{4.8}$$

$$= -\frac{2}{\pi}\int_0^\infty \cos(\omega t)dt \int_0^\infty \chi''(\zeta)\sin(\zeta t)d\zeta, \tag{4.9}$$

where $\mathcal{P}$ denotes a principal-value integral, meaning the $\epsilon \to 0$ limit of the sum of two ζ integrals, from 0 to $\omega - \epsilon$, and from $\omega + \epsilon$ to ∞. However, as written in Eq. (4.9), this is equivalent to successive sine and cosine transforms of $\chi''(\omega)$ which can be conveniently performed for the discrete data points of a long time series [10]. The second KKR which conversely relates the imaginary part of the response function to the real part is given by

$$\chi''(\omega) = -\frac{2\omega}{\pi}\mathcal{P}\int_0^\infty d\zeta \frac{\chi'(\zeta)}{\zeta^2 - \omega^2} \tag{4.10}$$

In the time-domain, the equation defining the response function, Eq. (4.2), becomes

$$\langle x(t)\rangle = \int_0^\infty \chi(\tau)F_{\mathrm{ext}}(t-\tau)d\tau. \tag{4.11}$$

For the special case of the system of a trapped bead immersed in a viscoelastic medium, the response function $\chi(\tau)$ describes how the average position $\langle x(t)\rangle$ of the trapped bead responds to an applied time-dependent force history $F_{\mathrm{ext}}(t-\tau)$. In general, the response $\chi(\tau)$ must be

zero for $\tau < 0$ since a system cannot respond to a force before it is applied. It can be shown that this causality condition implies that the Fourier transform $\chi(\omega)$ is analytic in the upper half plane.

The Kramers-Kronig relations have a physical interpretation. The imaginary part of a response function describes how a system dissipates energy, since it is out of phase with the driving force. The Kramers-Kronig relations imply that observing the dissipative response of a system is sufficient to determine its in-phase (reactive) response, and vice versa.

4.4 The fluctuation-dissipation theorem

The power spectrum, Eq. (3.23), and the response function, Eq. (4.4), are apparently related to each other. One has

$$\chi''(\omega) = -\frac{\omega}{2k_{\mathrm{B}}T} P(\omega) \tag{4.12}$$

which is the *fluctuation-dissipation theorem* (FDT), sometimes referred to as FDT of first kind in order to distinguish it from that of second kind which has been presented in section 3.3. The FDT of first kind is fundamental, it can derived from basic principles within linear response theory in a general way [37]. It states that the linear response of a given system to an external perturbation is expressed in terms of fluctuation properties of the system in thermal equilibrium. The minus sign in the FDT, Eq. (4.12), is due to our sign convention of the Fourier transform which has a " $-$ " sign in the argument of the exponential of the forward transform, see appendix A.2. Note that in microrheology one frequently uses the other sign convention with a " $+$ " sign, e.g. in Refs. [10, 11, 25, 45].

4.5 Relocating the laser

Moving the position of the trap center which corresponds to a relocation of the laser, is one possibility to drive the system of the trapped bead immersed in a viscoelastic medium. It was applied already in the context of calibration of optical tweezers [55] for the factor $\beta = x(t)/x^{\mathrm{volt}}(t)$ which gives the conversion of the quadrant photo diode (QPD) voltage signal to actual particle positions. The equation of motion for a particle which is trapped by a relocatable optical tweezers inside a viscoelastic medium is given by

$$\begin{aligned} m\ddot{x}(t) = & - \int_0^\infty \gamma_1(\tau)\dot{x}(t-\tau)d\tau \\ & - \int_0^\infty \gamma_2(\tau)\ddot{x}(t-\tau)d\tau \\ & - \kappa \left(x(t) \underbrace{-x_{\mathrm{L}}(t)}_{\text{laser driving}} \right) + F_{\mathrm{R}}(t). \end{aligned} \tag{4.13}$$

The position $x(t)$ is measured in the resting frame of the stage. Within this frame, the laser is moved with the driving function $x_{\mathrm{L}}(t)$ which represents the time-dependent position of the laser.

This situation is denoted as *laser driving*. The situation described by Eq. (4.13) is sketched in Fig. 4.1 (panel (a)). Laser driving is one approach to drive the system within the active part

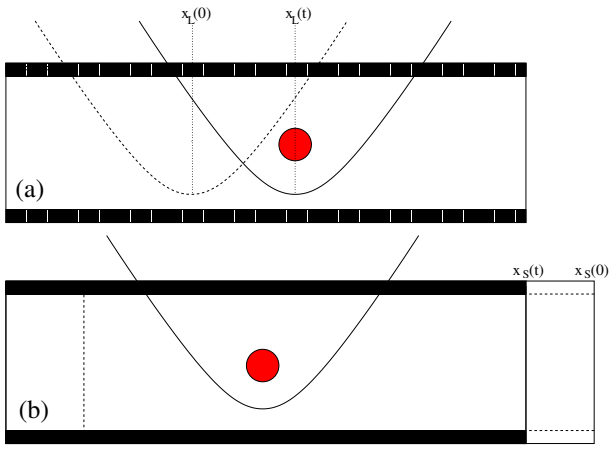

Figure 4.1: (a): Sketch of the situation described by Eq. (4.1). The trapped particle is situated inside a resting medium. The optical tweezers which acts approximately like a harmonic potential on the bead is moving. (b): Sketch of the situation described by Eq. (4.14). The trapped particle is situated inside a medium which is placed on the moving stage. The optical tweezers which acts like a harmonic potential on the bead is at rest.

of our new calibration method which will be presented in chapter 6. Laser driven systems have been simulated in the course of the verification of the novel calibration method, see chapter 7.

4.6 Relocating the stage

Another possibility to drive the system is moving the stage, as performed in recent work on calibration in viscous media [56]. The equation of motion for a particle which is trapped by a stationary laser while the stage is moved is given by

$$\begin{aligned} m\ddot{x}(t) = &- \int_0^\infty \gamma_1(\tau) \left(\dot{x}(t-\tau) \underbrace{-v_\mathrm{S}(t-\tau)}_{\text{stage driving}} \right) d\tau \\ &- \int_0^\infty \gamma_2(\tau) \left(\ddot{x}(t-\tau) \underbrace{-\dot{v}_\mathrm{S}(t-\tau)}_{\text{stage driving}} \right) d\tau \\ &- \kappa x(t) + F_\mathrm{R}(t). \end{aligned} \tag{4.14}$$

The position $x(t)$ is now measured in the resting frame of the laser. The stage is moved within this frame with the driving function $x_\mathrm{S}(t)$. We denote this situation *stage driving*. The velocity of the stage is represented by $v_\mathrm{S}(t) = \dot{x}_\mathrm{S}(t)$. The integral terms contain now the past relative velocities $\dot{x}(t-\tau) - v_\mathrm{S}(t-\tau)$ and accelerations $\ddot{x}(t-\tau) - \dot{v}_\mathrm{S}(t-\tau)$ of the particle relative to the medium, which is assumed to be co-moving with the stage. With a sample holder that is not sealed at

the ends, one has open boundary conditions and this assumption is only exact if the stage is not driven too fast and the bead is close to one of the coverslips[1]. On the contrary, for a stage oscillating a non-sealed sample holder at higher driving frequencies, the liquid motion midway between the coverslips can deviate considerably from the motion of the stage [56]. Fig. 4.1(b) shows a sketch of the situation described by Eq. (4.14). Beside laser driving, stage driving is another approach to drive the system within the active part of the novel calibration method which is be presented in chapter 6. For the verification of the calibration method, trajectories from stage driven systems have been used which were generated in simulations, see section 7, or measured in experiments, see section 8.

4.7 The active spectrum

In this section two measurable quantities are introduced which are denoted as active spectrum for laser/stage driving, $\tilde{R}_{\mathrm{L/S}}(\omega)$. These active spectra are complex magnitudes which are derived from the response function $\chi(\omega)$. Their real parts are very similar to the power spectrum of the undriven system. The latter fact is crucial, since it will allow to write down the fluctuation-dissipation theorem of section 4.4 in a convenient way. This will directly lead to the novel calibration method as presented in chapter 6. This section mainly serves as a formula collection, in which the active spectrum will be introduced formally and relations will be derived which will be used later in this thesis.

4.7.1 Definition of the active spectrum

In sections 4.5 and 4.6 two ways to drive the system were proposed which are relocating the laser (L) and relocating the piezo stage (S). These perturbations correspond to external forces which are characterized according to

$$\tilde{F}_{\mathrm{ext,L/S}} = \tilde{c}_{\mathrm{L/S}}(\omega)\tilde{d}_{\mathrm{L/S}}(\omega) \tag{4.15}$$

by a coupling part,

$$\tilde{c}_{\mathrm{L}}(\omega) = \quad -\tfrac{\kappa}{\mathrm{i}\omega} \qquad (\mathrm{L}), \tag{4.16}$$

$$\tilde{c}_{\mathrm{S}}(\omega) = \quad \tilde{\gamma}(\omega) \qquad (\mathrm{S}), \tag{4.17}$$

which is a function of the system's internal parameters κ and $\tilde{\gamma}(\omega)$ and by a controlled part

$$\tilde{d}_{\mathrm{L}}(\omega) = \quad -\mathrm{i}\omega\tilde{x}_{\mathrm{L}}(\omega) \qquad (\mathrm{L}), \tag{4.18}$$

$$\tilde{d}_{\mathrm{S}}(\omega) = \quad \mathrm{i}\omega\tilde{x}_{\mathrm{S}}(\omega) \qquad (\mathrm{S}). \tag{4.19}$$

which is proportional to the laser/stage velocity spectrum[2]. The *active spectrum for laser/stage driving* $\tilde{R}_{\mathrm{L/S}}(\omega)$ is then defined as the ratio between the average positional spectrum of the trapped particle $\langle\tilde{x}(\omega)\rangle$ and the controlled part $\tilde{d}_{\mathrm{L/S}}(\omega)$,

$$\tilde{R}_{\mathrm{L/S}}(\omega) := \frac{\langle\tilde{x}(\omega)\rangle}{\tilde{d}_{\mathrm{L/S}}(\omega)}. \tag{4.20}$$

[1] Very close to one of the coverslips the medium can be assumed to be co-moving with the stage due to non-slip boundary conditions.

[2] The sign convention in Eq. (4.18) is made for later convenience.

Note that the unit of $\tilde{R}_{\mathrm{L/S}}(\omega)$ is a time. From Eqs. (4.2), (4.15) and (4.20) one finds for the active spectrum

$$\tilde{R}_{\mathrm{L/S}}(\omega) = \tilde{c}_{\mathrm{L/S}}(\omega)\chi(\omega), \tag{4.21}$$

so it turns out that the active spectrum is equal to the product of the coupling part $\tilde{c}_{\mathrm{L/S}}(\omega)$ and the response function $\chi(\omega)$. According to Eq. (4.21) one has from Eqs. (4.16)/(4.17)

$$\tilde{R}_{\mathrm{L}}(\omega) = -\tfrac{\kappa}{\mathrm{i}\omega}\chi(\omega) \qquad (\mathrm{L}), \tag{4.22}$$

$$\tilde{R}_{\mathrm{S}}(\omega) = \tilde{\gamma}(\omega)\chi(\omega) \qquad (\mathrm{S}). \tag{4.23}$$

4.7.2 The active spectrum $\tilde{R}_{\mathrm{L/S}}(\omega)$ in terms of amplitudes and phase angles

The definition of the active spectrum, Eq. (4.20), gives a general measurement prescription. In an experiment, one typically determines amplitudes and phase angles instead of the pure spectra $\langle\tilde{x}(\omega)\rangle$ and $\tilde{d}_{\mathrm{L/S}}(\omega)$. In this paragraph, general relations for the active spectrum in terms of the laser/stage amplitude $A_{\mathrm{L/S}}(\omega)$, the particle amplitude $A_{\mathrm{P}}(\omega)$ and the phase shift $\Delta\phi(\omega)$ between laser/stage and trapped particle are derived. Here, the frequency ω should be understood as parameter of the Fourier spectrum and the amplitudes $A_{\mathrm{P/L/S}}(\omega)$ are the absolute values and $\phi_{\mathrm{P/L/S}}(\omega)$ are the phase angles of the Fourier transform of the particle/laser/stage motion at frequency ω. From the controlled part, Eqs. (4.18)/(4.19), and the definition, Eq. (4.20), one has

$$\tilde{R}_{\mathrm{L}}(\omega) = \tfrac{\langle\tilde{x}(\omega)\rangle}{-\mathrm{i}\omega\tilde{x}_{\mathrm{L}}(\omega)} \qquad (\mathrm{L}), \tag{4.24}$$

$$\tilde{R}_{\mathrm{S}}(\omega) = \tfrac{\langle\tilde{x}(\omega)\rangle}{\mathrm{i}\omega\tilde{x}_{\mathrm{S}}(\omega)} \qquad (\mathrm{S}). \tag{4.25}$$

The active spectrum is complex magnitude and therefore one can write it as

$$\tilde{R}_{\mathrm{L/S}}(\omega) = \mathrm{Re}\{\tilde{R}_{\mathrm{L/S}}(\omega)\} + \mathrm{i}\,\mathrm{Im}\{\tilde{R}_{\mathrm{L/S}}(\omega)\} = |\tilde{R}_{\mathrm{L/S}}(\omega)|\exp(\mathrm{i}\psi(\omega)) \tag{4.26}$$

with the phase angle $\psi(\omega)$. The particle positional spectrum and the laser/stage positional spectrum are complex functions, too,

$$\langle\tilde{x}(\omega)\rangle = A_{\mathrm{P}}(\omega)\exp(-\mathrm{i}\phi_{\mathrm{P}}(\omega)), \tag{4.27}$$

$$\tilde{x}_{\mathrm{L}}(\omega) = A_{\mathrm{L}}(\omega)\exp(-\mathrm{i}\phi_{\mathrm{L}}(\omega)), \tag{4.28}$$

$$\tilde{x}_{\mathrm{S}}(\omega) = A_{\mathrm{S}}(\omega)\exp(-\mathrm{i}\phi_{\mathrm{S}}(\omega)), \tag{4.29}$$

with the amplitudes $A_{\mathrm{P/L/S}}(\omega)$ and phase angles $\phi_{\mathrm{P/L/S}}(\omega)$ of the particle, the laser and the stage, respectively. With the definitions, Eq. (4.24)/(4.25), one can put the active spectrum into the following form,

$$\tilde{R}_{\mathrm{L}}(\omega) = \tfrac{A_{\mathrm{P}}}{\omega A_{\mathrm{L}}(\omega)}\exp(\mathrm{i}(\Delta\phi(\omega)+\pi/2)) \qquad (\mathrm{L}), \tag{4.30}$$

$$\tilde{R}_{\mathrm{S}}(\omega) = \tfrac{A_{\mathrm{P}}}{\omega A_{\mathrm{S}}(\omega)}\exp(\mathrm{i}(\Delta\phi(\omega)-\pi/2)) \qquad (\mathrm{S}),, \tag{4.31}$$

with the *phase shift* $\Delta\phi(\omega) := \phi_{\mathrm{L/S}}(\omega) - \phi_{\mathrm{P}}(\omega)$. For the amplitude of the active spectrum one finds

$$|\tilde{R}_{\mathrm{L/S}}(\omega)| = \frac{A_{\mathrm{P}}(\omega)}{\omega A_{\mathrm{L/S}}(\omega)}. \tag{4.32}$$

By comparison between Eq. (4.26) and Eqs. (4.30)/(4.31), relationships between the the phase angle $\psi(\omega)$ of the active spectrum and the phase shift $\Delta\phi(\omega)$ between laser/stage and particle can be found,

$$\psi(\omega) = \Delta\phi(\omega) + \pi/2 \qquad \text{(L)}, \tag{4.33}$$

$$\psi(\omega) = \Delta\phi(\omega) - \pi/2 \qquad \text{(S)} \tag{4.34}$$

From that result one immediately obtains relationships between the trigonometric functions,

$$\sin[\psi(\omega)] = \cos[\Delta\phi(\omega)] \quad \text{(L)}, \tag{4.35}$$

$$\sin[\psi(\omega)] = -\cos[\Delta\phi(\omega)] \quad \text{(S)}, \tag{4.36}$$

and

$$\cos[\psi(\omega)] = -\sin[\Delta\phi(\omega)] \quad \text{(L)}, \tag{4.37}$$

$$\cos[\psi(\omega)] = \sin[\Delta\phi(\omega)] \quad \text{(S)}, \tag{4.38}$$

and further

$$\tan[\psi(\omega)] = -\cot[\Delta\phi(\omega)] \quad \text{(L)}, \tag{4.39}$$

$$\tan[\psi(\omega)] = -\cot[\Delta\phi(\omega)] \quad \text{(S)}. \tag{4.40}$$

Later the real part and the imaginary part of the active spectrum will be needed. In terms of the amplitude and the phase angle of the active spectrum the real part is given by

$$\mathrm{Re}\{\tilde{R}_\mathrm{L}(\omega)\} = -\frac{A_\mathrm{P}(\omega)}{\omega A_\mathrm{L}(\omega)}\sin[\Delta\phi(\omega)] \qquad \text{(L)}, \tag{4.41}$$

$$\mathrm{Re}\{\tilde{R}_\mathrm{S}(\omega)\} = \frac{A_\mathrm{P}(\omega)}{\omega A_\mathrm{S}(\omega)}\sin[\Delta\phi(\omega)] \qquad \text{(S)}. \tag{4.42}$$

For the imaginary part one has

$$\mathrm{Im}\{\tilde{R}_\mathrm{L}(\omega)\} = \frac{A_\mathrm{P}(\omega)}{\omega A_\mathrm{L}(\omega)}\cos[\Delta\phi(\omega)] \qquad \text{(L)}, \tag{4.43}$$

$$\mathrm{Im}\{\tilde{R}_\mathrm{S}(\omega)\} = -\frac{A_\mathrm{P}(\omega)}{\omega A_\mathrm{S}(\omega)}\cos[\Delta\phi(\omega)] \qquad \text{(S)}. \tag{4.44}$$

To obtain Eqs. (4.41) to (4.44), Eqs. (4.26), (4.32), (4.35)/(4.36) and (4.37)/(4.38) have been used and the decomposition of the complex exponential function into real and imaginary parts,

$$\exp[\mathrm{i}\psi(\omega)] = \cos[\psi(\omega)] + \mathrm{i}\sin[\psi(\omega)]. \tag{4.45}$$

To summarize, the active spectrum $\tilde{R}_{\mathrm{L/S}}(\omega)$ can now be expressed in terms of the amplitudes $A_{\mathrm{P/L/S}}(\omega)$ and the phase shift $\Delta\phi$,

$$\tilde{R}_\mathrm{L}(\omega) = \frac{A_\mathrm{P}(\omega)}{\omega A_\mathrm{L}(\omega)}\{-\sin[\Delta\phi(\omega)] + \mathrm{i}\cos[\Delta\phi(\omega)]\} \qquad \text{(L)}, \tag{4.46}$$

$$\tilde{R}_\mathrm{S}(\omega) = \frac{A_\mathrm{P}(\omega)}{\omega A_\mathrm{S}(\omega)}\{\sin[\Delta\phi(\omega)] - \mathrm{i}\cos[\Delta\phi(\omega)]\} \qquad \text{(S)}. \tag{4.47}$$

4.7.3 The active spectrum $\tilde{R}_{\mathrm{L/S}}(\omega)$ in analytical terms

Starting from Eqs. (4.22)/(4.23), analytical expression for the real and imaginary part of the active spectrum and the tangent of its phase angle are derived in this paragraph. Limiting cases for simple viscous media and for low frequencies are considered. The relations established in the following will be applied in the derivation of the calibration method in chapter 6.

From Eqs. (4.22)/(4.23) one finds analytical expressions for the real and imaginary parts of the active spectrum. One has for the real parts

$$\mathrm{Re}\{\tilde{R}_{\mathrm{L}}(\omega)\} = \kappa|\chi(\omega)|^2\mathrm{Re}\{\tilde{\gamma}(\omega)\} = -\tfrac{\kappa}{\omega}\mathrm{Im}\{\chi(\omega)\} \quad \text{(L)}, \tag{4.48}$$

$$\mathrm{Re}\{\tilde{R}_{\mathrm{S}}(\omega)\} = (\kappa-\omega^2 m)|\chi(\omega)|^2\mathrm{Re}\{\tilde{\gamma}(\omega)\} = -\tfrac{\kappa-\omega^2 m}{\omega}\mathrm{Im}\{\chi(\omega)\} \quad \text{(S)}. \tag{4.49}$$

In the border case of low frequencies, $\omega \to 0$, this gives

$$\mathrm{Re}\{\tilde{R}_{\mathrm{L}}(\omega)\} \simeq \tfrac{\mathrm{Re}\{\tilde{\gamma}(\omega)\}}{\kappa}, \quad \text{for low frequencies} \quad \text{(L)}, \tag{4.50}$$

$$\mathrm{Re}\{\tilde{R}_{\mathrm{S}}(\omega)\} \simeq \tfrac{\mathrm{Re}\{\tilde{\gamma}(\omega)\}}{\kappa}, \quad \text{for low frequencies} \quad \text{(S)}, \tag{4.51}$$

which gives $\gamma_0/\kappa = 1/\omega_{\mathrm{c}}$ with the angular corner frequency ω_{c} in the case of a purely viscous medium with $\mathrm{Re}\{\tilde{\gamma}(\omega)\} = \gamma_0$ and $\mathrm{Im}\{\tilde{\gamma}(\omega)\} = 0$. For the imaginary part one has

$$\mathrm{Im}\{\tilde{R}_{\mathrm{L}}(\omega)\} = \tfrac{\kappa}{\omega}|\chi(\omega)|^2[(\kappa-\omega^2 m) - \omega\mathrm{Im}\{\tilde{\gamma}(\omega)\}] \quad \text{(L)}, \tag{4.52}$$

$$\mathrm{Im}\{\tilde{R}_{\mathrm{S}}(\omega)\} = |\chi(\omega)|^2[\mathrm{Im}\{\tilde{\gamma}(\omega)\}(\kappa-\omega^2 m) - \omega|\tilde{\gamma}(\omega)|^2] \quad \text{(S)}. \tag{4.53}$$

In the limiting case of a particle in a purely viscous medium at low frequencies, this gives approximately

$$\mathrm{Im}\{\tilde{R}_{\mathrm{L}}(\omega)\} \simeq \tfrac{1}{\omega}, \quad \text{for low frequencies} \quad \text{(L)}, \tag{4.54}$$

$$\mathrm{Im}\{\tilde{R}_{\mathrm{S}}(\omega)\} \simeq \tfrac{\omega}{\omega_{\mathrm{c}}}, \quad \text{for low frequencies} \quad \text{(S)}. \tag{4.55}$$

One obtains for the tangency of the phase angle $\psi(\omega)$ of the active spectrum,

$$\tan[\psi(\omega)] = \tfrac{\mathrm{Im}\{\tilde{R}_{\mathrm{L}}(\omega)\}}{\mathrm{Re}\{\tilde{R}_{\mathrm{L}}(\omega)\}} = \tfrac{(\kappa-\omega^2 m)-\omega\mathrm{Im}\{\tilde{\gamma}(\omega)\}}{\omega\mathrm{Re}\{\tilde{\gamma}(\omega)\}}, \quad \text{(L)}, \tag{4.56}$$

$$\tan[\psi(\omega)] = \tfrac{\mathrm{Im}\{\tilde{R}_{\mathrm{S}}(\omega)\}}{\mathrm{Re}\{\tilde{R}_{\mathrm{S}}(\omega)\}} = \tfrac{-\omega|\tilde{\gamma}(\omega)|^2+\mathrm{Im}\{\tilde{\gamma}(\omega)\}(\kappa-\omega^2 m)}{\mathrm{Re}\{\tilde{\gamma}(\omega)\}(\kappa-\omega^2 m)}. \quad \text{(S)}, \tag{4.57}$$

In the limiting case of a particle in a purely viscous medium at low frequencies, one has

$$\tan[\psi(\omega)] = \tfrac{\kappa}{\omega\gamma_0} = \tfrac{\omega_{\mathrm{c}}}{\omega}, \quad \text{for low frequencies} \quad \text{(L)}, \tag{4.58}$$

$$\tan[\psi(\omega)] = \tfrac{-\omega\gamma_0}{\kappa} = -\tfrac{\omega}{\omega_{\mathrm{c}}}, \quad \text{for low frequencies} \quad \text{(S)}. \tag{4.59}$$

5 Bound and bio-active systems

In a typical experiment with optical tweezers on a biological system, the trapped particle is bound to some biological structure like a protein in the cell membrane, the cell nuclear membrane, a motor protein or an RNA molecule. In those *bound* systems the trapped particle is mostly used as a *handle* which is mediating the manipulation of the biological structure by the optical tweezers. The motion of the trapped particle can be detected with high temporal resolution which yields information about the motion of the biological structure and about exerted forces.
In solutions of actin and myosin, the activity of molecular motors alters the bead motion. Similarly, within living cells the motion of the bead can be influenced by the remodelling of the cytoskeleton. I call systems which exhibit molecular motor activity or in which a filament network is remodelled *bio-active*. In this chapter both bound and bio-active systems will be addressed. In section 5.1 suggestions are made, how systems could be described when the trapped particle is bound to a linearly or a non-linearly responding biological structure. The effects of bio-active processes on the motion of a trapped particle are described in section 5.2.

5.1 Bound systems

Biomolecules as well as organelles can often not be trapped with sufficient force by the optical tweezers. Therefore in most experiments, the biological structure which is of interest is not trapped itself. Rather, a small artificial bead of, e.g., polystyrene, silicon or gold is trapped. The bead is biofunctionalized, so that it binds specifically to the biological structure. The link between bead and biological structure can be approximated as a stiff Hookean spring. An example for such a strong link is the binding between a streaptavidin-coated polystyrene bead and the biotinylated λ-receptor in the outer membrane of *Escherichia coli* [57]. In general, it is desirable that the link is as rigid as possible, so that the bead follows the motion of the biological structure.

5.1.1 Linearly responding biological structures

Assuming now that a rigid link between the trapped bead and the biological object has been established, one may ask, how the response function $\chi(\omega)$ of the unbound system can be used for force spectroscopy on the bound system. If the link is rigid, the bead and the biological structure can be considered to be moving *as one object* [57] at not too high frequencies. I will show this by an argumentation which is very similar to that given in Ref. [57], where a trapped bead which is bound to the *E. coli* λ-receptor has been described. However, I assume a viscoelastic instead of a simply viscous medium. Consider the following coupled set of Fourier transformed equations of motion for an *undriven bound system*,

$$\begin{aligned} -\omega^2 m\tilde{x}(\omega) &= -\mathrm{i}\omega\tilde{\gamma}(\omega)\tilde{x}(\omega) - \kappa(\omega)\tilde{x}(\omega) + \tilde{F}_{\mathrm{R}}(\omega) \\ &\quad +\kappa_{\mathrm{bead-struct}}\left[\tilde{x}_{\mathrm{struct}}(\omega) - \tilde{x}(\omega)\right]. \qquad (5.1) \\ -\omega^2 m_{\mathrm{struct}}\tilde{x}_{\mathrm{struct}}(\omega) &= -\mathrm{i}\omega\tilde{\gamma}_{\mathrm{struct}}(\omega)\tilde{x}_{\mathrm{struct}}(\omega) - \kappa_{\mathrm{struct}}(\omega)\tilde{x}_{\mathrm{struct}}(\omega) + \tilde{F}_{\mathrm{R,struct}}(\omega) \\ &\quad -\kappa_{\mathrm{bead-struct}}\left[\tilde{x}_{\mathrm{struct}}(\omega) - \tilde{x}(\omega)\right]. \qquad (5.2) \end{aligned}$$

Eq. (5.1) describes the spatial coordinate x of the trapped bead, while Eq. (5.2) describes the spatial coordinate x_{struct} of the biological structure which is bound to the bead. In Eq. (5.1), the parameters κ, $\tilde{\gamma}(\omega)$, m and $\tilde{F}_{\mathrm{R}}(\omega)$ represent the same quantities as in the previous chapters of this work, i.e., the trap stiffness of the optical tweezers, the friction retardation spectrum of the trapped object moving in a viscoelastic medium, the mass of that object and the random thermal force, respectively. In Eq. (5.2) the motion of the biological structure which is attached to the trapped bead is described by similar parameters. $\tilde{\gamma}_{\mathrm{struct}}(\omega)$, m_{struct} and $\tilde{F}_{\mathrm{R,struct}}(\omega)$ represent the friction retardation spectrum of its motion within the medium, its mass and the random thermal force acting on the structure, respectively. κ_{struct} represents a harmonic bond within the biological structure or between the biological structure and the coverslip or another biological structure like the cell wall. The remaining parameter $\kappa_{\mathrm{bead-struct}}$ describes the bond between bead and biological structure which is assumed to be spring-like. The stiffness $\kappa_{\mathrm{bead-struct}}$ is assumed to be much larger than the quantities κ_{struct}, $\mathrm{i}\omega\gamma_{\mathrm{struct}}(\omega)$ and $-\omega^2 m_{\mathrm{struct}}$ at not too high frequency ω. Then, solving Eq. (5.2) for $\tilde{x}_{\mathrm{struct}}(\omega)$ and insertion into Eq. (5.1) yields

$$-\omega^2 m_{\mathrm{bound}}\tilde{x}(\omega) = -\mathrm{i}\omega\tilde{\gamma}_{\mathrm{bound}}(\omega)\tilde{x}(\omega) - \kappa_{\mathrm{bound}}(\omega)\tilde{x}(\omega) + \tilde{F}_{\mathrm{R,bound}}(\omega) \tag{5.3}$$

This equation has nearly the same structure as Eq. (5.1). But instead of the last two terms in Eq. (5.1), which characterize the binding between bead and biological structure, Eq. (5.3) has modified parameters describing the bound system, i.e., a modified mass $m_{\mathrm{bound}} := m + m_{\mathrm{struct}}$, a modified friction retardation spectrum $\tilde{\gamma}_{\mathrm{bound}}(\omega) := \tilde{\gamma}(\omega) + \tilde{\gamma}_{\mathrm{struct}}(\omega)$ and a modified spring constant $\kappa_{\mathrm{bound}} := \kappa + \kappa_{\mathrm{struct}}$. The random force acting on the bound system is the sum of the random force contributions which act on the bead and on the biological structure, respectively, $\tilde{F}_{\mathrm{R,bound}}(\omega) = \tilde{F}_{\mathrm{R}}(\omega) + \tilde{F}_{\mathrm{R,struct}}(\omega)$. In that way the bead and the biological system appear like moving as one object. Accordingly, the power spectrum of the undriven bound system is given by

$$P_{\mathrm{bound}}(\omega) = \frac{2k_{\mathrm{B}}T\mathrm{Re}\left\{\tilde{\gamma}_{\mathrm{bound}}(\omega)\right\}}{|\kappa_{\mathrm{bound}} + \mathrm{i}\omega\tilde{\gamma}_{\mathrm{bound}}(\omega) - \omega^2 m_{\mathrm{bound}}|^2}. \tag{5.4}$$

Getting back to the response function $\chi(\omega)$, Eq. (4.4), which is useful to describe driven systems, one obtains

$$\langle\tilde{x}(\omega)\rangle = \chi(\omega)\left[-\kappa_{\mathrm{struct}} - \mathrm{i}\omega\tilde{\gamma}_{\mathrm{struct}}(\omega) + \omega^2 m_{\mathrm{struct}} + \tilde{F}_{\mathrm{ext}}(\omega)\right] = \chi_{\mathrm{bound}}(\omega)\tilde{F}_{\mathrm{ext}}(\omega) \tag{5.5}$$

by adding an external force $\tilde{F}_{\mathrm{ext}}(\omega)$ to Eq. (5.3) and using Eq. (4.4) for the response function $\chi(\omega)$ of the unbound system of only bead, trap and medium. This gives

$$\chi_{\mathrm{bound}}(\omega) = \frac{1}{\frac{1}{\chi(\omega)} + \frac{1}{\chi_{\mathrm{struct}}(\omega)}}, \tag{5.6}$$

where $\chi_{\mathrm{struct}}(\omega) = (\kappa_{\mathrm{struct}} + \mathrm{i}\omega\tilde{\gamma}_{\mathrm{struct}}(\omega) + \omega^2 m_{\mathrm{struct}})^{-1}$. Note that Eq. (5.6) mathematically equals to adding up conductances in serial connections of elements in electric circuits. Instead of conductances, effective inverse spring constants are added up here.

This procedure reminds of the system of springs and dashpots which have been used for the description of viscoelastic materials for a long time [33]. Such a model has been applied to the description of the viscoelastic properties of the cytoplasm of a living cell [28]. Unlike in our case, where we want to describe the bound system of bead and biological structure, in that models the cytoplasm itself is described as serial combination of springs and dashpots. A problem of

these models is that a finite number of *scalar* parameters which corresponds to a finite number of springs and dashpots cannot account for a continuum spectrum of relaxation times as found in cells [30, 34]. In the description used in this work, such a problem is avoided by using a general *frequency dependent* friction relaxation spectrum $\tilde{\gamma}_{\text{bound}}(\omega)$. The response function $\chi_{\text{bound}}(\omega)$ comprises on the one hand the optical tweezers and attachments of the biological structure to the coverslip or to another biological structure as well as filament cages which trap the particle permanently. Those contributions all appear as springs which are summing up to κ_{bound}. On the other hand, transient interactions of viscous or elastic nature between the bound system of bead and biological structure and the medium appear as "continuous system of dashpots and springs" which is not necessarily described by a finite number of relaxation times. Those interactions contribute to $\tilde{\gamma}_{\text{bound}}(\omega)$ which is as well included in $\chi_{\text{bound}}(\omega)$.

The linear parameters κ_{struct} and $\tilde{\gamma}_{\text{struct}}(\omega)$ have been determined experimentally for the *E. coli* λ-receptor system by evaluation of histograms, mean square displacements and power spectra by assuming that the bound system of bead and λ-receptor moves in simple viscous media [57]. This assumption is critical since the bead performs Brownian motion near a surface which is the outer membrane of *E. coli* [58] and since the λ-receptor moves in a complex liquid which is the outer membrane bilayer. Hence potentially important effects have been neglected.

In the general case of a viscoelastic medium and where hydrodynamic effects are to be taken into account, κ_{bound}, $\chi_{\text{bound}}(\omega)$ and $\tilde{\gamma}_{\text{bound}}(\omega)$ might be found by *calibration* however, using the novel FDT method presented in chapter 6 with stage driving in-situ *directly at the bound system.* Frequently, bound systems are also bio-active which involves that the noise affecting the motion of the bound system is not purely thermal. In this case the calibration has to be performed at frequencies which are higher than those frequencies at which the bio-active motion takes place, see section 5.2.

Note that all arguments which were put forward in this section are made in linear response theory. Many biological structures exhibit non-linear mechanical properties. Then $\chi_{\text{bound}}(\omega)$ can only be used in the linear range.

5.1.2 Small non-linearly responding biological structures

If a small biological structure exhibits non-linear mechanical properties already at modest strains, i.e., its force-extension relationship $f^{\text{struct}}(x)$ is non-linear, the description of the bound system in linear response theory is inappropriate. The (unbound) system of the trapped bead immersed in the viscoelastic medium could remain in the linear regime, however, and in this case the response function $\chi(\omega)$, Eq. (4.4), may still be helpful. In this case on can describe the action of the biomolecule on the bead as an external force $\tilde{F}_{\text{struct}}(\omega)$. One finds

$$\tilde{x}(\omega) = \chi(\omega)\left\{\tilde{F}_{\text{struct}}(\omega) + \tilde{F}_{\text{ext}}(\omega)\right\}, \tag{5.7}$$

where $\tilde{F}_{\text{ext}}(\omega)$ is a chosen external force, i.e., a non-equilibrium protocol, which is implemented by relocating the trap position or the piezo stage within a time interval $[t_{\text{i}}; t_{\text{f}}]$. If $\chi(\omega)$ is known for all frequencies, the time dependence of the force exerted by the biological structure on the trapped bead, $F_{\text{struct}}(t)$, can be extracted by means of Fourier back transform. The structure's position during the course of the experiment is characterized by the bead position coordinate $x(t)$, since

the trapped bead is bound to the biological structure. Then the following relationship connects the force-extension relationship $f^{\mathrm{struct}}(x)$ and the experimentally determined force $F_{\mathrm{struct}}(t)$,

$$f^{\mathrm{struct}}(x(t)) = F_{\mathrm{struct}}(t). \quad \forall t \tag{5.8}$$

From $f^{\mathrm{struct}}(x(t))$ the work performed by the structure can be calculated,

$$W^{\mathrm{struct}} = \int_{t_\mathrm{i}}^{t_\mathrm{f}} f^{\mathrm{struct}}\left(x(t)\right) \dot{x} dt, \tag{5.9}$$

It is important to note that for a correct thermodynamic treatment of small systems it is not enough to consider only the *average* work $\langle W^{\mathrm{struct}} \rangle$ in order to determine correct free energy differences $\Delta G^{\mathrm{struct}}$. For this reason, Eq. (5.7) has not been written in terms of averages. Since the force is a fluctuating quantity, W^{struct} will also fluctuate for different trajectories [59]. For the work one gets

$$W^{\mathrm{struct}} = \int_{t_\mathrm{i}}^{t_\mathrm{f}} f^{\mathrm{struct}}\left(x(t)\right) \dot{x} dt. \tag{5.10}$$

For the average work the *inequality* $\langle W^{\mathrm{struct}} \rangle \geq \Delta G^{\mathrm{struct}}$ holds, which is a statement of the second law of thermodynamics [59]. The *Jarzynski equality* [60] however states that

$$\exp\left(-\frac{\Delta G^{\mathrm{struct}}}{k_\mathrm{B}T}\right) = \left\langle \exp\left(-\frac{W^{\mathrm{struct}}}{k_\mathrm{B}T}\right)\right\rangle. \tag{5.11}$$

The Jarzynski equality enables one to determine the free energy difference $\Delta G^{\mathrm{struct}}$ between the equilibrium states at initial and at final times from a large ensemble of measured forces. A more general relation is given by the Crooks fluctuation theorem [61].

5.2 Bio-active systems

Activity in the cytoplasm of a living cell or in a solution of actin and myosin can arise for example from growing and shrinking of microtubuli or from activity of molecular motors. This activity can be so strong that even a trapped bead, which was engulfed in a macrophage cell, can be moved in a directed way by molecular motors [2].

Biological activity affecting the motion of trapped particles inside the cell can be divided into two different classes. The first class is direct action on the trapped particle, e.g., by binding of molecular motors. Such processes might have a certain direction, e.g., like the transport of a vesicle towards the nucleus of an *E. coli* cell, as has been observed with fluorescence microscopy [62]. But in most cases, such action appears random and it can be taken into account as random force $F_{\mathrm{R,bio}}(t)$ which is zero in average, $\langle F_{\mathrm{R,bio}}(t) = 0 \rangle$. Furthermore, such activity happens on relatively large time scales, i.e., on the order of 10 ms to seconds. The second class of biological activity comprises processes which alter the environment of the trapped particle. For example, myosin motors within an actin solution become processive at low ATP concentration and generate tension on the actin network. Mizuno et al. [49] have shown that this process increases the stiffness of the network. This stiffening affects the diffusive motion of the trapped particle and it modifies the response function $\alpha(\omega)$. This means that the friction retardation

spectrum $\gamma(\omega)$ is also altered, see Eq. (4.5). In the following, the friction retardation spectrum altered by biological activity will be denominated as $\tilde{\gamma}_{\mathrm{bio}}(\omega)$.

Taking into account these two classes of bio-active processes, the Fourier transformed equation of motion for the trapped particle in the viscoelastic medium, Eq. (3.6), is modified to

$$-\omega^2 m\tilde{x}(\omega) = -\mathrm{i}\omega\tilde{\gamma}_{\mathrm{bio}}(\omega)\tilde{x}(\omega) - \kappa\tilde{x}(\omega) + \tilde{F}_{\mathrm{R}}(\omega) + \tilde{F}_{\mathrm{R,bio}}(\omega). \tag{5.12}$$

With this description of the system, the violation of the FDT observed by Mizuno et al. [49] can be easily explained. The FDT, Eq. (4.12), relates systems slightly out of equilibrium to systems in thermal equilibrium. Due to the bio-active processes of the first class, the system is no longer in equilibrium. This is reflected in the power spectrum of the motion of the trapped particle: The random force $\tilde{F}_{\mathrm{R,bio}}(\omega)$ adds extra low-frequency noise to the system, hence the power spectrum

$$P(\omega) = \lim_{T_{\mathrm{m}}\to\infty} \frac{\langle|\hat{x}_k|^2\rangle}{T_{\mathrm{m}}} \tag{5.13}$$

is modified. The response function

$$\chi(\omega) = \frac{\langle\tilde{x}(\omega)\rangle}{\tilde{F}_{\mathrm{ext}}(\omega)} \tag{5.14}$$

on the other hand is not altered, since $\langle F_{\mathrm{R,bio}}(t) = 0\rangle$. Therefore, the FDT is not valid for a medium which contains bio-active processes of the first class.

Moreover, the presence of extra noise due to bio-active processes of the first class is relevant for the calibration method presented in the next chapter. The method is based on the validity of the FDT, and we have just seen that the presence of the term $\tilde{F}_{\mathrm{R,bio}}(\omega)$ violates the FDT. Hence for a calibration inside a bio-active medium, $\tilde{F}_{\mathrm{R,bio}}(\omega)$ must be negligible. The data of Mizuno et al. [49] show that this is the case for frequencies $\gtrsim 20\,\mathrm{Hz}$. Thus, in solutions of actin and myosin at low ATP, calibration with the novel method would yield reliable results only for driving frequencies $f_{\mathrm{K}} \gtrsim 20\,\mathrm{Hz}$. On the other hand, bio-active processes of the second class which only alter the environment of the trapped particle, do not violate the FDT and hence they do not affect the result of the calibration method. Here, the novel calibration method rather enables to measure the altered friction retardation spectrum $\tilde{\gamma}_{\mathrm{bio}}(\omega)$ and to receive accurate force values.

6 The FDT method for the calibration of optical tweezers in viscoelastic media

In this chapter, the main analytical result of this thesis will be presented, which is the derivation of a novel calibration method for optical tweezers in general viscoelastic media, the so-called FDT method. The FDT method is based on the description of the particle by one degree of freedom in linear response theory in continuous media. This description has been introduced in chapters 3 and 4. In the FDT method, no specific model for the friction force is assumed, which is applied on the trapped particle by the medium. The central assumption of the FDT method is rather the validity of the fluctuation-dissipation theorem (FDT) which gives the method its name. In fact, the basic equations of this method are convenient formulations of the FDT. For the FDT method to work, it is *not* necessary that the FDT is valid *for all frequencies*. This is especially important if the calibration is to be performed in bio-active media like the cytoplasm.

I will introduce the problem of finding a calibration method for optical tweezers in section 6.1. A precise and effective calibration method in water is the purely passive power spectrum method. In section 6.2 it will be explained why such a purely passive method is not sufficient in viscoelastic media with unknown frictional behavior and why also a purely active method would fail. The FDT method, which is a combined active and passive approach, is presented in section 6.3.

6.1 Introduction to the calibration of optical tweezers

6.1.1 Calibrating optical tweezers

As briefly explained in the introductory section on optical tweezers, section 2.1, the tweezers act as a spring of stiffness κ on the trapped particle if the particle is not deflected too far from the equilibrium trapping position. Thus, if the deflection of the trapped particle from the equilibrium position is known, knowledge of the spring constant κ would allow for determining the force which the tweezers exert on the trapped particle.

In principle, κ is determined by the electromagnetic field distribution around the trapped object and by the ratio of the refractive indices of object and medium. While the latter is mostly known with precision, the exact electromagnetic field distribution and hence the force on the trapped particle are difficult to determine. For not too complicated situations a quantitative agreement between the trap stiffnesses κ, as obtained from electromagnetic theory and from the experiment, has been found [7].

For general situations, κ has to be found by *calibration*. Calibration means that the trapped particle is observed while it is performing motion in response to defined *calibration forces*. These calibration forces can be the thermal force or an external force or both of them. By analysis of the observed motion finally the trap stiffness κ is found. Generally, it is desired to apply as few different forces as possible to keep the calibration as simple as possible. Furthermore, the forces should be applied in a way so that the statistical error of κ is minimal.

For an analysis of the particle's motion it is important how much information about other relevant parameters of the system is available. These other parameters are those of the Fourier transformed equation of motion for the trapped particle in the undriven system, Eq. (3.6), i.e. the mass m, the friction retardation spectrum $\tilde{\gamma}(\omega)$ and the temperature T[1]. These parameters might be known with high precision. This is the case, for example, for spherical polystyrene beads that are trapped in water. But for particles of unknown volume or density that are trapped in arbitrary viscoelastic media, both m and $\tilde{\gamma}(\omega)$ are usually unknown.

Beside the spring constant κ, both the mass m and the friction retardation spectrum $\tilde{\gamma}(\omega)$ enter the response function $\chi(\omega)$, according to Eq. (4.4). The response function is thus in general unknown, too. According to its definition in Eq. (4.2), the response function can be understood as an effective reciprocal spring constant [10]. Whereas $1/\kappa$, which represents the low-frequency limit of $\chi(\omega)$, contains information only about the static long-time limit of the particle position at a given trap force, the response function contains all information about the *dynamics* of the linear response of the trapped object to any time-dependent external force. Vice versa, external forces acting on the trapped object can be found by measuring its positions and averaging, if one *knows* the response function $\chi(\omega)$. Thus $\chi(\omega)$ represents a very helpful quantity for the implementation of force spectroscopy.

In fact, the *response* function $\chi(\omega)$ is a central quantity at the calibration where one observes the particle moving in *response* to a force. However, typically the response function is not directly measured. One rather measures quantities like the power spectrum, Eq. (3.23), which are combinations of $\chi(\omega)$ and other parameters of the motion.

Moreover, particle position detection at high sampling rates is typically achieved with quadrant photo diodes (QPD). With the QPD no positions are measured, but voltages. Within a certain range, these voltages are proportional to the positions, so the proportionality factor needs to be known in order to relate voltages to positions. This proportionality factor is usually defined as ratio β between positions and voltages. For example one has for the x coordinate $\beta = x/V_x$ [§]. The factor β has to be found by calibration. Since forces are always computed via positions, according to $F_{\text{trap}} = \kappa x$ or $\langle \tilde{x}(\omega) \rangle = \chi(\omega) \tilde{F}_{\text{ext}}(\omega)$, the determination of β must be regarded as an essential part of every force calibration.

I will summarize this section by giving the following definition for the *problem of calibration of optical tweezers*:

Apply as few different defined calibration forces as possible on the trapped particle, so that the parameters κ, β and preferably also $\chi(\omega)$ can be determined unambiguously and with minimum statistical error from the analysis of the motion of the particle in response to the defined calibration forces.[2]

Note that knowledge of both κ and $\chi(\omega)$ would entail that also $\tilde{\gamma}(\omega)$ and m are determined, see Eq. (4.4)[3].

[1] The temperature shows up in the random force spectrum, Eq. (3.20).

[§] This definition allows to simply *multiply* measured voltages with β to find positions. However, sometimes β is defined the other way around, $\beta = V_x/x$, so one has to watch out which definition is used.

[2] A defined force which is "applied" can also mean here the thermal force, though this is not externally applied, but always apparent in the medium.

[3] The parameters $\tilde{\gamma}(\omega)$ and m could be separated from each other by a fitting procedure, if $\chi(\omega)$ is known for

6.1.2 Friction models for the calibration of optical tweezers

In many calibration methods a model for the frequency-dependence of the parameter function $\tilde{\gamma}(\omega)$ is used. The measured quantity, e.g. the power spectrum, can be fitted according to that model. Thus in most cases, the parameters of the model for $\tilde{\gamma}(\omega)$ have to be known.

The simplest example for such a model is the *simple Stokes friction* for spherical particles, see section 3.2.2. Here, the particle radius R and the medium viscosity $\eta(T)$ describe the friction. If only one kind of calibration force is applied on the trapped particle, e.g., the thermal force is acting while the laser and the piezo stage are at rest, these two parameters need to be known a priori, in order to unambiguously determine κ and β by calibration. Accordingly, the polydispersity of the bead size as well as the temperature and solute dependence of the viscosity lead to calibration errors.

If not only one but rather two different forces are applied on the particle, it is possible to calibrate for κ and β without knowing the parameters R and $\eta(T)$. For example one can analyse both the motion of the bead in response to the thermal force and in response to the external force from oscillating the piezo stage as shown by Tolić-Nørrelykke et al. [56]. The FDT method presented later in this chapter, is also based on the application of two different forces on the trapped particle, but I will additionally abandon the assumption of simple Stokes friction.

A more elaborate model for the friction between a spherical particle and an aqueous medium is taking into account the *proximity of the coverslip*, see section 3.2.3. This model has been successfully applied in the *power spectrum method* for the calibration of optical tweezers in simple viscous media [40]. This is a purely passive method, see section 6.1.4. Additionally to the parameters of simple Stokes friction, two more parameters are taken into account in the model for the friction retardation spectrum $\tilde{\gamma}(\omega)$. These parameters, which have to be known for the calibration, are the distance from the coverslip l and the penetration depth $d(\omega)$, where the latter is given by the kinematic friction coefficient ν, see Eq. (3.12).

The main focus of this work is the calibration in *viscoelastic media*. So one might ask here, if it is feasible to calibrate with a friction model for a bead in a viscoelastic medium like actin. For example, the friction between a bead and a *network of crosslinked actin filaments* is described within the model of Mizuno et al. [49] by five parameters for the frequency-dependence of the friction retardation spectrum $\tilde{\gamma}(\omega)$, see section 3.2.4. These parameters are l_c, ζ, $l_p(T)$, R, ρ_{actin}[4]. If the network is additionally under tension, e.g., due to local stress exerted by myosin motors, one more parameter has to be taken into account which is the tension σ. For the calibration of the optical tweezers, it should theoretically be possible to fit the measured power spectrum of the motion of a bead inside the actin network according to that friction model, if the model's parameters are known[5]. However, the model of Mizuno et al. agrees with the data only for a certain frequency range, i.e., not for too small frequencies, but fitting could be done only in that frequency range. Much more severe problems are, firstly, that some of the model parameters are

several frequency values.

[4] Some of these parameters depend on each other. But the relationship between them is not trivial. See [49, 63].

[5] In principle, one could also think about fitting the power spectrum with the friction model of Mizuno et al., by assuming that the model parameters are unknown fit parameters. Unfortunately, the power spectrum is a smooth function, which cannot be unambiguously fitted for a large number of parameters, so that this idea would not work out.

difficult if not impossible to control or to determine exactly. Secondly, some of these parameters can exhibit a large spatial variability in the unordered actin network. For those two reasons I am convinced that calibration with a friction model is at least impracticable, if not impossible in a complex medium like a crosslinked actin network.

What is about calibration with a friction model inside the *cytoplasm*? The cytoplasm contains a large amount of crosslinked actin and in addition many more components which make the situation even more complicated than in purified actin networks. Moreover, bio-active processes occur in the cytoplasm which do not only cause a modified friction retardation spectrum, but they also add noise to the system, see section 5.2. I conclude that it would be impossible to calibrate inside the cytoplasm by fitting to a friction model.

6.1.3 Calibration of optical tweezers without friction model

From the arguments given in the last section I conclude that in arbitrary viscoelastic media it has to be calibrated without a specific friction model. A simple possibility for doing so would use the *Equipartition theorem* which states that for large observation times, the mean-square displacement of the trapped particle is equal to the half-width of the trap,

$$\lim_{t\to\infty} \sigma^2(t) = k_\mathrm{B}T/\kappa. \tag{6.1}$$

The mean-square displacement is always positive, because it is derived from the square of a quantity [3]. Noise, drift, and low pass filtering give biased errors on the mean-square displacement [3, 40]. Similarly, on long time-scales, bio-active processes would add to the mean-square displacement. These are shortcomings of the equipartition method which are so severe that it is no capable choice for a calibration in viscoelastic and bio-active media.

Instead of simply computing the variance of a distribution as in the equipartition method, the whole distribution of particle positions can be determined. This method gives more information about the optical potential exerted by the optical tweezers, than just the spring constant. It even gives information about non-harmonic contributions to that potential. Therefore this method is called *optical potential analysis* [3, 64]. The probability for the displacement of a trapped object in a potential well is given by the Boltzmann distribution

$$\mathcal{P}(x) \propto \exp\left\{-\frac{E(x)}{k_\mathrm{B}T}\right\}, \tag{6.2}$$

where $E(x)$ is the potential energy. However, just as the equipartition method, this approach is not useful in practise without a considerable amount of low-noise/low-drift position data [3]. Moreover, both the equipartition method and optical potential analysis do not reveal any information about the *dynamics* of the trapped particle. Both techniques require an independent calibration of the voltage-position conversion factor β. Furthermore, in viscoelastic media it is not clear a priori if optical potential analysis could separate the potential exerted by elastic contributions of the friction force $-\omega\tilde{x}(\omega)\tilde{\gamma}''(\omega)$ from the optical trapping force κx.

To my knowledge, except from the equipartition method and the optical potential analysis there is so far no other calibration approach which does not need a friction model. If no specific friction model is given, the assumptions of the validity of continuum limit, linear response theory and the

description of the trapped particle by one degree of freedom x should remain for the most cases. In this chapter a calibration method is presented which is only based on these assumptions and not on a specific friction model.

6.1.4 Passive, active and combined calibration approaches

In the last two subsections, calibration methods for optical tweezers have been classified according to their use of a model for the friction between trapped particle and medium. Another possibility to classify calibration methods is according to the defined calibration forces which the trapped particle is subjected to. In this respect, the most coarse sub-division is into passive, active and combined methods.

Passive methods use the internal *random thermal force* $F_{\mathrm{R}}(t)$ as calibration force. They are experimentally very easy to put into practice, since all one has to do is to record the trajectory of the trapped particle which performs Brownian motion inside the optical trap's potential. Information about the response of the particle to the thermal force is then obtained from evaluating the position autocorrelation function [65], the mean-squared displacement, the position histogram [64], or the power spectrum [40]. The power spectrum method is especially robust, since it operates in the frequency-domain. Typically, systematic errors caused by drift or instrumental noise, occur at certain frequencies. These frequencies can be left out in the fitting procedure of the power spectrum method.

In *active methods* the system is driven with *external forces*, i.e., laser driving or stage driving, as described in sections 4.5 and 4.6. Calibration using stage driving is known as drag force method and it has been performed with oscillating or triangular stage motion or with a stage which is moving with constant velocity. The latter option is frequently applied and it is called *constant flow* method [66, 67], since the medium is moved with a constant velocity relative to the trapped particle. Laser driving by means of galvanometric mirrors has been performed with oscillate laser motion [8]. A fast oscillating laser has been used for that part of the calibration in order to find the conversion factor β [55].

A *combined method* which makes use of both the thermal force and the external force from an oscillated stage was presented recently by Tolić-Nørrelykke et al. [56]. A trapped particle was immersed in an aqueous medium which is placed on the oscillating stage. From the evaluation of the power spectrum of the particle's motion, both the trap stiffness κ and the conversion factor β could be found. This approach is based on the assumption that the particle is immersed in a simple viscous fluid. This requirement is not necessary FDT method which is presented later in this chapter.

6.2 On purely passive and purely active approaches

In viscous media optical tweezers can be calibrated by applying a purely passive method, like the power spectrum method [40,53]. Rhetorically, one may ask why a passive method is not sufficient for the calibration of optical tweezers inside viscoelastic media? In subsection 6.1.2 it has been explained why it would be impossible to calibrate optical tweezers in complex viscoelastic media

like crosslinked actin networks or the cytoplasm with a method which makes use of a model for the friction which the trapped particle feels inside such a medium. This implies that for the general case it has to be calibrated without a friction model. In this section I will show that in this case a purely passive or a purely active method can not be a solution to the *problem of calibration* as stated in subsection 6.1.1. Basically, a purely passive or a purely active method alone gives too few equations for too many unknowns.

6.2.1 Why a purely passive method is not sufficient

As indicated in the paragraph 6.1.4, a passive method is very convenient, since only the Brownian motion of the trapped particle has to be observed. From the observed trajectory of the particle one can determine for example the power spectrum, Eq. (3.23). The power spectrum contains the parameters temperature T, trap stiffness κ, friction retardation spectrum $\tilde{\gamma}(\omega)$ and mass m. Whereas the temperature can be determined with good precision, the other parameters must be considered as being unknown. The friction retardation spectrum $\tilde{\gamma}(\omega)$ is unknown, since we do not assume a model for the friction. Already at intermediate frequencies the particle inertia term $\omega^2 m$ can become comparable to κ or to $\omega\tilde{\gamma}(\omega)$. Instead of neglecting it, the particle mass m is assumed unknown and treated as a parameter. Finally, κ is the unknown parameter which is of main interest at the calibration[6].

Fitting of the power spectrum for so many unknown parameters would not give unambiguous results. Hence, Eq. (3.23) gives *one equation* for the unknowns κ, $\tilde{\gamma}(\omega)$, and m for each frequency. Thus, additional information is required in order to solve for these unknowns.

According to the fluctuation-dissipation theorem, the power spectrum is related to the imaginary part of the response function $\chi''(\omega)$, see Eq. (4.12). The imaginary part of a response function describes how a system dissipates energy, when it is out of phase with the driving force. The so-called *Kramers-Kronig relations* imply that observing the dissipative response of a system is sufficient to determine its in-phase response, and vice versa. Hence one could use in principle the Kramers-Kronig relation, Eq. (4.9) in order to obtain also the real part of the response function and thus more information about the system. This is done in the microrheology approach by Schnurr, Gittes, et al. introduced in section 2.3 and applied in chapter 9 of this thesis. However, the Kramers-Kronig integral has to be cut at the Nyquist frequency, which results in an underestimation of the real part of the response function [45][7].

For media with a static elastic modulus that is not too large, one might find the trap stiffness κ from the low-frequency limit of the elastic modulus, that is derived from the obtained complex response function $\chi(\omega)$, see Atakhorrami et al. [25]. The statistical error on the value of κ thus obtained would be non-negligible, since typically only few data points are available in the quasi-static limit. Secondly, the trap stiffness and the elastic contribution to the response function which arises from the medium, $-\omega\mathrm{Im}\{\tilde{\gamma}(\omega)\}$, would be difficult to separate from each other. Therefore it could be intricate to validate the assumption of a negligible static elastic modulus.

[6] Furthermore, the conversion factor β in principle represents another unknown parameter, but it can be found by an independent calibration.

[7] The cut-off of the Kramers-Kronig integral at the Nyquist frequency is a general problem in passive microrheology. This will be demonstrated in chapter 9 of this work.

In *bio-active* media, i.e., viscoelastic media in which active biological processes appear, the validity of an approach based on the power spectrum *in its entire frequency range* would be debatable: bio-active media such as the cytoplasm contain low-frequency processes which arise from the biological activity, e.g. of molecular motors, see section 5.2. As describe in section 5.2, those processes render the FDT invalid at low frequencies, presumably up to the order of tens of Hz. At those frequencies, the power spectrum may no longer be related to the imaginary part of the response function. Since the imaginary part of the response function would be needed at *all* frequencies for the computation of the Kramers-Kronig integral, the real part of the response function can not be determined properly. I thus consider it impossible to perform microrheological and trap stiffness calibration measurements with a purely passive method in bio-active media.

As explained in subsection 6.1.3, a first rough estimate of κ could in principle be obtained by the equipartition method. There, the mean-square displacement is considered for large times, which is equal to the half-width of the trap, see Eq. (6.1). Since the mean-square displacement is a biased estimator, this method is not recommendable. The mean square displacement as a function of time contains further information. Under the assumption of the validity of the FDT, it's Laplace transform fulfills [24, 68]

$$\mathcal{L}_s[\sigma^2(t)] := \hat{\sigma}^2(s) = \frac{2k_\mathrm{B}T}{s\kappa + s^2\hat{\gamma}(s) + s^3 m}. \tag{6.3}$$

Eq. (6.3) appears to give us one complex relation for the response function $\chi(s)$. However, since $\chi'(\omega)$ and $\chi''(\omega)$ must obey the Kramers-Kronig relations, $\chi(s)$ for a real argument s contains the entire information [24]. Effectively, one has again only *one equation* for the unknowns κ, $\tilde{\gamma}(\omega)$ and m.

Another passive approach is optical potential analysis, but this exhibits the same main shortcomings as the equipartition method, as explained in subsection 6.1.3.

Yet another option is *ex situ* calibration in water with trapped particles of the same kind as those used in the viscoelastic medium [25, 49]. The short-comings of this method are due to particle polydispersity and different optical properties of water and viscoelastic medium.

I conclude that the observation of the Brownian motion of a trapped particle is not sufficient for the exact calibration of optical tweezers in viscoelastic media with unknown frictional behavior.

6.2.2 Why a purely active method is not sufficient

Similarly to the insufficiency of a purely passive method demonstrated in the previous section, a *purely active* method would not give enough information either. For example, in active methods with an harmonically oscillating external force one typically measures an amplitude and a phase shift of the trapped particle which performs oscillations in response to the external force. These two quantities do not yield enough information to solve for the unknowns κ, $\tilde{\gamma}(\omega)$, and m.

6.3 The FDT method

In the last section it has been demonstrated that a purely passive method is not sufficient for the calibration in arbitrary viscoelastic media. A purely active method would not yield enough information about the system parameters, either. Here, an approach is presented which combines the passive and active methods. The combination of data requires the FDT to be valid for the viscoelastic medium and experimental situations considered. The approach is not based on a friction model, only very general assumptions were made. These assumptions are that the medium is continuous and at least locally homogeneous. Furthermore, the description of the particle by one degree of freedom and in linear response theory must be justified.

The requirement that the FDT must not be violated, implies that the active driving amounts to a small perturbation of the equilibrium system only. By reformulating the FDT conveniently for two ways in which this perturbation may be done in practice, simple relations for the calibration of the trap stiffness κ are found, as presented in paragraph 6.3.1. Moreover, relations to determine the response function $\chi(\omega)$, the friction retardation spectrum $\tilde{\gamma}(\omega)$ and the conversion factor β are derived in the paragraphs 6.3.2 to 6.3.4.

6.3.1 Trap stiffness calibration

In this paragraph, the basic equations of the FDT method are derived, These basic equations relate the trap stiffness κ to measurable quantities. A formulation in terms of amplitudes and phase angles is given in this paragraph as well. Finally it is described how the frequency dependent results of the basic equations can be fitted in order to obtain a reliable value for the trap stiffness.

The FDT with perturbative laser motion

The first of the two ways to apply an external perturbation to the system is to deflect the laser slightly. Thereby the center of the trap is moving according to an arbitrarily chosen trajectory $x_{\mathrm{L}}(t)$ as described in section 4.5. The trajectory is in principle infinitesimal around the resting position $x_{\mathrm{L}} = 0$. For that case, the FDT, Eq. (4.12), can be formulated in a more convenient way. By multiplying the FDT with $-\kappa/\omega$ and thereafter identifying the left-hand side $-\kappa/\omega\chi''(\omega)$ with the real part of the active spectrum $\tilde{R}_{\mathrm{L}}(\omega)$ according to Eq. (4.48), one obtains the basic equation of the FDT method for the case of laser driving,

$$\boxed{\kappa_\omega = \frac{2k_{\mathrm{B}}T}{P(\omega)}\mathrm{Re}\{\tilde{R}_{\mathrm{L}}(\omega)\}} \qquad \text{(L)}. \tag{6.4}$$

Eq. (6.4), is still the FDT, which in this form represents a general measurement prescription for finding the unknown κ. Note that $P(\omega)$ in Eq. (6.4) still represents the power spectrum of the *unperturbed* system and is therefore obtained in the passive part of the measurements.

The FDT with perturbative stage motion

The second way to apply an external perturbation to the system is to move the piezo stage on which the sample is placed, as described in section 4.6. If the sample container is sealed on all sides, the liquid in which the trapped particle is immersed can be assumed to be co-moving with the piezo stage. Also for that case, the FDT, Eq. (4.12), can be formulated in a more convenient way. By substituting Eq. (4.49) into the FDT one obtains the basic equation of the FDT method for the case of stage driving,

$$\boxed{(\kappa - \omega^2 m)_\omega = \frac{2k_\mathrm{B}T}{P(\omega)}\mathrm{Re}\{\tilde{R}_\mathrm{S}(\omega)\}} \qquad \text{(S)}. \tag{6.5}$$

Similar to Eq. (6.4), Eq. (6.5) represents a general measurement prescription for the unknowns κ and m.

The FDT with perturbative sinusoidal motion of stage or laser

The simulation results and analytical considerations presented in chapter 7 suggest that for a calibration, it is most practical and reliable to perturb the system with harmonic oscillations. In the special case of a sinusoidally moved trap, $x_\mathrm{L}(t) = A_\mathrm{L}\sin(\omega_\mathrm{L}t + \phi_\mathrm{L})$, the trapped particle responds with sinusoidal motion, $\langle x_\mathrm{P}(t)\rangle = A_\mathrm{P}\sin(\omega_\mathrm{S}t + \phi_\mathrm{P})$. By using Eq. (4.41) to express the real part of the active spectrum $\mathrm{Re}\{\tilde{R}_\mathrm{L}(\omega)\}$ in terms of amplitudes and phase angles, the FDT Eq. (6.4) becomes

$$\boxed{\kappa_{\omega_\mathrm{L}} = -\frac{2k_\mathrm{B}T}{P(\omega_\mathrm{L})}\frac{A_\mathrm{P}}{\omega_\mathrm{L}A_\mathrm{L}}\sin(\Delta\phi)} \qquad \text{(L)}, \tag{6.6}$$

where $\Delta\phi$ is the phase difference between laser and particle oscillations, $\Delta\phi = \phi_\mathrm{L} - \phi_\mathrm{P}$. Similarly, if the stage is moved sinusoidally, $x_\mathrm{S}(t) = A_\mathrm{S}\sin(\omega_\mathrm{S}t + \phi_\mathrm{S})$, one obtains from Eqs. (4.42) and (6.5)

$$\boxed{(\kappa - \omega^2 m)_{\omega_\mathrm{S}} = \frac{2k_\mathrm{B}T}{P(\omega_\mathrm{S})}\frac{A_\mathrm{P}}{\omega_\mathrm{S}A_\mathrm{S}}\sin(\Delta\phi)} \qquad \text{(S)}, \tag{6.7}$$

where $\Delta\phi$ is now the phase difference between stage and particle oscillations, $\Delta\phi = \phi_\mathrm{S} - \phi_\mathrm{P}$. Eqs. (6.6) and (6.7) represent simple formulas for the experimental determination of the trap stiffness, since all magnitudes on the right-hand sides can be directly obtained from measurements.

Fitting of the results

Eqs. (6.4)/(6.5)[‡] allow the trapping stiffness to be determined experimentally from the power spectrum $P(\omega)$ and the active spectrum $\tilde{R}_\mathrm{L/S}(\omega)$. The equations hold for each frequency ω individually. In the case of stage driving, the mass still appears in an extra frequency-dependent term. This is an obvious disadvantage of stage driving with respect to laser driving. In principle,

[‡]The forward slash in "Eqs. (6.4)/(6.5)" does *not* mean dividing one equation by the other. It indicates that *either* Eq. (6.4) *or* Eq. (6.5) is meant, depending on if laser or stage driving is considered.

one can fit the data according to the quadratic frequency behavior of the mass term. But, since stage driving operates at low frequencies, one may choose to neglect the mass term, if the trap is not too weak and the bead is not too heavy. In that case and in the case of *laser driving* one would fit a constant value[8]. In the experiment, statistical fluctuations are always present in the active spectrum and in the power spectrum. Therefore it is appropriate to average over the recorded frequency interval (averaging denoted by $\langle . \rangle_\omega$) to obtain a value with lower statistical error,

$$\kappa^{(\mathrm{av})} = \langle \kappa_\omega \rangle_\omega \qquad \text{(L)}. \tag{6.8}$$

$$\kappa^{(\mathrm{av})} = \langle (\kappa - \omega^2 m) \rangle_\omega \simeq \langle \kappa_\omega \rangle_\omega \qquad \text{(S)}. \tag{6.9}$$

Frequencies for which measurements are unreliable due to, e.g., drift, bio-active processes or numerical errors like aliasing, could and should be omitted in the averaging procedure, Eq. (6.8)/(6.9). Thus it is an important task to determine the "correct" frequencies over which one has to average. A major advantage of the whole calibration method is that "faulty frequencies" can be omitted[9].

6.3.2 Determination of the response function

Eqs. (6.4) / (6.5) allow for an experimental determination of the stiffness κ of the optical tweezers. The knowledge of κ enables the determination of the trapping force at any position where the trapping potential is harmonic. On the other hand, the response function $\chi(\omega)$ introduced in section 4.2, can be understood as an effective reciprocal spring constant [10]. It contains all information about the dynamics of the response of the trapped object to any external force, according to the Eq. (4.2). Hence, external forces acting on the trapped object can be found by measuring its positions and averaging, if one knows the response function. From the general relation for the response function, Eq. (4.4), and the analytical relations for the active spectrum, Eqs. (4.22)/(4.23), one obtains

$$\boxed{\chi(\omega) = -\frac{\mathrm{i}\omega \tilde{R}_\mathrm{L}(\omega)}{\kappa_\omega}} \qquad \text{(L)}, \tag{6.10}$$

and

$$\boxed{\chi(\omega) = \frac{1 - \mathrm{i}\omega \tilde{R}_\mathrm{S}(\omega)}{(\kappa - \omega^2 m)_\omega}} \qquad \text{(S)}, \tag{6.11}$$

for the laser and stage driven cases, respectively. Eqs. (6.10)/(6.11) represent measurement prescriptions for the response function. For the denominators in Eqs. (6.10)/(6.11), the averaged value, Eqs. (6.8)/(6.9), from the trap stiffness calibration should be used. This would yield a result for the response function $\chi(\omega)$ with relatively low statistical error. The active spectrum

[8] Fitting to a constant value in principle corresponds to averaging.

[9] In general it is convenient to work in the frequency domain since physical processes are typically *localized in frequency space*. The possibility to omit frequencies which are governed by different physics than contained in the fit model is of course given for all calibration methods which are based on fitting in the frequency domain. An example is the usual omission of very low frequencies when fitting with the power spectrum method to avoid errors due to drift [40].

in the numerators in Eqs. (6.10)/(6.11) can be expressed in terms of amplitudes and the phase difference $\Delta\phi(\omega)$ by using Eqs. (4.46)/(4.47).

Moreover, Eqs. (6.10)/(6.11) can be expressed entirely in terms of amplitudes and the phase difference $\Delta\phi(\omega)$ by using Eqs. (4.46)/(4.47). This yields

$$\chi(\omega) = -\frac{\omega P(\omega)}{2k_\mathrm{B}T}\left[\mathrm{i} + \cot(\Delta\phi(\omega))\right] \qquad \text{(L)}, \tag{6.12}$$

$$\chi(\omega) = -\frac{\omega P(\omega)}{2k_\mathrm{B}T}\left[\mathrm{i} - \cot(\Delta\phi(\omega)) - \frac{A_\mathrm{S}(\omega)}{A_\mathrm{P}(\omega)\sin(\Delta\phi(\omega))}\right] \qquad \text{(S)}. \tag{6.13}$$

Eqs. (6.12)/(6.13) are complex equations which contain the original FDT, Eq. (4.12), in their imaginary parts, respectively. In the border case of a particle in a purely viscous medium where $\mathrm{Re}\{\tilde{\gamma}(\omega)\} = \gamma_0$ and $\mathrm{Im}\{\tilde{\gamma}(\omega)\} = 0$ at low frequencies, $\omega \to 0$, one has for the case of stage driving a relation which is independent of the amplitudes,

$$\chi(\omega) \simeq -\frac{\omega P(\omega)}{2k_\mathrm{B}T}[\mathrm{i} - \tan(\Delta\phi)], \quad \text{viscous medium, for low frequencies} \qquad \text{(S)} \tag{6.14}$$

since

$$\frac{A_\mathrm{S}}{A_\mathrm{P}\sin(\Delta\phi)} \overset{(4.42)}{=} \frac{1}{\omega\mathrm{Re}\{\tilde{R}_\mathrm{S}(\omega)\}} \overset{(4.51)}{\simeq} \frac{\omega_\mathrm{c}}{\omega} \overset{(4.59)}{\simeq} -\frac{1}{\tan[\psi(\omega)]} \overset{(4.40)}{=} \frac{1}{\cot[\Delta\phi(\omega)]} = \tan[\Delta\phi(\omega)], \tag{6.15}$$

and because the $\cot(\Delta\phi(\omega))$ term in Eq. (6.13) is negligible, cf. Eqs. (4.40) and (4.59). Relation (6.14) will later be used in the context of positional calibration in viscous media, see subsection 6.3.4.

6.3.3 Determination of the friction retardation spectrum

Finally, one can solve for more unknowns of the equation of motion. From Eq. (4.4) one obtains for the friction retardation spectrum

$$\boxed{\tilde{\gamma}(\omega) + \mathrm{i}\omega m = -\frac{\kappa_\omega}{\mathrm{i}\omega}\left(\frac{1}{\mathrm{i}\omega\tilde{R}_\mathrm{L}(\omega)} + 1\right)} \quad \text{(L)}, \tag{6.16}$$

for the case of laser driving and

$$\boxed{\tilde{\gamma}(\omega) = \tilde{R}_\mathrm{S}(\omega)/\chi(\omega)} \qquad \text{(S)}, \tag{6.17}$$

for the case of stage driving. The additional mass term on the left-hand side of Eq. (6.16) could be fitted. For spherical particles with known radius R and negligible mass in an incompressible medium, the friction retardation spectrum $\tilde{\gamma}(\omega)$ can then be related via the generalized Stokes-Einstein relation to the dynamic shear modulus $G(\omega)$ of the medium, see section 2.3.

6.3.4 Positional calibration

Calibration from the voltage signal results in the case of *laser driving* in $\kappa^{(\mathrm{volt})} = \kappa^{(\mathrm{ex})}\beta$ and $\chi^{(\mathrm{volt})}(\omega) = \chi^{(\mathrm{ex})}(\omega)/\beta^2$. Since the zero frequency limit of $\mathrm{Re}\{\chi(\omega)\}$ is $1/\kappa$, one may find β

through the relation

$$\boxed{\beta = \frac{1}{\mathrm{Re}\{\chi^{(\mathrm{volt})}(\omega)\}\kappa^{(\mathrm{volt})}}} \quad \text{for low frequencies} \quad \text{(L)}. \tag{6.18}$$

For the determination of $\mathrm{Re}\{\chi^{(\mathrm{volt})}(\omega)\}$, Eq. (6.10), can be used. For the case of *stage driving*, the situation is more complicated, since there is no meaningful expression for $\chi^{(\mathrm{volt})}(\omega)$, see Eq. (6.11). For purely viscous media, one may use Eq. (6.14) however, to find β from the low frequency limit. One has

$$\boxed{\beta = \frac{2k_{\mathrm{B}}T}{\omega P^{(\mathrm{volt})}(\omega)} \cdot \frac{\cot(\Delta\phi)}{\kappa^{(\mathrm{volt})}}} \quad \text{for low frequencies, viscous media} \quad \text{(S)}. \tag{6.19}$$

A value with lower statistical error can then be obtained from Eqs. (6.18)/(6.19) by averaging,

$$\beta^{(\mathrm{av})} = \langle\beta\rangle_{\omega} \quad \text{for low frequencies} \tag{6.20}$$

which may be used in case β appears constant for a range of frequencies $\omega \to 0$.

7 Driving method and investigation of the FDT method with simulations

The equations of the FDT method are of general nature, i.e., they are in principle valid for arbitrary profiles with which the laser/stage is moved. In practice, there are important differences between a relocation of the trap and a relocation of the piezo stage, and it is important how the time-dependence of the driving is chosen. In section 7.1, laser and stage driving will be discussed and compared from a practical point of view. Moreover, it will be explained with which profile the laser/stage should be driven.

Furthermore, the FDT method is exact in the frequency domain and it is exact for thermal averages which have to be taken over an infinite number of ensemble members. In practice, one records data for one particle in form of finite time series, however. Therefore, even under ideal conditions, i.e., i) if the system behaves ideally in that sense that it follows exactly the equations of motions given in chapters 3 and 4 and ii) if there are not any experimental imperfections, one will always have certain numerical and statistical errors. In principle one may ask here the question if the method is applicable at all for finite time series of reasonable length, i.e., for measuring times of order $10 - 1000\,\mathrm{s}$. Before starting any experiments, simulations have been performed in order to answer that question. The applied simulation technique will be explained in section 7.2. In section 7.3, the results of the simulations will be presented. In section 7.4, I will present error calculations, in which the statistical errors of the quantities which are obtained from the simulated calibration are derived. Finally, the simulation results will be discussed in section 7.5.

7.1 How to drive?

In the active part of the proposed calibration method a small time-dependent perturbation is applied to the system. For a reliable calibration it has to be ensured that this perturbation is truly small and that it excites the system with frequencies at which the fluctuation-dissipation theorem is valid. Further, the statistical error should be low. The perturbation amplitudes and frequencies are controlled via the choice of the external force $F_{\mathrm{ext}}(t)$. According to Eq. (4.15) the Fourier transformed external force $\tilde{F}_{\mathrm{ext}}(\omega)$ is the product of a coupling part which is different for laser and for stage driving and a controllable part which contains information about the time-dependence and the amplitude of the applied perturbation. Therefore one might ask the following questions:

- Which driving method should one rather choose for a reliable calibration - laser or stage driving?
- Which time-dependence of the driving should one choose for a reliable calibration?
- Which laser/stage amplitudes should one choose for a reliable calibration?

The first two questions are addressed in the following two subsections. The third question is discussed in the context of the performed experiments in paragraph 8.4.1.

7.1.1 Laser or stage driving?

On one hand, there are several reasons to prefer laser driving. Firstly, in the basic equation of the FDT method for laser driving, Eq. (6.4), the mass is eliminated, whereas in the basic equation for stage driving, Eq. (6.5), the mass appears as an frequency-dependent extra term. Secondly, for stage driving with open boundary conditions, the medium will not follow the stage motion exactly, especially at fast driving speeds and far away from the coverslips. With laser driving, this problem does not exist, since when the laser is moved the medium stays at rest. Thirdly, the positional calibration with the FDT method, as explained in paragraph 6.3.4, is working for general media when driving the laser. For stage driving, the positional calibration works only in simply viscous media, so another method for finding the conversion factor β has to be applied within general viscoelastic media. Fourth, in lateral directions the trap can be moved faster than the stage. Thus, with laser driving, a higher bandwidth can be obtained. The result of the basic equation can then be fitted taking into account many frequencies, as explained in paragraph 6.3.1. Acousto-optic modulators (AOM), electro-optic modulators (EOM) and dual traps generated by beam polarization splitters provide tools to change the trapping position very fast, up to the order of GHz with EOM, in lateral directions. In contrast, stage driving allows to change the stage position only relatively slowly, up to the order of sub-kHz.

On the other hand, moving the stage requires less instrumental effort than implementing a moving trap and it is easily possible in all directions. Moving the trapping center relative to the stage in axial direction is, however, a fairly slow process as it happens by means of diffractive optical elements (DOE). Further, the maximum oscillation frequency of a fast piezo stage should be sufficiently much higher than those frequencies at which bio-active processes typically occur so that the new calibration method should be applicable in bio-active media also with stage driving[1]. Moreover, at a given displacement of the trapped particle[2] and at low frequencies, stage driving would give a lower statistical error than laser driving since it has to operate with higher amplitudes[3], see figure 8.2 in paragraph 8.4.1 and the text to that figure.

Thus the choice between moving the laser or the stage depends on the directions for which the calibration is to be performed and on the instrumental effort which one wants to make.

7.1.2 Time-dependence of driving - driving sinusoidally or non-sinusoidally?

The controllable part $\tilde{d}(\omega)$ of the external force spectrum $\tilde{F}_{\text{ext}}(\omega)$ contains information about the time-dependence and the amplitudes of the applied perturbation, see Eq. (4.15). According to Eqs. (4.18)/(4.19) $\tilde{d}(\omega)$ is equal to the (negative) velocity spectrum of the laser/stage,

[1] The piezo stage on setup 2 in the optical tweezers lab at the Niels Bohr Institute (Physik Instrumente, P-517.3CL) performs very accurate small-amplitude oscillations at 100 Hz. Bio-active processes are presumably only relevant at lower frequencies up to 20 Hz [49].

[2] The trapped particle should be displaced as little as possible to ensure that the fluctuation-dissipation theorem holds. See subsection 8.4.1.

[3] The relative statistical error is proportional to the laser/stage amplitude, *not* to the particle amplitude.

$\pm i\omega\tilde{x}_{L/S}(\omega)$. A general classification of time-dependencies of the laser/stage position $x_{L/S}(t)$ is into sinusoidal and non-sinusoidal functions. In the following, some characteristics of sinusoidal and non-sinusoidal driving with respect to the new calibration method will be explained. Furthermore, example profiles, which will be applied in the simulations in section 7.2, will be presented.

Non-sinusoidal driving

With *non-sinusoidal driving*, the laser/stage is typically deflected by a distance $A_{L/S}$ according to a chosen profile $x_{L/S}(t)$. The basic equations Eq. (6.4)/(6.5) can be applied simultaneously at many frequencies, i.e., these frequencies which are contained in the non-singular driving velocity spectrum $i\omega\tilde{x}_{L/S}(\omega)$. Fitting as described in paragraph 6.3.1 then yields a decrease in the statistical error.

Example 1: Laser driving with a jump profile
At non-sinusoidal driving, the laser motion profile $x_L(t)$ is required to exhibit an extended frequency spectrum which allows for a reliable calculation of the active spectrum according to Eq. (4.24). Such a driving function is given by a jump in the laser position

$$x_L(t) = A_L(1 - \theta(t)) = A_L\theta^-(t), \tag{7.1}$$

where we have introduced $\theta^-(t) := \theta(-t)$ as the Heaviside function with a negative time argument. A_L is a positive constant with dimensions of a length. The negative driving velocity spectrum is then given by

$$-i\omega\tilde{x}_L(\omega) = A_L(1 - i\pi\omega\delta(\omega)), \tag{7.2}$$

This spectral function is easily inserted in Eq. (4.24), since it is constant for non-zero frequencies. One has

$$\tilde{R}_L(\omega) = \frac{\langle\tilde{x}(\omega)\rangle}{A_L} \quad (\text{for } \omega \neq 0), \tag{7.3}$$

where $\tilde{x}(\omega)$ is the positional spectrum of the trapped particle in the driven system. Since the active spectrum at non-zero frequency is easily obtained by dividing the positional spectrum by A_L, the entire accessible frequency spectrum can be used for the calibration. Eq. (7.1) corresponds to a jump in the laser position from the deflection A_L to the value 0[4], see Fig. 7.1 (dashed line) on page 57 . Describing the jump of the laser position by a θ-function is realistic, because with fast equipment the time to switch the laser position laterally is very small compared to the time scales on which the movement of the trapped object takes place.

Example 2: Stage driving with error-function profile
The stage motion can be controlled only on a relatively slow time scale on the order of sub-ms. This is slower or comparable to typical time scales of the particle motion, like the relaxation time in the trap which is on the order of ms. Therefore it is impossible to choose the driving function $x_S(t)$ to contain a Heaviside function. Instead a function with an extended velocity spectrum is chosen, namely

$$x_S(t) = \frac{A_S}{2}\left\{\text{erf}\left(\frac{t}{\sqrt{2\sigma_S^2}}\right) + 1\right\}, \tag{7.4}$$

[4]Since the laser position defines the zero-point of the QPD measurement, the jump would go from A_L to 0.

with the error function

$$\mathrm{erf}(t) = \frac{2}{\sqrt{\pi}} \int_0^t \exp(-t'^2) dt', \tag{7.5}$$

the amplitude A_S and the width σ_S. $x_\mathrm{S}(t)$ is plotted in Fig. 7.7 (dashed line) on page 63. The discrete driving velocity spectrum is given by the Gaussian function

$$\mathrm{i}\omega\tilde{x}_\mathrm{S}(\omega) = A_\mathrm{S} \exp\left(-\frac{1}{2}\sigma_\mathrm{S}^2(\omega)^2\right), \tag{7.6}$$

According to Eq. (4.25), the active spectrum becomes

$$\tilde{R}_\mathrm{S}(\omega) = \frac{\langle\tilde{x}(\omega)\rangle}{A_\mathrm{S} \exp\left(-\frac{1}{2}\sigma_\mathrm{S}^2(\omega)^2\right)}. \tag{7.7}$$

Sinusoidal driving

Sinusoidal driving profiles like

$$x_\mathrm{L/S}(t) = A_\mathrm{L/S} \sin(\omega_\mathrm{L/S,0} t + \phi_\mathrm{L/S}), \tag{7.8}$$

where $A_\mathrm{L/S}$ is the laser/stage amplitude, $\omega_\mathrm{L/S,0}$ is the oscillation frequency and $\phi_\mathrm{L/S}$ is the phase shift, are singular in frequency space. Hence, the calibration equations in terms of amplitudes and angles, Eqs. (6.6)/6.7), can be applied at *one* frequency only and one obtains *one* values for κ or $\kappa - \omega^2 m$. For a reliable calibration result, Eqs. (6.6)/(6.7) should therefore be applied for K_Max different driving frequencies $\omega_{\mathrm{L/S},K}$, with $K = 1, ..., K_\mathrm{Max}$. This reduces the statistical error and enables fitting for the mass in the case of stage driving. Further and most importantly, it allows the recognition of systematic errors that may occur at certain frequencies: For stage driving, e.g., the spectrum of the calibration results should give a parabolic function, cf. Eq. (6.7). Deviations from that functional form may indicate frequencies for which systematic errors occur and they may be excluded in the calibration procedure. This identification of systematic errors is especially relevant for calibration inside living cells. Here, the FDT is likely to be broken at low frequencies due to active processes [49]. In general, it is recommendable to choose the values of $\omega_{\mathrm{S/L},K}$ in an interval as broad as possible with the equipment available. The K_Max angular frequencies $\omega_K = 2\pi f_K$ were chosen to be an integer multiple of the angular frequency spacing $2\pi/T$ to avoid leaking[5],

$$\omega_K = K \cdot 2\pi/T, \quad K = 1, \ldots, K_\mathrm{Max}. \tag{7.9}$$

The driving velocity spectrum then becomes for $\phi_\mathrm{L/S} = 0$

$$\mathrm{i}\omega\tilde{x}_\mathrm{L/S}(\omega) = A\pi\omega_K[\delta(\omega + \omega_K) + \delta(\omega - \omega_K)]. \tag{7.10}$$

Calibration with sinusoidal driving has been tested with simulations, see section 7.3. Further, for the verification of the novel calibration method in the lab, we use exclusively sinusoidal driving, see chapter 8.

[5] For the simulations presented in section 7.3, the measuring time T is given by the window length T_wind, see section 7.2.2.

7.2 Simulation of the calibration with the FDT method

Real data is recorded as finite time series. With a finite measurement time, averaging will leave some *noise*. Furthermore, the Fourier transform of the finite time data to the frequency domain can cause *leaking* and the finite sampling frequency causes *aliasing* [40, 69]. The simulations presented in the following sections serve to demonstrate that the novel calibration method works well under realistic conditions. The motion of the particle itself and also the position tracking with a finite sampling frequency have been simulated. In this section, the applied simulation technique is explained and it is described how the simulated data is evaluated according to the FDT method.

7.2.1 Propagation of the equations of motion

In the simulations, the undriven equation of motion, Eq. (3.5), and the driven equations of motion, Eq. (4.13)/(4.14), were propagated with a modification of the fourth order Runge-Kutta (RK) method[6] to solve the ordinary differential equation

$$\frac{d\dot{x}(t)}{dt} = \frac{1}{m} f\left(t, x(t), \dot{x}(t)\right) \tag{7.11}$$

iteratively. The function $f\left(t, x(t), \dot{x}(t)\right)$ is given by the right hand sides of Eqs. (3.5), (4.13)/(4.14). The trapped particle is assumed to be a spherical bead of radius R and density ρ. For the trap stiffness of the optical tweezers, a value κ_{input} has been chosen as input to the simulations[7]. The friction retardation functions $\gamma_{1/2}(t)$ are chosen according to a certain frictional behavior, namely i) instantaneous simple Stokes friction, i.e.,

$$\gamma_1(t) = \gamma_0 \delta(t), \tag{7.12}$$
$$\gamma_2(t) = 0. \tag{7.13}$$

with the friction coefficient $\gamma_0 = 6\pi\eta R$ corresponding to a spherical object situated in water, or ii) exponentially retarded friction,

$$\gamma_1(t) = \gamma_0/\tau_{\text{fr}} \cdot \exp(-t/\tau_{\text{fr}}), \tag{7.14}$$
$$\gamma_2(t) = 0, \tag{7.15}$$

where τ_{fr} is a characteristic decay time of order μs. Case ii) represents a simple model for a viscoelastic medium. The acceleration dependence can be omitted at the numerical propagation, since in all simulations $\gamma_2(t)$ is set to zero. The most intricate steps at the propagation of the equation of motion have thus been the determination of the velocity memory term

$$-\int_0^\infty \gamma_1(\tau)\dot{x}(t-\tau)d\tau \tag{7.16}$$

[6]The Runge-Kutta method solves initial value problems with an ordinary differential equations of type $\dot{y} = f(t, y(t))$ and an initial value $y(t_0) = y_0$. Here that method has been applied for $y = \dot{x}$ and a position dependence was included. Then two initial values must be given, $x(t_0)$ and $\dot{x}(t_0)$.

[7]The main goal of the simulations is to check if the value of κ_{input} can be reproduced by applying the FDT method.

and the determination of the random force term $F_{\mathrm{R}}(t)$. The velocity memory term, Eq. (7.16), has been computed by numerical integration, whereby several approximations for obtaining a fast propagation have been applied[8]. The random force term was obtained by numerical inverse Fourier transform of Eq. (3.20), thereby generating the right noise color of the time-domain random force. In the case of simple Stokes friction, however, both the velocity memory term and the random force term become trivial. The velocity memory term becomes the well known Stokes friction $-\gamma_0\dot{x}$, while the random force is white noise, see section 3.3. Then, the equation of motion of the undriven system, Eq. (3.5), has been propagated with its analytical solution, Eq. (15) of [40], which is much faster on the computer.
Trajectories corresponding to windows of duration T_{wind} and $T_{\mathrm{wind,D}}$ for the undriven and for the driven system, respectively, were found, cf. paragraph 7.2.2. The initial positions and velocities for each window were taken as the final positions and velocities of the previous window. Also the previous velocities, relevant for the initial velocity memory term calculations, were handed over from one window to the next. On the obtained raw trajectory data, windowing and the numerical Fourier transform were applied as described in section 7.2.2. The mean squared displacement $\sigma^2(t) = \langle [x(t) - x(t_0)]^2 \rangle$ was calculated in order to check if the equipartition theorem

$$\lim_{t\to\infty} \sigma^2(t) = k_{\mathrm{B}}T/\kappa, \tag{7.17}$$

is fulfilled (data not shown). Then the calibration method has been applied like explained in paragraph 7.2.3. The frequency-dependent results were plotted against the frequency $f = \omega/(2\pi)$.

7.2.2 Handling data

In practice, one records data for one particle in form of finite time series. In the following it will be explained how to deal with simulated data series $x_j^{(\mathrm{sim})}$. Thermal averages are calculated by windowing and the discrete Fourier transform is applied in order to change to the frequency domain. Further, thermal averages are calculated by windowing and blocking. Moreover, one has to perform positional calibration.

Discrete Fourier transform

Data are recorded for a time T with frequency f_{sample}. From the resulting time series $x_j^{(\mathrm{sim})}$, $\quad j = 1, ..., N$, one forms the discrete Fourier transform,

$$\hat{x}_k^{(\mathrm{sim})} = \Delta t \sum_{j=1}^{N} e^{-\mathrm{i}2\pi f_k t} x_j^{(\mathrm{sim})} = \Delta t \sum_{j=1}^{N} e^{-\mathrm{i}2\pi jk/N} x_j^{(\mathrm{sim})}, \tag{7.18}$$

$k = -N/2+1, ..., N/2$, where $\Delta t = 1/f_{\mathrm{sample}}$, $t_j = j\Delta t$, and $N\Delta t = T$. The discrete data have a frequency spacing of $1/T$ and a maximum frequency $f_{\mathrm{Nyq}} = f_{\mathrm{sample}}/2$. The discrete frequencies are given by $f_k = \omega_k/(2\pi) = k/T$ [40].

[8] The upper integration limit in Eq. (7.16) has been cut-off at a frequency on order ms. Furthermore, blocked velocity values have been used, in order to reduce the number of terms contributing to the sum which approximates the integral.

Windowing

Windowing as a tool of data compression has already been used in power spectral analysis for optical tweezers [40]. Windowing essentially means that a long time series is cut into shorter pieces, from this pieces one calculates observables like the power spectrum or the active spectrum, and finally one averages over the resulting spectra. When the number of windows is large, the values of the compressed spectra are statistically independent and Gaussian distributed and the statistical error decreases, see the error calculation in section 7.4.
In the simulations presented in section 7.3, no long time series vectors were created and then cut into pieces, however. Instead many relatively small data windows were generated a priori, both for the driven and the undriven system[9]. Over these windows it was averaged then, $\langle . \rangle_{\mathrm{wind}}$, to obtain an estimate for the thermal average, $\langle . \rangle$. To avoid leakage, the window length for the undriven system T_{wind} must not be chosen too small[10]. For the driven part, many relaxation processes over a time interval $T_{\mathrm{wind,D}}$ are recorded and then it is averaged. $T_{\mathrm{wind,D}}$ must be chosen high enough to cover the whole relaxation process. For non-sinusoidal driving, $T_{\mathrm{wind,D}}$ may be chosen smaller than T_{wind}, since the relaxation process is typically in the order of ms. Therefore it is convenient to add zeros to the recorded driven data, a procedure called zero padding [69], so that again a window of length T_{wind} is obtained. For sinusoidal driving, $T_{\mathrm{wind,D}}$ should be chosen equal to T_{wind}. Then both the undriven and the driven data sets will have a frequency spacing of $\Delta f = 1/T_{\mathrm{wind}}$. The total measuring time is given by

$$T_{\mathrm{meas}} = N_{\mathrm{wind,U}} T_{\mathrm{wind}} + N_{\mathrm{wind,D}} T_{\mathrm{wind,D}}, \tag{7.19}$$

where $N_{\mathrm{wind,U}}$ and $N_{\mathrm{wind,D}}$ denote the window numbers for the undriven and the driven system, respectively.
Also in the undriven part of the experiments shown in chapter 8, windowing has been applied in that sense that small data windows have been recorded and the resulting power spectra have been averaged.

Blocking

Blocking [40, 69] basically means to average the obtained spectra over adjacent discrete frequencies f_k which are so close to each other that the theoretical spectrum values do not vary much over these frequencies. In the simulations, the trajectories are only generated for short times T_{wind}. One obtains a very large frequency spacing $\Delta f = 1/T_{\mathrm{wind}}$ on the order of 100 Hz. Thus one may not simply block the spectrum over several discrete frequencies, since the theoretical value of the spectrum would vary for these frequencies considerably. However, it can be blocked over the ratio between measured and theoretical spectrum which ideally would be equal to 1. Further, one may block over the results of the basic equations Eqs. (6.4)/(6.5), which ideally would be equal to the simulation input value κ_{input}[11]. Blocked data is indicated by a bar above the quantity symbol, e.g. $\bar{\kappa}_k^{(\mathrm{sim/ex})}$ for the result of the calibration equation which is obtained from blocking of frequencies around f_k.

[9] Only small data windows of sub-second length could be generated due to finite computer memory and speed.
[10] Typically, a window should have a length which is at least a few times the time scale t_c which is given by the corner frequency, $t_c = 1/f_c$.
[11] For stage driving, this requires the negligibility of the mass term.

7.2.3 Calibration from simulated data

In this paragraph it is explained how the FDT method is applied to the data from the simulations.

Trap stiffness calibration

From $\hat{x}_k^{(\mathrm{sim})}$ and windowing as described in paragraph 7.2.2, the simulated, discrete power spectrum,

$$P_k^{(\mathrm{sim})} = \frac{\langle |\hat{x}_k^{(\mathrm{sim})}|^2 \rangle_{\mathrm{wind}}}{T_{\mathrm{wind}}} \tag{7.20}$$

and active spectrum

$$\hat{R}_{\mathrm{L},k}^{(\mathrm{sim})} = \frac{\langle \hat{x}_k^{(\mathrm{sim})} \rangle_{\mathrm{wind}}}{-\mathrm{i}2\pi f_k \hat{x}_{\mathrm{L},k}} \qquad (\mathrm{L}), \tag{7.21}$$

$$\hat{R}_{\mathrm{S},k}^{(\mathrm{sim})} = \frac{\langle \hat{x}_k^{(\mathrm{sim})} \rangle_{\mathrm{wind}}}{\mathrm{i}2\pi f_k \hat{x}_{\mathrm{S},k}} \qquad (\mathrm{S}), \tag{7.22}$$

are obtained from the trajectories of the driven and the undriven system, respectively. Using both spectra it is calibrated with the discretized versions of Eqs. (6.4)/(6.5)[12],

$$\kappa_k^{(\mathrm{sim})} = 2k_{\mathrm{B}}T \cdot \frac{\mathrm{Re}\{\hat{R}_{\mathrm{L},k}^{(\mathrm{sim})}\}}{P_k^{(\mathrm{sim})}} \qquad (\mathrm{L}), \tag{7.23}$$

$$(\kappa - (2\pi f)^2 m)_k^{(\mathrm{sim})} = 2k_{\mathrm{B}}T \cdot \frac{\mathrm{Re}\{\hat{R}_{\mathrm{S},k}^{(\mathrm{sim})}\}}{P_k^{(\mathrm{sim})}} \qquad (\mathrm{S}). \tag{7.24}$$

The frequency dependent calibration results thus obtained are finally averaged over frequencies[13],

$$\kappa^{(\mathrm{av})} = \langle \kappa_k^{(\mathrm{sim})} \rangle_k \qquad (\mathrm{L}), \tag{7.25}$$

$$\kappa^{(\mathrm{av})} = \langle \kappa_k^{(\mathrm{sim})} \rangle_k \simeq \langle (\kappa - (2\pi f)^2 m)_k^{(\mathrm{sim})} \rangle_k \qquad (\mathrm{S}), \tag{7.26}$$

where the average is denoted by $\langle . \rangle_k$. Local blocking of frequencies is also applied in the case of laser driving, one obtains $\bar{\kappa}_k^{(\mathrm{sim})}$.

Response function and friction retardation spectrum

The response function at frequency f_k is obtained from the discretized versions of Eq. (6.10)/(6.11),

$$\chi_k^{(\mathrm{sim})} = -\frac{\mathrm{i}2\pi f_k \hat{R}_{\mathrm{L},k}^{(\mathrm{sim})}}{\kappa^{(\mathrm{av})}} \qquad (\mathrm{L}), \tag{7.27}$$

$$\chi_k^{(\mathrm{sim})} = \frac{1 - \mathrm{i}2\pi f_k \hat{R}_{\mathrm{S},k}^{(\mathrm{sim})}}{\kappa^{(\mathrm{av})}} \qquad (\mathrm{S}). \tag{7.28}$$

[12] For sinusoidal driving with frequency f_K, results are obtained only at f_K, not at generic frequencies f_k, see paragraph 7.1.2

[13] For sinusoidal driving, one averages over the results of several driving frequencies f_K, see paragraph 7.1.2

Finally one can find the friction retardation spectrum at frequency f_k from the discretized version of Eq. (6.16)/(6.17),

$$(\hat{\gamma} + \mathrm{i}2\pi f m)_k^{(\mathrm{sim})} = -\frac{\kappa^{(\mathrm{av})}}{\mathrm{i}2\pi f_k}\left(\frac{1}{\mathrm{i}2\pi f_k \hat{R}_{\mathrm{L},k}^{(\mathrm{sim})}} + 1\right) \quad \text{(L)}, \tag{7.29}$$

$$\hat{\gamma}_k^{(\mathrm{sim})} = \hat{R}_{\mathrm{S},k}^{(\mathrm{sim})}/\chi_k^{(\mathrm{sim})} \quad \text{(S)}. \tag{7.30}$$

In favour of a lower statistical error in Eqs. (7.27) to (7.29) we have used the averaged stiffness $\kappa^{(\mathrm{av})}$ from Eqs. (7.25)/(7.26) instead of the local stiffness values from Eqs. (7.23)/(7.24).

Positional calibration

Since the zero frequency limit of $\mathrm{Re}\{\chi(\omega)\}$ is $1/\kappa$, for the case of laser driving one may find experimental values β_K through the relation

$$\beta_k = \mathrm{Re}\{\chi_k^{(\mathrm{volt})}\}\kappa^{(\mathrm{av,volt})} \quad \text{for low frequencies,} \quad \text{(L)} \tag{7.31}$$

which is valid if f_k is low, cf. section 6.3.4. A value with lower statistical error can be obtained by averaging

$$\beta^{(\mathrm{av})} = \langle \beta_k \rangle_k \quad \text{for low frequencies,} \quad \text{(L)} \tag{7.32}$$

which may be used in case β_k appears constant for a number of frequencies $f_k \to 0$. With the conversion factor thus found, one can now calculate the actual values $\kappa_k^{(\mathrm{sim})}$, $\chi_k^{(\mathrm{sim})}$ and $\hat{\gamma}_k^{(\mathrm{sim})}$[14].

7.3 Simulation results

The calibration method has been tested for different cases, i) fast relocation of the laser in a medium with retarded friction, see paragraph 7.3.1, ii) slow relocation of the stage in a simple viscous medium, see paragraph 7.3.2, iii) slow sinusoidal motion of laser or stage in a simple viscous medium, see paragraph 7.3.3 and iv) fast sinusoidal motion of the laser in a medium with retarded friction, see paragraph 7.3.4. In paragraph 7.3.5 the parameters of the simulations are subsumed in tables. Finally, in paragraph 7.5 I will discuss why sinusoidal driving would perform best in a real experiment.

7.3.1 Calibration with fast relocation of the laser (non-sinusoidal driving)

A calibration for the trap stiffness while simultaneously probing the system's response function and the friction retardation spectrum at *high* frequencies can be implemented by *fast* laser driving. In an experiment, high spatial and temporal resolution of the positional detection system is required. Such a situation has been simulated, whereby a relatively strong trap of stiffness $\kappa_{\mathrm{input}} = 0.1$ pN/nm has been driven non-sinusoidally. As suggested in paragraph 7.1.2, a driving

[14] In our simulations, a volt-meter conversion has not been included, i.e., it is assumed that one measures positions. β_{input} is therefore 1. β_k and $\beta^{(\mathrm{av})}$ have been determined only for the case of laser driving for which positional calibration with the FDT method works for general media.

profile which corresponds to a jump in the laser position from the deflection A_{L} to the value 0, Eq. (7.1), has been used. The laser position is plotted in Fig. 7.1 (dashed line). The friction retardation function $\gamma_1(t)$ chosen is the exponentially decaying function Eq. (7.14). The results of the simulation are shown in Figs. 7.1–7.6.

In Figs. 7.1 and 7.2(a) the system's behaviour in the absence of thermal noise is shown. This

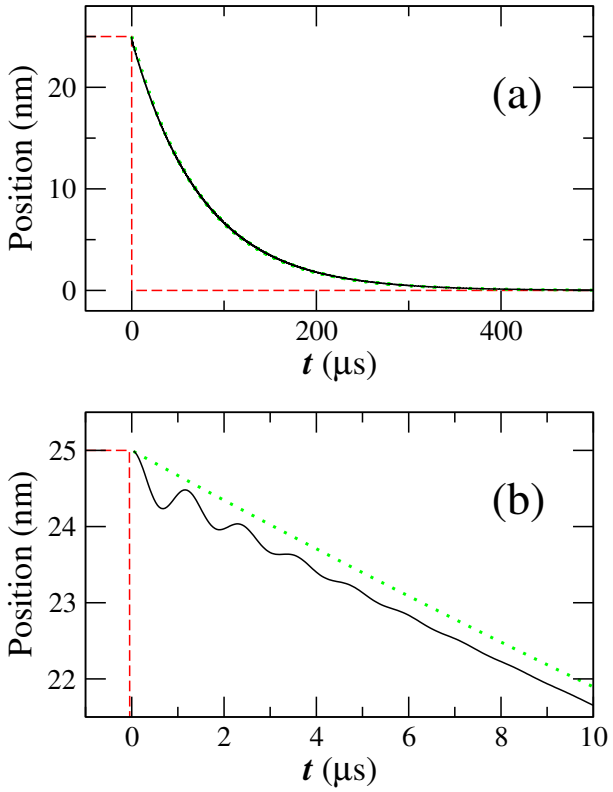

Figure 7.1: Simulation results for the case of non-sinusoidal laser driving, Eq. (7.1), with exponentially decaying friction retardation function, Eq. (7.14), I: Trajectory $x_j^{(\mathrm{sim})}$ (solid line) of the driven system, simulated without thermal noise ($F_{\mathrm{R}}(t_j) = 0$). Averaging over windows is not necessary here, because there is no thermal part of the motion. The data are sampled with a high sampling frequency of $f_{\mathrm{sample}} = 10$ MHz. (a): The entire relaxation process. After the jump of the laser position (dashed line) at time $t = 0$ the trapped particle relaxes into the new trap center. The bead follows a trajectory similar to $x_0(t) = A\exp(-\kappa_{\mathrm{input}}/\gamma_0 t)$ (dotted line). (b): Beginning of the relaxation process. The trajectory deviates from $x_0(t)$. This is due to the exponential friction retardation function in the memory kernel. Because of the delayed impact of the friction, initially the particle is accelerated relatively too much and an oscillating contribution to the motion of the particle results.

corresponds to averaging the thermal noise. In this case one obtains the driven, non-thermal part of the motion without averaging over a large number of windows. The driven part has an oscillating contribution due to the complex friction, see Fig. 7.1(b).

This leads to a resonance peak in the real part of the active spectrum $\mathrm{Re}\{\hat{R}^{(\mathrm{sim})}_{\mathrm{L},k}\}$, see Fig. 7.2(a), which is also present in the power spectrum $P^{(\mathrm{sim})}_k$ of the corresponding undriven system, Fig. 7.2(b). Similar resonance peaks appear at power spectra of AFM, but at lower frequen-

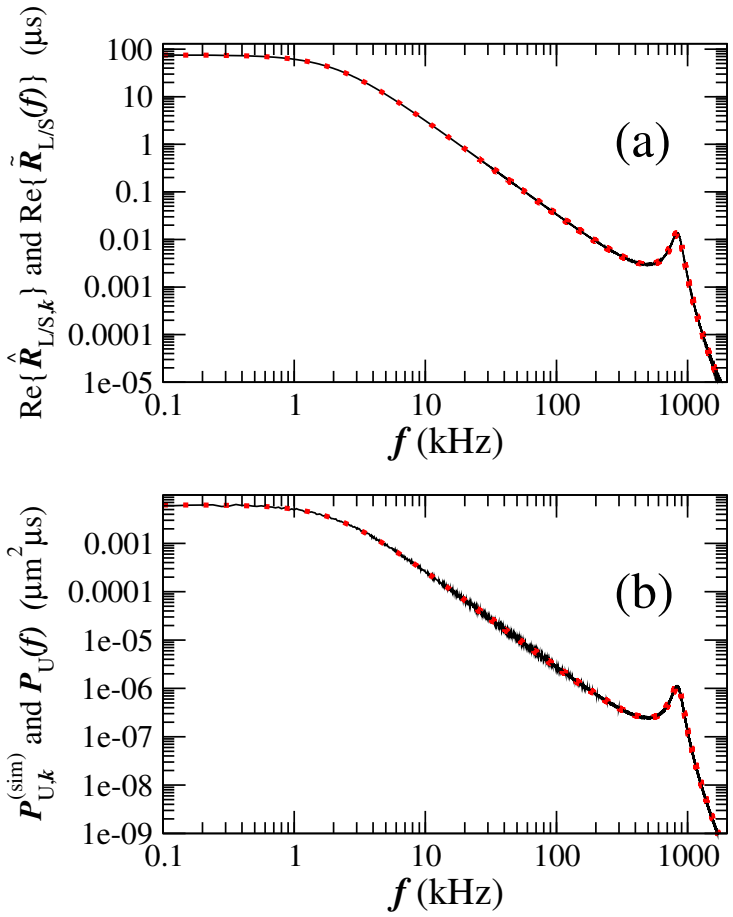

Figure 7.2: Simulation results for the case of non-sinusoidal laser driving, Eq. (7.1), with exponentially decaying friction retardation function, Eq. (7.14), II: (a): Same data as in Fig. 7.1. The oscillating contribution at the particle's motion produces a resonance peak in the real part of the active spectrum $\mathrm{Re}\{\hat{R}^{(\mathrm{sim})}_{\mathrm{L},k}\}$ (solid line) at about 830 kHz. The analytical result, Eq. (4.48), is indicated by a dotted line. (b): A corresponding peak occurs also at the power spectrum of the corresponding undriven system. The simulation result $P^{(\mathrm{sim})}_k$ is indicated by a solid line, the analytical result, Eq. (3.23), by a dotted line.

cies [70,71]. Comparing the two panels of Fig. 7.2, one can clearly recognize the proportionality between the real part of the active spectrum and the power spectrum which is a consequence of the FDT.

In Figs. 7.3 to 7.6 however, data from a simulation with more realistic parameters is presented, on which the new calibration method finally has been applied. Thermal noise was added and a sampling frequency of $f_{\mathrm{sample}} = 300\,\mathrm{kHz}$ has been used. In Fig. 7.3 the results for the power spectrum (left side) and the real part of the active spectrum (right side) are shown, respectively. Both spectra exhibit significant aliasing errors for frequencies higher than 10 kHz.

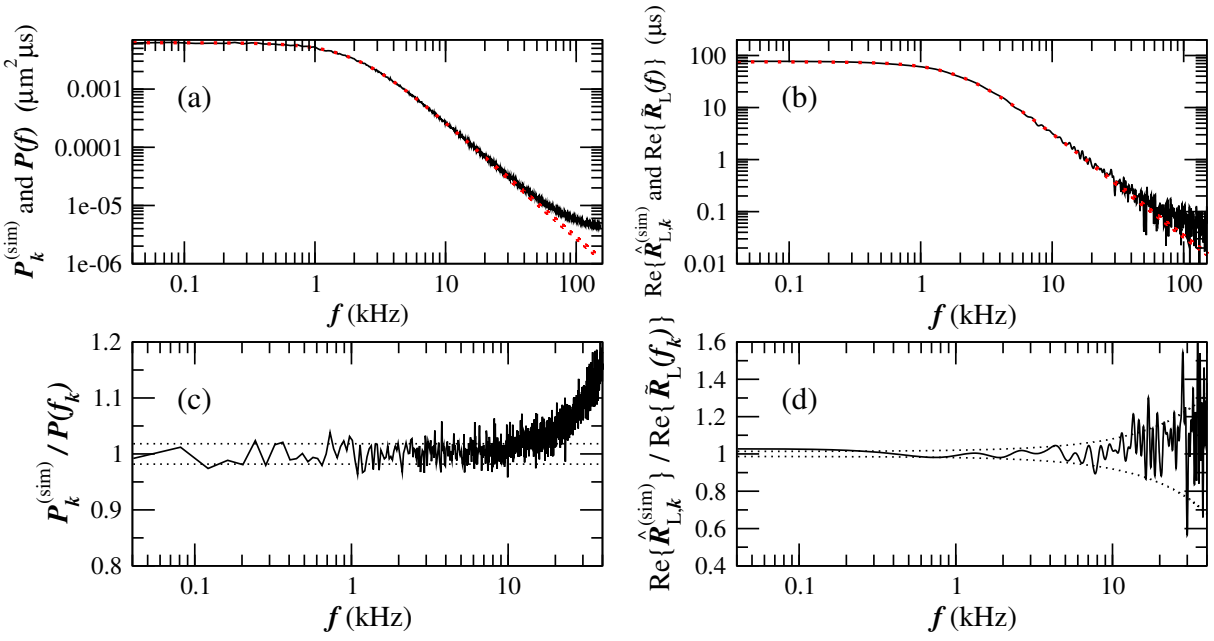

Figure 7.3: Simulation results for the case of non-sinusoidal laser driving, Eq. (7.1), with exponentially decaying friction retardation function, Eq. (7.14), III: Left side: Power spectrum $P_k^{(\mathrm{sim})}$ of the undriven system compared to the theoretical spectrum $P(f)$, Eq. (3.23). Right side: Real part of the active spectrum $\mathrm{Re}\{\hat{R}_{\mathrm{L},k}^{(\mathrm{sim})}\}$ of the driven system, calculated with Eq. (7.3), compared to the real part of the theoretical spectrum $\mathrm{Re}\{\tilde{R}_{\mathrm{L}}(f)\}$, Eq. (4.48). (a),(b): Simulated spectrum (solid line) and theoretical spectrum (dotted line) in a double-logarithmic plot. Aliasing for high frequencies is visible. (c),(d): Simulated spectrum divided by theoretical spectrum (solid line). Aliasing which becomes relevant at about 10 kHz leads to two- to threefold exceeded values at the Nyquist frequency. The results for the real part of the active spectrum are correlated for adjacent frequencies which is due to zero-padding of the data, see paragraph 7.2.2. The plotted standard deviation of the power spectrum and the statistical error estimate for the real part of the active spectrum (dotted lines) are given in Eq.'s (7.38) and (7.45).

Fig. 7.4 shows the results of the application of the calibration method. The trap stiffness values $\kappa_k^{(\mathrm{sim})}$ have a bias for intermediate frequencies lower than about 40 kHz, they tend to be high. Due to the large statistical error of $\kappa_k^{(\mathrm{sim})}$, this bias is only identifiable when considering the blocked data $\bar{\kappa}_k^{(\mathrm{sim})}$, see Fig. 7.4(b). This bias is probably due to errors occurring at the numerical propagation of the equation of motion in the initial phase of each window, when the bead is accelerated very much due to its initially large relative displacement from the trap center. Thus the bias is an artifact of the simulation which would not appear in real experiments. For frequencies higher than 40 kHz the results for $\kappa_k^{(\mathrm{sim})}$ and $\bar{\kappa}^{(\mathrm{sim})}$ do not deviate more from κ_{input} than one would expect from the statistical error, however. Only for frequencies higher than about 80 kHz the result for $\kappa_k^{(\mathrm{sim})}$ becomes too high due to aliasing. This shows that aliasing effects of the power spectrum and of the real part of the active spectrum *compensate for each other* to a large extent, also for frequencies higher than 10 kHz. When averaging according to Eq. (7.25),

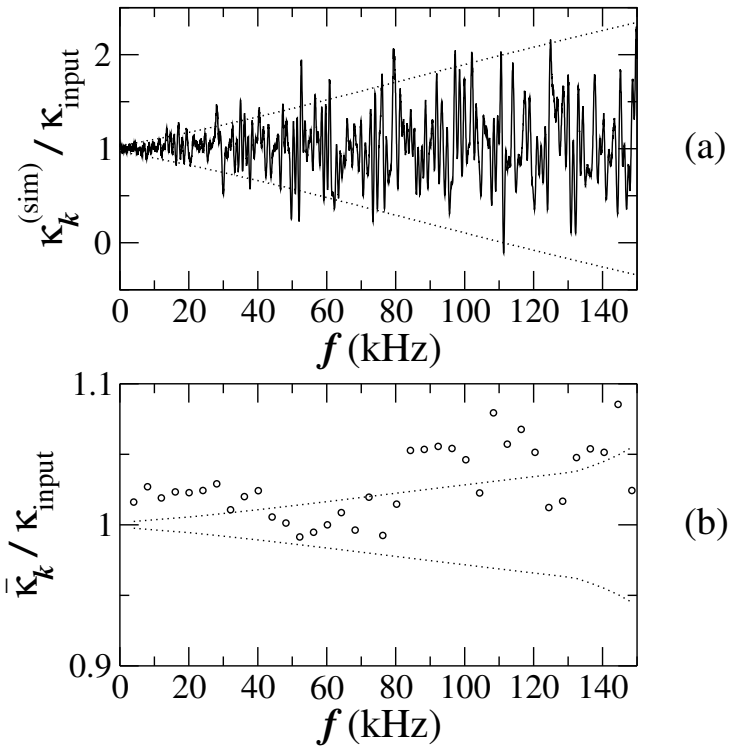

Figure 7.4: Simulation results for the case of non-sinusoidal laser driving, Eq. (7.1), with exponentially decaying friction retardation function, Eq. (7.14), IV:Application of the calibration equation, Eq. (7.23), to the results shown in Fig. 7.3. The statistical error estimates are given in section 7.4. (a): $\kappa_k^{(\mathrm{sim})}$ (solid line), obtained from the application of the calibration equation Eq. (7.23). (b): Blocked results $\bar{\kappa}_k^{(\mathrm{sim})}$. Biases due to numerical errors at the generation of the raw data and due to aliasing are only visible when looking at the blocked data.

it is not a priori given which frequencies to include. One suggestion is to include frequencies in an interval where one assumes the result to be reliable. Calculating the average over the interval

$[f_{\min}, f_{\max}]$ with $f_{\min} = 40\,\mathrm{Hz}$ and $f_{\max} = 4\,\mathrm{kHz}$[15] yields

$$\frac{\kappa^{(\mathrm{av})}}{\kappa_{\mathrm{input}}} = 1.005 \pm 0.023. \tag{7.33}$$

Higher frequencies have not been included in the averaging procedure because of the above-mentioned bias due to numerical errors at the propagation of the equation of motion. Further, it would not be recommendable to include higher frequencies, since the statistical error of $\kappa_k^{(\mathrm{sim})}$ increases fast with frequency.
Fig. 7.5 shows the result from application of the response function calibration equation, Eq. (7.27). It can be seen that the response function can be determined with good precision for frequencies lower than 10 kHz. For higher frequencies, aliasing errors become very large, especially for the real part $\mathrm{Re}\{\chi_k^{(\mathrm{sim})}\}$.

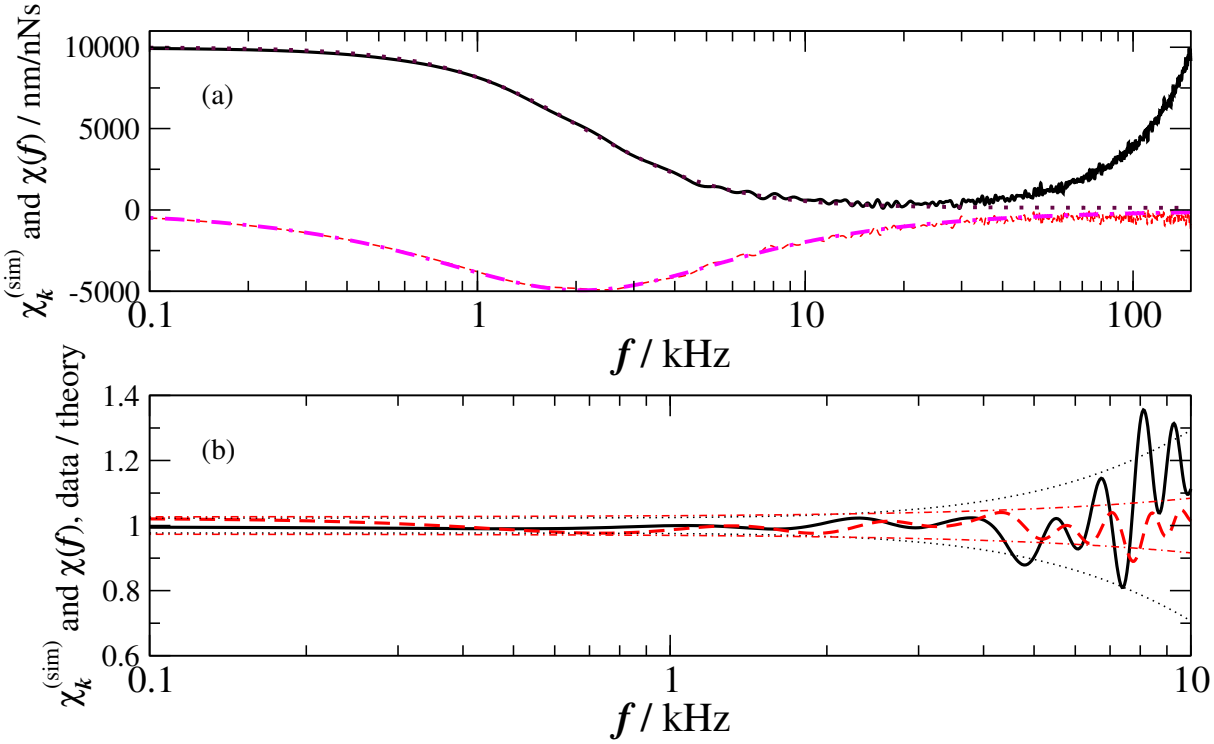

Figure 7.5: Simulation results for the case of non-sinusoidal laser driving, Eq. (7.1), with exponentially decaying friction retardation function, Eq. (7.14), V: Application of the response function calibration equation, Eq. (7.27). (a),(b): Absolute values for $\mathrm{Re}\{\chi_k^{(\mathrm{sim})}\}$ (solid line) and $\mathrm{Im}\{\chi_k^{(\mathrm{sim})}\}$ (dashed line) and the theoretical curves, Eq. (4.4), for $\mathrm{Re}\{\chi(f)\}$ (dotted line) and $\mathrm{Im}\{\chi(f)\}$ (dashed-dotted line). Aliasing is visible for high frequencies. (c),(d): Data/theory plots for same data set. The relative errors for real part (dashed lines) and for the imaginary part (dashed-dotted lines) are increasing with frequency, the absolute values are decreasing. The correlation of the data for different frequencies due to zero-padding is apparent.

[15] At these low frequencies, the above-mentioned bias due to numerical errors at the propagation of the equation of motion is not present.

Finally, the friction retardation spectrum can be found by application of Eq. (7.29), see Fig. 7.6. For the real part $\mathrm{Re}\{\tilde{\gamma}(f)\}$, Fig. 7.6(left), one obtains good results for frequencies lower than $\sim 10\,\mathrm{kHz}$. For higher frequencies, both aliasing errors and statistical errors become large. For the imaginary part $\mathrm{Im}\{\tilde{\gamma}(f)\}$, Fig. 7.6(right), one obtains for all frequencies results with a statistical error which is larger than 100%. Especially for low frequencies one obtains a very high statistical error, since the absolute value of $\mathrm{Im}\{\tilde{\gamma}(f)\}$ is close to zero. For frequencies larger than $\sim 10\,\mathrm{kHz}$, aliasing errors are high for the imaginary part, too.

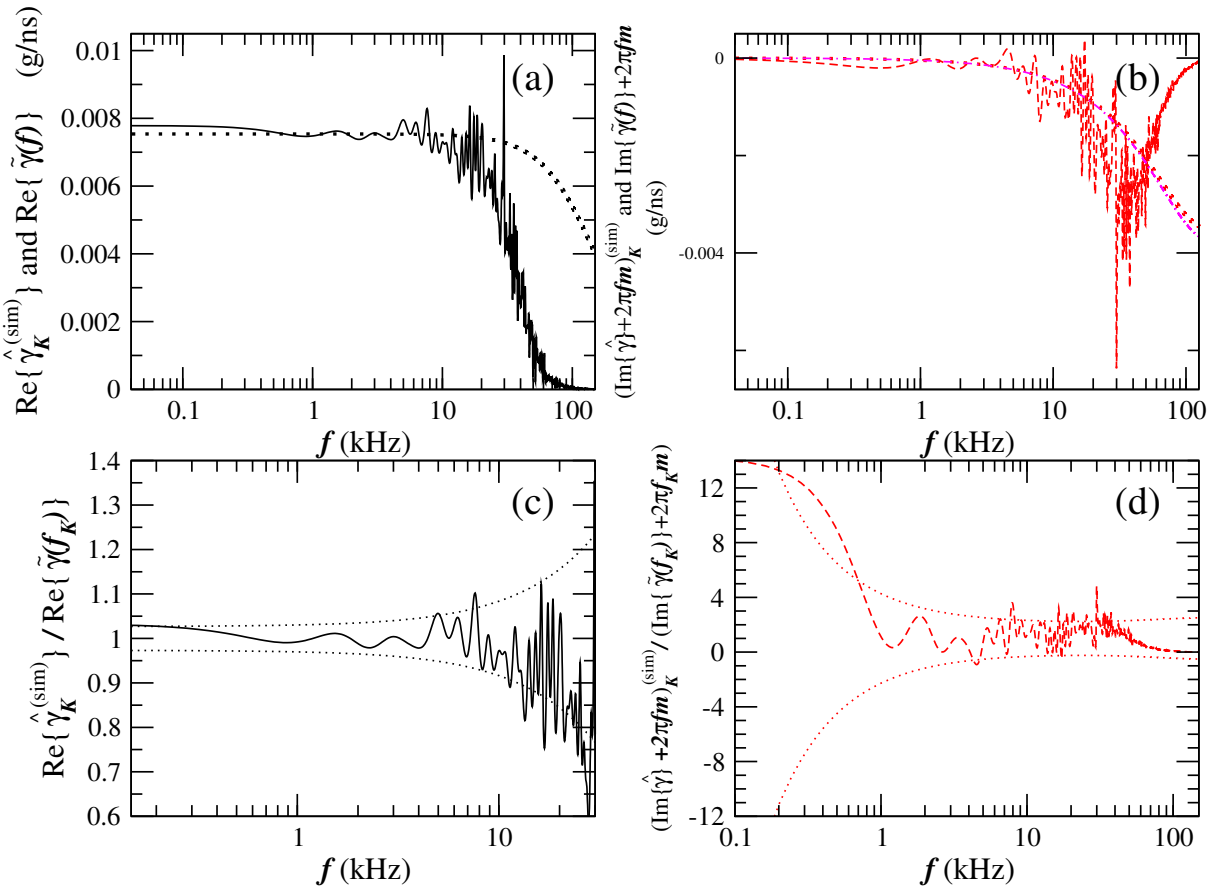

Figure 7.6: Simulation results for the case of laser driving, Eq. (7.1), with exponentially decaying friction retardation function, Eq. (7.14), V: Application of Eq. (7.29) for the determination of the friction retardation spectrum. For the real part, $\mathrm{Re}\{\tilde{\gamma}(f)\}$ (left side), one obtains good results for frequencies lower than $\sim 10\,\mathrm{kHz}$. For the imaginary part, $\mathrm{Im}\{\tilde{\gamma}(f)\}$, one obtains results with a statistical error which is larger than 100% for all frequencies. In (b) both analytical expressions $\mathrm{Im}\{\tilde{\gamma}(\omega)\} + \mathrm{i}\omega\mathrm{m}$ (dotted line) and $\mathrm{Im}\{\tilde{\gamma}(\omega)\}$ (dashed-dotted line) have been plotted. Apparently the difference between these two expressions is much smaller than the error of the simulation imaginary part.

7.3.2 Calibration with slow relocation of the stage (non-sinusoidal driving)

In this paragraph simulation results for non-sinusoidal stage driving with a relatively weak trap with a stiffness of $\kappa_{\mathrm{input}} = 0.01\,\mathrm{pN/nm}$ are presented. A stage which is driven by piezo elements can not be relocated as fast as the laser trap can be deflected by means of AOD/EOD. Therefore, as stage driving profile $x_{\mathrm{S}}(t)$, the smooth s-shaped function proposed in paragraph 7.1.2, Eq. (7.4), is used. The friction retardation functions, Eqs. (7.12)/(7.13) used in this simulation correspond to simple Stokes friction. The results of this simulation are presented in Figs. 7.7 to 7.9.
In Fig. 7.7 the response of the trapped object to the stage deflection is shown. One can see that for small times after the initiation of the stage deflection the trapped object follows the stage motion, but for larger times, it feels the influence of the trap and relaxes back to the resting trap center.

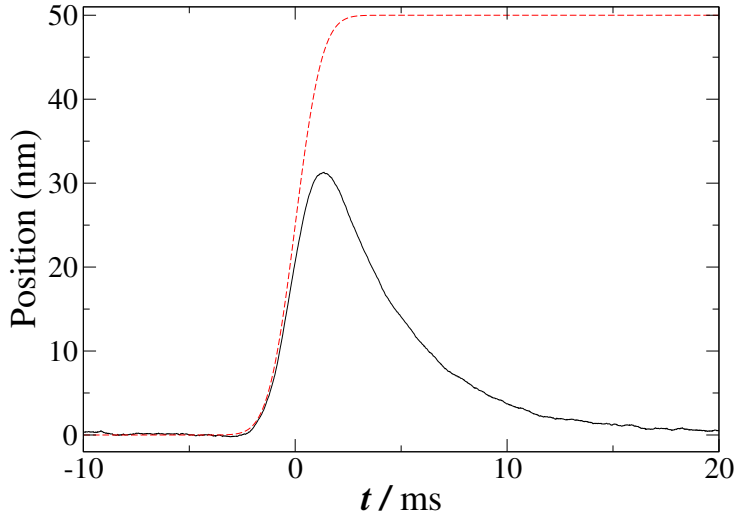

Figure 7.7: Simulation results for the case of non-sinusoidal stage driving, Eq. (7.4), with simple Stokes friction, Eqs. (7.12)/(7.13), I: Averaged trajectory $\langle \hat{x}_j^{(\mathrm{sim})} \rangle_{\mathrm{wind}}$ of the trapped object of the driven system (solid line) averaged over $N_{\mathrm{wind,D}} = 7500$ windows of length $T_{\mathrm{wind,D}} = 0.1\,\mathrm{s}$. The stage position is indicated by a dashed line. The stage velocity reaches its maximum at time $t = 0$.

Fig. 7.8 shows the results for the observables $P_k^{(\mathrm{sim})}$ and $\mathrm{Re}\{\hat{R}_{\mathrm{S},k}^{(\mathrm{sim})}\}$ as well as the results $(\kappa - (2\pi f)^2 m)_k^{(\mathrm{sim})}$. The statistical error of the power spectrum $P_k^{(\mathrm{sim})}$, see Fig. 7.8(a), is fre-

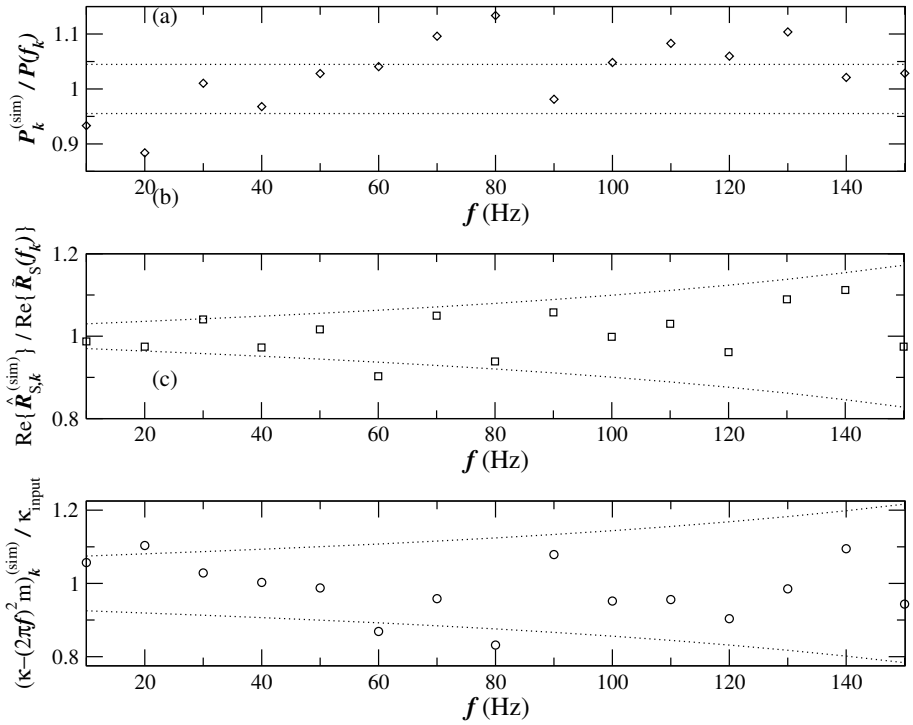

Figure 7.8: Simulation results for the case of non-sinusoidal stage driving, Eq. (7.4), with simple Stokes friction, Eqs. (7.12)/(7.13), II: (a): Power spectrum $P_k^{(\mathrm{sim})}$ of the undriven system divided by the theoretical spectrum $P(f_k)$, Eq. (3.23). (b): Real part of the active spectrum $\mathrm{Re}\{\hat{R}_{\mathrm{S},k}^{(\mathrm{sim})}\}$ of the driven system, calculated with Eq. (7.7), divided by the real part of the theoretical spectrum $\mathrm{Re}\{\hat{R}_{\mathrm{S}}(f_k)\}$, Eq. (4.49). (c): Result of the application of the calibration equation, Eq. (7.24), divided by the input trap stiffness κ_{input}.

quency independent. The statistical error of the real part of the active spectrum $\mathrm{Re}\{\hat{R}_{\mathrm{S},k}^{(\mathrm{sim})}\}$, see Fig. 7.8(b), increases fast with frequency, however. This is mainly due to the choice of the driving function. Since contributions to $\mathrm{i}2\pi f\tilde{x}_{\mathrm{S}}(f)$ are getting smaller with increasing frequency, the thermal part of the motion becomes more relevant, thereby causing a higher relative statistical error of $\mathrm{Re}\{\hat{R}_{\mathrm{S},k}^{(\mathrm{sim})}\}$, see the error calculation in section 7.4. Based on this increase in statistical error on $\mathrm{Re}\{\hat{R}_{\mathrm{S},k}^{(\mathrm{sim})}\}$, the upper limit $f_{\max}$ of the frequency interval over which $(\kappa-(2\pi f)^2 m)_k^{(\mathrm{sim})}$ is averaged according to Eq. (7.26), was chosen at a rather low value, $f_{\max} = 150\,\mathrm{Hz}$. One obtains

$$\frac{\kappa^{(\mathrm{av})}}{\kappa_{\mathrm{input}}} = 0.983 \pm 0.036. \tag{7.34}$$

This calibration result with a for most purposes acceptable relative statistical error of 3.6% has been reached by choosing a very high number of windows $N_{\mathrm{wind,D}} = 7500$ at the driven system. With a window time of $T_{\mathrm{wind,D}} = 0.1\,\mathrm{s}$ this involves a large total measuring time of $T_{\mathrm{meas}} = 800\,\mathrm{s}$, however, which is clearly unfavorable[16]. Since it has been calibrated only at low frequencies, the

[16] In principle, one could imagine to reduce the total measuring time by moving the stage according to the same

mass term $-(2\pi f)^2 m$ is negligible, although the motion of a *large particle* in a *weak trap* was simulated. The mass term would be relevant however, if frequencies higher than a few hundred Hz would be taken into account.
Fig. 7.9 shows the simulation results for the response function $\chi_k^{(\mathrm{sim})}$ and the friction retardation spectrum $\hat{\gamma}_k^{(\mathrm{sim})}$. The analytical expression for $\chi(\omega)$ was obtained by using the constant friction

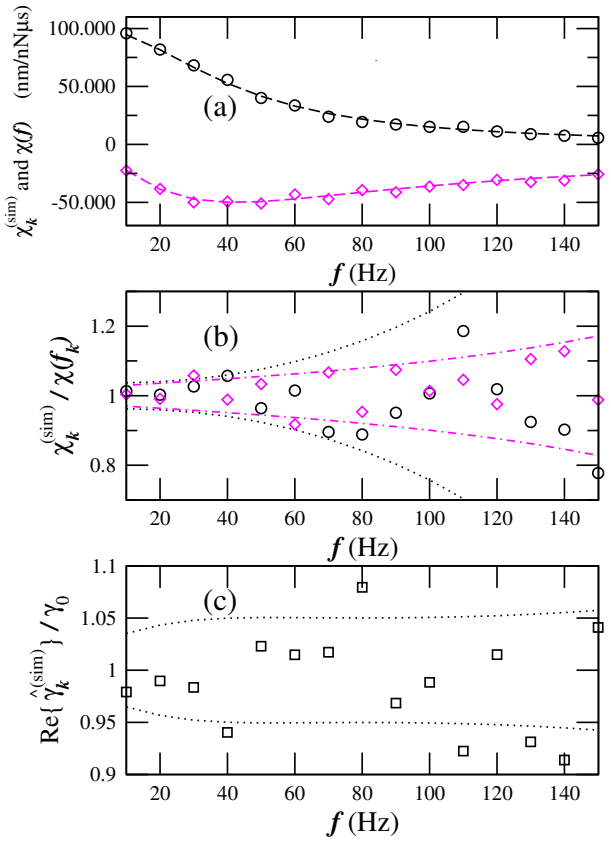

Figure 7.9: Simulation results for the case of non-sinusoidal stage driving, Eq. (7.4), with simple Stokes friction, Eqs. (7.12)/(7.13), III: (a),(b): Application of the response function calibration equation, Eq. (7.28). Simulation results for real part (circles) and imaginary part (diamonds) of $\chi_k^{(\mathrm{sim})}$ in absolute numbers (a) and as scatter plots for data/theory (b). The analytical expression for the response function $\chi(\omega)$, Eq. (4.4), is indicated by a dashed line (a). (c): Determination of the friction retardation spectrum (real part), Eq. (7.30), as scatter plot. Statistical error estimates are given for the real parts ((b),(c), dotted lines) and the imaginary part ((b), dashed-dotted lines). All statistical errors are increasing with frequency. For $\mathrm{Re}\{\chi_k^{(\mathrm{sim})}\}$ and $\mathrm{Im}\{\chi_k^{(\mathrm{sim})}\}$ they are on order 10% for frequencies up to 50 Hz, for $\mathrm{Re}\{\hat{\gamma}_k^{(\mathrm{sim})}\}$ the statistical error is on order 5%.

coefficient γ_0 as the theoretical value for $\tilde{\gamma}(\omega)$. For frequencies below 50 Hz the statistical errors are on order 5-10%, see Fig. 7.9(c,d).

error-function profile, but faster than in the given example, thereby reducing the window time $T_{\mathrm{wind,D}}$. Then one could also calibrate at higher frequencies. In practice, this is rather unrealistic, however, since a state-of-the-art piezo stage can reliably perform motion according to given profiles only up to a time scale of sub-kHz. At the presented example, the stage is performing motion which is on that time scale, see Fig. 7.7.

7.3.3 Calibration with slow sinusoidal motion of laser/stage

Calibration with slow sinusoidal laser and stage driving have been simulated for a $R = 1\,\mu$m bead in water. The friction retardation function is given by Eqs. (7.12)/(7.13) which corresponds to simple Stokes friction. A number of $K_{\mathrm{Max}} = 100$ driving frequencies between 1 Hz and 100 Hz have been used to drive the system. The results of such a simulation are shown in Figs. 7.10 to 7.12.

Fig. 7.10 shows the power spectrum and the real part of the active spectrum of the trapped bead. The theoretical curves were obtained with Eqs. (3.23) and (4.48)/(4.49), using the constant

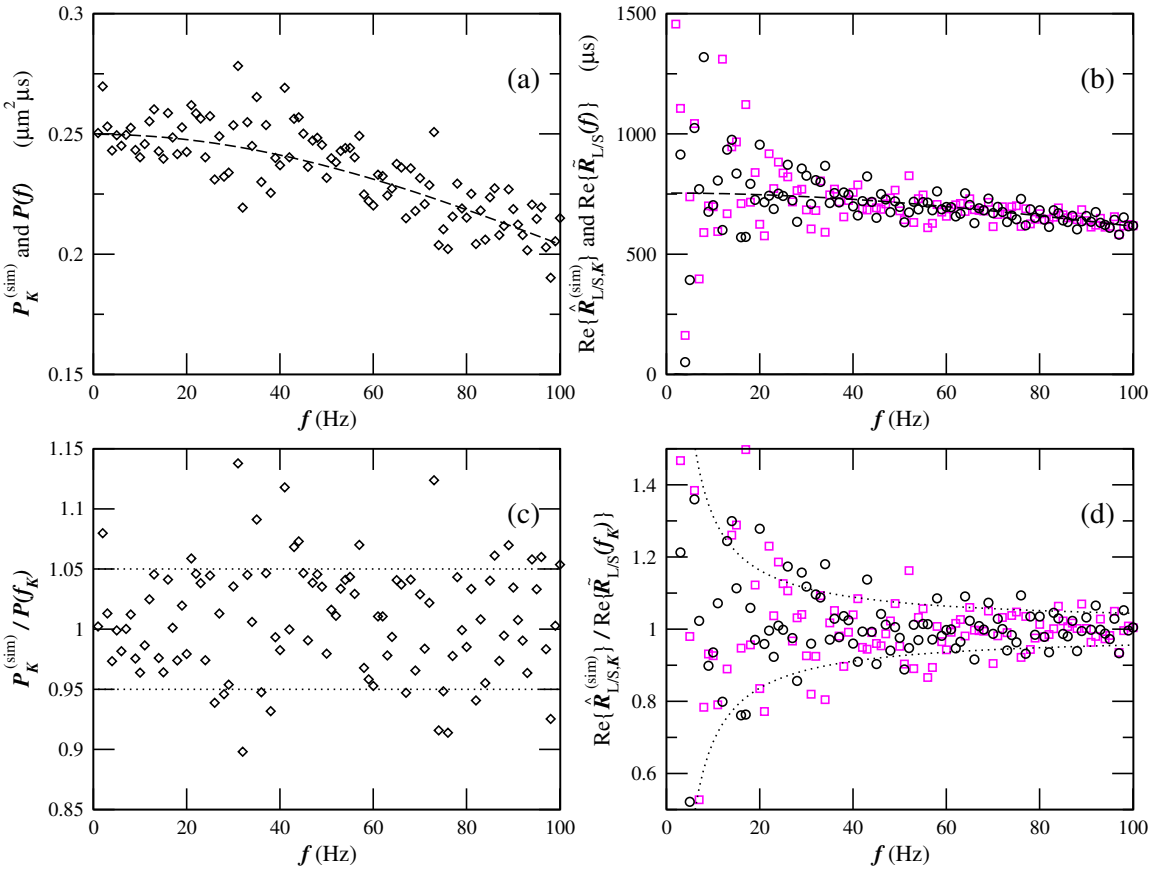

Figure 7.10: Simulation results for the case of slow sinusoidal laser/stage driving, Eq. (7.8), with simple Stokes friction, Eqs. (7.12)/(7.13), I: Absolute results for power spectrum (a) and real part of the active spectrum (b) for slow driving. (c) and (d): Scatter plots of data/theory for the same data set. Simulation results for power spectrum (diamonds) and real part of the active spectrum, the latter for laser (circles) and stage (squares) driving, are indicated by symbols, analytical expressions are indicated by dashed lines. Statistical error estimates are indicated by dotted lines ((c),(d)). The statistical error of the power spectrum is frequency independent while the statistical error of the real part of the active spectrum decreases fast with frequency.

friction coefficient γ_0 as the theoretical value for $\tilde{\gamma}(\omega)$. The simulated values were calculated with Eqs. (7.20) and (7.21)/(7.22). When driving at low frequencies, the mass term is unimportant.

The scatter plots of data/theory in Fig. 7.10(c,d) demonstrate that the statistical error for the power spectrum is frequency independent while that of the active spectrum decreases fast with frequency. The high error of $\hat{R}^{(\mathrm{sim})}_{\mathrm{L/S},K}$ at lower frequencies is due to the relatively short duration per window $T_{\mathrm{wind}} = 1\,\mathrm{s}$.
In Fig. 7.11, the results from the application of the calibration equations, Eqs. (7.23)/(7.24) are shown, for both laser (a) and stage (b) driving. From a comparison of the results and the error

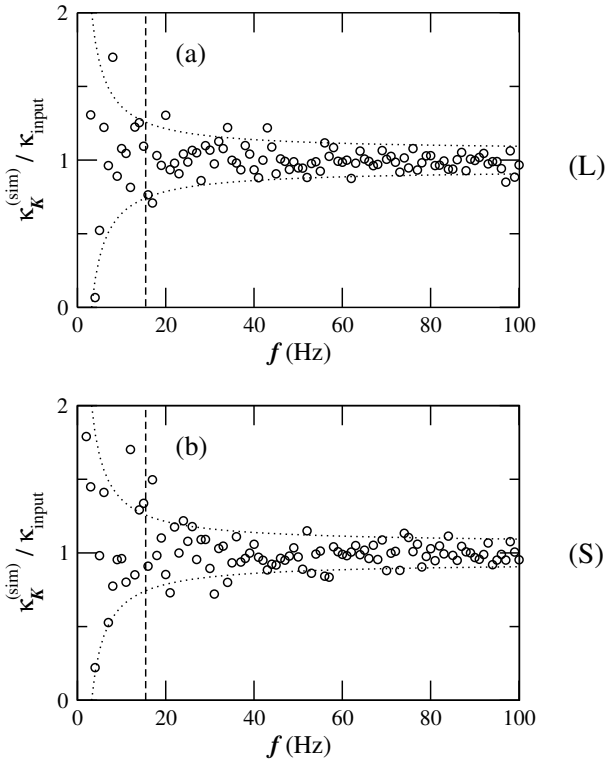

Figure 7.11: Simulation results for the case of slow sinusoidal laser/stage driving, Eq. (7.8), with simple Stokes friction, Eqs. (7.12)/(7.13), II: Application of calibration equation (circles) for slow laser (a) and stage (b) driving. Statistical error estimates indicated by dottes lines show that the calibration is more reliable at higher driving frequencies. By comparing (a) and (b) one can see that laser and stage driving perform equally well with respect to the calibration results and statistical error estimates. The dashed lines indicate the lower boundary for the frequency range over which the calibration results $\kappa_K^{(\mathrm{sim})}$ were averaged to obtain $\kappa^{(\mathrm{av})}$ (see text).

estimates in Fig. 7.11(a,b), we conclude that laser and stage driving perform equally well at low driving frequencies[17]. Like the statistical error of the real part of the active spectrum, the statistical error of the values $\kappa_K^{(\mathrm{sim})}$ decreases with frequency. This implies that calibrating at lower frequencies is less reliable than calibrating at higher frequencies, if the driving amplitude

[17]Note that for a given driving amplitude $A_{\mathrm{L/S}}$ and for a given driving frequency f_K, the resulting amplitudes of the oscillations of the trapped bead are in general different for laser and for stage driving. This can be of relevance for the validity of the assumption of the FDT that the external perturbation is small. See paragraph 8.4.1.

$A_{\mathrm{L/S}}$ is chosen constant for all frequencies, as done in the simulations[18]. Since statistical errors are high at low frequencies, it was chosen to include only driving frequencies f_K higher than 15 Hz in the averaging procedure, Eqs. (7.25)/(7.26). This results in average values of

$$\frac{\kappa^{(\mathrm{av})}}{\kappa_{\mathrm{input}}} = 0.996 \pm 0.01 \tag{7.35}$$

for laser driving and

$$\frac{\kappa^{(\mathrm{av})}}{\kappa_{\mathrm{input}}} = 0.995 \pm 0.01 \tag{7.36}$$

for stage driving. The relative statistical error of $\kappa^{(\mathrm{av})}$ of 1% shows that the calibration method works well with slow driving. When driving the stage, the mass term $(2\pi f)^2 m$ gives a systematic error on $\kappa_K^{(\mathrm{sim})}$ of about -0.003% at $f_{K_{\mathrm{Max}}} = 100$ Hz which is negligible.

[18]For experiments it is recommended however, to choose frequency-dependent driving amplitudes , as described in paragraph 8.4.1.

Figure 7.12 shows the results for the response function from Eqs. (7.27)/(7.28), and for the calculation of the friction retardation spectrum from Eqs. (7.29)/(7.30). The theoretical curve

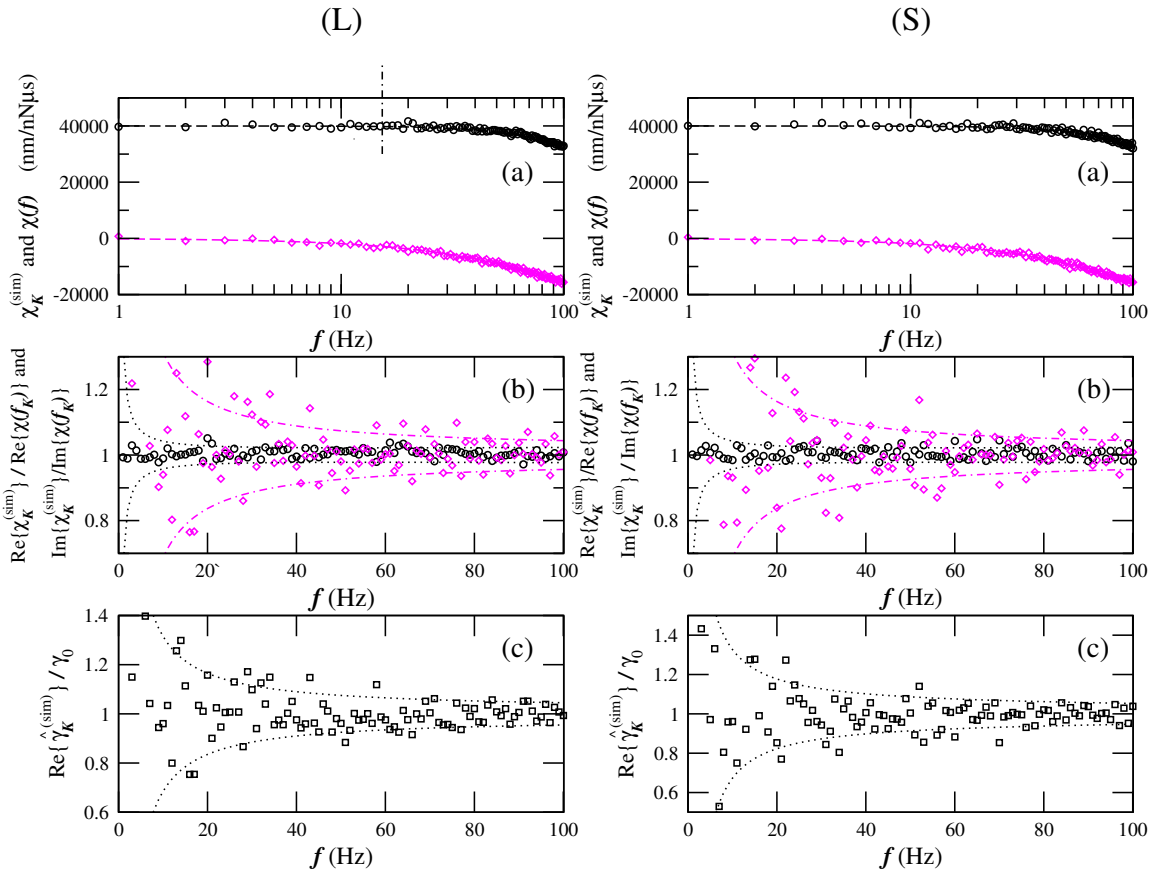

Figure 7.12: Simulation results for the case of slow sinusoidal laser/stage driving, Eq. (7.8), with simple Stokes friction, Eqs. (7.12)/(7.13), III: Application of response function calibration equations ((a),(b)) and determination of the friction retardation spectrum (real part, (c)) for slow laser (left) and stage (right) driving. Simulation results for real parts (circles) and imaginary parts (diamonds) of $\chi_K^{(\mathrm{sim})}$ and $\mathrm{Re}\{\hat{\gamma}_K^{(\mathrm{sim})}\}$ (squares), respectively. Analytical expressions are indicated by dashed lines. The vertical dashed-dotted line ((a), left) indicates the upper boundary of the frequency interval over which the results of Eq. (7.32) were averaged to obtain $\beta^{(\mathrm{av})}$. Statistical error estimates are given for the real parts (dotted lines) and for the imaginary parts (dashed-dotted lines). For frequencies above a few tens of Hz, the statistical errors are on the order of 5-10%.

for $\chi(\omega)$ was calculated with Eq. (4.4). For laser driving, the conversion factor β was calculated by using Eqs. (6.18) and (7.32). The fifteen lowest driving frequencies f_K were used for $\mathrm{Re}\{\chi_K^{(\mathrm{sim})}\}$. In this way the average value $\beta^{(\mathrm{av})} = (0.993 \pm 0.02)$ [72] was found. The imaginary mass term in Eq. (7.29) is negligible since it is driven at low frequencies. Fig. 7.12(b,c) displays also the statistical errors (dotted lines) on $\chi_K^{(\mathrm{sim})}$ and $\mathrm{Re}\{\hat{\gamma}_K^{(\mathrm{sim})}\}$. These errors decrease with frequency. For frequencies above a few tens of Hz, the statistical errors are on the order of 5-10%. Note that the imaginary part of the response function can alternatively be obtained through its relation to the power spectrum [10, 54] with a frequency independent statistical error of 5%.

7.3.4 Calibration with fast sinusoidal motion of laser

Fast laser driving for a simultaneous calibration of the trap stiffness and probing of the system's response function and the friction retardation spectrum at *high* frequencies has been simulated for non-sinusoidal driving, see paragraph 7.3.1. In this paragraph, simulation results will be presented where the laser has been driven fast and *sinusoidal* with $K_{\mathrm{Max}} = 50$ frequencies between 2.1 kHz and 106.9 kHz. The friction retardation function $\gamma_1(t)$ chosen is again decaying exponentially, according to Eq. (7.14). Figures 7.13 to 7.17 show the results of the simulation. In Fig. 7.13 the trajectory of the object for driving with $f_{K_{\mathrm{Max}}} = 106.9$ Hz is shown. The thermal

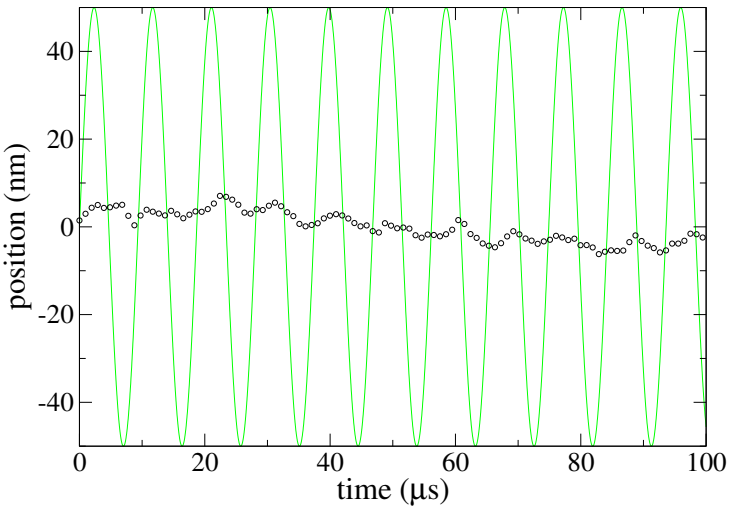

Figure 7.13: Simulation results for the case of fast sinusoidal laser driving, Eq. (7.8), with exponentially decaying friction retardation function, Eq. (7.14), I: Trajectory (circles) $\hat{x}_j^{(\mathrm{sim})}$ for laser driving with $f_{K_{\mathrm{Max}}} = 106.9$ kHz, sampled at $f_{\mathrm{sample}} = 1$ MHz. The laser position $x_{\mathrm{L}}(t)$ is indicated by a solid line. The motion of the object is a superposition of thermal and driven parts, with a large noise contribution from the former. The driven part of the object's motion follows the oscillating motion of the stage with an average phase lag of order $\pi/2$ which means that viscosity dominates over elasticity. The average amplitude of the oscillations of the object is much smaller than the driving amplitude A. This implies that even though $A_{\mathrm{L/S}}$ is chosen somewhat larger than the average amplitude of Brownian motion fluctuations in the undriven system, the amplitudes of the driven fluctuations stay well below and the condition of small disturbances for Onsager's regression hypothesis is automatically fulfilled.

part of the object's motion gives a large contribution. The driven part of the trapped bead's motion follows the oscillating stage motion with an average phase lag of order $\pi/2$. The average amplitude of the object's oscillations is much smaller than the driving amplitude A_{L}.

Figure 7.14 shows the power spectrum and the real part of the active spectrum of the trapped bead, calculated from the simulated trajectories with Eqs. (7.20) and (7.21). The theoretical

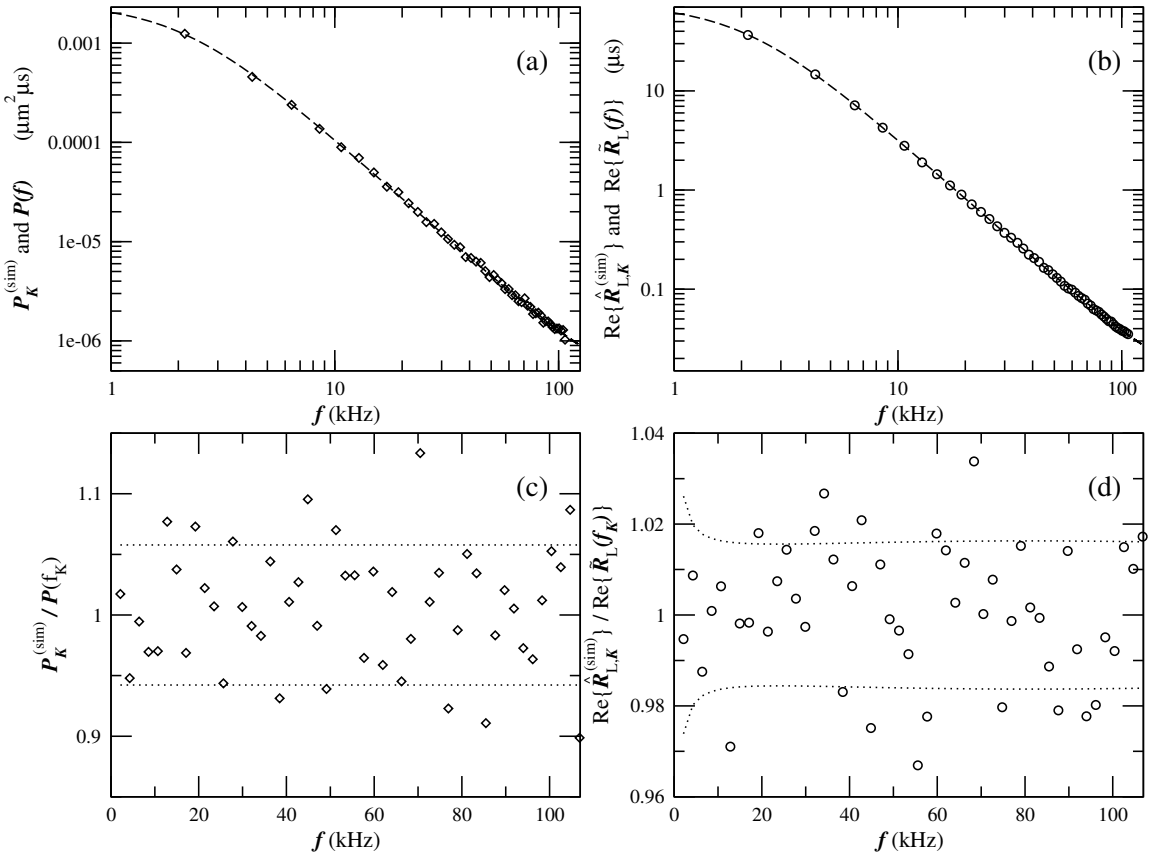

Figure 7.14: Simulation results for the case of fast sinusoidal laser driving, Eq. (7.8), with exponentially decaying friction retardation function, Eq. (7.14), II: Absolute results for power spectrum (a) and real part of the active spectrum (b) at fast laser driving in *log-log* representation. Simulation results for power spectrum (diamonds) and real part of the active spectrum (circles) are indicated by symbols, analytical expressions are indicated by dashed lines. Power spectrum and real part of active spectrum are proportional to each other. (c),(d): Scatter plots of data/theory for the same data set. Statistical error estimates are indicated by dotted lines. The statistical error of the power spectrum is frequency independent while the statistical error of the real part of the active spectrum decreases slightly with frequency.

curves were obtained by using Eqs. (3.23) and (4.48). In Fig. 7.14(a,b) the proportionality between power spectrum and real part of the active spectrum is clear. Fig. 7.14(c,d) shows that the statistical error of the power spectrum is frequency independent while that of the real part of the active spectrum is decreasing slightly with frequency.

The relative statistical error of the power spectrum is higher and is therefore the dominating contribution to the statistical error of the calibration result, as demonstrated by Fig. 7.15. In

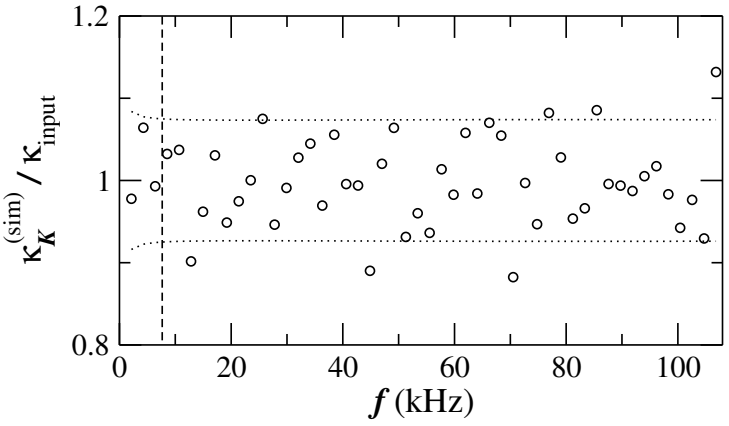

Figure 7.15: Simulation results for the case of fast sinusoidal laser driving, Eq. (7.8), with exponentially decaying friction retardation function, Eq. (7.14), III: Application of calibration equation (circles) for fast laser driving. Statistical error estimates are indicated by dotted lines. The dashed line indicates the lower boundary for the frequency range over which the calibration results $\kappa_K^{(\mathrm{sim})}$ were averaged to obtain $\kappa^{(\mathrm{av})}$.

that figure, the results from the application of the calibration equation, Eq. (7.23) are shown. Application of Eq. (7.25) yields an average

$$\frac{\kappa^{(\mathrm{av})}}{\kappa_{\mathrm{input}}} = 0.997 \pm 0.011 \tag{7.37}$$

found for driving frequencies equal to or larger than 8.5 kHz. This result confirms that the proposed method works well also at high driving frequencies. Frequencies smaller than 8.5 kHz were excluded from the averaging because of the high statistical error on the real part of the active spectrum for low frequencies.

Figure 7.16 shows the result when applying the response function calibration equation, Eq. (7.27). The result is compared to the theoretical expression, Eq. (4.4). Fig. 7.16(c,d) shows that the

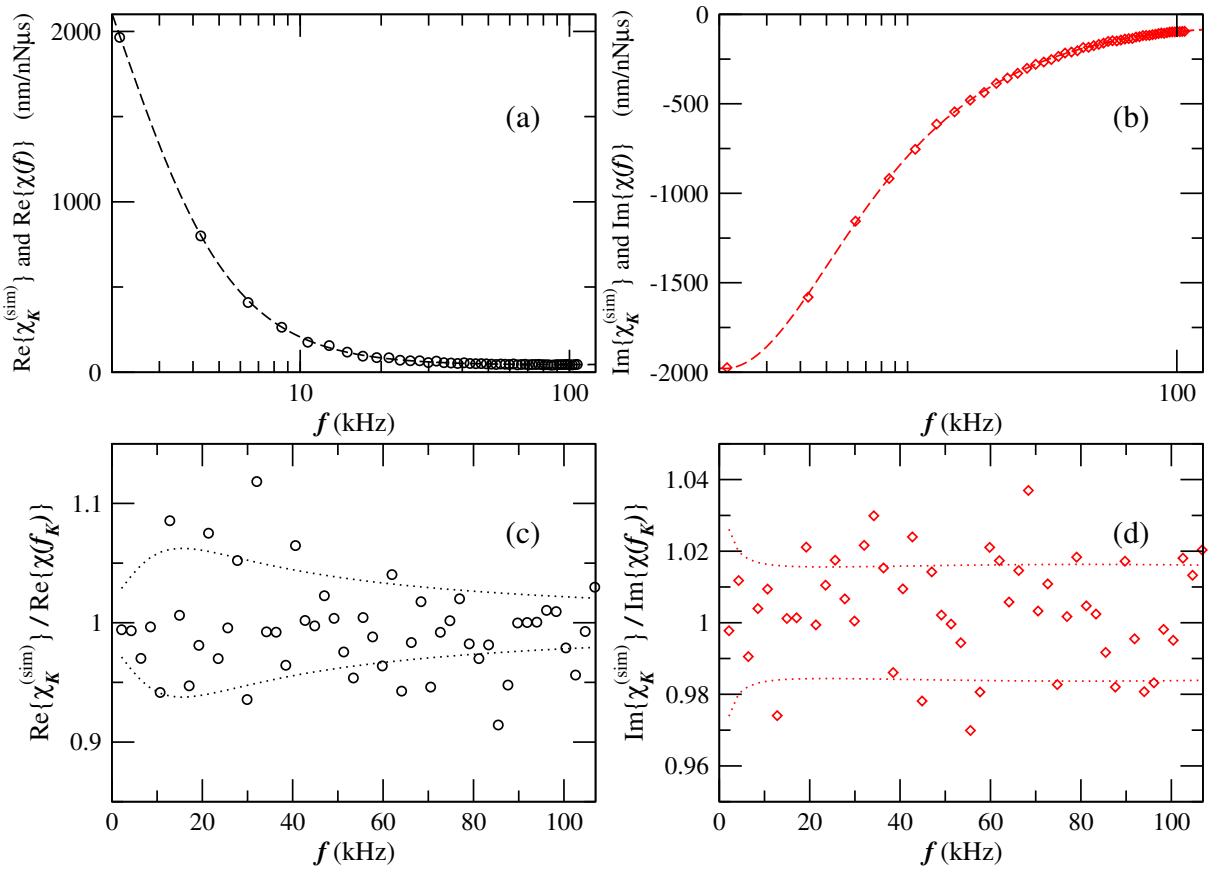

Figure 7.16: Simulation results for the case of fast sinusoidal laser driving, Eq. (7.8), with exponentially decaying friction retardation function, Eq. (7.14), IV: Application of the response function calibration equation for fast laser driving. Simulation results for real part (left) and imaginary part (right) of $\chi_K^{(\mathrm{sim})}$ are indicated by symbols. (a),(b): Absolute results. Analytical expressions are indicated by dashed lines. (c),(d): Data/Theory plots. Statistical error estimates are indicated by dotted lines. The statistical error is on the order of 5% for $\mathrm{Re}\{\chi_K^{(\mathrm{sim})}\}$ and somewhat lower for $\mathrm{Im}\{\chi_K^{(\mathrm{sim})}\}$. Note that the relative error of $\mathrm{Re}\{\chi_K^{(\mathrm{sim})}\}$ is not increasing with frequency though absolute values are approaching zero. Those results demonstrates that the response function calibration yields precise results also at high frequencies.

resulting real part, $\mathrm{Re}\{\chi_K^{(\mathrm{sim})}\}$, has a slightly frequency-dependent statistical error of order 5%. The imaginary part has a lower error of order 2% which is roughly frequency independent. If the imaginary part of the response function $\mathrm{Im}\{\tilde{\gamma}(\omega)\}$ was found through its relationship to the power spectrum [10, 54], the statistical error would be $\sim 6\%$.

Figure 7.17 shows our results from the calculation of the friction retardation spectrum, Eq. (6.16). For the imaginary part (Fig. 7.17, right), both analytical expressions $\tilde{\gamma}(\omega)$ and $\tilde{\gamma}(\omega) + \mathrm{i}\omega\mathrm{m}$ have

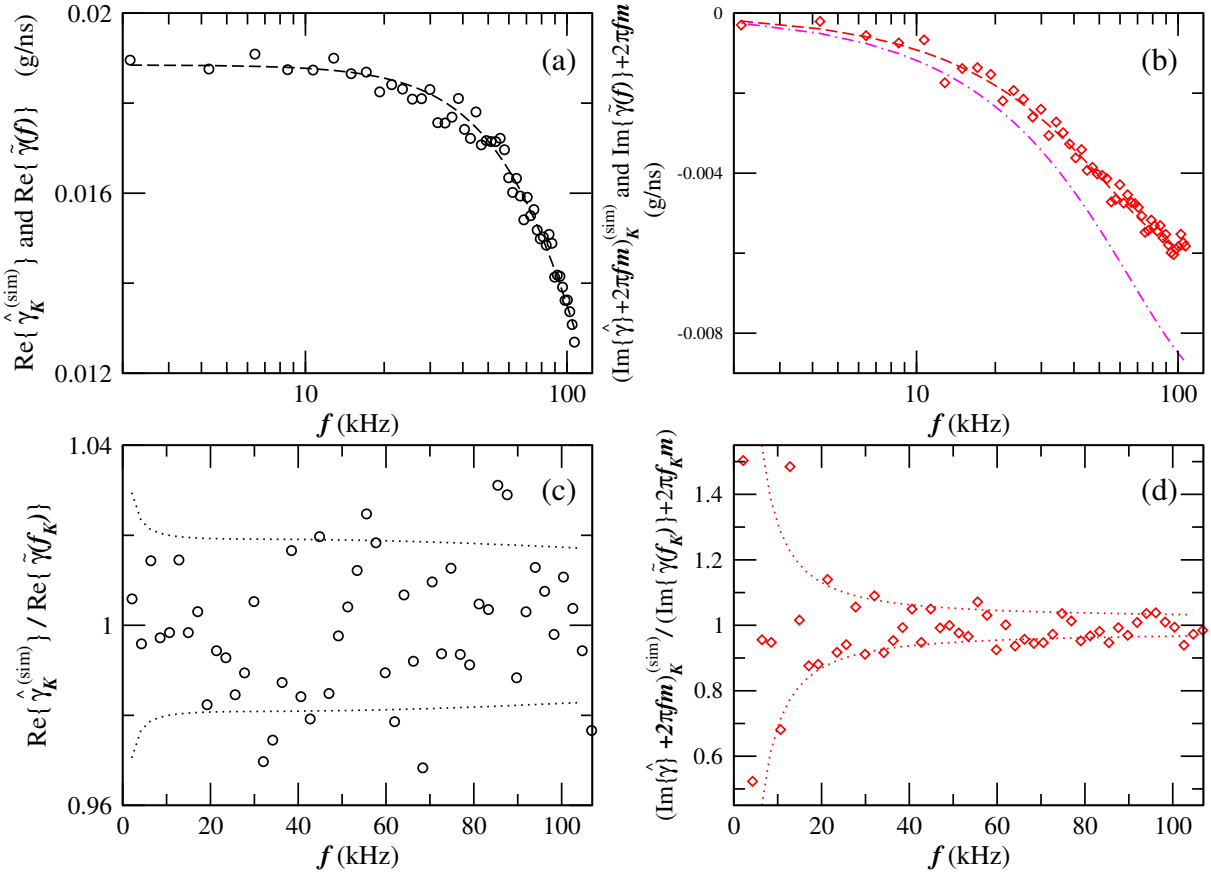

Figure 7.17: Simulation results for the case of fast sinusoidal laser driving, Eq. (7.8), with exponentially decaying friction retardation function, Eq. (7.14), V: Determination of the friction retardation spectrum with Eq. (6.16) for fast laser driving. Simulation results (symbols) for real parts (left) and imaginary parts (right) of $(\hat{\gamma} + \mathrm{i}2\pi\mathrm{fm})_{\mathrm{K}}^{(\mathrm{sim})}$ in absolute numbers ((a),(b)) and as scatter plot ((c),(d)). Analytical expressions are indicated by dashed lines, statistical error estimates by dotted lines. The imaginary part includes the mass term. In (b) both analytical expressions $\mathrm{Im}\{\tilde{\gamma}(\omega)\} + \mathrm{i}\omega\mathrm{m}$ (dashed line) and $\mathrm{Im}\{\tilde{\gamma}(\omega)\}$ (dashed-dotted line) have been plotted. While the statistical error is relatively small for the real part, it is very high for the imaginary part at lower frequencies where $\mathrm{Im}\{\tilde{\gamma}(\omega)\}$ is close to zero. The graph demonstrates that the method reproduces complex viscoelastic properties properly.

been plotted. This serves to demonstrate the importance of the imaginary mass term, even for a small bead of $R = 1\,\mu$m. In an experiment, the mass term should be fitted for. Further, for $\mathrm{Re}\{\hat{\gamma}_K^{(\mathrm{sim})}\}$ we obtain a roughly frequency independent statistical error, while the results for $(\mathrm{Im}\{\hat{\gamma}\} + 2\pi f m)_K^{(\mathrm{sim})}$ have frequency dependent statistical errors which decrease markedly with frequency. For the highest frequencies around 100 kHz, the statistical errors for both the real and the imaginary part are 2-3%.

7.3.5 Tables of simulation parameters

In table 7.1, the friction and driving characteristics for the presented simulations are summarized. The numerical values for parameters of our simulations and of some characteristic quantities are given in tables 7.2 and 7.3 for simulations with non-sinusoidal and sinusoidal driving, respectively.

Table 7.1: Friction types and driving characteristics for data sets shown in Figs. 7.3-7.6, 7.8-7.9, 7.10-7.12 and 7.14-7.17.

Quantity	Figs. 7.3-7.6	Figs. 7.8-7.9	Figs. 7.10-7.12	Fig. 7.14-7.17
Friction relaxation function $\gamma_1(t)$	$\gamma_0/\tau_{\rm fr} \cdot \exp(-t/\tau_{\rm fr})$	$\gamma_0 \delta(t)$	$\gamma_0 \delta(t)$	$\gamma_0/\tau_{\rm fr} \cdot \exp(-t/\tau_{\rm fr})$
Friction relaxation function $\gamma_2(t)$	0	0	0	0
Friction relaxation spectrum $\tilde{\gamma}(\omega)$	$\gamma_0/(1 + {\rm i}2\pi f_k/\tau_{\rm fr})$	γ_0	γ_0	$\gamma_0/(1 + {\rm i}2\pi f_k/\tau_{\rm fr})$
Driving position $x_{\rm L/S}(t)$	$A_{\rm L}\theta^-(t)$	$\frac{A_{\rm S}}{2}(\mathrm{erf}(t/\sqrt{2\sigma_{\rm S}^2}) + 1)$	$A_{\rm L/S}\sin(\omega_{\rm L/S,}{}_K t)$	$A_{\rm L}\sin(\omega_{\rm L,}{}_K t)$
Driving velocity $\dot{x}_{\rm L/S}(t)$	$-A_{\rm L}\delta(t)$	$\frac{A_{\rm S}}{\sqrt{2\pi\sigma_{\rm S}^2}} \exp\left(-t^2/(2\sigma_{\rm S}^2)\right)$	$A_{\rm L/S}\omega_{\rm L/S,}{}_K \cos(\omega_{\rm L/S,}{}_K t)$	$A_{\rm L}\omega_{\rm L,}{}_K \cos(\omega_{\rm L,}{}_K t)$
Driving vel. spctr. $\mathrm{i}2\pi f_k \hat{x}_{\rm L/S,}{}_k$	$-A_{\rm L}(1 - i2\pi^2 f_k \delta_{k,0})$	$A_{\rm S} \exp\left(-\frac{1}{2}\sigma_{\rm S}^2(2\pi f_k)^2\right)$	$A_{\rm L/S}\pi\omega_K \Delta_K$ *	$A_{\rm L}\pi\omega_K \Delta_K$ *

* : $\Delta_K = [\delta(\omega + \omega_K) + \delta(\omega - \omega_K)]$

Table 7.2: Notation used and characteristic values of quantities used for data sets with non-sinusoidal driving, shown in Figs. 7.3-7.6 and 7.8-7.9.

Quantity	Notation	Equal to	Value (Figs. 7.3- 7.6)	Value (Figs. 7.8-7.9)
Prop. Time Step (Runge-Kutta)	Δt_{prop}		50 ns	500 ns
Sampling frequency	f_{sample}		300 kHz	100 kHz
Nyquist frequency	f_{Nyq}	$f_{\mathrm{sample}}/2$	150 kHz	50 kHz
Frequency spacing	Δf	$1/T_{\mathrm{wind}}$	40 Hz	10 Hz
Corner frequency	f_{c}	$\kappa_{\mathrm{input}}/(2\pi\gamma_0)$	(13.3 kHz)*	263 Hz
Time between measurements	Δt	f_{sample}^{-1}	4.95 μs	10 μs
Lowest frequency used for averaging	f_{min}		40 Hz	10 Hz
Highest frequency used for averaging	f_{max}		4 kHz	150 Hz
No. of data windows (undriven system)	$N_{\mathrm{wind,U}}$		3000	500
No. of data windows (driven system)	$N_{\mathrm{wind,D}}$		30000	7500
Duration of window (undr. syst.)	T_{wind}	$N\Delta t$	25 ms	0.1 s
Duration of window (driv. syst.)	$T_{\mathrm{wind,D}}$		1 ms	0.1 s
Total duration of measurements	T_{msr}	$N_{\mathrm{wind,U}}T_{\mathrm{wind}} + N_{\mathrm{wind,D}}T_{\mathrm{wind,D}}$	105 s	800 s
No. of data pts. (window, undr. syst.)	N		750	10,000
No. of frequencies in averaging interval	N_k	$(f_{\mathrm{max}} - f_{\mathrm{min}})/\Delta f$	99	14
No. of points in one block	N_{block}		999	19
Diameter of bead	$2R$		0.8 μm	4 μm
Density of bead and water	ρ		1.0 g/cm^3	1.0 g/cm^3
Mass of bead	m		2.7×10^{-13} g	3.4×10^{-11} g
Temperature	T		300 K	300 K
Thermal energy	$k_{\mathrm{B}}T$		4.1 pN nm	4.1 pN nm
Thermal velocity	$\langle v^2(t)\rangle^{1/2}$	$(k_BT/m)^{1/2}$	3.8 mm/s	0.35 mm/s
Dynamic viscosity	η		0.001 Pa s	0.001 Pa s
Kinematic viscosity	ν	η/ρ	$1.0\,\mu\mathrm{m}^2/\mu\mathrm{s}$	$1.0\,\mu\mathrm{m}^2/\mu\mathrm{s}$
Reynolds number	N_{Re}	$R\langle v^2\rangle^{1/2}/\nu$	$3 \cdot 10^{-3}$	$1.4 \cdot 10^{-3}$
Drag/friction coefficient	γ_0	$6\pi\eta R$	$7.5 \cdot 10^{-6}$ g/s	$3.8 \cdot 10^{-5}$ g/s
Input trap stiffness	κ_{input}		0.1 pN/nm	0.01 pN/nm
Relaxation time in trap	t_{trap}	$\gamma_0/\kappa_{\mathrm{input}} = 1/(2\pi f_{\mathrm{c}})$	(75 μs)*	3.8 ms
Diffusion coefficient	D	$k_{\mathrm{B}}T/\gamma_0$	$(0.55\,\mathrm{nm}^2/\mu\mathrm{s})^*$	$0.11\,\mathrm{nm}^2/\mu\mathrm{s}$
Inertial time scale	t_{inert}	m/γ_0	(36 ns)*	0.9 μs
Half-width of trap	$\langle x^2(t)\rangle^{1/2}$	$(k_{\mathrm{B}}T/\kappa_{\mathrm{input}})^{1/2}$	6.4 nm	20.2 nm
Decay time of friction relaxation funct.	τ_{fr}		1 μs	-**
Laser or stage deflection	$A_{\mathrm{L/S}}$		10 nm (laser)	0.2 μm (stage)
Width of the stage deflection function	σ_{S}		-	1 ms
Input conversion factor [72]	β_{input}		1	1

*: f_{c}, t_{trap}, t_{inert} and D are not well-defined, since γ_0 is not the friction coefficient of instantaneous friction

**: simple Stokes friction is instantaneous

Table 7.3: Notation used and characteristic values of quantities encountered for data sets with sinusoidal driving, shown in Figs. 7.10-7.12 and 7.14-7.17 .

Quantity	Notation	Equal to	Value (Figs. 7.10 to 7.12)	Value (Figs. 7.14 to 7.17)
Prop. Time Step (Runge-Kutta)	Δt_{prop}		100 ns	25 ns
Sampling frequency	f_{sample}		5 kHz	1 MHz
Nyquist frequency	f_{Nyq}	$f_{\mathrm{sample}}/2$	2.5 kHz	500 kHz
Frequency spacing	Δf	$1/T_{\mathrm{wind}}$	1 Hz	85 Hz
Corner frequency	f_{c}	$\kappa_{\mathrm{input}}/(2\pi\gamma_0)$	210 Hz	2.1 kHz*
Time between measurements	Δt	f_{sample}^{-1}	0.2 ms	1 μs
No. of data windows (undriven system)	$N_{\mathrm{wind,U}}$		400***	300
No. of driving frequencies	K_{Max}		100	50
Lowest driving frequency	f_1		1 Hz	2.1 kHz
Highest driving frequency	$f_{K_{\mathrm{Max}}}$		100 Hz	106.9 kHz
Duration of one data window	T_{wind}		1 s	11.7 ms
Total duration of measurements	T_{msr}	$(N_{\mathrm{wind}} + K_{\mathrm{Max}}) * T_{\mathrm{wind}}$	500 s***	4.1 s
Diameter of bead	$2R$		2 μm	2 μm
Density of bead and water	ρ		1.0 g/cm^3	1.0 g/cm^3
Mass of trapped object	m	$4/3\pi R^3\rho$	4.2×10^{-12} g	4.2×10^{-12} g
Temperature	T		300 K	300 K
Thermal energy	$k_{\mathrm{B}}T$		4.1 pN nm	4.1 pN nm
Thermal velocity	$\langle v^2\rangle^{1/2}$	$(k_BT/m)^{1/2}$	0.99 mm/s	0.99 mm/s
Dynamic viscosity	η		0.001 Pa s	0.001 Pa s
Kinematic viscosity	ν	η/ρ	1.0 $\mu\mathrm{m}^2/\mu$s	1.0 $\mu\mathrm{m}^2/\mu$s
Reynolds number	N_{Re}	$R\langle v^2\rangle^{1/2}/\nu$	$1 \cdot 10^{-3}$	$1 \cdot 10^{-3}$
Drag/friction coefficient	γ_0	$6\pi\eta R$	$1.9 \cdot 10^{-5}$ g/s	$1.9 \cdot 10^{-5}$ g/s
Input trap stiffness	κ_{input}		0.025 pN/nm	0.25 pN/nm
Relaxation time in trap*	t_{trap}	$\gamma_0/\kappa_{\mathrm{input}} = 1/(2\pi f_{\mathrm{c}})$	0.76 ms	76 μs*
Diffusion coefficient	D	$k_{\mathrm{B}}T/\gamma_0$	0.22 nm^2/μs	0.22 nm^2/μs
Inertial time scale	t_{inert}	m/γ_0	223 ns	223 ns*
Half-width of trap	$\langle x^2\rangle^{1/2}$	$(k_{\mathrm{B}}T/\kappa_{\mathrm{input}})^{1/2}$	12.8 nm	4 nm
Decay time of memory fct. $\gamma_1(\tau)$	τ_{fr}		-**	1 μs
Laser or stage deflection	$A_{\mathrm{L/S}}$		50 nm (L/S)	50 nm (L)
Input conversion factor [72]	β_{input}		1	1

*: f_{c}, t_{trap} and t_{inert} are not well-defined, since γ_0 is not the friction coefficient of instantaneous friction

**: simple Stokes friction is instantaneous

***: A high number of data windows at the undriven system $N_{\mathrm{wind,U}}$ was chosen resulting in a relatively long total measuring time T_{msr}. In that way a low relative statistical error of $\kappa^{(\mathrm{av})}$ of 1% has been reached. If less precision is required, $N_{\mathrm{wind,U}}$ may be chosen lower in favor of a shorter measuring time.

7.4 Statistical errors of simulation results

If one neglects systematic and statistical errors due to electronic noise or numeric or experimental imperfections, like leaking, aliasing, inaccuracies of the stage/laser positioning and detection or inaccuracies of the detection of the particle, one is left with the statistical error of the particle motion due to thermal noise. Calculations of the statistical errors of the measured and calibrated spectral quantities $P_k^{(\mathrm{sim})}$, $\kappa_k^{(\mathrm{sim})}$, $\hat{R}_{\mathrm{L/S},k}^{(\mathrm{sim})}$, $\chi_k^{(\mathrm{sim})}$ and $\hat{\gamma}_k^{(\mathrm{sim/ex})}$ are bulky. In this section it is demonstrated how to calculate the most relevant statistical errors for the results of the simulations with non-sinusoidal driving. The errors found in the following are plotted in the figures of sections 7.3.1 and 7.3.2.

The standard deviation $\sigma[P_k^{(\mathrm{sim})}] = \langle (P_k^{(\mathrm{sim})} - P(f_k))^2 \rangle^{1/2}$ of the simulated power spectrum relative to the theoretical value is simply determined by the number of windows for the undriven system,

$$\epsilon_{\mathrm{rel}}[P_k^{(\mathrm{sim})}] = \frac{\sigma[P_k^{(\mathrm{sim})}]}{P(f_k)} = \frac{1}{\sqrt{N_{\mathrm{wind,U}}}}. \tag{7.38}$$

The estimate of the relative statistical error of $\mathrm{Re}\left\{\hat{R}_{\mathrm{L},k}^{(\mathrm{sim})}\right\}$ is more complicated. It is given by

$$\epsilon_{\mathrm{rel}}[\mathrm{Re}\{\hat{R}_{\mathrm{L/S},k}^{(\mathrm{sim})}\}] = \frac{\epsilon[\mathrm{Re}\{\hat{R}_{\mathrm{L/S},k}^{(\mathrm{sim})}\}]}{\mathrm{Re}\{\tilde{R}_{\mathrm{L/S}}(\omega_k)\}}, \tag{7.39}$$

where $\epsilon[\mathrm{Re}\{\hat{R}_{\mathrm{L/S},k}^{(\mathrm{sim})}\}] = \mathrm{Re}\{\hat{R}_{\mathrm{L/S},k}^{(\mathrm{sim})}\} - \mathrm{Re}\{\tilde{R}_{\mathrm{L/S}}(\omega_k)\}$ is the absolute error. Using Eq. (4.24)/(4.25), one can write the relative error as

$$\epsilon_{\mathrm{rel}}[\mathrm{Re}\{\hat{R}_{\mathrm{L/S},k}^{(\mathrm{sim})}\}] = \frac{\epsilon[\mathrm{Re}\{\langle \hat{x}_k^{(\mathrm{sim})} \rangle_{\mathrm{wind}}\}]}{\mathrm{Re}\{\langle \tilde{x}(\omega_k) \rangle\}}. \tag{7.40}$$

The theoretical value $\mathrm{Re}\{\langle \tilde{x}(\omega) \rangle\}$ in the denominator of Eq. (8.35) is given by

$$\mathrm{Re}\{\langle \tilde{x}(\omega) \rangle\} = A_{\mathrm{L}} \kappa \tilde{\gamma}'(\omega) |\chi(\omega)|^2, \quad (\omega \neq 0) \qquad (\mathrm{L}), \tag{7.41}$$

$$\mathrm{Re}\{\langle \tilde{x}(\omega) \rangle\} = A_{\mathrm{S}} \exp(-\tfrac{1}{2}\sigma_{\mathrm{S}}^2 \omega^2)(\kappa - \omega^2 m)\tilde{\gamma}'(\omega)|\chi(\omega)|^2 \qquad (\mathrm{S}), \tag{7.42}$$

where Eqs. (4.48)/(4.49), (4.24)/(4.25) and (7.2)/(7.6) have been used. We use here the shorter notation $\tilde{\gamma}'(\omega)$ and $\tilde{\gamma}''(\omega)$ for the real and imaginary part of the active spectrum.

The statistical error of the simulated value $\epsilon[\mathrm{Re}\{\langle \hat{x}_k^{(\mathrm{sim})} \rangle\}]$ in the numerator of Eq. (8.35) is given by the standard deviation of the real part of the thermal part of the motion $\sigma[\mathrm{Re}\{\hat{x}_{\mathrm{th},k}^{(\mathrm{sim})}\}] = \langle (\mathrm{Re}\{\hat{x}_{\mathrm{th},k}^{(\mathrm{sim})}\})^2 \rangle^{1/2}$, averaged over windows. The thermal part of the driven motion is given by

$$\hat{x}_{\mathrm{th},k}^{(\mathrm{sim})} = \hat{F}_{\mathrm{random},k}^{(\mathrm{sim})} \chi(\omega_k) = \frac{\sqrt{2k_{\mathrm{B}}T\tilde{\gamma}'(\omega_k)}}{\kappa + \mathrm{i}\omega_k \tilde{\gamma}(\omega_k) - \omega_k^2 m} \hat{\eta}_k^{(\mathrm{sim})}. \tag{7.43}$$

By windowing with a number of $N_{\mathrm{wind,D}}$ windows for the driven system, the statistical error due to the standard deviation $\sigma[\mathrm{Re}\{\hat{x}_{\mathrm{th},k}^{(\mathrm{sim})}\}]$ is decreased by a factor of $\sqrt{N_{\mathrm{wind,D}}}$,

$$\epsilon[\mathrm{Re}\{\langle \hat{x}_{\mathrm{th},k}^{(\mathrm{sim})} \rangle_{\mathrm{wind}}\}] = \sigma\left[\mathrm{Re}\left\{\hat{x}_{\mathrm{th},k}^{(\mathrm{sim})}\right\}\right] \cdot \frac{1}{\sqrt{N_{\mathrm{wind,D}}}}. \tag{7.44}$$

Combining all prior equations one obtains for the relative statistical error of the simulated real part

$$\epsilon_{\rm rel}[{\rm Re}\{\hat{R}^{\rm (sim)}_{{\rm L},k}\}] = C_{\rm L}(\omega_k)\left\{1+\frac{\omega_k\left[\tilde{\gamma}'(\omega_k)-\tilde{\gamma}''(\omega_k)\right]-\omega_k^2 m}{\kappa}\right\} \qquad ({\rm L}) \qquad (7.45)$$

$$\epsilon_{\rm rel}[{\rm Re}\{\hat{R}^{\rm (sim)}_{{\rm S},k}\}] = \exp(\frac{1}{2}\sigma_{\rm S}^2\omega_k^2)\cdot C_{\rm S}(\omega_k)\left\{1+\frac{\omega_k\left[\tilde{\gamma}'(\omega_k)-\tilde{\gamma}''(\omega_k)\right]}{\kappa-\omega_k^2 m}\right\} \qquad ({\rm S}) \qquad (7.46)$$

for laser and stage driving, respectively, whereby the dimensionless function $C_{\rm L/S}(\omega)$ is given by

$$C_{\rm L/S}(\omega) = \frac{\sqrt{2k_{\rm B}TT_{\rm wind,D}}}{\sqrt{2N_{\rm wind,D}\tilde{\gamma}'(\omega_k)}A_{\rm L/S}} \qquad (7.47)$$

We have used here that $\langle\hat{\eta}_k^*\hat{\eta}_{k'}\rangle = T_{\rm wind,D}\delta_{k,k'}$. Note that the relative errors, Eqs. (7.45)/(7.46), scale like the square root of the measuring time $T_{\rm wind,D}$ which is due to diffusion[19]. Therefore one obtains results with lower statistical error, if one cuts the raw data into *many small* windows instead of using only few larger data windows. In fact, that kind of behavior was found in the simulations.

The relative error of $\kappa_k^{\rm (sim)}$ (laser driving) and of $(\kappa-\omega^2 m)_k^{\rm (sim)}$ (stage driving) is then given by the sum of the relative error of the power spectrum of the undriven system, Eq. (7.38), and of the relative error of the active spectrum of the driven system, Eqs. (7.45)/(7.46). One obtains

$$\epsilon_{\rm rel}[\kappa_k^{\rm (sim)}] = \underbrace{\epsilon_{\rm rel}[P_k^{\rm (sim)}]}_{\text{Eq. (7.38)}} + \underbrace{\epsilon_{\rm rel}[{\rm Re}\{\hat{R}^{\rm (sim)}_{{\rm L},k}\}]}_{\text{Eq. (7.45)}} \qquad ({\rm L}), \qquad (7.48)$$

$$\epsilon_{\rm rel}[(\kappa-\omega^2 m)_k^{\rm (sim)}] = \underbrace{\epsilon_{\rm rel}[P_k^{\rm (sim)}]}_{\text{Eq. (7.38)}} + \underbrace{\epsilon_{\rm rel}[{\rm Re}\{\hat{R}^{\rm (sim)}_{{\rm S},k}\}]}_{\text{Eq. (7.46)}} \qquad ({\rm S}), \qquad (7.49)$$

respectively. From these errors one obtains the relative error of $\kappa^{\rm (av)}$ by averaging,

$$\epsilon_{\rm rel}[\kappa^{\rm (av)}] = \sqrt{\frac{T_{\rm wind}}{T_{\rm wind,D}}}\cdot\frac{1}{N_k}\sqrt{\sum_k(\epsilon_{\rm rel}[\kappa_k])^2} \qquad ({\rm L}), \qquad (7.50)$$

$$\epsilon_{\rm rel}[\kappa^{\rm (av)}] = \sqrt{\frac{T_{\rm wind}}{T_{\rm wind,D}}}\cdot\frac{1}{N_k}\sqrt{\sum_k(\epsilon_{\rm rel}[(\kappa-\omega^2 m)_k])^2} \qquad ({\rm S}), \qquad (7.51)$$

with N_k being the number of frequencies within the interval over which one has averaged. The first root factor in Eqs. (7.50)/(7.51) accounts for correlations due to zero padding, see paragraph 7.2.2. The relative error of the real part of the response function $\chi_k^{\rm (sim)}$, which is calculated as

[19] Note that at sinusoidal driving, the corresponding error scales like $1/\sqrt{T_{\rm meas}}$, see Eq. (8.40). There, diffusion produces *noise*, too, and this as well increases as the square root of the measuring time. But simultaneously one has a peak *signal* of the driven part of the motion which is growing proportionally to the measuring time. So the relative error which basically is the noise-to-signal ratio goes as $1/\sqrt{T_{\rm meas}}$. That is an important advantage of sinusoidal driving.

described in paragraph 7.2.3, is given by

$$\begin{aligned}\epsilon_{\mathrm{rel}}[\mathrm{Re}\{\chi_k^{(\mathrm{sim})}\}] &= \frac{1}{|\mathrm{Re}\,\{\chi(\omega_k)\}\,|}\times \\ &\left[\left(\mathrm{Re}\left\{\frac{\partial\chi(\omega_k)}{\partial\kappa^{(\mathrm{av})}}\right\}\epsilon[\kappa^{(\mathrm{av})}]\right)^2+\left(\mathrm{Re}\left\{\frac{\partial\chi(\omega_k)}{\partial\mathrm{Re}\{\tilde{R}_{\mathrm{L/S}}(\omega_k)\}}\right\}\epsilon[\mathrm{Re}\{\hat{R}^{(\mathrm{sim})}_{\mathrm{L/S},k}\}]\right)^2\right. \\ &\left.+\left(\mathrm{Re}\left\{\frac{\partial\chi(\omega_k)}{\partial\mathrm{Im}\{\tilde{R}_{\mathrm{L/S}}(\omega_k)\}}\right\}\epsilon[\mathrm{Im}\{\hat{R}^{(\mathrm{sim})}_{\mathrm{L/S},k}\}]\right)^2\right]^{1/2}, \qquad (7.52)\end{aligned}$$

where the partial derivatives are to be calculated by using Eqs. (6.10)/(6.11) and the individual error contributions are given by

$$\epsilon[\kappa^{(\mathrm{av})}] = \epsilon_{\mathrm{rel}}[\kappa^{(\mathrm{av})}]\kappa, \qquad (7.53)$$

$$\epsilon[\mathrm{Re}\{\hat{R}^{(\mathrm{sim})}_{\mathrm{L/S},k}\}] = \epsilon_{\mathrm{rel}}[\mathrm{Re}\{\hat{R}^{(\mathrm{sim})}_{\mathrm{L/S},k}\}]\mathrm{Re}\{\tilde{R}_{\mathrm{L/S}}(\omega_k)\}, \qquad (7.54)$$

$$\epsilon[\mathrm{Im}\{\hat{R}^{(\mathrm{sim})}_{\mathrm{L/S},k}\}] = \epsilon_{\mathrm{rel}}[\mathrm{Im}\{\hat{R}^{(\mathrm{sim})}_{\mathrm{L/S},k}\}]\mathrm{Im}\{\tilde{R}_{\mathrm{L/S}}(\omega_k)\}, \qquad (7.55)$$

of which the first two are given in Eqs. (7.50)/(7.51) and Eqs. (7.45)/(7.46). The relative errors of the imaginary part of $\chi_k^{(\mathrm{sim})}$ and of the real and imaginary parts of $\hat{\gamma}_k^{(\mathrm{sim})}$ can be obtained from error calculations similar to that of Eq. (7.52).

In the simulations, only data relative to their theoretical values and the results of the discrete calibration equations, Eqs. (7.23)/(7.24), have been blocked, see paragraph 7.2.2. The relative error of blocked spectra was in each case obtained by multiplying the relative error of the unblocked data with $1/\sqrt{N_{\mathrm{block}}}$, where N_{block} is the number of points in one block.

7.5 Discussion of the simulation results and comparison between non-sinusoidal and sinusoidal driving

The big advantage of calibration with *non-sinusoidal driving* and actually the reason why this possibility has been taken into consideration is that calibration results are obtained for many frequencies simultaneously from driving with only one profile of active motion, see, e.g., Fig. 7.5. The results found in the two examples in paragraphs 7.3.1 and 7.3.2 are for the most part acceptable, except for that $\mathrm{Im}\{\hat{\gamma}_k\}$ has a huge statistical error in Fig. (7.6) and that the total measuring time in the case of slow non-sinusoidal stage driving has to be chosen very high, $T_{\mathrm{meas}} = 800\,\mathrm{s}$, in order to obtain a result for $\kappa^{(\mathrm{av})}$ on order of a few procent, Eq. (7.34). However, some severe disadvantages of non-sinusoidal driving with respect to sinusoidal driving must be stated.

One problem is the high-frequency behavior. For *non-sinusoidal driving*, the statistical error of the active spectrum $\mathrm{Re}\{\hat{R}^{(\mathrm{sim})}_{\mathrm{L/S},k}\}$ diverges with increasing frequency, especially in the case of stage driving, see Figs. 7.3 and 7.8 and Eqs. (7.45)/(7.46). Hence the statistical errors of all frequency-dependent quantities obtained from the calibration, namely these of $\kappa_k^{(\mathrm{sim})}$, $\chi_k^{(\mathrm{sim})}$

and $\hat{\gamma}_k^{(\mathrm{sim})}$, diverge for high frequencies, too. This implies that the results are reliable only for relatively small frequencies and only these small frequencies can be taken into account to obtain the average value $\kappa^{(\mathrm{av})}$. For *sinusoidal driving* however, the spectral density of the laser/stage velocity diverges at the driving frequency f_K. Therefore, the spectral density of $\mathrm{Re}\{\hat{R}_{\mathrm{L/S},K}^{(\mathrm{sim})}\}$ diverges at f_K, too, and all statistical errors remain limited for high f_K, see Figs. (7.10) and (7.14) and Eq. (7.46)[20]. In both cases, aliasing due to the finite sampling frequency sets an upper frequency limit for the applicability of the calibration method, however.

Another disadvantage of *non-sinusoidal driving* is the experimental effort. First, it would be difficult to move the piezo stage fast and precisely with the error-function (s-shape) profile, given by Eq. (7.4)[21]. Second, the non-sinusoidal motion has to be repeated many times in order to reduce the statistical error. Then it would further be rather difficult to temporally align laser/stage motion and sampling of particle motion for each trial/window with a length of only fractions of a second[22].

Sinusoidal driving with frequency f_K gives calibration results only at one frequency which is f_K. But it yields very good signal-to-noise ratios. Further it is very easy to implement experimentally. Therefore it is clearly recommended to apply sinusoidal driving in the experiment.

[20] In other words, at sinusoidal driving the signal at frequency f_K becomes very large for large measuring times, so that the noise from diffusion is negligible. At non-sinusoidal driving, however, diffusion creates large noise at high frequencies and the signal-to-noise ratio, which is given by the ratio between the spectral densities of diffusion and driven motion, becomes small for high frequencies.

[21] Moving the piezo stage *precisely* with the chosen profile is necessary for a correct determination of the active spectrum. Potential deviations of the stage motion from that profile and their impact on the calibration result would probably be difficult to quantify.

[22] For the example of the fast relocated laser, the particle position detection should ideally start exactly in the moment of the laser deflection.

8 Verification of the FDT method by experiments

Major prerequisites for the FDT method to work are that the particle motion can be described by three independent degrees of freedom within linear response theory in continuous media. Furthermore, the FDT must hold for the frequencies with which the system is driven at the active part. Whether these prerequisites are fulfilled for a chosen system can not be examined by simulations, but only experimentally. Ideas for testing the method in different experimental situations are presented in paragraph 8.1. In the optical tweezers lab at the Niels Bohr Institute, experiments have been performed in which a trapped bead was immersed in water. These experiments are described in sections 8.2-8.5. The application of the FDT method to the measured data is shown in section 8.6. In section 8.7 statistical errors for the obtained results are calculated. The experimental results are finally discussed in section 8.8.

8.1 Suggestions for experimental tests of the FDT method

Only sinusoidal driving should be applied in the experiments, since the simulations presented in chapter 7 have shown that this is a better choice than non-sinusoidal driving. As argued in paragraph 7.1.2, the calibration method should be tested with a broad spectrum of driving frequencies $f_{\mathrm{L/S},K}$. An experimental verification of the calibration method can be performed for different trapped objects, e.g.,

- spherical beads of different size and material,
- cylindrical nano-rods
- lipid granules, or
- bacteria,

in different media or for certain hydrodynamic conditions, e.g.,

- in water at a given distance l to the microscope coverslip,
- in an actin solution,
- in an actin-myosin solution,
- in a living cell,

and for different driving forces, arising from

- stage driving, or
- laser driving.

In the following paragraphs, some suggestions will be given for a progression of tests.

8.1.1 Phase 1: Viscous media

A first check is the calibration for the most simple case which is trapping of a spherical bead with known radius which is immersed in water at a given distance l to the microscope coverslip. For this case, all three prerequisites of the proposed calibration method can safely be assumed to hold. Therefore, this check is mainly intended for testing the performance and precision of the used equipment. In water, the trap stiffness value obtained with the novel calibration method can be compared with that one obtained from the well-tried power spectrum method [40]. Also the friction retardation spectrum $\tilde{\gamma}(\omega)$ obtained from the new calibration method can be checked for consistency with expectations from the model for friction in the proximity to a hard wall, see paragraph 3.2.3. In the optical tweezers lab at the Niels Bohr Institute it has been worked on that first check so far and the results will be presented in the sections 8.2-8.8.

8.1.2 Phase 2: Viscoelastic media

The next check would be calibration with spherical beads trapped in a viscoelastic medium with known refractive index. For viscoelastic media, there is not any other *in-situ* method which gives a trap stiffness value to compare with. Therefore, one could calibrate with the same laser power for two beads from one batch, but one immersed in water and the other in the viscoelastic medium. The trap stiffness values obtained for the two trapped beads can now be checked for consistency with theoretical expectations due to the difference in the refractive indexes, see the discussion of the impact of the refractive index on in-vivo measurements with optical tweezers by Gross [73]. Further, the obtained friction retardation spectrum $\tilde{\gamma}(\omega)$ can be compared to results from microrheology literature. E.g., for an actin solution, one could compare both the frequency dependence and the density dependence of $\tilde{\gamma}(\omega)$ with the results obtained by Gardel et al. [63].

8.1.3 Phase 3: Bio-active media

As next, measurements in bio-active systems should be performed. It has recently been found by Mizuno et al. [49] that in actin-myosin solutions the FDT is broken for low frequencies. Due to molecular motor activity, the power spectrum is *enhanced* at frequencies below $\sim 20\,\mathrm{Hz}$, see section 5.2. In the basic equations of the FDT method, Eqs. (6.4)/(6.5), the trap stiffness is proportional to the *inverse* of the power spectrum. Therefore one expects a *reduced* trap stiffness due to the breaking of the FDT[1]. The goal of testing in bio-active media would be to examine, if the spectrum of calibrated trap stiffness values $\kappa_K^{(\mathrm{ex})}$ clearly exhibits plateau regions where $\kappa_K^{(\mathrm{ex})}$ is nearly constant and where one can assume the FDT to hold. If one can find such plateau regions, one can average over their values $\kappa_K^{(\mathrm{ex})}$ in order to find a reliable value $\kappa^{(\mathrm{av})}$ with low statistical error[2].

[1] The power spectrum can also be enhanced due to instrumental noise. Of course, also this would lead to a reduction of the obtained trap stiffness. Since the noise sources exhibit a certain frequency dependence, it is important to keep track of the frequency dependence of the trap stiffness values $\kappa_K^{(\mathrm{ex})}$, obtained from sinusoidal driving with frequencies f_K.

[2] mass term ignored.

8.2 Brief description of the experiments

In the following sections, calibration experiments are presented which have been performed in the optical tweezers lab at the Niels Bohr Institute with my experimental colleagues Prof. S. N. S. Reihani, A. Richardson and Prof. L. Oddershede. Prof. Reihani installed the hardware and software which was required by these experiments at one of the available optical tweezers setups. The hardware enables simultaneous acquisition of bead and stage positions, which is necessary for determining the phase shift $\Delta\phi(\omega)$ between bead and stage. The software allows convenient data acquisition and driving of the stage. The experiments were performed by A. Richardson and Prof. Reihani. In the data evaluation, Prof. Reihani has performed image analysis and pixel calibration for the independent positional calibration.

For the experiments, a sample chamber was prepared, with polystyrene beads of radius 825 nm immersed in water. Then one bead was trapped with the optical tweezers at a distance of $l = 5\,\mu$m to the microscope coverslip. The bead motion has been recorded with the quadrant photo diode. The power of the laser has been kept constant during the course of the calibration.

At the passive part of the calibration, the Brownian motion of the trapped bead was observed $N_{\rm wind} = 10$ times[3], each time for 3 s, with a sampling frequency of 22 kHz. The power spectrum of the 10 data windows was calculated. By windowing and blocking, power spectrum estimates with lower statistical error were obtained. More details about the passive part are given in section 8.3.

To drive the system at the active part, the piezo stage has been oscillated into the $x-$direction sinusoidally with 7 different frequencies between 10 Hz and 70 Hz, each time for 10 s, and the bead motion was recorded with a sampling frequency of 10 kHz. The driving amplitudes have been chosen as described in paragraph 8.4.1. The stage motion has been recorded with the inbuilt stage position monitoring system. Bead and stage positions were acquired with a fast data acquisition card[4]. The measurements on the driven system are explained in more detail in section 8.4.

Finally, an independent positional calibration with sinusoidal motion of the piezo stage with large amplitudes has been performed, too, as portrayed in section 8.5.

8.3 Measurements on the undriven system

From the undriven Fourier transformed data $\hat{x}_k^{(\rm volt)}$ recorded with the QPD, one obtains the power spectrum $P_k^{(\rm volt)}$. From windowing by averaging over the $N_{\rm wind} = 10$ data sets and blocking by averaging over $N_{\rm block} = 20$ adjacent frequencies, one obtains the windowed and blocked power spectrum,

$$\overline{\langle P_k^{(\rm volt)}\rangle_{\rm wind}} = \frac{\overline{\langle|\hat{x}_k^{(\rm volt)}|^2\rangle_{\rm wind}}}{T}, \tag{8.1}$$

[3]Of the $N_{\rm wind} = 10$ data sets of the passive part of the calibration, 5 have been recorded before and 5 after the active measurements.

[4]data acquisition card: NI PCI-MIO-16E-4 (old model designation), NI PCI-6040E (new model designation).

which will be applied in the FDT method[5]. The undriven data from the bead immersed in water can be evaluated with the power spectrum (PSD) method [40], too, see Fig. 8.1. The PSD

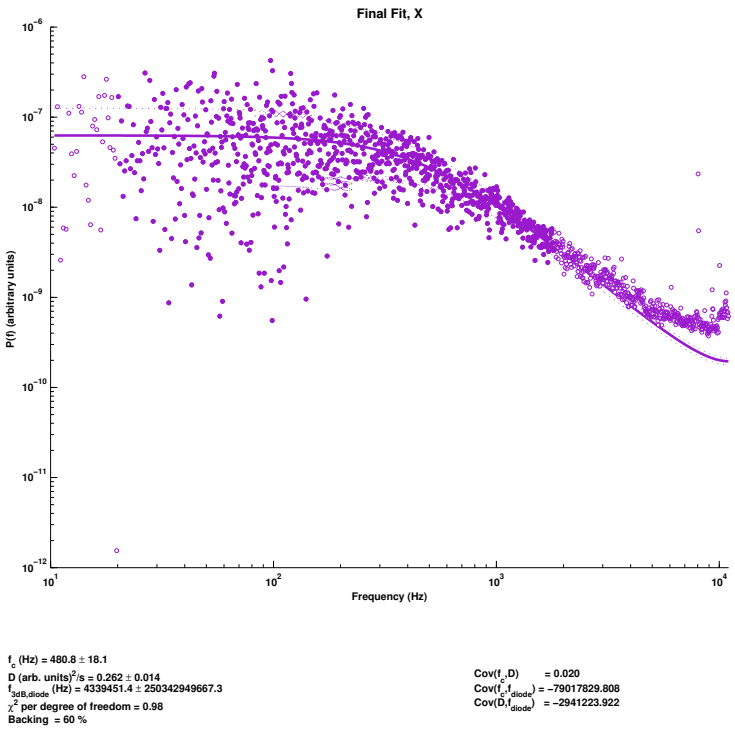

Figure 8.1: Fitting of the experimental power spectrum with the PSD method [40], using the MATLAB® program *Tweezercalib 2.1* [74]. Here, the fitting result for one of the $N_{\mathrm{wind}} = 10$ data sets is shown. The experimental power spectrum values are indicated by symbols, the fit is indicated by a solid line. Aliasing, filtering by the QPD and the finite distance between bead and microscope coverslip alter the power spectrum of the trapped bead. These effects have been taken into account in the fitting procedure.

method basically gives two fit values, the corner frequency $f_{\mathrm{c}}^{(\mathrm{PSD})}$ and the diffusion coefficient $D^{(\mathrm{PSD,volt})}$[§]. The trap stiffness is then obtained according to

$$\kappa^{(\mathrm{PSD})} = 2\pi\gamma_0^* f_{\mathrm{c}}^{(\mathrm{PSD})}, \tag{8.2}$$

with the friction coefficient

$$\gamma_0^* = 6\pi\eta R\left(1 + \frac{9R}{16l}\right), \tag{8.3}$$

where it has been accounted for the finite distance $l = 5\,\mu\mathrm{m}$ between bead and microscope coverslip[6]. With $\eta(\vartheta = 24.5\,^{\circ}\mathrm{C}) = 0.0009\,\mathrm{Pa\,s}$, one obtains from averaging over the $N_{\mathrm{wind}} = 20$

[5] Windowing and blocking are explained in paragraph 7.2.2.

[§] The fitted diffusion coefficient $D^{(\mathrm{PSD,volt})}$ has units (volt unit)^2/s. The exact magnitude of the volt unit depends on the amplification factor set by the QPD electronics and is not relevant.

[6] In first order, the presence of a hard wall only results in an increase of the constant friction coefficient $\gamma_0 = 6\pi\eta R$ to the value γ_0^*. See Eq. (3.14).

data sets,

$$\kappa^{(\mathrm{PSD,av})} = (46.1 \pm \underbrace{0.5}_{\text{statistical error, } 1.1\%} \pm \underbrace{1.0}_{\text{error from temperature uncertainity, } 2.2\%}) \,\mathrm{pN}/\mu\mathrm{m}, \tag{8.4}$$

The temperature is entering this result indirectly, because of the temperature dependence of the viscosity. The error of 2.2% from the temperature uncertainity has been obtained by assuming that the temperature at the bead position is known with an uncertainity of $\sim 1\,\mathrm{K}$[§]. At $\vartheta = 25\,^{\circ}\mathrm{C}$, the viscosity changes by $\sim 20\,\mu\mathrm{Pa\,s}$ per Kelvin which corresponds to a relative error of 2.2%. The conversion factor β is determined with the PSD method from the relation

$$\beta^{(\mathrm{PSD})} = \sqrt{D/D^{(\mathrm{PSD,volt})}}, \tag{8.5}$$

with the theoretical value for the diffusion coefficient $D = k_{\mathrm{B}}T/\gamma_0^*$. We obtain

$$\beta^{(\mathrm{PSD,av})} = (1087 \pm \underbrace{17}_{\text{statistical error, } 1.6\%} \pm \underbrace{27}_{\text{error from temperature uncertainity, } 2.5\%}) \,\mathrm{nm/(volt\ unit)}, \tag{8.6}$$

where it has been used that the relative error of the square root of a quantity is equal to the relative error of that quantity itself.

8.4 Measurements on the driven system

8.4.1 Choice of the driving amplitude

Before addressing our measurement results, the question of choice of the deflection amplitude $A_{\mathrm{L/S}}$ is discussed for both cases of laser and stage driving[§]. The larger the deflection of the laser/stage is chosen, the larger is the deflection of the trapped particle and the better is the signal-noise ratio after averaging. On the other hand, the deflection $A_{\mathrm{L/S}}$ has to be chosen relatively small, due to several constraints. Firstly, the bead should stay in the harmonic trapping region, while the laser or the stage is deflected to ensure a linear response of the trap. Secondly, the center of the bead must remain within the linear detection range of the QPD[7]. Thirdly, since the method is based on the FDT, the stage/laser motion should generate a small perturbation of the equilibrium system, i.e., the amplitude $A_{\mathrm{L/S}}$ should be as low as possible. This third constraint is apparently the most stringent one. Since one has to choose some finite value, a reasonable choice would be to set $A_{\mathrm{S/L}}$ so that the bead amplitude A_{B} would be equal to the half width of the trap, $(k_{\mathrm{B}}T/\kappa)^{1/2}$. That choice should still ensure a linear response. We can now use the response function $\chi(\omega)$ to calculate the required stage/laser amplitudes for sinusoidal driving with angular frequency ω_K according to the laser/stage trajectory

$$x_{\mathrm{L/S}}(t) = A_{\mathrm{L/S}} \sin(\omega_K t). \tag{8.7}$$

[§]In prinicple, the temperature can be measured in proximity to the bead, which requires additional experimental effort. Laser-induced heating is discussed by Peterman et al. [75].

[§]In our experiments, only stage driving has been applied.

[7]For the first and second constraints one should take into account that the motion is a superposition of driven motion and diffusion in a harmonic potential.

One has Eq. (4.2), with the external force from the laser/stage being

$$\tilde{F}_{\mathrm{L}}(\omega) = \frac{\kappa}{\mathrm{i}\omega}\mathrm{i}\omega\tilde{x}_{\mathrm{L}}(\omega), \tag{8.8}$$

$$\tilde{F}_{\mathrm{S}}(\omega) = \tilde{\gamma}(\omega)\mathrm{i}\omega\tilde{x}_{\mathrm{S}}(\omega), \tag{8.9}$$

cf. Eq. (4.15). By taking the norm of Eq. (4.2), inserting the laser/stage velocity spectrum for sinusoidal driving, Eq. (7.10), and requiring for the bead amplitude $A_{\mathrm{B}}(\omega_K) \equiv |\langle\tilde{x}(\omega_K)\rangle| \stackrel{!}{=} (k_{\mathrm{B}}T/\kappa)^{1/2}$, one obtains

$$A_{\mathrm{S}}(\omega_K) = \frac{1}{|\chi(\omega_K)||\omega_K\tilde{\gamma}(\omega_K)|}\sqrt{\frac{k_{\mathrm{B}}T}{\kappa}}, \tag{8.10}$$

$$A_{\mathrm{L}}(\omega_K) = \frac{1}{|\chi(\omega_K)|\kappa}\sqrt{\frac{k_{\mathrm{B}}T}{\kappa}}. \tag{8.11}$$

Those two results are plotted over the frequency $f_K = \omega_K/(2\pi)$ for different spring constants κ in Fig. (8.2) for a polystyrene bead with radius $R = 500\,\mathrm{nm}$ and density $\rho = 1.05\,\mathrm{g/cm^3}$ in a simple viscous medium of viscosity $\eta = 0.0009\,\mathrm{Pa\,s}$. Note that the curves plotted in Figure 8.2

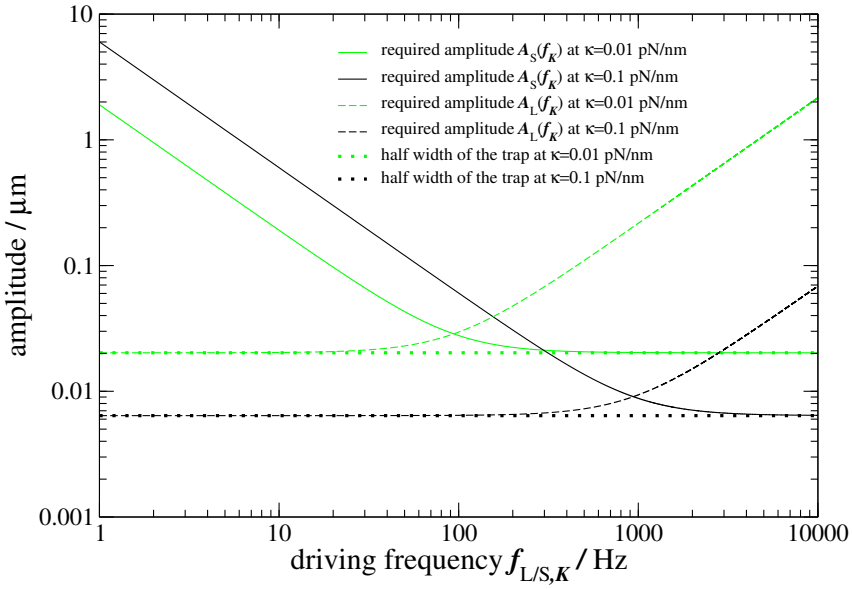

Figure 8.2: Required stage (solid lines) and laser (dashed lines) amplitudes for obtaining particle oscillations with an amplitude equal to the half-width of the trap (dotted lines) for two different spring constants κ. The particle is assumed to be a spherical bead of radius $R = 500\,\mathrm{nm}$ and density $\rho = 1.05\,\mathrm{g/cm^3}$ which moves in water with viscosity $\eta = 0.0009\,\mathrm{Pa\,s}$. Hydrodynamic interactions beyond simple Stokes friction are neglected.

are from analytical considerations. In reality, state-of-the-art stages can be oscillated only up to frequencies of order 100 Hz. For laser driving one must keep in mind that the harmonic trapping region has a finite extension, so for a linear response the laser oscillation amplitude should not exceed a value which is half of that extension. Note further the difference between stage and laser driving in Figure 8.2: While high stage position amplitudes are necessary at *low* stage

driving frequencies, high laser position amplitudes are required at *high* laser driving frequencies. The physical reason for that is that the interaction between the particle and the laser trap is proportional to their relative *positions*, but the coupling between particle and medium is only via their relative *velocities*. Thus at *low* frequencies when the stage is moving only slowly, one needs a high stage amplitude to deflect the bead from its equilibrium position. Vice versa, at high frequencies, when the laser is moved fast, the bead interacts strongly with the medium and one needs high laser amplitudes to deflect the bead. Note further that the cross-over frequency between the curves for required stage and laser amplitudes in Figure 8.2 is very close to the corner frequency $f_c = \kappa/(2\pi\gamma_0)$.

To find driving amplitudes $A_S(\omega_K)$ required for our experiments with stage oscillations, Eq. (8.10) has been applied by using estimates for the parameters κ, $\tilde{\gamma}(\omega)$ and $\chi(\omega)$. In experiments in general viscoelastic media, these parameters are unknown before the calibration. Then, Eqs. (8.10)/(8.11) can not be applied a priori for the calculation of the required stage/laser amplitude $A_{S/L}(\omega_K)$. These amplitudes have rather to be adjusted in a way that the response of the particle exhibits an amplitude which is equal to the observed half-width of the trap.

8.4.2 Stage and bead amplitudes and profiles at the driven system

From our experimental data, both the stage and the bead oscillation amplitudes A_S and A_B have to be determined for the calibration. This has been done by fitting with the least-squares method to the time line data[8]. The fitting routine gives not only the amplitudes of the sinusoidal motion, but also phase shifts, offsets and all errors. For a reliable calibration it is required that the piezo stage performs precise sinusoidal motion with a known small amplitude at a chosen frequency. Therefore one may ask, how precise the sinusoidal motion of our stage actually is, especially for high frequencies, and if the stage really oscillates with the desired amplitude and frequency?

[8]Fitting of the driven data for the parameters A_S, A_P and $\Delta\phi$ is performed by a custom-written MATLAB® program. Furthermore, alternatively to fitting, the three parameters can be obtained from the Fourier transforms of the bead and stage trajectories. This method is implemented in the MATLAB® program, too.

Firstly, the detected stage positions which have been recorded are not continuous values. They are binned, i.e. they are projected onto discrete position levels corresponding to voltages generated by the stage monitoring system, see Fig. 8.3. However, this is no problem for the determination

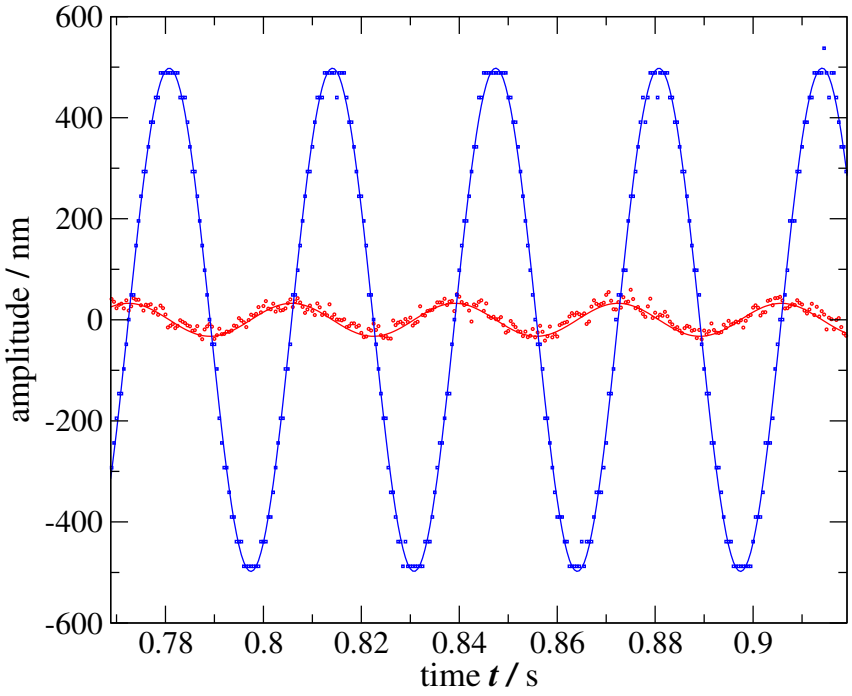

Figure 8.3: Detected stage (squares) and bead (circles) positions and sinusoidal fits (solid lines) obtained from the least squares method. The stage positions are projected on discrete levels. This causes no problem for the fitting routine to determine a reliable fit value $A_{\mathrm{S}}^{(\mathrm{fit,ex})}$. The obtained value $A_{\mathrm{S}}^{(\mathrm{fit,ex})} = 498\,\mathrm{nm}$ is significantly lower than the desired value of $A_{\mathrm{S}}^{(\mathrm{set})} = 600\,\mathrm{nm}$ which was entered during the experiment at the stage controlling interface. For higher frequencies and smaller amplitudes, the discrepancy between chosen amplitude and actually performed amplitude becomes even larger, see Fig. 8.4. The bead positions in meter units were obtained by using the conversion factor β obtained from the power spectrum method.

of the stage amplitude A_{S}, as long as these continuous levels are not separated by a distance comparable to A_{S}. The reason for that is that A_{S} is determined by a fitting procedure which is based on the least squares method. That fitting procedure determines the most probable amplitude with very high precision for our binned data[9].

[9]The relative error of the fitted stage amplitude $A_{\mathrm{S}}^{(\mathrm{fit,ex})}$ is on order 0.01%. The fitted value has further been checked for consistency with the amplitude of the Fourier transform of the stage motion, see Fig. 8.5.

It must be noted that the obtained amplitude values $A_S^{(fit,ex)}$ are significantly lower than the desired values $A_S^{(set)}$ which have been determined by using plots like this one of Fig. 8.2. The discrepancy between chosen amplitude and actually performed amplitude becomes larger for higher frequencies and smaller amplitudes, see Fig. 8.4.

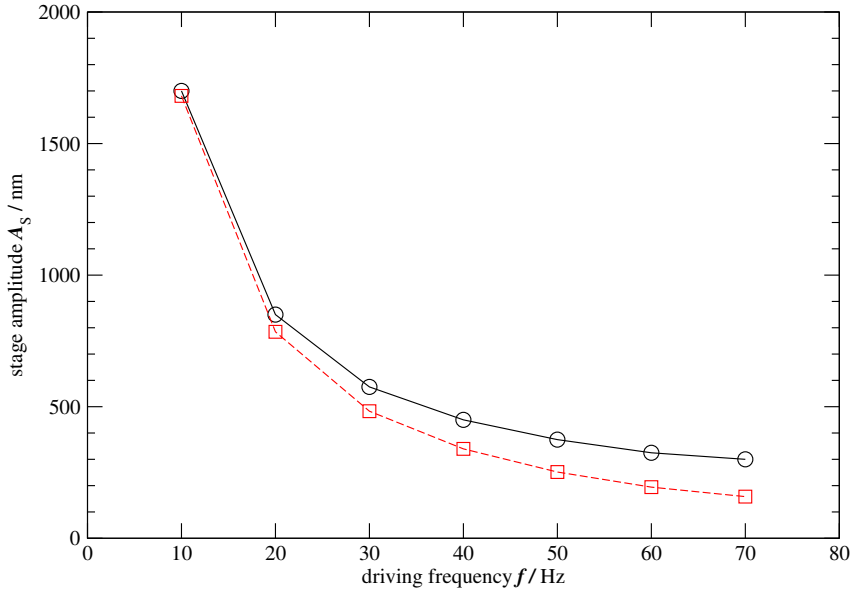

Figure 8.4: Whereas for the lowest frequency the chosen (circles) and the actually performed (squares) stage amplitudes nearly agree, there is an increasing discrepancy between $A_S^{(set)}$ and $A_S^{(fit,ex)}$ for higher frequencies and lower amplitudes. The statistical error of the fitted stage amplitudes is negligible, it is on the order of 0.01% for all frequencies.

Secondly, having now established that the stage amplitude can be obtained with high precision by fitting to the stage position time line, the next step is to ask, if the motion is precisely *sinusoidal* at all, especially if it is a fast motion. It could be that the actual motion deviates slightly from a sinusoidal profile when the stage is driven with a frequency of order 100 Hz, which is fast for a heavy mechanical device. One could expect some inertia or overshooting effects similar to those reported by the piezo stage manufacturer for fast changes of the stage position. Such deviations of the stage motion from a sinusoidal profile can possibly not be seen in the time line, but they should be visible in the Fourier transform of the stage trajectory. The sinusoidal function $x_S(t) = A_S \sin(\omega_{S,0} t)$ has a Fourier transform which is proportional to the sum of two delta functions, one at the driving frequency $\omega_{S,0}$ and one at the negative driving frequency,

$$\tilde{x}_S(\omega) = A_S \pi \mathrm{i}[\delta(\omega + \omega_{S,0}) - \delta(\omega - \omega_{S,0})], \tag{8.12}$$

On the computer, a *discrete* Fourier transform with rectangular windows has been applied to the data set of finite measuring time T_{meas}. Then, the absolute value of the Fourier transform becomes for frequencies f_k which are close to the driving frequency $f_{S,0}$ [76]

$$|\hat{x}_{S,k}| = A_S \left| \frac{\sin(\pi T_{meas} f_{S,0}}{\pi T_{meas}(f_k - f_{S,0})} \right|, \tag{8.13}$$

with $f_{S,0} = \omega_{S,0}/(2\pi)$[10]. In Fig. 8.5 the Fourier transform of the motion of the piezo stage which has been oscillated with frequency $f_{S,0} = 100\,\mathrm{Hz}$ and observed for $T_{\mathrm{meas}} = 100\,\mathrm{s}$ has been plotted for frequencies around $f_{S,0}$. Also Eq. (8.13) has been plotted in Fig. 8.5, with the value

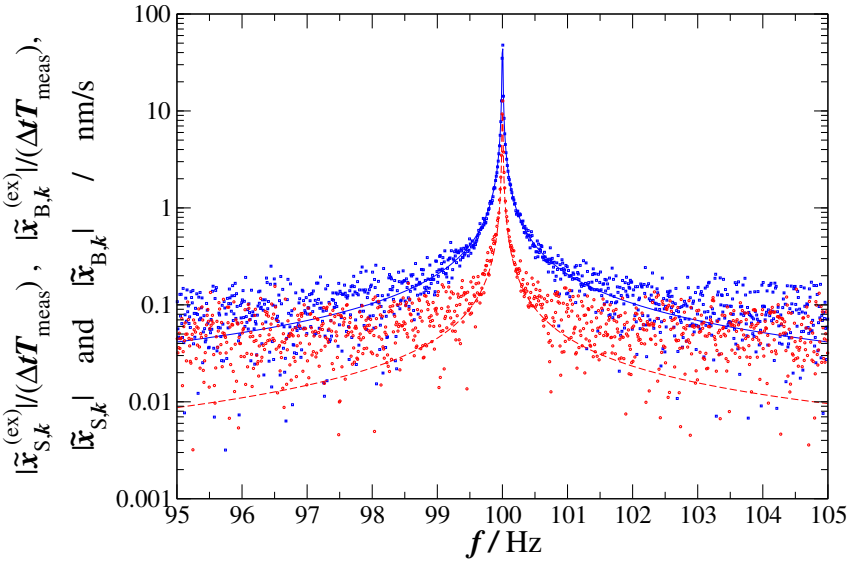

Figure 8.5: Shape of the peak of the numerical Fourier transform of the sinusoidal stage motion of stage (blue) and trapped bead (red) with frequency $f_{S,0} = 100\,\mathrm{Hz}$ in a *log-lin* plot. The experimental spectra $\hat{x}^{(\mathrm{ex})}_{S,k}$ and $\hat{x}^{(\mathrm{ex})}_{B,k}$ are indicated by symbols. The analytical stage position spectrum $\tilde{x}_S(\omega)$ (solid line) is obtained from Eq. (8.13), the analytical bead position spectrum $\tilde{x}_S(\omega)$ (dashed line) from Eq. (8.14). Note that the peak amplitude $\hat{x}_{S,\max} = 47.8\,\mathrm{nm}$ of the Fourier transform of the stage motion is in general not equal with the amplitude $A_S^{(\mathrm{fit,ex})} = 65.3\,\mathrm{nms}$ obtained from sinusoidal fitting to the time series, see Fig. 8.4. $\hat{x}_{S,\max}$ is somewhat lower. Therefore, it is recommended to determine A_S from fitting to the time series. Note that the full spectra also contain side peaks which are not shown in the figure.

$A_S^{(\mathrm{fit,ex})} = 65.3\,\mathrm{nm}$ from the time line fit. It can be seen that the curve describes the data well for frequencies close to $f_{S,0} = 100\,\mathrm{Hz}$ which indicates that the stage indeed performs precise sinusoidal motion. Furthermore, this shows that the stage amplitude $A_S^{(\mathrm{fit,ex})}$ obtained from time line fitting and the Fourier spectrum of the stage position data are consistent with each other. For frequencies more distant to $f_{S,0}$, the measured stage position spectrum lies above the analytical curve which is probably due to electronic noise in the stage detection system. The peak amplitude $x_{S,\max} = 47.8\,\mathrm{nm}$ of the Fourier transform is not equal with the amplitude $A_S^{(\mathrm{fit,ex})} = 65.3\,\mathrm{nm}$ obtained from sinusoidal fitting to the time series. $\hat{x}_{S,\max}$ and $A_S^{(\mathrm{fit,ex})}$ would only be equal, if the measuring time of $T_{\mathrm{meas}} = 100\,\mathrm{s}$ would precisely be a multiple of the driving periode $T_{S,0} = 1/f_{S,0} = 0.01\,\mathrm{s}$[11]. In general $\hat{x}_{S,\max}$ is somewhat lower than $A_S^{(\mathrm{fit,ex})}$. To avoid any complications with the choices of driving frequency, sampling frequency and measuring time, it is not recommended to determine A_S from the Fourier transform, but rather by fitting to the

[10] Note that the general spectrum is a superposition of main peak and side peaks, see [76]. Eq. 8.13 gives only the magnitude of the main peak which is the only non-negligible contribution around $f_{S,0}$.

[11] This is not exactly the case, since actually the measuring time is slightly lower than 100 s, $T_{\mathrm{meas}} = 99.9945\,\mathrm{s}$ and the driving frequency is slightly higher than 100 Hz, $f_{S,0} = 100.0008\,\mathrm{Hz}$.

time series.

The trapped bead performs sinusoidal motion in response to the stage oscillations. This response is characterized by the response function, Eq. (4.4). The mass m of the small bead can safely be neglected at frequencies in the order of 100 kHz. From Eq. (4.2) one obtains for the magnitude of the bead position spectrum

$$|\hat{x}_{\mathrm{B},k}| = |\chi_k| 2\pi f_k \gamma_0 |\hat{x}_{\mathrm{S},k}| = \frac{f_k}{\sqrt{f_\mathrm{c}^2 + f_k^2}} |\hat{x}_{\mathrm{S},k}|, \tag{8.14}$$

Eq. (8.14) is plotted in Fig. 8.5 as a dashed line. It can be seen that it agrees well with the measured bead position data for frequencies close to $f_{\mathrm{S},0} = 100\,\mathrm{Hz}$. The corner frequency used in Eq. (8.14) and the voltage conversion factor for finding $\tilde{x}_{\mathrm{B},k}^{(\mathrm{ex})}$ from the measured QPD voltages, have both been obtained with the power spectrum method. It can further be seen in Fig. 8.5 that for frequencies more distant to $f_{\mathrm{S},0}$, the spectrum $|\hat{x}_{\mathrm{B},k}^{(\mathrm{ex})}|$ is dominated by contributions from the thermal motion of the bead.

8.4.3 Phase difference between stage and bead

For the calibration, not only the stage and bead amplitudes are required, also the phase differences $\Delta\phi = \phi_\mathrm{S} - \phi_\mathrm{B}$ between stage and bead oscillations have to be measured. As the amplitudes, $\Delta\phi$ is obtained from fitting of the time line data with a sinusoidal function. However, at each sampling interval, stage positions are acquired a little later than bead positions by the data acquisition card. The delay time between bead and stage position measurements appears to give an extra phase difference which must be taken into account. This can be seen in Fig. 8.6. The fitted phase difference values $\Delta\phi_K^{(\mathrm{fit})}$, indicated by black error bars[12], lie all far above the analytical curve which is according to Eqs. (4.40) and (4.59) given by

$$\Delta\phi = \arctan\left(\frac{\omega_\mathrm{c}}{\omega}\right), \tag{8.15}$$

and which is indicated by a red line in Fig. 8.6[13]. Correcting each phase difference by an extra, constant phase difference according to

$$\Delta\phi_K^{(\mathrm{corr})} = \Delta\phi_K^{(\mathrm{fit})} - \Delta t_\mathrm{delay} f_K \tag{8.16}$$

with a constant delay time of $\Delta t_\mathrm{delay} \sim 256\,\mu\mathrm{s}$ appears to yield much better results, since the values for $\Delta\phi_K^{(\mathrm{corr})}$ are much closer to the analytical curve, Eq. (8.15). The constant delay time of $\Delta t_\mathrm{delay} \sim 256\,\mu\mathrm{s}$ is very large though, it is larger than the sampling time step of $\Delta t_\mathrm{sample} = 100\,\mu\mathrm{s}$. The data acquisition card should actually perform much faster, rather with a delay time of only $\sim 4\,\mu\mathrm{s}$ for each of its eight channels. Possible reasons for the obtained large delay could be

[12] The black and blue error bars have the measured value in their midpoints and indicate the statistical error obtained from fitting of the time-line data. Fourier transformation of the data yields very similar phase differences and errors (data not shown).

[13] Note that the bead mass has been neglected in Eq. (8.15) which can safely be done at frequencies of order 100 Hz or lower.

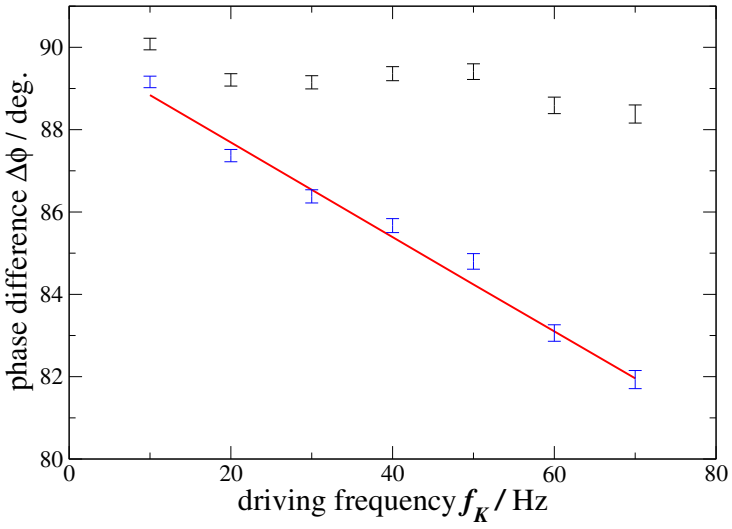

Figure 8.6: Appearance of an extra phase difference: The phase differences $\Delta\phi_K^{(\mathrm{fit})}$ (black error bars) do not match the analytical curve Eq. (8.15) (red line). Only by correcting the phase according to Eq. (8.16) using a very large delay time of $\Delta t_{\mathrm{delay}} \sim 256\,\mu$s one obtains values $\Delta\phi_K^{(\mathrm{corr})}$ (blue error bars) which roughly match the analytical curve.

data-processing in between measurements at consecutive channels[14] or re-adjustment of signal amplification factors[15].

8.5 Independent positional calibration

An independent positional calibration has been tried initially by triangular stage motion. The idea of this technique is that the bead alternately assumes two different equilibrium position due to the positive and negative flow generated by the triangular stage motion. The histogram of bead positions is recorded i) with video microscopy and ii) with the QPD. The ratio of the distances between the two histogram peaks gives then the position calibration factor β. A severe problem of this approach is the low repetition rate of the video microscopy, however. Only few images could be taken at each equilibrium position and several images showed the bead on its way between the equilibrium positions. This resulted in an unreliable value for the conversion factor β.

We have therefore tried an approach with sinusoidal stage motion. Here, the piezo stage has been oscillated in the $y-$direction with a large amplitude $A_{\mathrm{S}} = 11\,\mu$m at a low frequency $f_{\mathrm{S}} = 2\,$Hz. In Fig. 8.7, the responding bead motion is shown as obtained from video microscopy and image analysis. From fitting of that motion to a sinusoidal function, by using the same fitting routines

[14] For example, both channels 1 and 2 acquire the x-component of the bead position. The two obtained values are then averaged.

[15] The voltage signals from bead and stage positions are on different orders of magnitude.

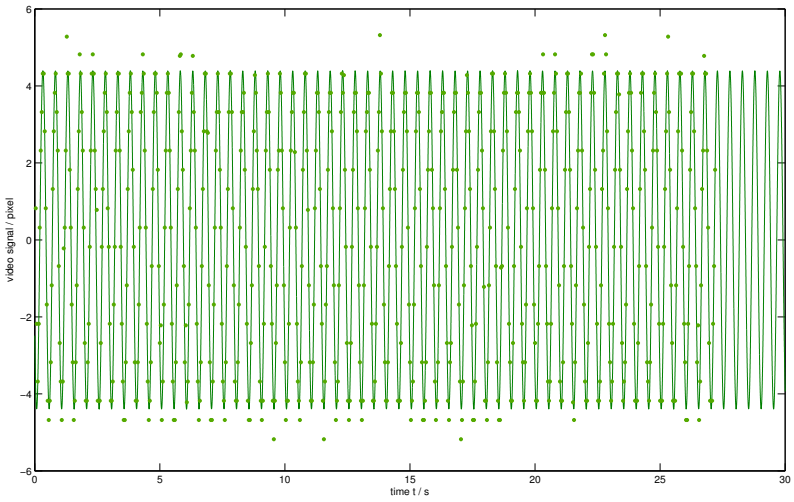

Figure 8.7: Bead motion (circles) in response to slow stage driving obtained from video microscopy and image analysis and sinusoidal fit (solid line). Binning of the data due to the spatial video resolution of $\sim 11\,\mathrm{nm}$ is visible. Also one can see that due to the low temporal video resolution of $\Delta t_{\mathrm{sample,video}} = 25\,\mathrm{Hz}$, only about 12 data points are recorded per cycle. Note that despite both the spatial and the temporal resolution limits, the fitting routine gives a reliable value for the bead amplitude $A_{\mathrm{B}}^{(\mathrm{vid})}$ with a statistical error of only 0.6%.

as for the driven part of the calibration, one obtains the amplitude

$$A_{\mathrm{B}}^{(\mathrm{vid})} = (4.39 \pm \underbrace{0.03}_{\text{statistical error, } 0.6\%})\,\mathrm{pixel}, \tag{8.17}$$

which has a very low statistical error. In Fig. 8.8 the bead motion in response to the 2 kHz oscillations is plotted as obtained from detection with the QPD.

From fitting of that motion to a sinusoidal function, one obtains the amplitude

$$A_{\mathrm{B}}^{(\mathrm{QPD})} = (0.03691 \pm \underbrace{0.00002}_{\text{statistical error, } 0.05\%})\ \text{volt units}. \tag{8.18}$$

Also in this case, the statistical error is very low. The pixel calibration gives a pixel-distance conversion factor of

$$\alpha^* = (11.39 \pm \underbrace{0.03}_{\text{statistical error, } 0.25\%})\,\mathrm{nm/pixel}. \tag{8.19}$$

From the results, Eqs. (8.17), (8.18) and (8.19), the conversion factor for the independent positional calibration with sinusoidal driving $\beta^{(\mathrm{SIN})}$ is found. One obtains

$$\beta^{(\mathrm{SIN})} \equiv \alpha^* \frac{A_{\mathrm{B}}^{(\mathrm{vid})}}{A_{\mathrm{B}}^{(\mathrm{QPD})}} = (1355 \pm \underbrace{12}_{\text{statistical error, } 0.9\%})\,\mathrm{nm/(volt\ unit)}. \tag{8.20}$$

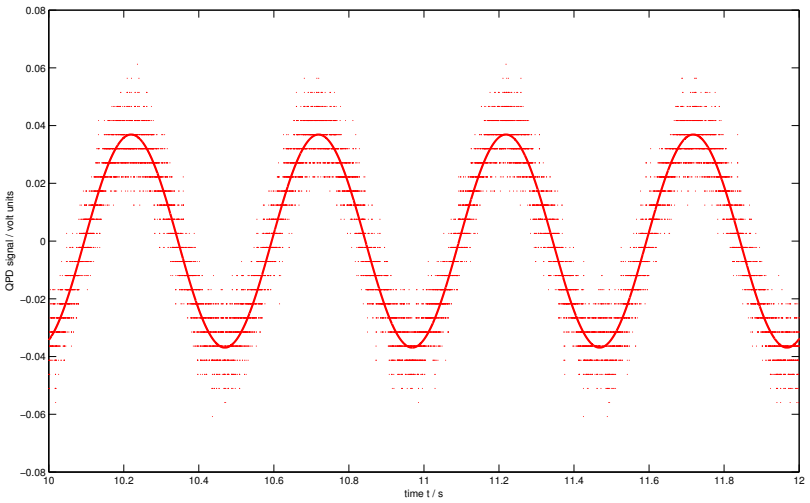

Figure 8.8: Bead motion (small symbols) in response to slow stage driving obtained from detection with the QPD and sinusoidal fit (solid line). Binning of the data is visible. Furthermore, a considerable amount of thermal noise is present. Nevertheless, the fitting routine gives a very precise result for the amplitude $A_{\mathrm{B}}^{(\mathrm{QPD})}$ with a statistical error of only 0.05%.

8.6 Application of the FDT method

8.6.1 Trap stiffness

For calibration with the FDT method, the discretized version of the basic equation in terms of amplitudes and angles, Eq. (6.7) is applied,

$$\kappa_K^{(\mathrm{FDT,volt})} = \frac{2k_\mathrm{B}T}{\langle P_K^{(\mathrm{volt})}\rangle_\mathrm{wind}} \cdot \frac{A_{\mathrm{B},K}^{(\mathrm{fit,volt})}}{2\pi f_K A_{\mathrm{S},K}^{(\mathrm{fit,ex})}} \sin(\Delta\phi_K^{(\mathrm{corr})}), \tag{8.21}$$

where the capital K is the index of the driving frequency f_K of the laser/stage and the mass term has been neglected. This result has units pN/(volt unit). For obtaining a result $\kappa_K^{(\mathrm{ex})}$ which

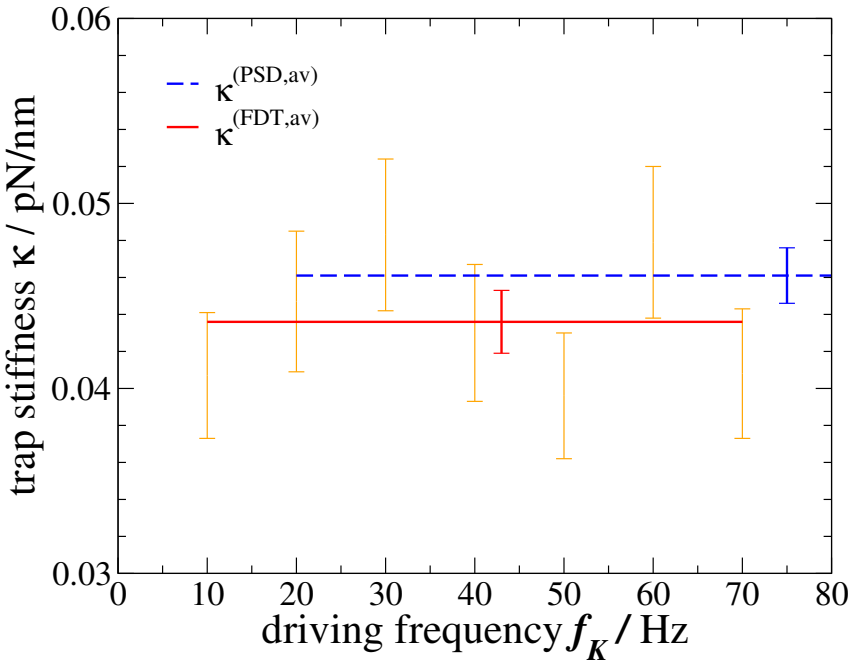

Figure 8.9: Trap stiffness values obtained with two different calibration methods. The value $\kappa^{(\mathrm{PSD,av})}$ obtained with the PSD method as described in section 8.3 is indicated by a blue dashed line over a part of its fitting range which extends up to 2 kHz. It has a relative error of 3.3 %. The frequency-dependent values $\kappa_K^{(\mathrm{FDT,ex})}$ from calibration with the FDT method are indicated by orange error bars, their relative errors are $\sim 8.5\%$, when taking into account statistical errors, errors from the positional calibration and the uncertainity of the temperature. The seven values for $\kappa_K^{(\mathrm{FDT,ex})}$ exhibit roughly overlapping error bars. Thus, all these values are taken into account for averaging in order to obtain $\kappa^{(\mathrm{FDT,av})}$ which is indicated by a red line. The average $\kappa^{(\mathrm{FDT,av})}$ has a relative error of 4.0%.

has units pN/nm, it has to be divided by the conversion factor $\beta^{(\mathrm{SIN})}$,

$$\kappa_K^{(\mathrm{FDT,ex})} = \frac{(\kappa - (2\pi f)^2 m)_K^{(\mathrm{volt})}}{\beta^{(\mathrm{SIN})}}. \tag{8.22}$$

Experimental spectra display statistical noise. Therefore it is appropriate to average those results to obtain a value with lower statistical error, see Eq. (6.9),

$$\kappa^{(\mathrm{FDT,av})} = \langle \kappa_K^{(\mathrm{FDT,ex})} \rangle_K. \tag{8.23}$$

The results for $\kappa_K^{(\mathrm{FDT,ex})}$ and $\kappa^{(\mathrm{FDT,av})}$ are plotted in Fig. 8.9 together with the result from the PSD method, Eq. (8.4).

For $\kappa^{(\mathrm{FDT,av})}$ one obtains

$$\kappa^{(\mathrm{FDT,av})} = (43.6 \quad \pm \underbrace{1.2}_{\text{statistical error, } 2.8\%} \pm \underbrace{0.1}_{\text{error from temperature uncertainity, } 0.3\%} \tag{8.24}$$

$$\pm \underbrace{0.4}_{\text{error from uncertainty in } \beta^{(\mathrm{SIN})},\, 0.9\%}) \,\mathrm{pN}/\mu\mathrm{m},, \tag{8.25}$$

a result with a total relative error of 4%. Thus, within their error bars, the calibration results from the PSD method and the FDT method agree.

8.6.2 Response function

The response function at frequency f_K is obtained from the discretized version of Eq. (6.11),

$$\chi_K^{(\mathrm{FDT,ex})} = \frac{1 - \mathrm{i}2\pi f_K \hat{R}_{\mathrm{S},K}^{(\mathrm{ex})}}{\kappa^{(\mathrm{FDT,av})}}. \tag{8.26}$$

The real and imaginary parts of the active spectrum which are necessary for that computation are obtained by using the relations

$$\mathrm{Re}\{\hat{R}_{\mathrm{S},K}^{(\mathrm{ex})}\} = \frac{A_{\mathrm{B},K}^{(\mathrm{fit,volt})}}{2\pi f_K A_{\mathrm{S},K}^{(\mathrm{fit,ex})} \beta^{(\mathrm{SIN})}} \sin(\Delta\phi^{(\mathrm{corr})}), \tag{8.27}$$

$$\mathrm{Im}\{\hat{R}_{\mathrm{S},K}^{(\mathrm{ex})}\} = -\frac{A_{\mathrm{B},K}^{(\mathrm{fit,volt})}}{2\pi f_K A_{\mathrm{S},K}^{(\mathrm{fit,ex})} \beta^{(\mathrm{SIN})}} \cos(\Delta\phi^{(\mathrm{corr})}), \tag{8.28}$$

cf. Eqs. (4.42) and (4.44). The result for the response function is shown in Fig. 9.7 in which also the expected response function

$$\chi(f) = \frac{1}{\kappa^{(\mathrm{FDT,av})} + \mathrm{i}2\pi f \gamma_0^*} \tag{8.29}$$

has been plotted, cf. Eq. (4.4).

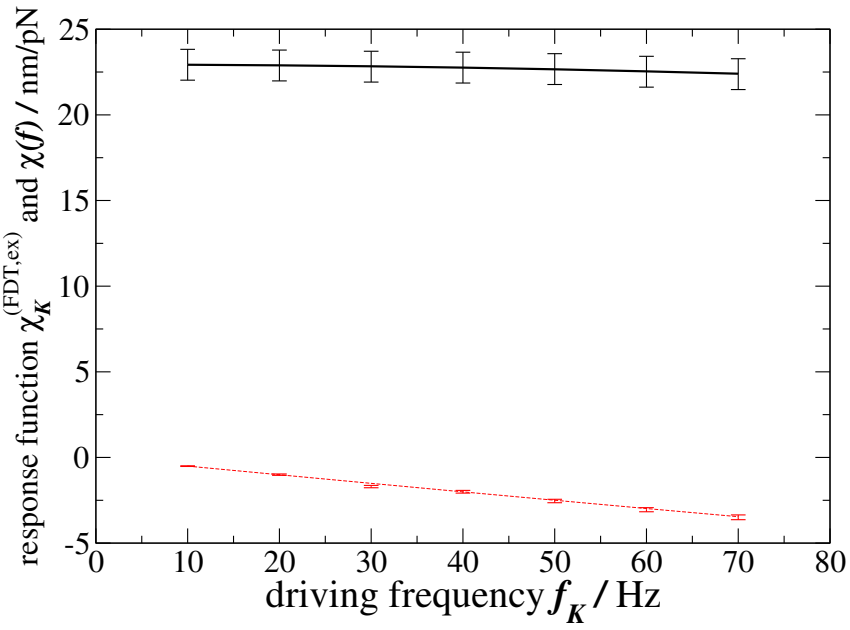

Figure 8.10: Calibration result for the response function $\chi_K^{(\mathrm{FDT,ex})}$ obtained with the FDT method. The real part $\mathrm{Re}\{\chi_K^{(\mathrm{FDT,ex})}\}$ is indicated by black error bars, the imaginary part $\mathrm{Im}\{\chi_K^{(\mathrm{FDT,ex})}\}$ by magenta error bars. The main contribution to the error is the error of the before obtained trap stiffness $\kappa^{(\mathrm{FDT,av})}$. The real part (solid line) and the imaginary part (dashed line) of the expected response function, Eq. (8.29), are shown in the figure, too.

8.6.3 Friction retardation spectrum

As next step, the friction retardation spectrum is determined from the discretized version of Eq. (6.17),

$$\hat{\gamma}_K^{(\mathrm{FDT,ex})} = \hat{R}_{\mathrm{S},K}^{(\mathrm{ex})} / \chi_K^{(\mathrm{FDT,ex})}, \tag{8.30}$$

by using the results from the calculation of the response function from the last paragraph. The result for the real part is plotted in Fig. 8.11. The data values lie roughly on a constant line given by γ_0^*. Thus, good agreement is achieved with the model for friction in the proximity of a hard wall[16]. However, for the imaginary part which is small compared to the real part and which represents the elastic contributions to the friction force, results are obtained which are not consistent with the model for friction close to a hard wall, see Fig. 8.12.

[16]For simple Stokes friction, the friction retardation spectrum $\tilde{\gamma}(\omega)$ is frequency-independent and equal to $\gamma_0 = 6\pi\eta R$. In first order, the model for friction close to a hard wall, only modifies this constant to γ_0^*.

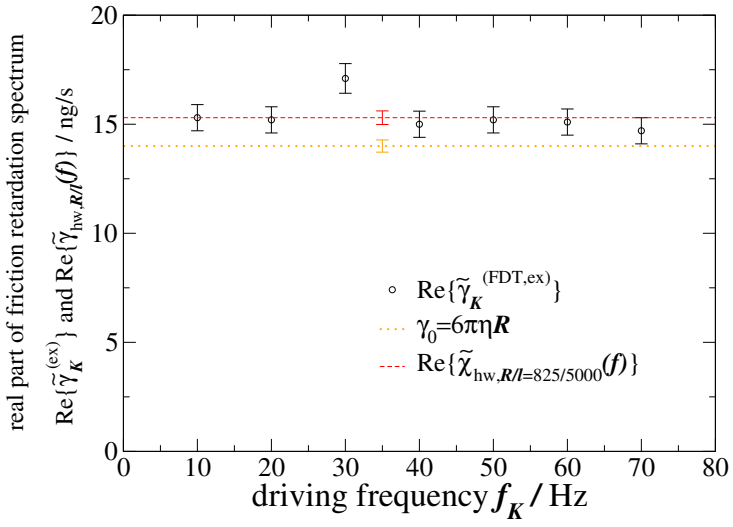

Figure 8.11: Calibration result for the real part of the friction retardation spectrum $\mathrm{Re}\{\hat{\gamma}_K^{(\mathrm{FDT,ex})}\}$. The data points (circles) lie above the value of $\gamma_0 = 14.0\,\mathrm{ng/s}$ (dotted line) which has a 2% error due to the uncertainity in temperature. However, this can be explained with the increase of friction due to finite distance $l = 5\,\mu\mathrm{m}$ between bead and the microscope coverslip. In first order, the friction is increased by a factor of $9R/(16l)$, see Eq. (3.14). The corrected value $\mathrm{Re}\{\tilde{\gamma}_{\mathrm{hw},R/l}\}(f) = \gamma_0^* = 15.3\,\mathrm{ng/s}$ is indicated by a dashed line. One can see that this value lies within the error bars of most of the data points. This demonstrates that the FDT method correctly reproduces the effect of increased viscosity due to the proximity of the microscope coverslip.

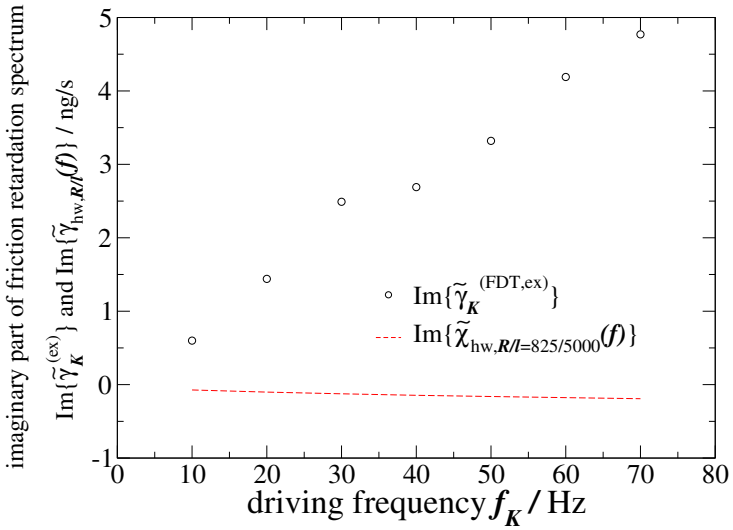

Figure 8.12: Calibration result for the imaginary part of the friction retardation spectrum $\mathrm{Im}\{\hat{\gamma}_K^{(\mathrm{FDT,ex})}\}$. The data points (circles) do not agree with the expected function $\mathrm{Im}\{\tilde{\gamma}_{\mathrm{hw},R/l}(f)$ from Eq. (3.14). This problem has remained unsolved at the time of submitting this thesis.

8.6.4 Positional calibration

Since it has been measured in water at low frequencies, the discretized version of the equation for positional calibration, Eq. (6.19) can be used,

$$\beta_K^{(\mathrm{FDT,ex})} = \frac{2k_\mathrm{B}T}{2\pi f_K \overline{\langle P_K^{(\mathrm{volt})} \rangle_\mathrm{wind}}} \cdot \frac{\cot(\Delta\phi_K^{(\mathrm{corr})})}{\kappa_K^{(\mathrm{FDT,av,volt})}}. \tag{8.31}$$

A value with lower statistical error is then obtained from by averaging,

$$\beta^{(\mathrm{FDT,av})} = \langle \beta_K^{(\mathrm{FDT,ex})} \rangle_K. \tag{8.32}$$

The results for $\beta_K^{(\mathrm{FDT,ex})}$ and $\beta^{(\mathrm{FDT,av})}$ are plotted in Fig. 8.13, together with the results from the PSD method, Eq. (8.6), and from the independent method, Eq. (8.20). We obtain good agreement between the results from the FDT method, $\beta^{(\mathrm{FDT,av})}$, and the independent method, $\beta^{(\mathrm{SIN})}$, whereas the PSD method yields a significantly lower result, $\beta^{(\mathrm{PSD,av})}$.

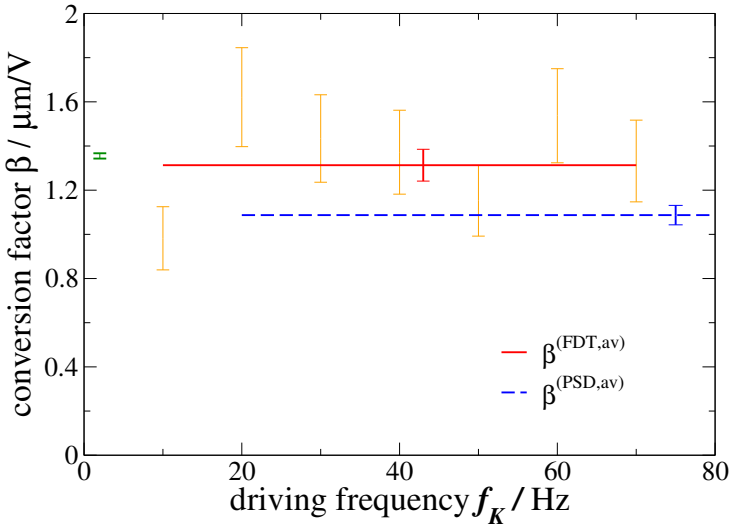

Figure 8.13: Voltage-position conversion factor values obtained with three different methods. The value $\beta^{(\mathrm{PSD,av})}$ obtained with the PSD method as described in section 8.3 is indicated by a blue dashed line over a part of its fitting range which extends up to 2 kHz. It has a relative error of 4.1 %. The frequency-dependent values $\beta_K^{(\mathrm{FDT,ex})}$ from calibration with the FDT method are indicated by orange error bars, their relative errors are $\sim 14\%$, when taking into account statistical errors and errors from the uncertainity of the temperature. We take all seven values for $\beta_K^{(\mathrm{FDT,ex})}$ into account for averaging in order to obtain $\beta^{(\mathrm{FDT,av})}$ which is indicated by a red line. The average $\beta^{(\mathrm{FDT,av})}$ has a relative error of 5.5%. Moreover, the conversion factor $\beta^{(\mathrm{SIN})}$ as obtained by the independent positional calibration shown in section 8.5 is marked as a green error bar over the oscillation frequency of 2 Hz. Within their error bars, the results from the independent method, $\beta^{(\mathrm{SIN})}$, and from the FDT method, $\beta^{(\mathrm{FDT,av})}$, are consistent with each other. The conversion factor obtained with the PSD method, $\beta^{(\mathrm{PSD,av})}$, is significantly lower, however.

8.7 Statistical errors of experimental results

In this section I will demonstrate how to calculate the most relevant statistical errors for the experiment presented in the previous sections. These errors are the relative errors of $\overline{\langle P_K^{(\mathrm{volt})}\rangle_{\mathrm{wind}}}$, $A_{\mathrm{B},K}^{(\mathrm{fit,volt})}$, $\sin(\Delta\phi_K^{(\mathrm{fit})})$, $\Delta\phi_K^{(\mathrm{fit})}$ and $\kappa_K^{(\mathrm{FDT,volt})}$.

For the *passive part* of the experiment, the standard deviation

$$\sigma[\overline{\langle P_K^{(\mathrm{volt})}\rangle_{\mathrm{wind}}}] = \langle(\overline{\langle P_K^{(\mathrm{volt})}\rangle_{\mathrm{wind}}} - P(f_K))^2\rangle^{1/2} \tag{8.33}$$

of the experimental power spectrum relative to the theoretical value is simply determined by the number of data sets/windows N_{wind} and blocks N_{block},

$$\epsilon_{\mathrm{rel}}[\overline{\langle P_K^{(\mathrm{volt})}\rangle_{\mathrm{wind}}}] = \frac{\sigma[\overline{\langle P_K^{(\mathrm{volt})}\rangle_{\mathrm{wind}}}]}{P(f_K)} = \frac{1}{\sqrt{N_{\mathrm{wind}}N_{\mathrm{block}}}}. \tag{8.34}$$

For the *active part* of the experiment, the estimate of the relative statistical error of the particle amplitude $A_{\mathrm{B},K}^{(\mathrm{fit,volt})} \equiv |\langle\hat{x}_K\rangle|/T_{\mathrm{meas}}$ is a bit more complicated. The relative error is given by

$$\epsilon_{\mathrm{rel}}[A_{\mathrm{B},K}^{(\mathrm{fit,volt})}] = \frac{\epsilon[A_{\mathrm{B},K}^{(\mathrm{fit,ex})}]}{A_{\mathrm{B}}(\omega_K)}, \tag{8.35}$$

if errors from the voltage-position conversion are neglected. The theoretical value $A_{\mathrm{B}}(\omega_K)$ in the denominator of Eq. (8.35) is given by

$$A_{\mathrm{B}}(\omega_K) = |\chi(\omega_K)||\omega_K\tilde{\gamma}(\omega_K)|A_{\mathrm{S}}(\omega_K), \tag{8.36}$$

where Eqs. (4.2) and (8.9) have been used. The motion of the trapped particle in the driven system is a superposition of thermal and driven motion,

$$\hat{x}_K = \hat{x}_{\mathrm{th},K} + \hat{x}_{\mathrm{dr},K}. \tag{8.37}$$

The statistical error of the experimental value $\epsilon_{\mathrm{rel}}[A_{\mathrm{B},K}^{(\mathrm{fit,volt})}]$ arises since at finite measurement time T_{meas}, the ratio between the thermal part of the motion $\hat{x}_{\mathrm{th},K}$ and the measured driven part of the motion $\hat{x}_{\mathrm{dr},K} = \langle\hat{x}_K\rangle$ is nonzero. In the calculation of the thermal average $\langle\hat{x}_K\rangle$, the thermal part therefore contributes the noise[17]. Hence the error is given by the standard deviation of the thermal part of the motion $\sigma[\hat{x}_{\mathrm{th},K}^{(\mathrm{ex})}] = \langle(\hat{x}_{\mathrm{th},K}^{(\mathrm{ex})})^2\rangle^{1/2}$, divided by T_{meas} because the spectral peak from the driven part of the motion increases in height with measurement time. In the active part of the experiment, the thermal part of the particle's motion is given by

$$\hat{x}_{\mathrm{th},K}^{(\mathrm{ex})} = \hat{F}_{\mathrm{random},K}^{(\mathrm{ex})}\chi(\omega_K) = \sqrt{2k_{\mathrm{B}}T\tilde{\gamma}'(\omega_K)}\hat{\eta}_K^{(\mathrm{ex})}\chi(\omega_K), \tag{8.38}$$

with the abbreviation $\tilde{\gamma}'(\omega_K) = \mathrm{Re}\{\tilde{\gamma}(\omega_K)\}$. With $\langle\hat{\eta}_K^{(\mathrm{ex})*}\hat{\eta}_k^{(\mathrm{ex})}\rangle = T_{\mathrm{meas}}\delta_{K,k}$ one obtains

$$\epsilon_{\mathrm{rel}}[A_{\mathrm{B},K}^{(\mathrm{fit,volt})}] = B(\omega_K)\frac{\tilde{\gamma}'(\omega_K)}{|\tilde{\gamma}(\omega_K)|} \propto \frac{1}{\sqrt{T_{\mathrm{meas}}}A_{\mathrm{S}}(\omega_K)}. \tag{8.39}$$

[17] Basically, the thermal averaging is performed by the fitting procedure who yields the most probable fit values for A_{P} and $\Delta\phi$.

with the frequency-dependent dimensionless number

$$B(\omega) = \frac{\sqrt{k_\mathrm{B}T}}{\sqrt{2T_\mathrm{meas}\tilde{\gamma}'(\omega)}A_\mathrm{S}(\omega)\omega}. \tag{8.40}$$

In a simple viscous medium where $\mathrm{Re}\{\tilde{\gamma}(\omega)\} = \gamma_0$ and $\mathrm{Im}\{\tilde{\gamma}(\omega)\} = 0$, the relative error $\epsilon_\mathrm{rel}[A_{\mathrm{B},K}^{(\mathrm{fit,volt})}]$ is equal to $B(\omega_K)$. In the experiments, errors were found which agree very well with such predictions, see Figure 8.14.

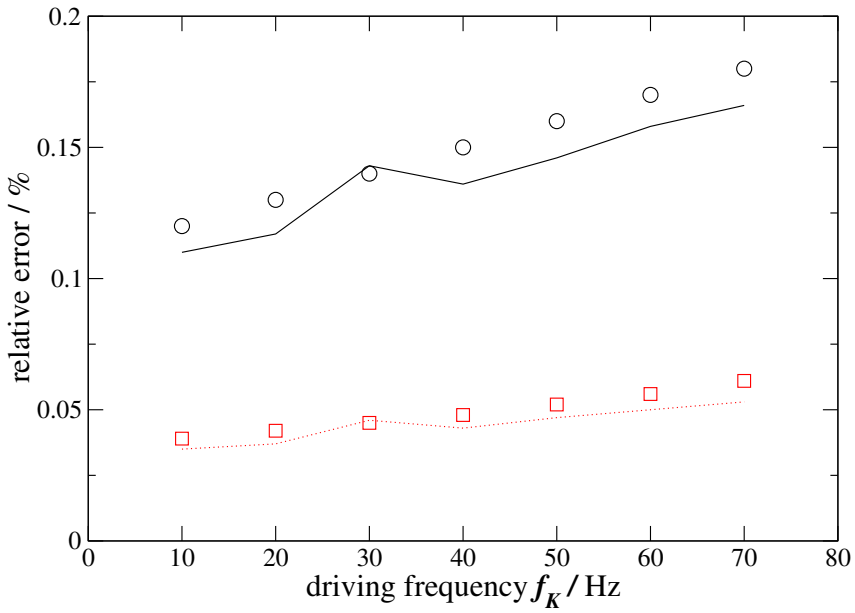

Figure 8.14: Relative errors of bead amplitudes $A_{\mathrm{B},K}^{(\mathrm{fit,volt})}$ (circles) and phase differences $\Delta\phi_K$ (squares) in the active part of the experiment described in section 8.4. The analytical values of relative errors obtained from Eqs. (8.39) and (8.48) are indicated by a solid line for the bead amplitude and by a dotted line for the phase difference, respectively. One can see that the errors found in the experiments are always somewhat higher than the analytical errors. This is reasonable as only thermal noise from the bead motion has been considered in the analytical error calculation.

For the calculation of the relative error of the sine of the phase difference $\epsilon_\mathrm{rel}[\sin(\Delta\phi_K^{(\mathrm{fit})})]$,

$$\mathrm{Re}\{\tilde{R}_\mathrm{S}(\omega_K)\} = |\tilde{R}_\mathrm{S}(\omega_K)|\sin(\Delta\phi(\omega_K^{(\mathrm{fit})})) \tag{8.41}$$

is used which implies

$$\epsilon_\mathrm{rel}[\sin(\Delta\phi_K^{(\mathrm{fit})})] = \epsilon_\mathrm{rel}[\mathrm{Re}\{\hat{R}_{\mathrm{S},K}\}] - \underbrace{\epsilon_\mathrm{rel}[|\hat{R}_{\mathrm{S},K}|]}_{=\epsilon_\mathrm{rel}[A_{\mathrm{B},K}^{(\mathrm{fit,volt})}]\ (\mathrm{Eq.\ (8.39)})}. \tag{8.42}$$

The relative error $\epsilon_\mathrm{rel}[\mathrm{Re}\{\hat{R}_{\mathrm{S},K}\}]$ can be found from the ratio of the standard deviation of the real part of the thermal part of the motion $\sigma[\mathrm{Re}\{\hat{x}_{\mathrm{th},K}^{(\mathrm{ex})}\}]$ divided by T_meas and the analytical value for the real part of the average bead trajectory $\mathrm{Re}\{\langle\tilde{x}(\omega_K)\rangle\}$. The former is found as $\sigma[\mathrm{Re}\{\hat{x}_{\mathrm{th},K}^{(\mathrm{ex})}\}] =$

$\langle(\mathrm{Re}\{\hat{x}_{\mathrm{th},K}^{(\mathrm{ex})}\})^2\rangle^{1/2}$, and the latter is given by $\mathrm{Re}\{\langle\tilde{x}(\omega_K)\rangle\} = A_\mathrm{S}(\omega_K)\omega_K|\chi(\omega_K)|^2(\kappa-\omega_K^2 m)\mathrm{Re}\{\tilde{\gamma}(\omega_K)\}$. One obtains

$$\epsilon_\mathrm{rel}[\mathrm{Re}\{\hat{R}_{\mathrm{S},K}\}] = B(\omega)\left\{1+\frac{\omega_K[\tilde{\gamma}'(\omega_K)-\tilde{\gamma}''(\omega_K)]}{\kappa-\omega_K^2 m}\right\}. \tag{8.43}$$

By inserting Eq. (8.43) into Eq. (8.42) one finds

$$\epsilon_\mathrm{rel}[\sin(\Delta\phi_K^{(\mathrm{fit})})] = B(\omega_K)\left\{1-\frac{\tilde{\gamma}'(\omega_K)}{|\tilde{\gamma}(\omega_K)|}+\frac{\omega_K[\tilde{\gamma}'(\omega_K)-\tilde{\gamma}''(\omega_K)]}{\kappa-\omega_K^2 m}\right\} \propto \frac{1}{\sqrt{T_\mathrm{meas}}A_\mathrm{S}(\omega_K)} \tag{8.44}$$

In the limit of a light particle in a simple viscous medium this expression reduces to

$$\epsilon_\mathrm{rel}[\sin(\Delta\phi_K^{(\mathrm{fit})})] = B(\omega_K)\cdot\frac{\omega_K}{\omega_\mathrm{c}}, \tag{8.45}$$

where $\omega_\mathrm{c} = \kappa/\gamma_0$ is the angular corner frequency. From that result, one can calculate the error of the phase difference $\Delta\phi_K$ itself which allows for a straight-forward comparison to experimentally found errors. One has

$$\epsilon_\mathrm{rel}[\Delta\phi_K^{(\mathrm{fit})}] = \frac{\epsilon_\mathrm{rel}[\sin(\Delta\phi_K^{(\mathrm{fit})})]}{\pi|\cos(\Delta\phi(\omega_K^{(\mathrm{fit})}))|} \tag{8.46}$$

which gives together with

$$\cos(\Delta\phi(\omega_K^{(\mathrm{fit})})) = \frac{\mathrm{Im}\{\tilde{R}_\mathrm{S}(\omega_K)\}}{|\tilde{R}_\mathrm{S}(\omega_K)|} \tag{8.47}$$

the error expression

$$\epsilon_\mathrm{rel}[\Delta\phi_K^{(\mathrm{fit})}] = \frac{B(\omega_K)}{\pi}\left\{\frac{1-\frac{\tilde{\gamma}'(\omega_K)}{|\tilde{\gamma}(\omega_K)|}+\frac{\omega_K[\tilde{\gamma}'(\omega_K)-\tilde{\gamma}''(\omega_K)]}{\kappa-\omega_K^2 m}}{|\chi(\omega_K)|\cdot\left|-\omega|\tilde{\gamma}(\omega_K)|+(\kappa-\omega_K^2 m)\frac{\tilde{\gamma}''(\omega)}{|\tilde{\gamma}(\omega)|}\right|}\right\}. \tag{8.48}$$

For a light particle in a simple viscous medium at low frequencies this simplifies to

$$\epsilon_\mathrm{rel}[\Delta\phi_K^{(\mathrm{fit})}] = \frac{B(\omega_K)}{\pi}. \tag{8.49}$$

Again, our experimental findings agree well with such predictions, see Figure 8.14. The good agreement of experimental and analytical errors indicates that the statistical error from the thermal motion of the bead is the most relevant error contribution in the driven part of the motion. Further it indicates that our method of sinusoidal driving and fitting of the bead response to a sinusoidal function are reliable approaches. The relative error of the calibration result $\kappa_K^{(\mathrm{FDT,volt})}$ is now simply given by the sum of the relative errors calculated previously,

$$\epsilon_\mathrm{rel}[\kappa_K^{(\mathrm{FDT,volt})}] = \underbrace{\epsilon_\mathrm{rel}[\overline{\langle P_K^{(\mathrm{volt})}\rangle_\mathrm{wind}}]}_{\text{Eq. (8.34)}} + \underbrace{\epsilon_\mathrm{rel}[A_{\mathrm{B},K}^{(\mathrm{fit,volt})}]}_{\text{Eq. (8.39)}} + \underbrace{\epsilon_\mathrm{rel}[\sin(\Delta\phi_K^{(\mathrm{fit})})]}_{\text{Eq. (8.44)}}. \tag{8.50}$$

Note that in Eq. (8.50) only the statistical errors arising from averaging over the particle motion for a finite time T_meas have been taken into account.

8.8 Conclusion and outlook

The results of the experiments show that the FDT method works well in water. The spring constants obtained from calibration with the FDT method and with the PSD method are in agreement with each other within their error margins. Furthermore, the real part of the friction retardation spectrum determined with the FDT method is in agreement with the friction coefficient which is expected for the bead motion at a distance of $l = 5\,\mu$m from the coverslip. A problem which has to be investigated, is, that the imaginary part of the friction retardation spectrum gives inconsistent results. This could be a problem of data evaluation, however.

The results from the FDT method and from the independent method for positional calibration are consistent with each other within their error margins. The conversion factor obtained with the PSD method is significantly lower than the values from the two other methods, however. Moreover, reasonable relative errors have been obtained with the FDT method which are in the order of a few percent for all quantities.

The *phase 1* test of the FDT method in water represents a proof of the method's principle. It also serves as a test of the performance of the equipment, since it is clear that the FDT must hold. It has been shown that the piezo stage used performs reliably sinusoidal motion at frequencies as high as 100 Hz. In future experiments, it should be tried to drive with frequencies higher than 100 Hz, in order to investigate in which frequency range the limit of a reliable sinusoidal stage motion lies.

Fitting to sinusoidal functions has been utilized in both the FDT method and at the independent positional calibration. It is a reliable procedure which enables to find amplitudes and phase angles with very small statistical errors even from binned data or from data with small temporal resolution. The agreement of the errors obtained from fitting with theoretical predictions has been shown.

The influence of the temperature uncertainty is much lower for the FDT method than for the PSD method. The reason for that is that the temperature dependence of the viscosity is not relevant for the FDT method, since the viscosity does not appear in its basic equations. The main error contribution in the FDT method is the statistical error arising from the thermal motion of the trapped particle. This error can be reduced to lower values by increasing the measuring time which has been only 30 s at the undriven system and 70 s at the driven system in our measurements.

The next step for testing the performance of the FDT method would be *phase 2* as described in section 8.1.

9 The trapped bead in proximity to a phagocyte cell membrane

In optical tweezers experiments, the trapped particle is frequently situated close to a *biological surface*, like the cell membrane. Biological surfaces are often soft, in most cases liquid and thermally fluctuating. So far there is no theoretical model which describes the friction which the particle feels close to such a complicated structure. In this chapter an analysis of data is presented which has been suggested by Prof. Dr. Alexander Rohrbach from the University of Freiburg (Germany). The data, which is a courtesy of Dr. Holger Kress from Yale University, is from an experiment in which a trapped bead was moved stepwise towards the membrane of a living phagocyte. The actual goal of that experiment was to study the process of binding of beads to the phagocyte membrane [2]. Here I investigate only the motion of the trapped bead *prior* to binding. The position data which was analyzed is shown in Fig. 9.1, where the initiation of the binding process at $t \sim 52\,\mathrm{s}$ is clearly visible.

The underlying biological question of this microrheological study is, how the frictional force close to the phagocyte membrane is altered, to enable an efficient binding of nearby particles. In particular, one might ask about the nature of this frictional force. Is it mainly a viscous drag which is enhanced due to the proximity of the membrane, similarly to the increase of viscosity close to a hard wall? Or are there rather major elastic contributions in the frictional force? In linear response theory, the frictional force is given by

$$\tilde{F}_{\mathrm{fric}}(\omega) = -\tilde{\gamma}(\omega)\tilde{v}(\omega), \tag{9.1}$$

see Eq. (3.6). Thus the problem is reduced to determine $\tilde{\gamma}(\omega)$.

In section 9.1, the microrheology approach is introduced, which will be applied in the data evaluation. A central quantity for the data evaluation is the response function $\chi(\omega)$ which is derived analytically for simple models in section 9.2. In the data evaluation, the real part of the response function has to be computed numerically from the imaginary part. I report about problems related to that in section 9.3. In section 9.4 the evaluation of the experimental data is presented. The results are discussed in section 9.5.

9.1 Model and method

There is no theoretical model to describe the bead motion in the proximity of a cell membrane. Due to this lack of an appropriate model I will resort to the model of friction close to a *hard wall*, which is given in paragraph 3.2.3. This means that the question to be answered is if the bead motion close to the phagocyte membrane can be described by that model. In order to answer that question, the friction retardation spectrum $\tilde{\gamma}^{(\mathrm{ex})}(\omega)$ from the experimental data is extracted in dependence of the distance l from the membrane. For that, an established microrheology approach is used. Then it is checked, if the observed spectrum is consistent with the model, Eq. (3.14).

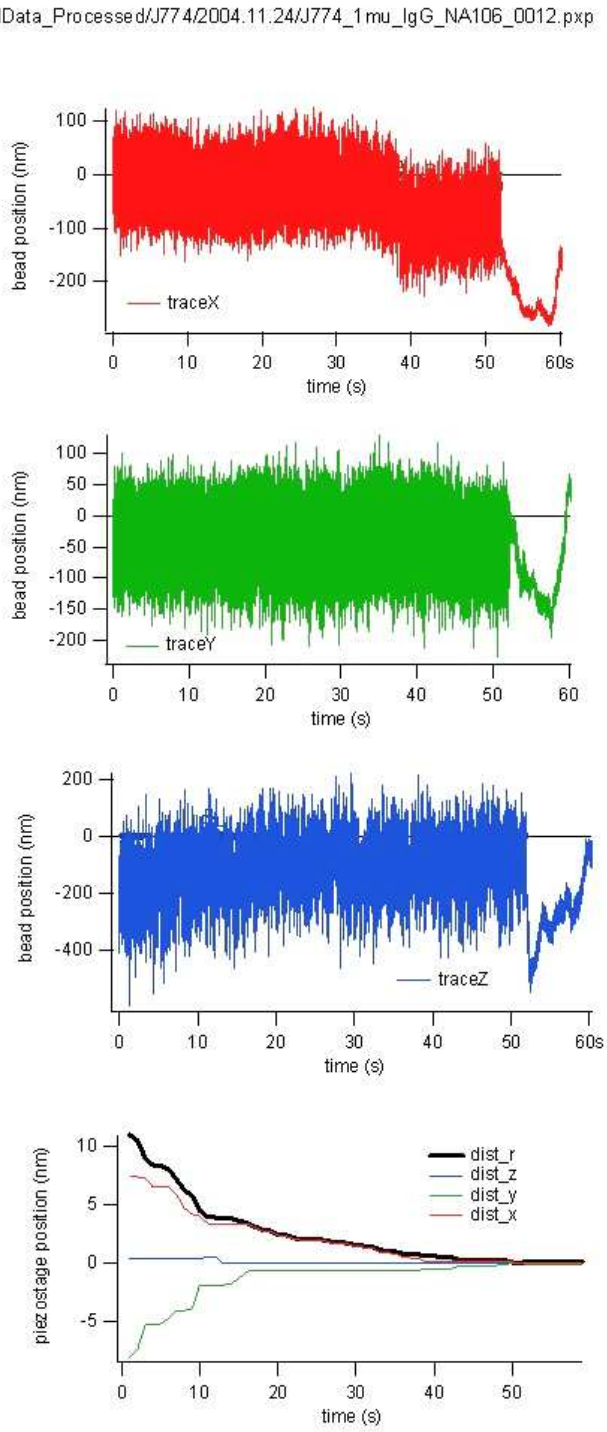

Figure 9.1: Position data (x,y,z component in the three upper panels, stage position in lower panel) of a trapped bead close to a phagocytic membrane, by courtesy of Dr. Holger Kress. The bead was moved stepwise closer to the membrane by moving the microscope piezo stage, until it was bound to the membrane, at about $t = 52\,\mathrm{s}$.

By moving the stage, the bead was stepwise brought closer to the phagocyte membrane. The motion of the bead is then a superposition of the driven part of the motion and the thermal part of the motion. At the frequency spectrum of the motion, the driven part is only relevant at low frequencies, since the stage was not moved very fast. The driven part will be neglected in the following[1].

The thermal motion can then be evaluated according to the passive one-point microrheology approach of Schnurr, Gittes et al. [10, 11] which results in an expression for $\tilde{\gamma}(\omega)$. For that approach, the trap stiffness κ has to be known and one has to evaluate one of the two Kramer-Kronig relations numerically, which involves numerical errors, as I will demonstrate in section 9.3. By application of the FDT, Eq. (4.12), the imaginary part[2] of the response function $\chi(\omega)$ is immediately obtained from the power spectrum $P(\omega)$. The real part of the response function, $\chi'(\omega)$, is obtained from the imaginary part $\chi''(\omega)$ by applying the Kramers-Kronig relation (KKR), Eq. (4.9). From both components of the response function, the friction retardation spectrum can be easily extracted, since it is assumed that the trap stiffness κ is determined by prior calibration. One has

$$\tilde{\gamma}(\omega) = \frac{1/\chi(\omega) - \kappa}{\mathrm{i}\omega}. \tag{9.2}$$

Moreover, microrheology would involve the determination of the viscoelastic modulus $G(\omega)$. It can be determined from the friction retardation spectrum by the generalized Stokes law, Eq. (2.6). In the following, $G(\omega)$ will not be calculated, however, since it is a pure material property. Here the main interest is in the friction retardation spectrum $\tilde{\gamma}(\omega)$ which describes the *interaction* between bead and surrounding. Therefore the microrheology method will only be applied until the determination of the friction retardation spectrum according to Eq. (9.2).

9.2 Analytical expressions for the response function

The *response function* is an inverse effective spring constant of the whole system, consisting of trap, medium and massive particle. It contains information about the elastic (real part) and viscous (imaginary part) response of the system to external forces. The Kramers-Kronig relations connect the real and the imaginary part of the response function. In this section the KKR, Eq. (4.9), is solved analytically for the special case of simple Stokes friction. Further, the response function is given for the special case in which the bead is situated in the proximity of a hard wall.

For the case of a light particle immersed in water far from any surface, it is easy to calculate the sine- and the cosine transform in Eq. (4.9) analytically: For the case of simple Stokes friction the friction retardation spectrum is constant,

$$\tilde{\gamma}(\omega) = \gamma_0, \tag{9.3}$$

and the response function for a particle of negligible mass becomes

$$\chi_{0,\mathrm{light}}(\omega) = \frac{1}{\kappa + \mathrm{i}\omega\gamma_0}, \tag{9.4}$$

[1] The driven part can not be determined anyway, since the exact stage trajectory is not known.

[2] The real and imaginary parts of a complex number z will be indicated by $\mathrm{Re}\{z\}$ and $\mathrm{Im}\{z\}$, or, equivalently, by z' and z'', respectively.

cf. Eq. (4.4). One has for the imaginary part of the response function

$$\chi''_{0,\mathrm{light}}(\omega) = -\frac{\omega\gamma_0}{|\kappa + \mathrm{i}\omega\gamma_0|^2}. \tag{9.5}$$

Inserting Eq. (9.5) into the sine transform of Eq. (4.9) gives

$$\begin{aligned}
\sqrt{\frac{2}{\pi}}\int_0^\infty \chi''_{0,\mathrm{light}}(\zeta)\sin(\zeta t)d\zeta &= -\sqrt{\frac{2}{\pi}}\int_0^\infty \frac{\zeta\gamma_0}{\kappa^2+\zeta^2\gamma_0^2}\sin(\zeta t)d\zeta \\
&= -\sqrt{\frac{2}{\pi}}\frac{1}{\gamma_0}\int_0^\infty \frac{1}{\omega_\mathrm{c}^2+\zeta^2}\sin(\zeta t)d\zeta \\
&= -\sqrt{\frac{\pi}{2}}\frac{1}{\gamma_0}\exp(-\omega_\mathrm{c}t),
\end{aligned} \tag{9.6}$$

where $\omega_\mathrm{c} = \kappa/\gamma_0$ is the corner frequency. This result can now be inserted into the cosine transform in Eq. (4.9) which gives,

$$\sqrt{\frac{2}{\pi}}\int_0^\infty \left\{-\sqrt{\frac{\pi}{2}}\frac{1}{\gamma_0}\exp(-\omega_\mathrm{c}t)\right\}\cos(\omega t)dt = \frac{1}{\gamma_0}\frac{\omega_\mathrm{c}}{\omega_\mathrm{c}^2+\omega^2} = \frac{\kappa}{\kappa^2+\omega^2\gamma_0^2}. \tag{9.7}$$

It is easy to check that this is really the real part of the response function,

$$\chi'_{0,\mathrm{light}}(\omega) = \frac{\kappa}{\kappa^2+\omega^2\gamma_0^2}. \tag{9.8}$$

For a particle of non-negligible mass, the response function $\chi_{0,\mathrm{light}}(\omega)$ of the trapped bead far from any surface, Eq. (9.4), must be modified to

$$\chi_0(\omega) = \frac{1}{\kappa + \mathrm{i}\omega\gamma_0 - \omega^2 m}. \tag{9.9}$$

For a trapped bead in the proximity of a hard wall, one has the response function

$$\chi_{\mathrm{hw},R/l}(\omega) = \frac{1}{\kappa + \mathrm{i}\omega\tilde{\gamma}_{\mathrm{hw},R/l}(\omega) - \omega^2 m} \tag{9.10}$$

with $\tilde{\gamma}_{\mathrm{hw},R/l}(\omega)$ given by Eq. (3.14). The response functions given in Eqs. (9.9) and (9.10), the latter for the ratio, $R/l = 0.837$, are shown in Fig. 9.2.

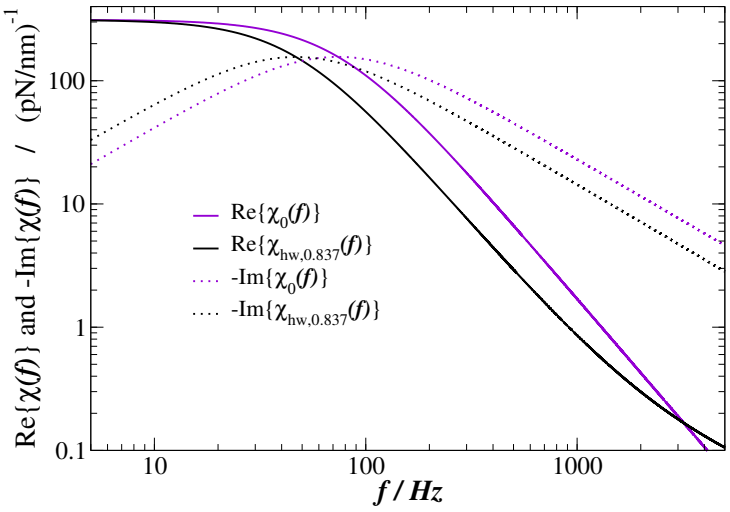

Figure 9.2: Analytically found response functions for a trapped bead, assuming simple Stokes friction, Eqs. (9.9) (violet lines), and at a distance $l = 615\,\mathrm{nm}$ to a hard wall, Eq. (9.10) (black lines). The real parts are indicated by full lines, the imaginary parts by dotted lines. The response functions are calculated for a trapped polystyrene bead of radius $R = 515\,\mathrm{nm}$ immersed in a viscous medium with viscosity $\eta = 0.0071\,\mathrm{Pa\,s}$. The stiffness of the optical trap is given by $\kappa = 0.0032\,\mathrm{pN/nm}$. The imaginary part is plotted with a negative sign in front, since it is always negative.

9.3 Numerical evaluation of the Kramers-Kronig relation

If the friction retardation spectrum $\tilde{\gamma}(\omega)$ is unknown, the response function $\chi(\omega)$ can not be obtained analytically like in Eq. (9.10). It has to be measured. The imaginary part $\chi''(\omega)$ is easily obtained from the FDT, Eq. (4.12). In passive microrheology approaches one uses the KKR to derive the real part from the imaginary part of the response function[3]. The numerical evaluation of the KKR involves *aliasing errors* due to the cut-off of the sine transform, however. That error has already been discussed by Buchanan et al. [45] and it will appear in each analysis of experimental data from a purely passive experiment[4].
A large aliasing error involves an unreliable determination of $\chi'(\omega)$ which gives unreliable values especially for the elastic part of the friction retardation spectrum, $\tilde{\gamma}''(\omega)$, see Eq. (9.2). Before working on the data, in this section I investigate the dependence of the aliasing error on the cut-off frequency for the special case of friction close to a hard wall. It will turn out that the aliasing error of both $\tilde{\gamma}'(\omega)$ and $\tilde{\gamma}''(\omega)$ is very large for a *low* cut-off frequency. For a *high* cut-off frequency, the relative error due to aliasing is very large only for $\tilde{\gamma}''(\omega)$.

The real part of the response function is determined from numerical evaluation of the KKR,

[3] See discussion on passive approaches in section 6.2 of [77].
[4] Purely passive experiments are experiments where only the Brownian motion of a particle trapped by optical tweezers is observed.

Eq. (4.9),

$$\mathrm{Re}\{\chi_{\mathrm{hw},R/l}(f_k)\}^{(\mathrm{num},f_{\max})} = -\frac{1}{\pi^2}\sum_{i=0}^{N_{\max}}\cos(2\pi f_k t_i)\Delta t \sum_{k'=0}^{N_{\max}}\chi''_{\mathrm{hw},R/l}(f_{k'})\sin(2\pi f_{k'} t_i)\Delta f, \quad (9.11)$$

whereby $\chi''_{\mathrm{hw},R/l}(\omega)$ from Eq. (9.10) (imaginary part) has been taken into account at the discrete frequencies $f_{k'} = \omega_{k'}/(2\pi)$, with $k' = 0, \ldots, N_{\max}$, so that the sine transform integration is cut-off at frequency $f_{\max}/2 = f_{N_{\max}}$ [5]. The cosine transform is taken over the same number of data points $N_{\max}$. The discrete frequencies have a spacing of $\Delta f = f_{\max}/(2N_{\max})$. Then the time spacing is given by $\Delta t = 1/f_{\max}$.

In this section, the dependence of the result of Eq. (9.11) on the cut-off frequency $f_{\max}/2$ will be examined[6]. In Fig. 9.3(a,b), the real and imaginary parts of the response function $\chi_{\mathrm{hw},0.837}(\omega)$ are plotted as full lines for a bead of radius $R = 515\,\mathrm{nm}$ which is situated only $l = 615\,\mathrm{nm}$ away from a hard wall[7]. The dashed and dotted lines in Fig. 9.3 have been obtained from numerical evaluation of the KKR, according to Eq. (9.11), for two different cut-off frequencies $f_{\max}/2$. Note that in Eq. (9.11), the *analytical* expression for $\chi''(f)$, Eq. (9.10) (imaginary part), has been used[8]. In Fig. 9.3 it can be seen that $\mathrm{Re}\{\chi_{\mathrm{hw},0.837}(\omega)\}^{(\mathrm{num},f_{\max})}$ exhibits *aliasing* due to the cut-off of the sine transform integral at the Nyquist frequency. This numerical error is much larger for the smaller cut-off frequency $f_{\max}/2 = 5\,\mathrm{kHz}$ than for the larger cut-off frequency $f_{\max}/2 = 320\,\mathrm{kHz}$.

Fig. 9.4 shows the corresponding results from extracting the friction retardation spectrum $\tilde{\gamma}_{\mathrm{hw},R/l}(\omega)$. From the response function obtained from evaluation of the KKR, one has with Eq. (9.2)

$$\tilde{\gamma}_{\mathrm{hw},R/l}(f_k)^{(\mathrm{num},f_{\max})} = \frac{[\chi'_{\mathrm{hw},R/l}(f_k)^{(\mathrm{num},f_{\max})} + \mathrm{i}\chi''_{\mathrm{hw},R/l}(f_k)]^{-1} - \kappa}{\mathrm{i}2\pi f_k}. \quad (9.12)$$

For the lower cut-off frequency $f_{\max}/2 = 5\,\mathrm{kHz}$ (dotted lines), both the real and the imaginary parts of $\tilde{\gamma}_{\mathrm{hw},R/l}(f_k)^{(\mathrm{num},f_{\max})}$ exhibit very large aliasing errors. For the higher cut-off frequency $f_{\max}/2 = 320\,\mathrm{kHz}$ (dashed lines), the aliasing error is small ($< 0.4\%\,\forall f_k$) for the real part $\mathrm{Re}\{\tilde{\gamma}_{\mathrm{hw},R/l}(f_k)^{(\mathrm{num},f_{\max})}\}$ (black), but still very large ($> 100\%$ for most frequencies) for the imaginary part $\mathrm{Im}\{\tilde{\gamma}_{\mathrm{hw},R/l}(f_k)^{(\mathrm{num},f_{\max})}\}$ (magenta). Note that the imaginary part itself is much smaller than the real part.

The results of this section indicate how large aliasing errors have to be expected for the evaluation of the experimental data in the next section. The experimental results, e.g. $\mathrm{Re}\{\chi_{\mathrm{hw},R/l}(f_k)\}^{(\mathrm{ex},f_{\max})}$, will not have to be compared with the analytical expressions, e.g. $\mathrm{Re}\{\chi_{\mathrm{hw},R/l}(f_k)\}$ (full lines in Figs. 9.3 and 9.4), but instead with the numerical expression, e.g. $\mathrm{Re}\{\chi_{\mathrm{hw},R/l}(f_k)\}^{(\mathrm{num},f_{\max})}$ (dotted/dashed lines in Figs. 9.3 and 9.4).

[5] At the evaluation of experimental data, $f_{\max}/2$ will be identified with the Nyquist frequency f_{Nyq}, while $f_{\max}$ will be identified with the sampling frequency f_{sample}.

[6] The cut-cut-off of the time integration at the cosine transform is irrelevant, since the sine transform decays rapidly, see Eq. (9.6).

[7] Since the distance l is taken from the bead center to the wall, the distance between bead surface and wall is then only 100 nm. One has $R/l = 0.837$.

[8] At the data evaluation $\chi''(f_k)$ will be obtained from the FDT. This would involve additional aliasing errors due to the Fourier transform performed for the calculation of the power spectrum. That error is *not* discussed in this section, but it will *additionally* show up in the experimental results.

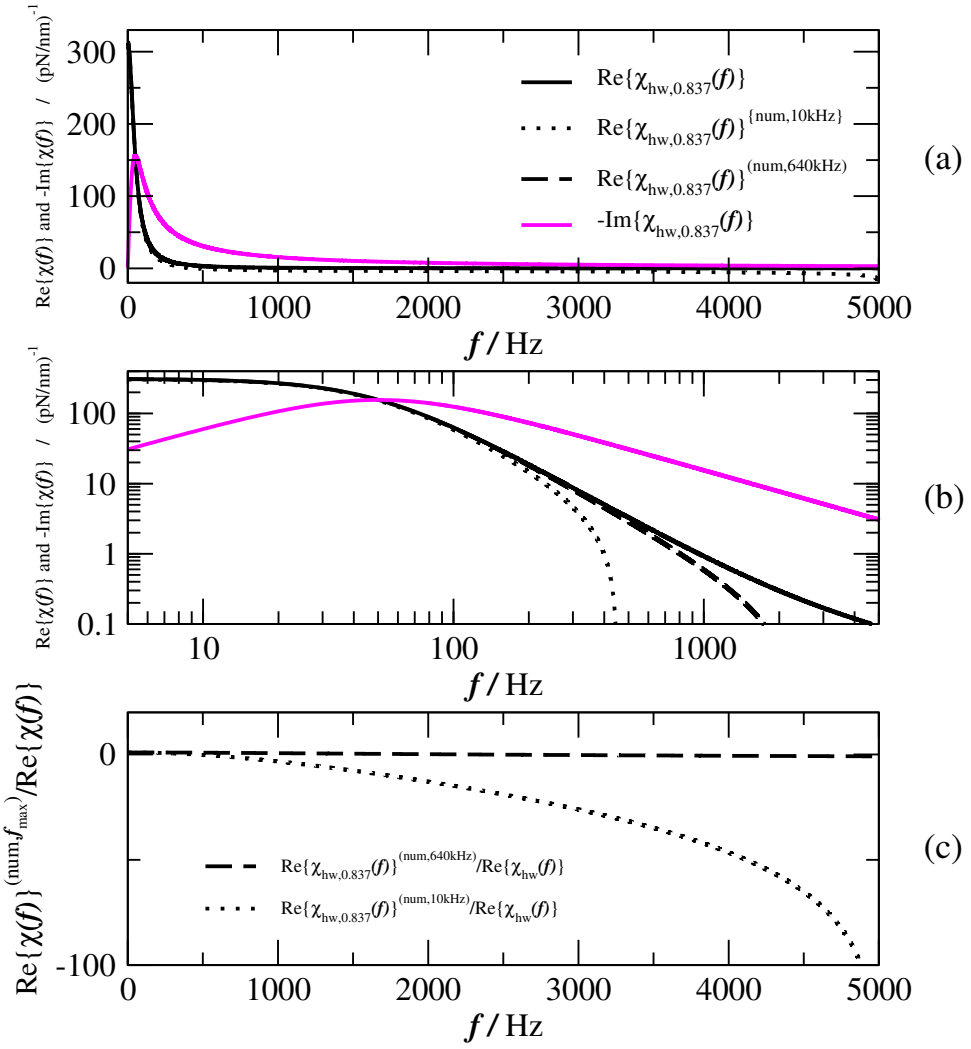

Figure 9.3: Response functions for a trapped bead close to a hard wall, analytical from Eq. (9.10) (solid lines) and by numerical evaluation of the Kramers-Kronig-relation, Eq. (9.11) for two different cut-off frequencies, $f_{\max}/2 = 5\,\mathrm{kHz}$ (dotted lines) and $f_{\max}/2 = 320\,\mathrm{kHz}$ (dashed lines).
The response functions are calculated for a trapped polystyrene bead of radius $R = 515\,\mathrm{nm}$ immersed in a viscous medium with viscosity $\eta = 0.0071\,\mathrm{Pa\,s}$ for a bead situated $l = 615\,\mathrm{nm}$ away from a hard wall in *lin-lin* (a) and *log-log* (b) representation. The stiffness of the optical trap is given by $\kappa = 0.0032\,\mathrm{pN/nm}$. The real part (black lines) and imaginary part (magenta lines) are shown in the plot. For high frequencies, $\mathrm{Re}\{\chi_{\mathrm{hw},0.837}(\omega)\}^{(\mathrm{num},f_{\max})}$ deviates from the analytical expression $\mathrm{Re}\{\chi_{\mathrm{hw},0.837}(\omega)\}$, due to the cut-off of the sine transform integral (aliasing). Note that the numerical curves become even negative for high frequencies. The ratio between $\mathrm{Re}\{\chi_{\mathrm{hw},0.837}(\omega)\}^{(\mathrm{num},f_{\max})}$ and $\mathrm{Re}\{\chi_{\mathrm{hw},0.837}(\omega)\}$ is plotted in panel (c). One can see that the aliasing error is much larger for the lower cut-off frequency $f_{\max}/2 = 5\,\mathrm{kHz}$. The figure indicates how large aliasing errors have to be expected at the data evaluation.

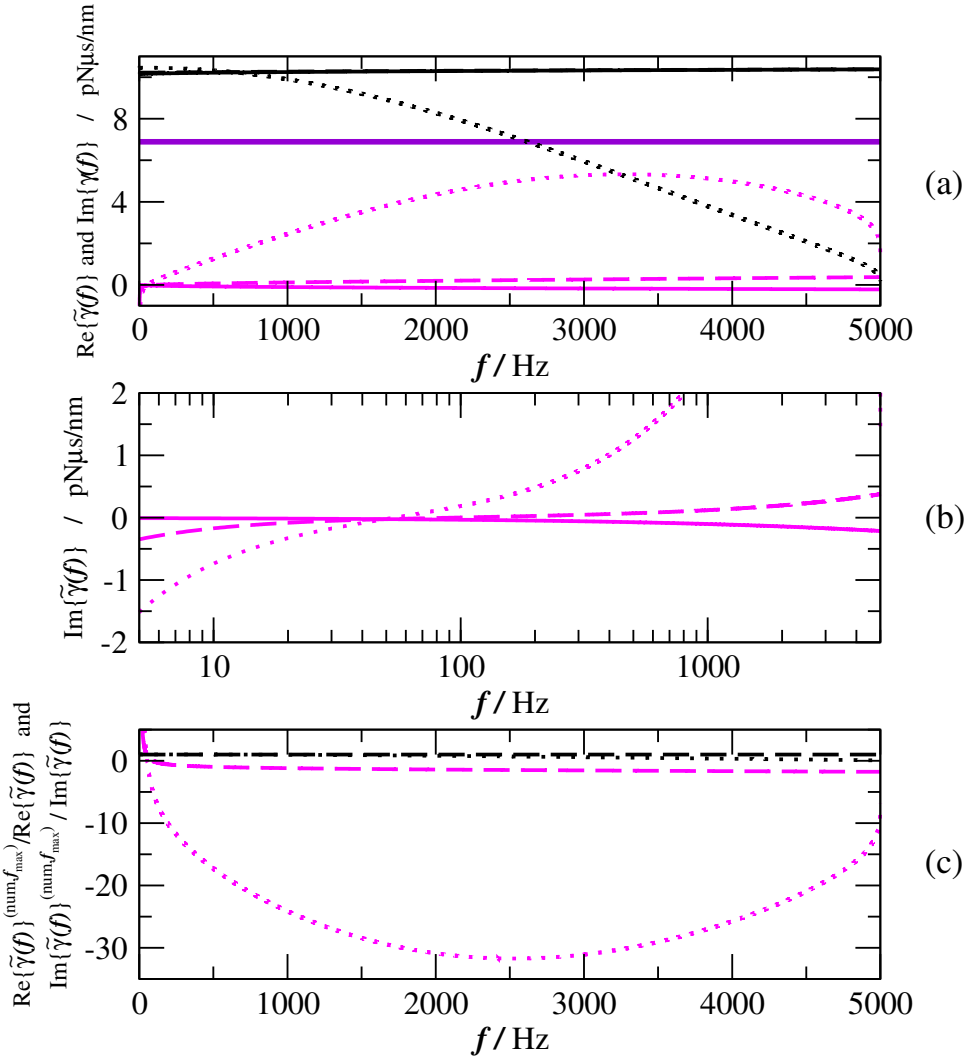

Figure 9.4: Friction retardation functions for a trapped bead close to a hard wall, analytical from Eq. (3.14) (solid lines) and by numerical evaluation of the Kramers-Kronig-relation, Eq. (9.11) and extraction of $\tilde{\gamma}_{\mathrm{hw},R/l}(f_K)^{(\mathrm{num},f_{\max})}$ with Eq. (9.12) for $R/l = 0.837$ and for two different cut-off frequencies $f_{\max}/2$. The full lines indicate the analytical curves γ_0 (violet), $\mathrm{Re}\{\tilde{\gamma}_{\mathrm{hw},R/l}(\omega)\}$ (black) and $\mathrm{Im}\{\tilde{\gamma}_{\mathrm{hw},R/l}(\omega)\}$ (magenta). $\mathrm{Re}\{\tilde{\gamma}_{\mathrm{hw},R/l}(f_k)^{(\mathrm{num},f_{\max})}\}$ is indicated by black lines, for $f_{\max}/2 = 5\,\mathrm{kHz}$ (dotted) and for $f_{\max}/2 = 320\,\mathrm{kHz}$ (dashed). $\mathrm{Im}\{\tilde{\gamma}_{\mathrm{hw},R/l}(f_k)^{(\mathrm{num},f_{\max})}\}$ is indicated by magenta lines, for $f_{\max}/2 = 5\,\mathrm{kHz}$ (dotted) and for $f_{\max}/2 = 320\,\mathrm{kHz}$ (dashed). Note that aliasing errors are much higher for $f_{\max}/2 = 5\,\mathrm{kHz}$ than for $f_{\max}/2 = 320\,\mathrm{kHz}$.

9.4 Evaluation of experimental data

The x-component of the experimental data shown in Fig. 9.1 has been analyzed for two time intervals which both have a length of $\sim 6\,\mathrm{s}$. Data set 1 covers the time interval $I_1 = [0\,\mathrm{s}, 6.03\,\mathrm{s}]$ when the bead was about $10\,\mu\mathrm{m}$ away from the phagocyte membrane. Data set 2 covers the time interval $I_2 = [42.21\,\mathrm{s}, 48.24\,\mathrm{s}]$ short before binding, when the bead was already very close to the membrane. The trap stiffness $\kappa = 0.0032\,\mathrm{pN/nm}$ is known from prior calibration.

9.4.1 Modification of data with low sampling frequency

In section 9.3 it was shown that the aliasing error on the real part of the response function obtained with the KKR becomes very high for low cut-off frequencies $f_{\mathrm{max}}/2$. In the experiment, the cut-off frequency corresponds to the Nyquist frequency of $f_{\mathrm{Nyq}} = f_{\mathrm{sample}}/2 = 5\,\mathrm{kHz}$. Since this frequency is very low, the data has to be modified in order to reduce the aliasing error. For that purpose, Buchanan et al. evaluated the KKR integral by assuming that the imaginary part of the response function continues to infinity with a slope of -1, i.e., as for a simple viscous liquid. From that continuation, the correction of the real part of the response function could be calculated, see Eq. (4) in Ref. [45].

This continuation approach for data modification introduces a point of discontinuity in the derivative of the imaginary part of the response function, however, since the slope changes to -1 at f_{Nyq}. Moreover, also the *imaginary part* of the response function exhibits aliasing at frequencies close to f_{Nyq} due to the numerical Fourier transform performed to obtain the power spectrum[9]. To obtain a more smooth behavior of $\mathrm{Im}\{\chi(\omega)\}$ and to avoid errors from aliasing of the power spectrum, I will use another technique which implements the continuation to higher frequencies already in the time domain, i.e., on the experimental data itself. This is the technique of *random walk interpolation* (RWI) which introduces simulated data points in between measured data points and therefore acts as "simulation supersampling", see Fig. 9.5. By RWI, an effective sampling frequency of $f_{\mathrm{sample,RWI}} = N_{\mathrm{I}} f_{\mathrm{sample}} = 640\,\mathrm{kHz}$ is obtained, with $N_{\mathrm{I}} - 1 = 63$ interpolated data points between two experimental data points. Hence aliasing due to the Fourier transform at the power spectrum calculation becomes irrelevant for frequencies up to $f_{\mathrm{Nyq}} = 5\,\mathrm{kHz}$. The convergence of the RWI method is demonstrated in Fig. 9.6. Further, aliasing due to the frequency cut-off of the KKR integral as described in section 9.3 is also "shifted" to higher frequencies, but remains still relevant, see dashed lines in Figs. 9.3 and 9.4. An additional error is introduced by the RWI method, however, since not all hydrodynamic interactions according to the model, Eq. (3.14), are taken into account and it is not clear if the model, Eq. (3.14), describes the high frequency motion at all.

[9] This aliasing error has not been discussed in section 9.3, but it is typically as high as $\sim 300\%$ at f_{Nyq}, if the data is not supersampled.

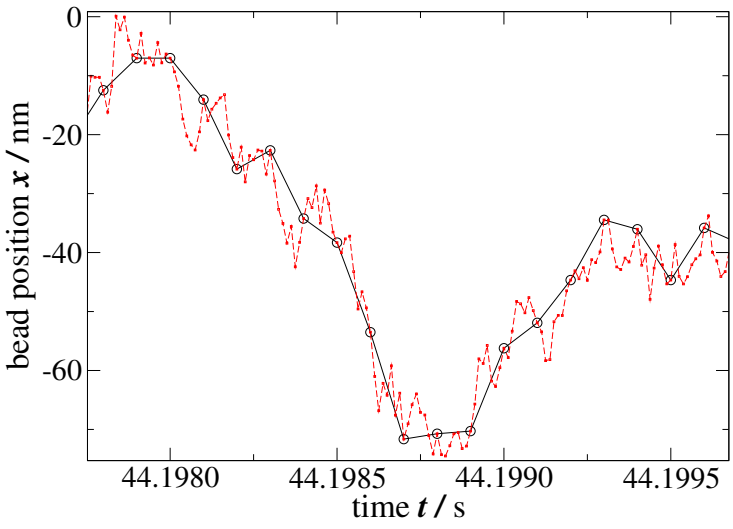

Figure 9.5: The technique of *random walk interpolation* (RWI). Between two data points (black circles) sampled in the experiment with low sampling frequency, $N_\mathrm{I}-1$ simulated data points (red squares) are placed, whereby $N_\mathrm{I}=2^n$ with an integer n. The simulated data points mimic a random walk in a harmonic trap. The parameters of that confined diffusion are temperature $\vartheta=37°$, trap stiffness $\kappa=0.0032\,\mathrm{pN/nm}$ and friction coefficient $\gamma=\gamma_0(1+9l/(16R))$ with $\gamma_0=6\pi\eta R=6.89\,\mathrm{pN}\mu\mathrm{s/nm}$. The viscosity $\eta=0.0071\,\mathrm{Pa\,s}$ and the distance to the wall l have been estimated from the experimental data. In the figure, random walk interpolation with $N_\mathrm{I}=8$ is shown. For the evaluation of the experimental data, a higher value of $N_\mathrm{I}=64$ has been used. One must keep in mind that the method of random walk interpolation introduces an error due to the neglecting of hydrodynamic interactions at the interpolated random walk.

9.4.2 Result for the response function

The imaginary part of the response function is obtained experimentally from the FDT,

$$\chi''^{(\mathrm{ex,f_{sample}})}(f_k)=-\frac{\pi f_k}{k_\mathrm{B}T}P^{(\mathrm{ex,f_{sample}})}(f_k), \tag{9.13}$$

whereby the experimental power spectrum $P^{(\mathrm{ex,f_{sample}})}(f_k)$ has been found by numerical Fourier transform of a time series of N data points, sampled with frequency f_sample. The imaginary part of the response function is inserted into the KKR

$$\mathrm{Re}\{\chi(f_k)\}^{(\mathrm{ex},f_\mathrm{sample})}=-\frac{1}{\pi^2}\sum_{i=0}^{N/2}\cos(2\pi f_k t_i)\Delta t\sum_{k'=0}^{N/2}\chi''^{(\mathrm{ex,f_{sample}})}(f_{k'})\sin(2\pi f_{k'}t_i)\Delta f, \tag{9.14}$$

whereby $\chi'^{(\mathrm{ex,f_{sample}})}(f_{k'})$ from Eq. (9.13) has been taken into account at the discrete frequencies $f_{k'}$, $k'=0,\ldots,N/2$, so that the sine transform integration is cut-off at frequency $f_\mathrm{sample}/2=f_{N/2}$. The cosine transform is taken over the same number of data points $N/2$. The discrete frequencies have a spacing of $\Delta f=f_\mathrm{sample}/N$. Then the time spacing is given by $\Delta t=1/f_\mathrm{sample}$. The results from the determination of the response function from the experimental data according to Eqs. (9.13) and (9.14) are shown in Fig. 9.7. It can be seen that for both data sets the negative

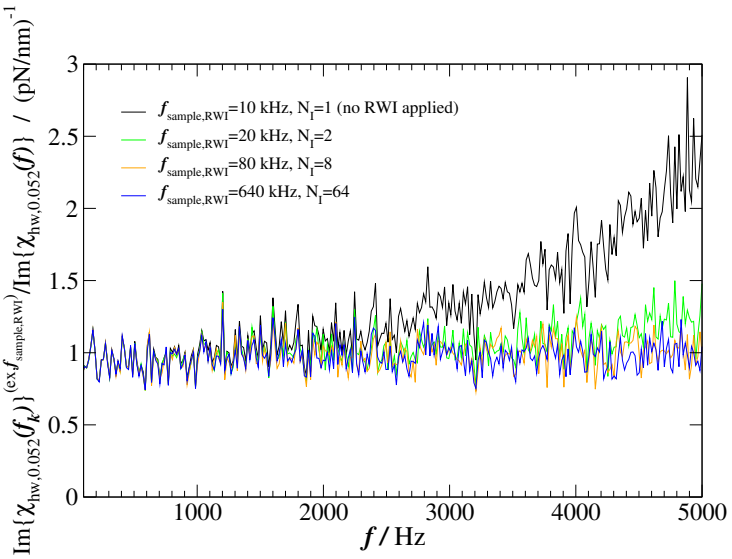

Figure 9.6: Demonstration of the convergence of the RWI method. Here it is shown for data set 1, how aliasing errors of the imaginary part of the response function decrease with increasing number of interpolated data points $N_\mathrm{I} - 1$. The imaginary part of the response function becomes more similar to the theoretical expression for a distance of $10\,\mu$m to a hard wall, if N_I is high. Hence the curves converge to $\mathrm{Im}\{\chi_{\mathrm{hw},0.052}(f_k)\}^{(\mathrm{ex},f_{\mathrm{sample,RWI}})}/\mathrm{Im}\{\chi_{\mathrm{hw},0.052}(f)\} = 1$. For data set 1, the bead was still located relatively far from the phagocyte membrane. Thus it can be assumed that the friction, which the bead feels is very similar to simple Stokes friction. Thus the error, which is introduced by the RWI method, can be expected to be small.

imaginary part (right side) $-\mathrm{Im}\{\chi(f_K)\}^{(\mathrm{ex},640\,\mathrm{kHz})}$ gives slightly too low values, compared to the analytical curves from the hard wall model $-\mathrm{Im}\{\chi_{\mathrm{hw,R/l}}(\omega)\}$ for certain values for R/l. For frequencies higher than a few hundred Hz, the real part (left side) $\mathrm{Re}\{\chi((f_K)\}^{(\mathrm{ex},640\,\mathrm{kHz})}$ deviates from the expected curve $\mathrm{Re}\{\chi_{\mathrm{hw,R/l}}((f_K)\}^{(\mathrm{num},640\,\mathrm{kHz})}$, however. Aliasing has been accounted for at the expected curve, and the deviation shows up in both data sets, i.e., far away and close to the membrane. Therefore, the deviation is most probable due to errors introduced by the RWI method.

9.4.3 Result for the friction retardation spectrum

The friction retardation spectrum can now be extracted from the response function found from the experimental data, according to the relation

$$\tilde{\gamma}(f_k)^{(\mathrm{ex},f_{\mathrm{sample}})} = \frac{[\chi'(f_k)^{(\mathrm{ex},f_{\mathrm{sample}})} + \mathrm{i}\chi''^{(\mathrm{ex},f_{\mathrm{sample}})}(f_k)]^{-1} - \kappa}{\mathrm{i}2\pi f_k}, \tag{9.15}$$

see Eq. (9.2). The result is shown in Fig. 9.8. It can be seen in Fig. 9.8(a) that the experimental results for the real part, $\mathrm{Re}\{\tilde{\gamma}(f_k)\}^{(\mathrm{ex},640\,\mathrm{kHz})}$, agrees well with the curve for the friction retardation spectrum from the hard wall model, $\mathrm{Re}\{\tilde{\gamma}_{\mathrm{hw},R/l}(\omega)\}$ for $R/l = 0.052\,\mu$m and $R/l = 0.912\,$nm for data set 1 (blue) and data set 2 (red), respectively. This indicates that in the considered

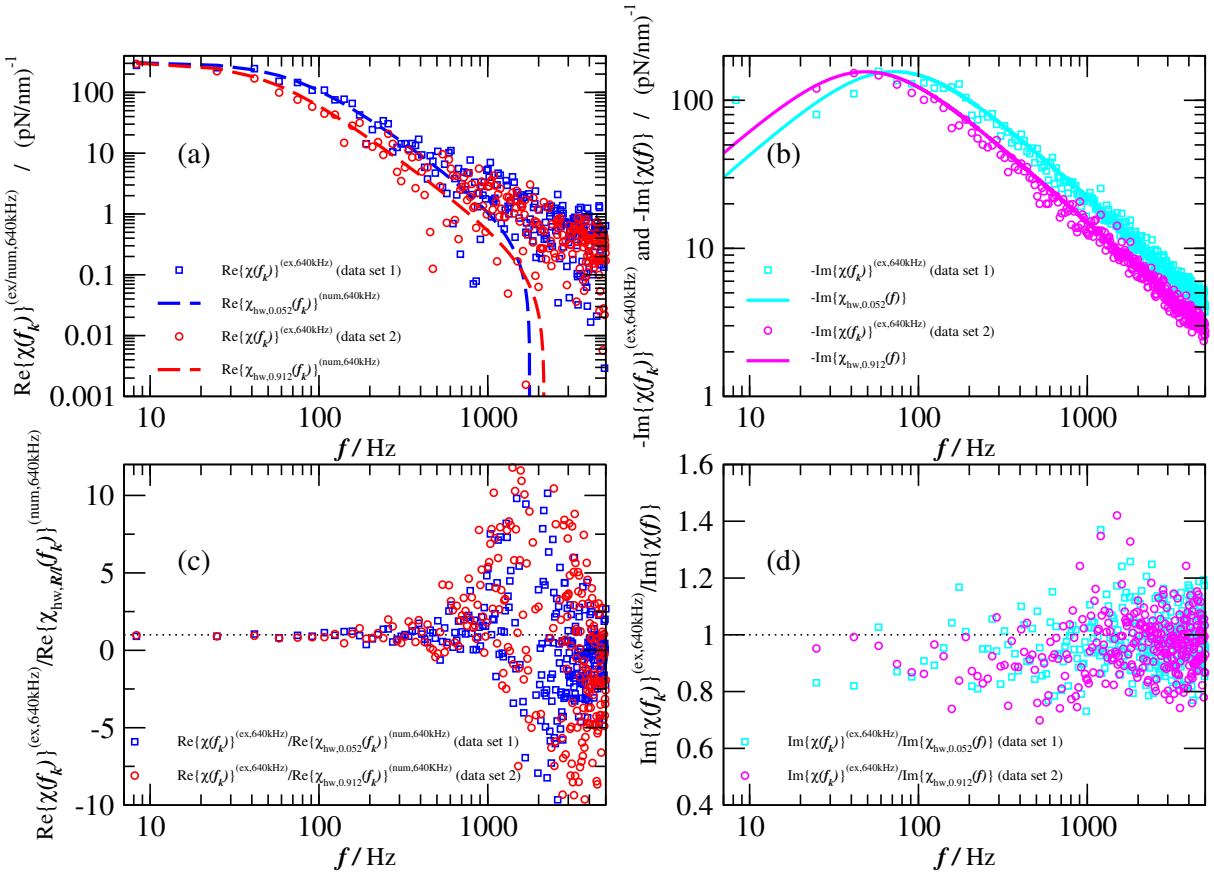

Figure 9.7: Response function obtained from the experimental data modified with the RWI method, the real part is shown on the left, the imaginary part on the right.
(a,b): Results for data set 1 (squares) are shown in blue/cyan color and are compared to the hard wall model with $R/l = 0.052$ (dashed line) which corresponds to a bead-membrane distance of $10\,\mu$m. Results for data set 2 (circles) are shown in red/magenta color and compared to the hard wall model with $R/l = 0.912$ (dashed line) which corresponds to a bead-membrane distance of 565 nm. The viscosity $\eta = 0.0071\,$Pa s which is another parameter in the hard wall model, has been estimated from the experimental data. (c,d): Corresponding data/theory scatter plots, in which the value 1 is indicated by a dotted line. *Left*: The real part obtained from the experimental data $\mathrm{Re}\{\chi(f_K)\}^{(\mathrm{ex,640\,kHz})}$ agrees only for frequencies up to $\sim 300\,$Hz with the expected curve $\mathrm{Re}\{\chi_{\mathrm{hw,R/l}}(f_K)\}^{(\mathrm{num,640\,kHz})}$. This is probably due to errors introduced by the RWI method. *Right*: The negative imaginary part obtained from the experimental data $-\mathrm{Im}\{\chi(f_K)\}^{(\mathrm{ex,640\,kHz})}$ seems to give slightly too low results for low frequencies.

frequency range $[0\,\mathrm{kHz}, 5\,\mathrm{kHz}]$ the viscous part of the friction force on the bead agrees with the hard wall model for distances of $l \sim 10\,\mu$m for data set 1 and $l \sim 565\,$nm for data set 2. Note that the value of $l \sim 565\,$nm corresponds to a separation of only 50 nm between bead surface and membrane. For the imaginary part of the friction retardation function which describes elastic interactions, the interpretation of the results is more difficult. The expected numerical curves $\mathrm{Im}\{\tilde{\gamma}_{\mathrm{hw},0.052}(f_k)\}^{(\mathrm{num,640\,kHz})}$ and $\mathrm{Im}\{\tilde{\gamma}_{\mathrm{hw},0.912}(f_k)\}^{(\mathrm{num,640\,kHz})}$ from Eq. (9.12) lie closely together compared to the spread of the data points. For both data sets, the data points tend to

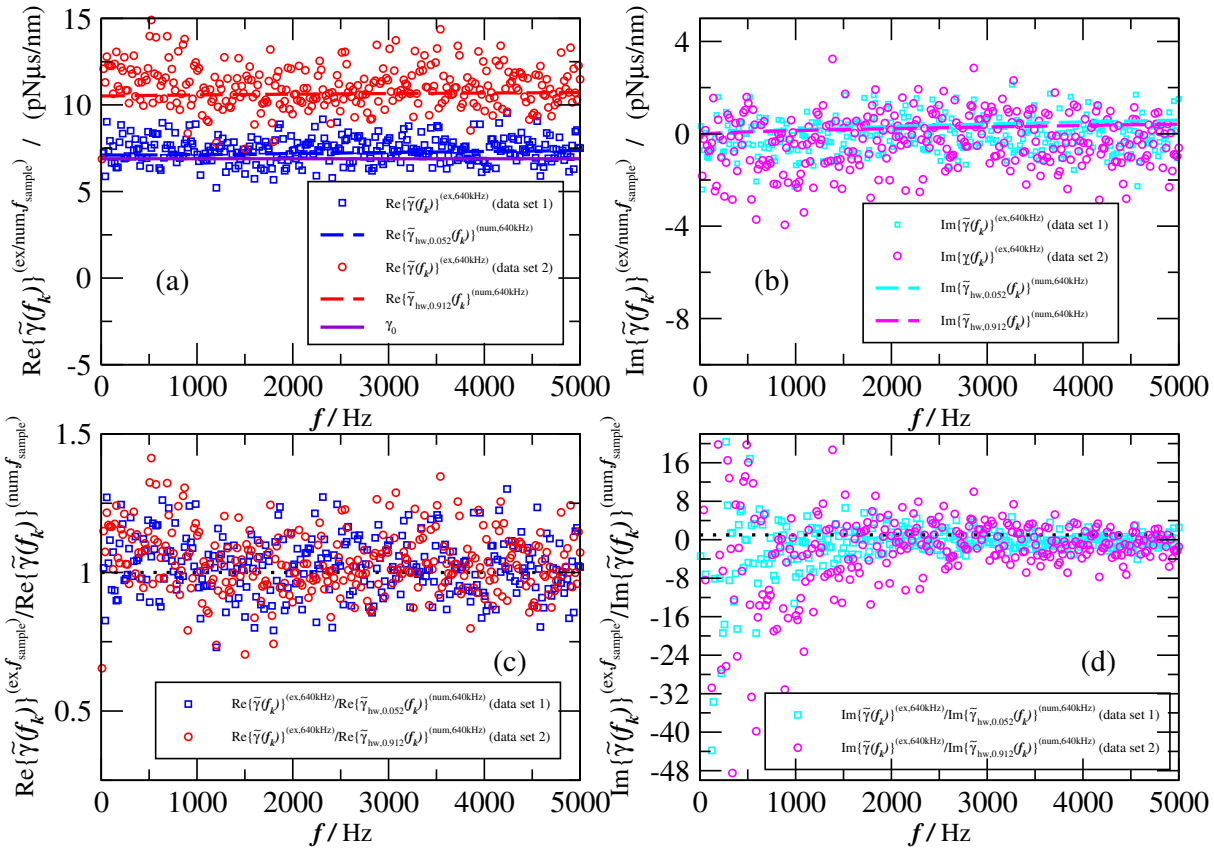

Figure 9.8: Friction retardation spectrum obtained from the experimental data modified with the RWI method, the real part is shown on the left, the imaginary part on the right.
(a,b): Results for data set 1 (squares) are shown in blue/cyan color and are compared to the hard wall model with $R/l = 0.052$ (dashed line) which corresponds to a bead-membrane distance of $10\,\mu$m. Results for data set 2 (circles) are shown in red/magenta color and compared to the hard wall model with $R/l = 0.912$ (dashed line) which corresponds to a bead-membrane distance of 565 nm. In (a) the friction coefficient γ_0 is indicated by a violet line. (c,d): Corresponding data/Theory scatter plots, in which the value 1 is indicated by a dotted line.
Left: The real part from the experimental data $\mathrm{Re}\{\tilde{\gamma}(f_k)\}^{(\mathrm{ex},640\,\mathrm{kHz})}$ agrees well with the hard wall model for distances of $l = 10\,\mu$m (data set 1, blue) and $l = 565\,$nm (data set 2, red). *Right*: For the imaginary part the expected curves from Eq. (9.12) (dashed lines) lie closely together for the two different distances l, compared to the spread of the data. Further, the data points tend to lie below the expected curves.

lie below the expected curves. As for the imaginary part of the response function, see Fig. 9.7, the reason for that are probably errors introduced by the RWI method.

9.5 Discussion

The final result of this investigation is that the obtained real part of the friction retardation spectrum, $\mathrm{Re}\{\tilde{\gamma}(f_k)\}^{(\mathrm{ex},f_{\mathrm{sample}})}$, which gives the *viscous part of the friction force* exerted on the trapped bead in the proximity of the phagocyte membrane is consistent with the hard wall model. The imaginary part of the friction retardation spectrum from the hard wall model, $\mathrm{Im}\{\tilde{\gamma}_{\mathrm{hw},R/l}(\omega)\}$, which gives the *elastic part of the friction force*, is small compared to the real part, see Fig. 9.4(a) (magenta and black solid lines). If obtained from numerical evaluation of the Kramers-Kronig relation, it has a large aliasing error, even at a high sampling frequency, see Fig. 9.4 (magenta dashed lines). The experimental result $\mathrm{Im}\{\tilde{\gamma}(f_k)\}^{(\mathrm{ex},f_{\mathrm{sample}})}$ additionally exhibits large statistical errors, see Fig. 9.8(d). The conclusion from that is that no clear statement can be made about the elastic contribution from the given data and with the applied microrheology method. This involves that no statement about a deviation of the elastic part from the hard wall model can be made.

For this investigation, data has been evaluated which was available from an experiment which had another main goal than examining the friction felt by the bead close to the cell membrane. Only short time series could be evaluated which resulted in a high statistical error. Systematic errors due to piezo stage motion in this experiment have been neglected in the data evaluation, but could have influenced the results. Furthermore, the distance l between bead and membrane was not kept constant during the evaluated time intervals, which gives another error source.

As data evaluation method, the passive microrheology approach established by Schnurr, Gittes et al has been applied. It employs the Kramers-Kronig relation to determine the elastic (real) part from the measured viscous (imaginary) part of the response function. One problem about that approach is that it involves aliasing errors of the elastic part of the friction retardation spectrum, $\mathrm{Im}\{\tilde{\gamma}(\omega)\}$ due to the cut-off of the sine transform integral which can be of same order or larger than $\mathrm{Im}\{\tilde{\gamma}(\omega)\}$. That problem is especially severe for media in which the elastic contribution is small compared to the viscous contribution, as it has been the case in this investigation. The aliasing error is still high for data taken with high sampling frequencies. Supersampling of data by simulations as applied here or continuation of $\chi''(\omega)$ as done by Buchanan et al. suppresses aliasing but introduces new errors which are difficult to assess.

Another problem of the passive microrheology approach is that it "mixes frequencies" through the determination of $\chi'(\omega)$ by the Kramers Kronig relation. In principle, $\chi'(\omega)$ depends on the power spectrum $P(\zeta)$ at all frequencies ζ. Experimental data usually exhibits errors in certain frequency ranges, e.g., drift at low frequencies of order 1 Hz. These errors which are local in the frequency domain at $P(\zeta)$ are outspread to other frequencies at $\chi'(\omega)$.

An approach to determine $\tilde{\gamma}(\omega)$ without these shortcomings is given by the novel combined optical tweezers calibration and microrheology method presented in chapter 6. This method involves an additional active measurement, where the stage or laser position is oscillated. For the investigation of the elastic contribution of the friction force close to a cell membrane, I suggest to perform new measurements according to this method, with high sampling frequency and with measuring times in the order of 100 s for both the passive and the active part of the experiment. A challenge at the experimental implementation of such an experiment would be the realization of sinusoidal bead motion which happens in a plane which is *parallel* to the membrane plane.

10 Networks of semiflexible solymers

10.1 Introduction

The complex phenomenon of viscoelasticity introduced in section 2.2 is exhibited by many biopolymers. Experimental investigations of viscoelastic properties are performed by rheology techniques as optical tweezers microrheology, which has been portrayed in section 2.3 and applied in chapter 9 of this thesis. Further, the novel calibration method introduced in chapter 6 includes a methodological contribution to the technique of optical tweezers microrheology.
Theoretical studies on viscoelasticity on the other hand are performed by both modelling and simulation approaches. In this chapter a simulation study on the microscopic origin of viscoelasticity is presented, which has been performed under supervision of Dr. Jan Kierfeld during my 3 months abroad project at the Max Planck Institute of Colloids and Interfaces in Golm (Germany) in 2005/2006. In this investigation the mechanical behavior of a network of crosslinked semiflexible filaments has been studied by Monte-Carlo Simulations. For simulating the individual filaments I have used the semiflexible harmonic chain (SHC) model published by Dr. Kierfeld before [78]. In the simulations, the thermally fluctuating network was exposed to shear stress in a way that imitates a macrorheological experiment with a twin plate shear cell. We have determined global and local bending energies of the sheared network and we have observed how the network architecture changes with varying shear angle.

After introducing semiflexible polymers in section 10.2, the SHC model will be presented in section 10.3. In section 10.4 a short review of research on semiflexible polymer networks will be given. The Monte-Carlo simulation technique is explained in section 10.5 and in section 10.6 simulation results from two example networks are presented. A discussion is given in section 10.7.

10.2 Semiflexible polymers

A *polymer* is a substance composed of large molecules composed of repeating structural units, or monomers, connected by covalent chemical bonds. Well known examples of polymers include plastics and DNA. Polymers typically exhibit *viscoelasticity*, a phenomena introduced in section 2.2. In the following I will shortly introduce some basic terms and models of polymer theory. A comprehensive account of the theory for the dynamical properties of polymer solutions is given for example in the book of Doi and Edwards [79].

An *ideal chain* or *freely-jointed chain* is the simplest model to describe a polymer. It assumes a polymer as a random walk and neglects any kind of interactions among monomers. Although it is simple, its generality gives some insights about the physics of polymers.

The *Kratky-Porod* or *worm-like chain* (WLC) model is used to describe stiffer polymers. The WLC model envisions an inextensible isotropic rod that is continuously flexible. It can be shown

that the mean square end-to-end distance of a polymer chain with *contour length* L is given by

$$\langle [\mathbf{r}(L) - \mathbf{r}(0)]^2 \rangle = 2L_{\mathrm{P}} L \left\{ 1 - \frac{L_{\mathrm{P}}}{L} \left[1 - \exp(-L/L_{\mathrm{P}}) \right] \right\}, \tag{10.1}$$

where L_{P} is called the polymer's *persistence length* which describes the stiffness of the filament. While for stiff filaments the persistence length is much larger than the contour length, $L_{\mathrm{P}} \gg L$, it is much smaller than the contour length for flexible filaments, $L_{\mathrm{P}} \ll L$. For *semiflexible filaments*, the persistence length is on the same order like the contour length, $L_{\mathrm{P}} \sim L$. Many bio-polymers consist of semi-flexible filaments.

The worm-like chain model has been successfully applied to single-molecule stretching experiments in order to interpret force-extension relations for polymer chains like DNA, titin or actin filaments, see, e.g., the references given in [78]. In many of these experiments performed with atomic force microscopy or optical tweezers, the force-extension relation obtained by Marko and Siggia for the wormlike chain has been used to interpret the results. The main characteristic of this relation for an inextensible worm-like chain of contour length L is an end-to-end extension L_f in the direction of the stretching force $\mathbf{f}$ that is saturating as $1 - L_f/L \propto 1/\sqrt{f}$ for large stretching forces $f = |\mathbf{f}|$ [80].

In the limit of large stretching forces, the extensibility of the chain due to stretchable bonds has to be taken into account, however. This means that the result of Marko and Siggia for the overall relative extension L_f/L has to be corrected by an additional term which contains the stretching modulus k of the polymer.

10.3 The semiflexible harmonic chain (SHC) model

A discrete description of extensible semiflexible polymers is given by the *semiflexible harmonic chain* (SHC) model established by Kierfeld et al. For that model, force-extension relations have been analytically obtained for strong and weak stretching regimes which include the effect of extensible bonds, discrete chain structure, and finite polymer length [78].

In the SHC model, a semiflexible filament can be modeled by a discrete chain of N bonds of length b_0 with directions described by tangent vectors $\mathbf{t}(n)$ with $|\mathbf{t}(n)| = 1$ that are indexed by the integer bond number $n = 1, \ldots, N$, see Fig. 10.1. The contour length of the polymer is $L = Nb_0$. The bonds can represent either actual chemical bonds in a polymer or larger segments of a filament, for example a helical repeat unit in F-actin. The bonds or segments can be tilted against each other and eventually stretched. The bond vectors connect $N + 1$ "beads" indexed by the integer bead number $i = 0, \ldots, N$ at positions $\mathbf{r}(i) = \mathbf{r}(0) + \sum_{n=1}^{i} b_0 \mathbf{t}(n)$, where $\mathbf{r}(0)$ is the position of the bead at the fixed end of the polymer.

In order to describe an *extensible* semiflexible chain, harmonic bonds of variable length $b(n)$ are introduced with a stretching energy

$$E_{\mathrm{s}} = \sum_{n=1}^{N} \frac{k(n)}{2} (b(n) - b_0)^2 = \sum_{n=1}^{N} \frac{k(n) b_0^2}{2} \Delta^2(n). \tag{10.2}$$

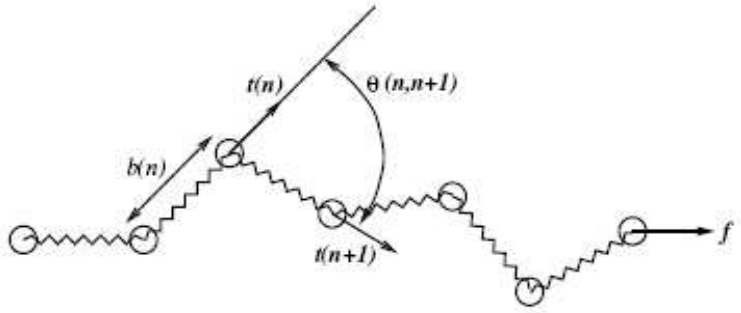

Figure 10.1: The semiflexible harmonic chain (SHC) model. $\mathbf{t}(n)$ are bond directions with $|\mathbf{t}(n)| = 1$, $b(n)$ the bond lengths, and $\mathbf{f}$ the external force applied to one end of the filament. The other end is fixed. (Graph taken from Kierfeld et al., *The European Physical Journal E*, 2004, Ref. [78])

Each bond has the equilibrium length b_0 and

$$\Delta(n) \equiv (b(n) - b_0)/b_0 \tag{10.3}$$

are the relative bond extensions. The bonds act as harmonic elastic springs characterized by bond stretching moduli $k(n)$ which are allowed to depend on the bond index n to model spatial heterogeneity.

For an extensible chain, the work done by the external force $\mathbf{f}$ applied to one end $\mathbf{r}(N)$ of the chain with the other end fixed is

$$E_f = -\mathbf{f} \cdot (\mathbf{r}(N) - \mathbf{r}(0)) = -\sum_{n=1}^{N} b_0(1 + \Delta(n))\mathbf{f} \cdot \mathbf{t}(n). \tag{10.4}$$

In a semiflexible chain, the tilting of neighbouring bonds costs a bending energy

$$\begin{aligned} E_\mathrm{b} &= \sum_{n=1}^{N-1} \frac{\kappa}{2b_0}(\mathbf{t}(n+1) - \mathbf{t}(n))^2 \\ &= \sum_{n=1}^{N-1} \frac{\kappa}{b_0}(1 - \cos\theta(n, n+1)) \end{aligned} \tag{10.5}$$

which only depends on the angles $\theta(n, n+1) = \arccos(\mathbf{t}(n) \cdot \mathbf{t}(n+1))$ enclosed by unit tangent vectors, see Fig. 10.1, and one material parameter, the bending rigidity κ. The sum of bending and stretching energies, Eqs. (10.5) and (10.2), together with the work, Eq. (10.4), of the external force gives the Hamiltonian for the discrete *semiflexible harmonic chain*,

$$\begin{aligned} &\mathcal{H}\{\mathbf{t}(n), \Delta(n)\} = E_\mathrm{b} + E_\mathrm{s} + E_f \\ &= \sum_{n=1}^{N-1} \frac{\kappa}{2b_0}(\mathbf{t}(n+1) - \mathbf{t}(n))^2 + \sum_{n=1}^{N} \frac{k(n)b_0^2}{2}\Delta^2(n) - \sum_{n=1}^{N} b_0(1 + \Delta(n))\mathbf{f} \cdot \mathbf{t}(n). \end{aligned} \tag{10.6}$$

From the Hamiltonian, Eq. (10.6), force-extension relations have been found in [78] for strong and weak stretching regimes. Therefore, the dependence of the free energy $F(f) = -T \ln Z(f)$ on the force $f = |\mathbf{f}|$ has been used together with the thermodynamic relation

$$L_f = \left\langle (\mathbf{r}(L) - \mathbf{r}(0)) \cdot \frac{\mathbf{f}}{f} \right\rangle = -\partial_f F(f). \tag{10.7}$$

10.4 Semiflexible networks

The understanding of properties of individual semiflexible filaments is today quite highly developed. If solutions of semiflexible biopolymers such as F-actin contain cross-linked or sterically entangled filaments, they form *semiflexible networks*. The remaining problem of understanding the rheology of the biologically important semiflexible networks, has proved quite subtle, however.

In 1995 MacKintosh et al. proposed a mechanism for the elasticity of semiflexible networks which is entropic in its origin and closely related to rubber elasticity [81]. The non-linear force-extension relation of that model has been successfully applied by Storm et al. in biological gels to describe *strain-stiffening* [82]. Strain stiffening is an important mechanical property of biological materials which prevents large deformations that could threaten tissue integrity. In another model the plateau modulus G^0 has been derived from the force-extension relation of the wormlike chain and also transverse filament fluctuations and buckling have been taken into account [83]. In the analytical approaches [81, 83], the deformation of the network has been assumed to be *affine*, however, which means that the strain distribution is homogeneous over the entire network.

Also numerical methods have been applied to investigate polymer networks. Wilhelm and Frey [84], Head et al. [85–87], Onck et al. [88] and DiDonna and Levine [89,90] applied two-dimensional discrete mechanical models for crosslinked networks to calculate the viscoelastic moduli of the networks. In semiflexible networks, Head et al. and Onck et al. found at large strains *non-affine* network deformations in semiflexible networks, i.e., the network re-arranges its architecture under a large shear strain in a non-trivial way, i.e., not in each point aligned with the shear deformation of the simulation box. This result indicates that beyond the non-linear elasticity of the individual filaments, non-affine network deformations represent another mechanism of strain stiffening. Some crosslinker proteins like the F-actin cross-linker filamin exhibit domain unfolding under applied tension. Didonna and Levine took that effect of domain unfolding additionally into account in their simulations [89,90]. They found viscoelastic behavior which reminds on the soft glassy rheology observed in the cytoplasm.

All numerical work mentioned in the last paragraph is based on purely mechanical models and energy minimization. In effect, these models consider zero-temperature systems in which filament undulations do not exist and consequently free energies can not be determined. This means that the effect of entropy on the network elasticity which is essential for rubber elasticity of flexible polymers, can not be taken into account. However, for networks made of flexible polymers the effect of entropy has been included by another numerical approach, which is Monte Carlo simulations [91, 92]. In the following I will present a Monte Carlo Simulation of a semiflexible network under shear stress.

10.5 Monte Carlo simulation approach

In this section the Monte Carlo approach is presented which has been applied to the simulation of rheological experiments on a semiflexible polymer network. At the Monte Carlo simulation, the thermal motion of the polymer network and its deformation due to externally applied shear forces have been simulated. Global and local energies are determined at the sheared network and the change of network architecture under shear can be observed. From the results, conclusions on the microscopic origin of the observed mechanical behavior can be drawn.

For performing Monte Carlo simulations of filament networks, a model is needed which describes the individual filaments. The model used here is the semiflexible harmonic chain (SHC) which has been introduced in section 10.3. In this section, the simulation of the thermal motion of the SHC filaments by means of the famous Metropolis is presented (paragraph 10.5.1). Further, in paragraph 10.5.2 the construction of a random network from many filaments is described. The application of a shear deformation and the measurement of energies at the sheared network are explained in paragraphs 10.5.3 and 10.5.4.

10.5.1 Simulation of the thermal motion of a single SHC filament

The discrete SHC consists of $N+1$ "beads" connected by N bonds. The thermal motion of the chain is simulated by displacing a randomly chosen bead i *by way of trial* from its original position $\mathbf{r}(i)$ to position $\mathbf{r}'(i)$ which lies within a small quadratic box around $\mathbf{r}(i)$. The internal energy $U(\{\mathbf{r}(i)\})$ of the system which is given through the Hamiltonian, Eq. (10.6), would then be changed to $U(\{\mathbf{r}'(i)\})$.

The probability of the system to be in some state is according to Boltzmann statistics proportional to

$$\mathcal{P}(\{\mathbf{r}(i)\}) \propto \exp\left\{-\frac{U(\{\mathbf{r}(i)\})}{k_{\mathrm{B}}T}\right\}, \tag{10.8}$$

with the internal energy $U(\{\mathbf{r}(i)\})$ of the system in state $\{\mathbf{r}(i)\}$. From the Boltzmann statistics, Eq. (10.8), an *acceptance criterion* for the trial displacement is formulated which decides on whether the bead i stays at position $\mathbf{r}(i)$ or whether it is moved to $\mathbf{r}'(i)$. For the acceptance criterion the ratio p between the probability of the trial state $\{\mathbf{r}(i)'\} = \{\mathbf{r}(0),\ldots,\mathbf{r}(i-1),\mathbf{r}'(i),\mathbf{r}(i+1),\ldots,\mathbf{r}(n)\}$ and the probability of the original state $\{\mathbf{r}(i)\} = \{\mathbf{r}(0),\ldots,\mathbf{r}(i-1),\mathbf{r}(i),\mathbf{r}(i+1),\ldots,\mathbf{r}(n)\}$ is used,

$$p = \frac{\mathcal{P}(\{\mathbf{r}'(i)\})}{\mathcal{P}(\{\mathbf{r}(i)\})} = \exp\left\{-\frac{U(\{\mathbf{r}'(i)\}) - U(\{\mathbf{r}(i)\})}{k_{\mathrm{B}}T}\right\}. \tag{10.9}$$

A very high value of $U(\{\mathbf{r}'(i)\})$ will then lead to a small p whereas a small $U(\{\mathbf{r}'(i)\})$ will lead to a high p. The acceptance criterion imposes automatic acceptance if $p > 1$ (going downhill in energy), otherwise, acceptance if a random number r between 0 and 1 happens to be smaller than p. This acceptance criterion guarantees that the system stays in equilibrium[1].

[1] The acceptance criterion ensures that the condition of detailed balance is fulfilled which guarantees equilibrium.

Repeating such displacement trials a large number of times forms the *Metropolis algorithm* which generates a *Markov chain*[2] of systems which mimics the thermal fluctuations of the entire filament. Any average quantity thus sampled is then, by construction, the statistical average that is sought

$$\langle A \rangle = \frac{\sum_k A_k}{N_\mathrm{s}}, \tag{10.10}$$

where A_k is the value of A at system k of the Markov chain, and N_s is the large total number of systems simulated[3].

10.5.2 Construction of a random network

N_P polymer chains described by the SHC model with equal bond number N and bond length b_0 are placed in two-dimensional quadratic box with area $A = L_\mathrm{box}^2$, see Fig. 10.2. The box has periodic boundary conditions on its horizontal and vertical boundaries, so that the space in which the polymer chains are placed can be imagined as being the surface of a torus. The position of bead number i of polymer chain j is indicated by $\mathbf{r}(i,j)$.

The system is then *thermalized* by applying a large number of Monte-Carlo steps as described in the previous paragraph on all chains. During the thermalisation, polymer chains diffuse freely[4] in the box and across its periodic boundary conditions and after a while the distribution of filament positions and orientations is completely random. To accelerate the randomization process, also other another kind of Monte Carlo trials is used[5].

After thermalisation, the filaments are *crosslinked*. This is done by distributing a chosen number of crosslinks N_x over the network in the following way: All pairs of two beads from different chains, i.e., the pairs $((i,j);(i',j'))$ with $j \neq j'$, are considered, and the distances $|\mathbf{r}(i,j) - \mathbf{r}(i',j')|$ between the beads of each pair are determined. Those N_x pairs with the smallest distances $|\mathbf{r}(i,j) - \mathbf{r}(i',j')|$ are now crosslinked, by shifting both bead positions of each chosen pair to the midpoint between the two original positions,

$$\mathbf{x}\left((i,j);(i',j')\right) = \frac{\mathbf{r}(i,j) - \mathbf{r}(i',j')}{2}. \tag{10.11}$$

where $\mathbf{x}\left((i,j);(i',j')\right)$ indicates the position of the constructed crosslink $((i,j);(i',j'))$. All crosslinks are *permanent*, i.e., both beads (i,j) and (i',j') can only move *as one* from now on. This involves that both beads are displaced simultaneously under a trial step and the acceptance criterion stated below Eq. (10.9) must then impose acceptance for both deflections in order to move the crosslink to a new position.

[2] A Markov chain is a "memoryless" chain of states: no given state has any causal connection with a previous state. To ensure that "memorylessness", the Metropolis algorithm runs between two systems k of the generated Markov chain with a number of N_sw *sweeps* through the entire system, i.e., each bead is tried to be displaced in average N_sw times.

[3] The Markov chain system index k is similar to a time, but it is not clear how to relate k to a real time scale. In general, Monte Carlo simulations can not yield information about time scales.

[4] Free diffusion involves that the polymers do not interact with each other.

[5] Since thermalisation would take a very long time, if only single beads would be replaced, also "kink moves" have been allowed, at which the entire filament is bend around one bead.

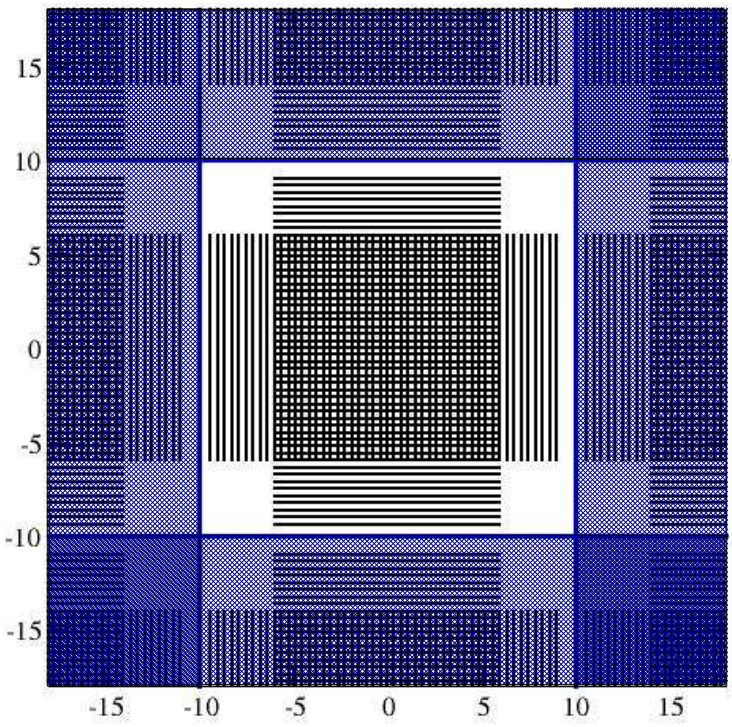

Figure 10.2: Initial placement of N straight filaments (black lines) in a periodic box with side length $L_{\mathrm{box}} = 20$. The margins of the box are indicated by solid blue lines. The periodic continuations of the original volume are indicated by blue shaded areas. The shown initial state is this one of example network 1 of section 10.6.

In this way a *random crosslinked network* has been generated which performs fluctuations in thermal equilibrium. Any local quantity $A(i,j)$, i.e. a quantity which characterizes A at bond i of chain j, can then be averaged over the network

$$\bar{A} = \frac{\sum_{i,j} A(i,j)}{N N_{\mathrm{P}}}. \tag{10.12}$$

10.5.3 Shear deformations

To simulate a rheology experiment with a twin plate shear cell, a shear deformation respecting the periodic boundary conditions is enforced by demanding that corresponding points on the left and right boundary of the simulation cell undergo equal displacement while the displacements of the corresponding points on the upper and lower boundary of the cell must agree vertically but differ horizontally by a distance ΓL where Γ is the shear angle. Shear angles of $\Gamma = 0.16, 0.31, 0.47, 0.63$ (in radian) have been imposed, corresponding to $\Gamma = 9.2°, 17.8°, 26.9°, 36.1°$ (in degree).

10.5.4 Energy and bond length measurements

According to Eq. (10.12), the stretching and bending energies and bond lengths per bead at a given Markov chain state k and at a given shear angle Γ, averaged over the entire network, $\bar{\epsilon}_{\mathrm{s},k}(\Gamma)$, $\bar{\epsilon}_{\mathrm{b},k}(\Gamma)$ and $\bar{b}_k(\Gamma)$, are determined by summing up the results of Eqs. (10.2) and (10.5) over all N_{P} chains of the network[6] and then dividing the result by $N N_{\mathrm{P}}$, see Figs. 10.4 and 10.8. The *thermal averages* of the stretching and bending energies are then obtained according to Eq. (10.10) by summing up $\bar{\epsilon}_{\mathrm{s},k}(\Gamma)$ and $\bar{\epsilon}_{\mathrm{b},k}(\Gamma)$ over a large number N_{s} of Markov chain states k and dividing by N_{s}. This yields $\langle \bar{\epsilon}_{\mathrm{s/b}}(\Gamma) \rangle$, see Figs. 10.5 and 10.9. Note that after the shear deformation has been enforced, one may only start the summation over the Markov chain states k after some "thermalisation time", since measurements have to be performed at equilibrium systems.

Similarly, the thermal averages have been calculated not as averages over all beads and chains, but *for each bead i on each chain j individually.* One obtains $\langle \epsilon_{\mathrm{s/b}}(i,j;\Gamma) \rangle$ which enables recognition of spatially inhomogeneous distributions of bending and stretching energies, see Figs. 10.6 and 10.10.

10.6 Results

In this section, simulation results from two differently behaving random networks are presented. The parameters of these two example networks are given in table 10.1. At both example networks, the bond stretching modulus K is much higher than the bending rigidity κ as it is the case for semiflexible biopolymers like F-actin. The parameters of the two simulated example networks are similar, but due to the different architecture of the networks, different behaviour is observed.

[6] The bar symbol " $\bar{}$ " indicates averaging over all beads on all chains.

Table 10.1: Parameters of the two simulated example networks.

Quantity	Notation	Example Network 1	Example Network 2
Bond stretching Modulus	K	1000	2000
Bending rigidity	κ	30	40
Equilibrium bond length	b_0	1	1
Number of bonds on a polymer chain	N	12	12
Number of polymer chains	N_p	100	60
Number of crosslinks	N_x	150	120
Side length of simulation box	L_box	20	16
Temperature	T	1	1
System sweeps between systems of Markov chain	N_sw	10	10
Total number of simulated systems	$N_\mathrm{s,tot}$	12000	16000
Program running time*		36 h	37 h

*: The simulation program has been run on a single PC at the Max Planck Institute of Colloids and Interfaces.

10.6.1 Example network 1

A snapshot of the undeformed example network 1 is shown in Fig. 10.3. One can see that there is an area with an increased density of crosslinks slightly left from the center of the simulation volume, which has formed spontaneously[7].

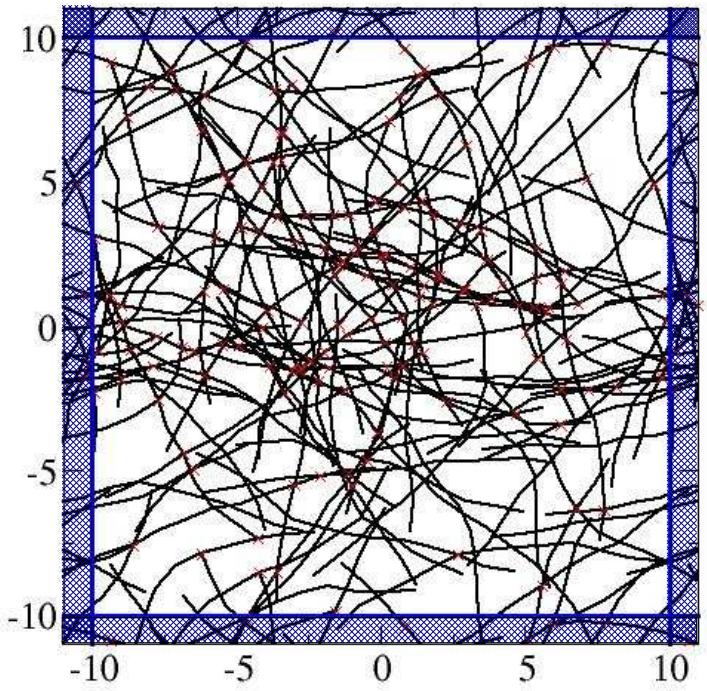

Figure 10.3: Snapshot of example network 1 after crosslinking and subsequent thermalisation at zero shear angle. Crosslinks between filaments are indicated by red crosses.

Example network 1: Global average energies and bond lengths

The spatially averaged stretching energy $\bar{\epsilon}_{\mathrm{s},k}(\Gamma)$, bending energy $\bar{\epsilon}_{\mathrm{b},k}(\Gamma)$ and bond length $\bar{b}_k(\Gamma)$ of the network are shown in Fig. 10.4. One can see that while the stretching energy and the bond length seem to remain largely unchanged at strain angles $\Gamma > 0$, the bending energy is somewhat increased, especially at bonds which share in a crosslink. That the overall energies do

[7] It has been taken care that cross linking is carried out only after sufficient thermalisation time of the uncrosslinked filaments of the initial state in Fig. 10.2 so that the distribution of uncrosslinked filaments was really random.

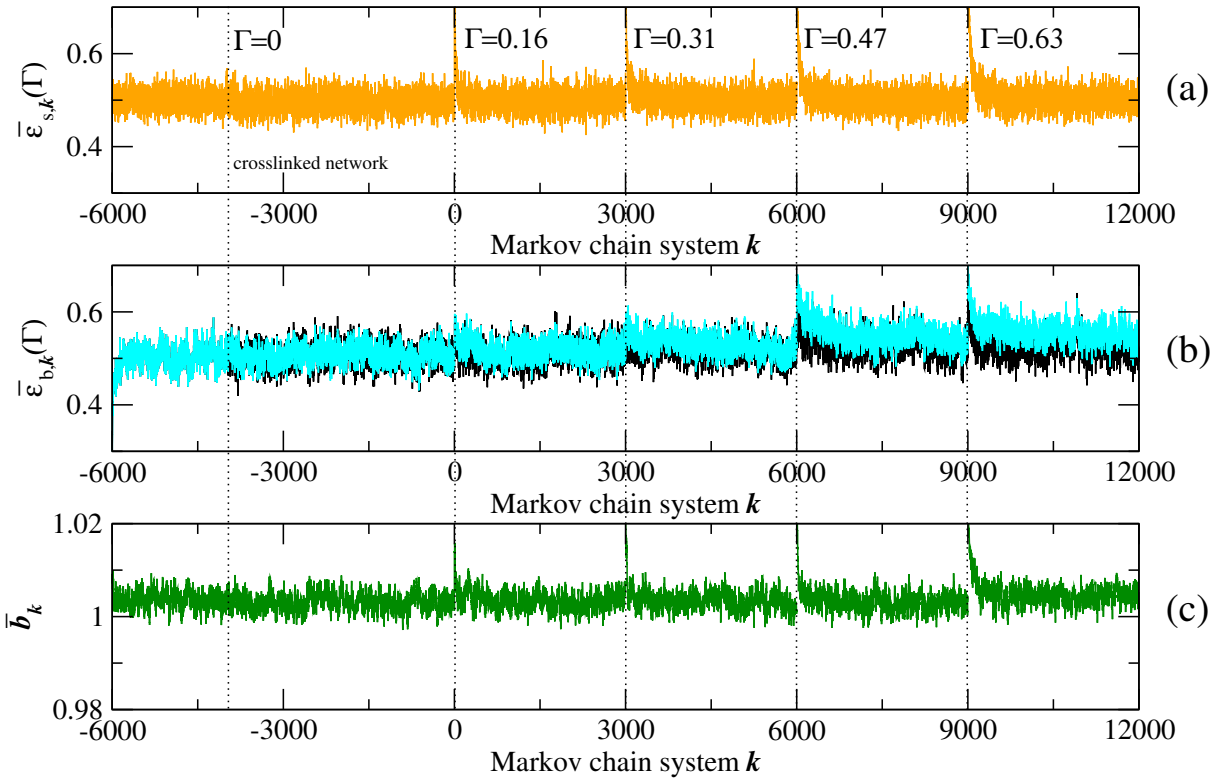

Figure 10.4: Example network 1: Spatially averaged stretching energy $\bar{\epsilon}_{\mathrm{s},k}(\Gamma)$ (a), bending energy $\bar{\epsilon}_{\mathrm{b},k}(\Gamma)$ (b) and bond length $\bar{b}_k(\Gamma)$ (c). The initial state in Fig 10.2 corresponds to the Markov chain system $k = -6000$, crosslinking happens at $k = -4000$. At $k = 0, 3000, 6000, 9000$ the shear angle of the system is changed to $\Gamma = 0.16, 0.31, 0.47, 0.63$, respectively. In (b) the bending energy averaged over all chain bonds is indicated in blue colour. The bending energy averaged over all chain bonds except for those which a part of a crosslink is shown in black. The difference between these two indicates that under strain the bending energy is more increased at the crosslinks than away from the crosslinks. Note that each time just after changing the shear angle, the energies and the bond length decrease which indicates that the network reacts to the new strain situation by rearranging its structure to find a new energy minimum.

not change much with increased shear can also be seen in Fig. 10.5 which shows the statistical averages of the globally averaged stretching energy $\langle\bar{\epsilon}_{\rm s}(\Gamma)\rangle$ and bending energy $\langle\bar{\epsilon}_{\rm b}(\Gamma)\rangle$ [8]. The

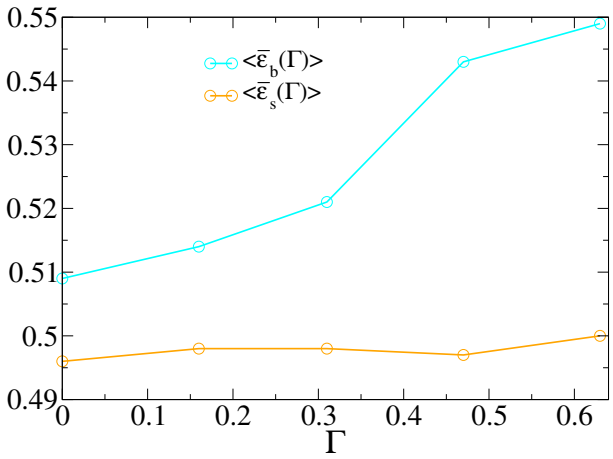

Figure 10.5: Example network 1: Global stretching energy $\langle\bar{\epsilon}_{\rm s}(\Gamma)\rangle$ and bending energy $\langle\bar{\epsilon}_{\rm b}(\Gamma)\rangle$ dependence on shear angle Γ. The stretching energy $\langle\bar{\epsilon}_{\rm s}(\Gamma)\rangle$ increases only very little while the bending energy $\langle\bar{\epsilon}_{\rm b}(\Gamma)\rangle$ is increased by about 8 % at a large shear angle of $\Gamma = 0.63$.

stretching energy $\langle\bar{\epsilon}_{\rm s}(\Gamma)\rangle$ increases only very little while the bending energy $\langle\bar{\epsilon}_{\rm b}(\Gamma)\rangle$ is increased moderately by about 8 % at a large strain angle of $\Gamma = 0.63$. One can conclude that for all shear angles the network is in the bending dominated regime.

Example network 1: Local energies

Fig. 10.6 shows the local distributions of stretching and bending energies. From comparing panels (a) and (b) of Fig. 10.6 it is apparent that the network is in the bending dominated regime for all four shear angles. Further it is clearly visible that the network changes its architecture under deformation. Bundles of parallel horizontal filaments and filaments tilted by an angle of $\sim \Gamma$ appear. While at $\Gamma = 0$ the orientation of filaments with increased bending energy is completely random, see Fig. 10.3, at $\Gamma > 0$ preferably individual filaments of the newly-formed bundles exhibit increased bending energy.

[8] Note that $\langle\bar{\epsilon}_{\rm s}(\Gamma)\rangle$ and $\langle\bar{\epsilon}_{\rm b}(\Gamma)\rangle$ is equal to 0.5 for uncrosslinked filaments at equilibrium due to equipartition.

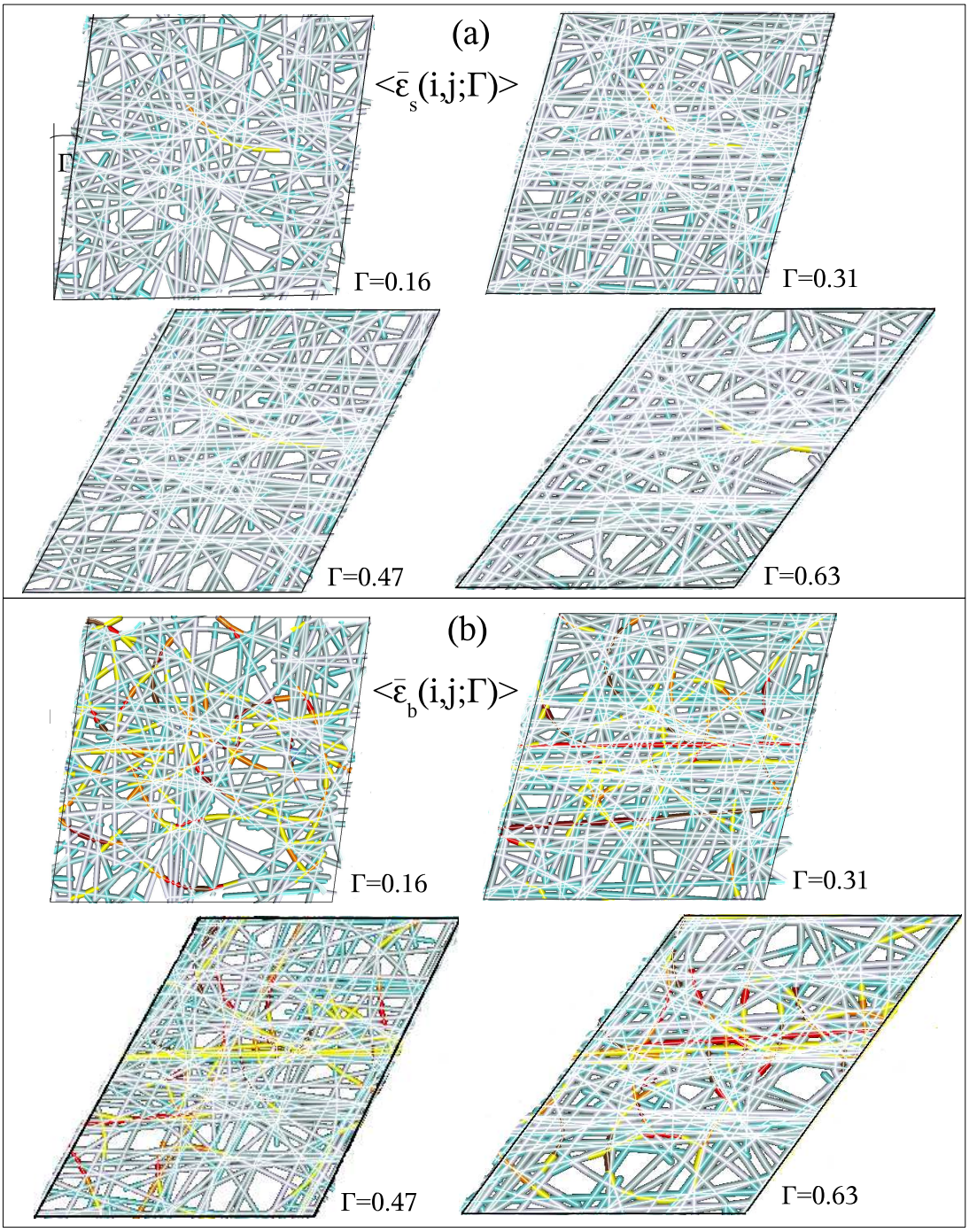

Figure 10.6: Local stretching energies $\langle \bar{\epsilon}_s(i,j;\Gamma) \rangle$ (a) and bending energies $\langle \bar{\epsilon}_b(i,j;\Gamma) \rangle$ (b) of example network 1 under shear. Only the original volume is shown. The positions of the bonds are no snapshots, but they show the average configuration at the respective shear angle Γ. This allows for identification of preferred filament orientations. The colors blue-silver-yellow-red-brown indicate the average local energy from lowest energies to highest energies within the network. While the stretching energy is hardly increased, the bending energy of individual filaments is increased. Such filaments with increased bending energy are frequently part of bundles which are formed in response to the shear deformation and which have horizontal orientation or align with the shear angle Γ.

10.6.2 Example network 2

An snapshot of the undeformed example network 2 is shown in Fig. 10.7. Note that slightly

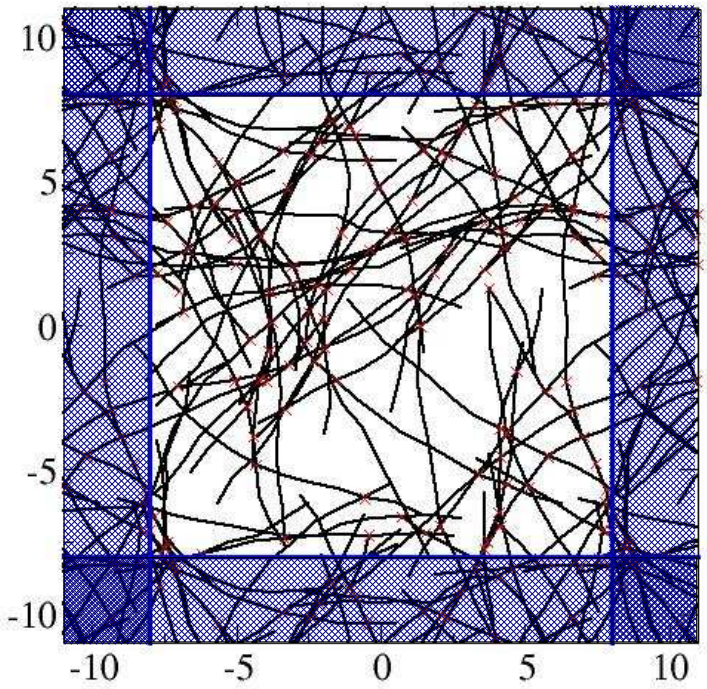

Figure 10.7: Snapshot of example network 2 after crosslinking and subsequent thermalisation at zero shear angle.

down to the right from the center of the simulation box is an area where filament density and cross link density is low.

Example network 2: Global average energies and bond lengths

The spatially averaged stretching energy $\bar{\epsilon}_{\mathrm{s},k}(\Gamma)$, bending energy $\bar{\epsilon}_{\mathrm{b},k}(\Gamma)$ and bond length $\bar{b}_k(\Gamma)$ of the network are shown in Fig. 10.8. One can see that the energies and the bond length increase remarkably with increased shear. The bending energy is mainly increased around the crosslinks, see Fig. 10.8(b). Fig. 10.9 shows the statistical averages of the global stretching $\langle\bar{\epsilon}_{\mathrm{s}}(\Gamma)\rangle$ and bending energy $\langle\bar{\epsilon}_{\mathrm{b}}(\Gamma)\rangle$. The stretching energy $\langle\bar{\epsilon}_{\mathrm{s}}(\Gamma)\rangle$ does not increase very much at the shear angles of $\Gamma = 0.16$ and $\Gamma = 0.31$, but it becomes very large for $\Gamma = 0.47$ and $\Gamma = 0.63$. The bending energy increases for small shear angles faster than the stretching energy, but for large

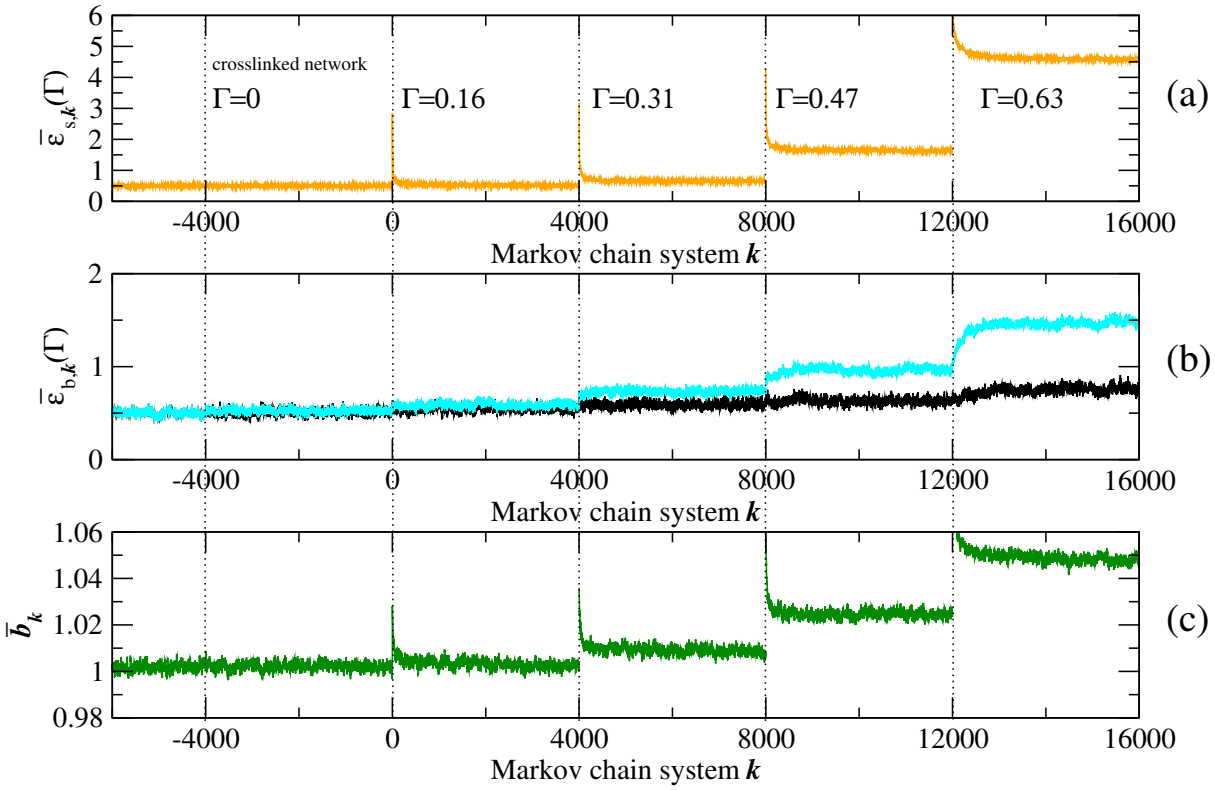

Figure 10.8: Example network 2: Spatially averaged stretching energy $\bar{\epsilon}_{\mathrm{s},k}(\Gamma)$ (a), bending energy $\bar{\epsilon}_{\mathrm{b},k}(\Gamma)$ (b) and bond length $\bar{b}_k(\Gamma)$ (c). The initial state in Fig 10.2 corresponds to the Markov chain system $k = -6000$, crosslinking happens at $k = -4000$. At $k = 0, 4000, 8000, 12000$ the shear angle of the system is changed to $\Gamma = 0.16, 0.31, 0.47, 0.63$, respectively. In (b) the bending energy averaged over all chain bonds is indicated in blue colour, while the bending energy averaged over all chain bonds except for those which a part of a crosslink is shown in black. The difference between these two indicates that under strain the bending energy is much more increased at the crosslinks than away from the crosslinks. Note that each time just after changing the shear angle, the stretching energy and the bond length decrease while the bending energy increases. This indicates that the network reacts to the new strain situation by rearranging its structure in a way that filaments are less stretched, but more bent which leads to a lower total energy. This might be a sign of the emergence of floppy modes, see the discussion in section 10.7.

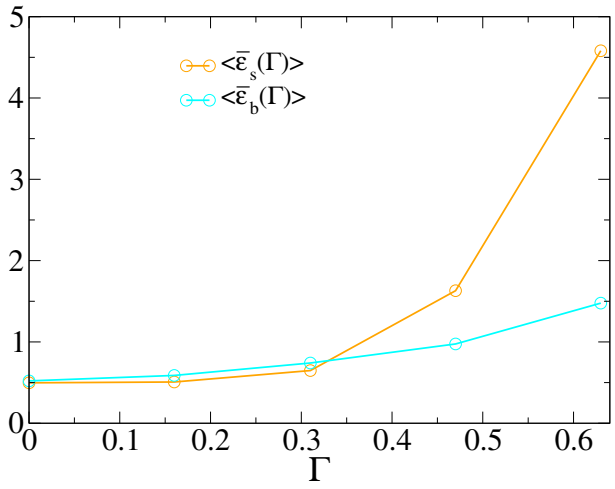

Figure 10.9: Example network 2: Global stretching energy $\langle \bar{\epsilon}_{\mathrm{s}}(\Gamma) \rangle$ and bending energy $\langle \bar{\epsilon}_{\mathrm{b}}(\Gamma) \rangle$ dependence on shear angle Γ. Both the stretching and the bending energy increase very much with growing strain. A crossover from a bending dominated to a stretching dominated strain response happens between $\Gamma = 0.31$ and $\Gamma = 0.47$.

shear angles it increases slower. Consequently there is a crossover from a bending dominated to a stretching dominated strain response between $\Gamma = 0.31$ and $\Gamma = 0.47$.

Example network 2: Local energies

Fig. 10.10 shows the local distributions of stretching and bending energies. One can see that the network progressively changes its architecture with increasing shear strain. The formation of four preferred filament orientations is visible. Remarkably, at high strain highly stretched filaments tilted by an angle of $\sim 45°$ appear.

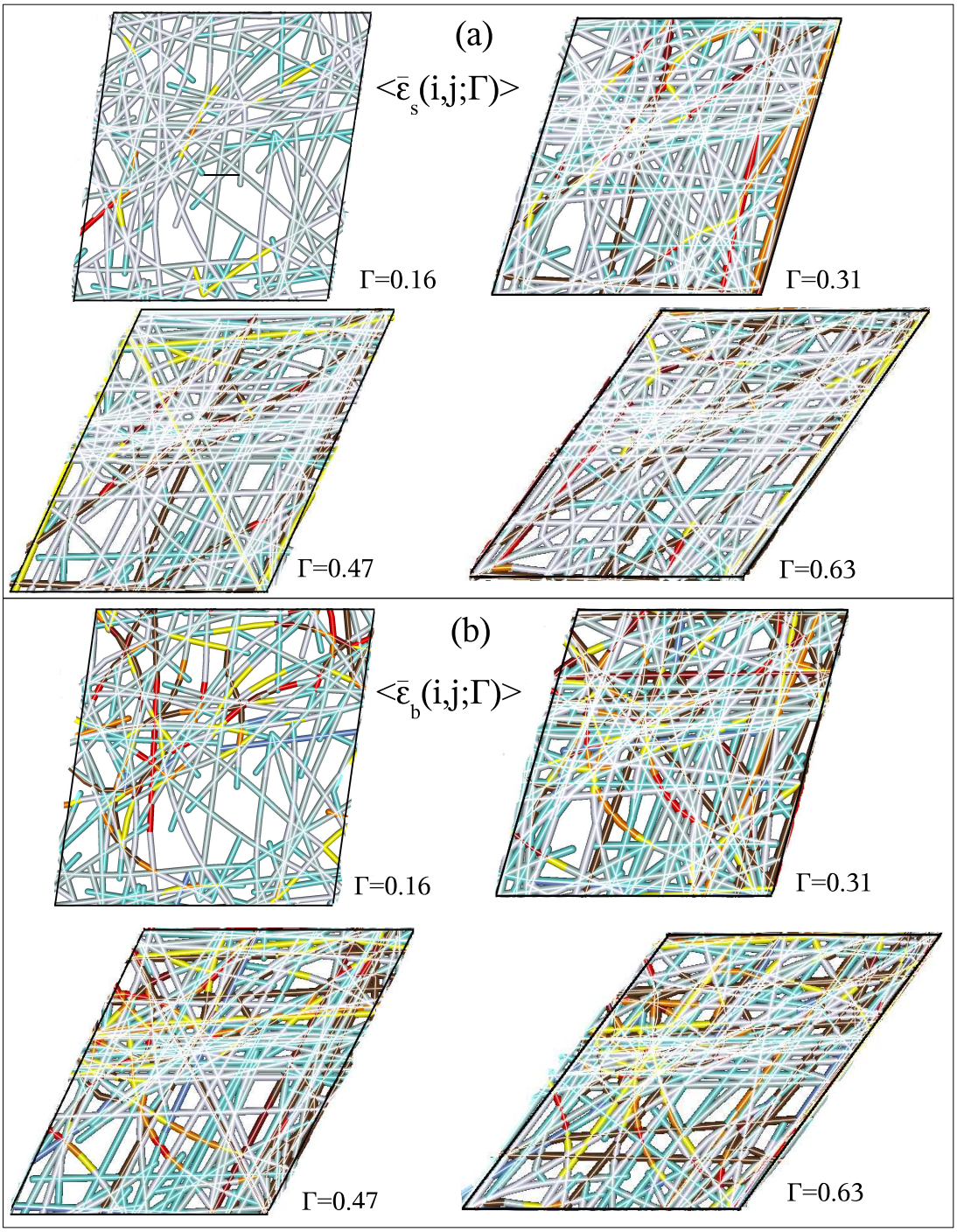

Figure 10.10: Local stretching energies $\langle \bar{\epsilon}_{\mathrm{s}}(i,j;\Gamma)\rangle$ (a) and bending energies $\langle \bar{\epsilon}_{\mathrm{b}}(i,j;\Gamma)\rangle$ (b) of example network 2 under shear. Formation of four preferred orientations of filaments is visible under growing shear strain: (i) Horizontal filaments with low stretching energy and partially high bending energy. Bundle formation appears not as distinct as in example network 1. (ii) Filaments tilted by an angle of $\sim \Gamma$, some with high stretching and bending energies. (iii) Filaments tilted by an angle of $\sim 45°$ with increased stretching energy. (iv) Filaments with an angle of $\sim 135°$, going from the upper left to the bottom right corner. These filament orientations appear at a shear angle of $\Gamma = 0.31$, but the filaments bend at $\Gamma = 0.63$.

10.7 Summary and discussion

10.7.1 Summary of the Results

The response of semiflexible random networks to moderate and large shear strain has been simulated by Monte Carlo simulations. The behavior of two example networks has been presented. These two example networks exhibit very different behavior in response to the imposed strain deformation. By rearranging its structure, example network 1 manages to exhibit only a moderate increase in internal energy even at high strain angle. Stretching of bonds due to the deformation hardly happens, for all probed shear angles the energy increase is mainly due to bending of filaments. Architectural constraints of example network 2 on the other hand do not allow an efficient energy minimization. Both stretching and bending energies are strongly enhanced. The strain response changes from a bending-dominated regime to a stretching-dominated regime between $\Gamma = 0.31$ and $\Gamma = 0.47$. After each increase of the shear angle, the system rearranges its architecture so that stretching is decreased and bending is increased.

10.7.2 Discussion and comparison to literature

The response of a random network to shear strain by increasing its bending energy seems to arise from a rearrangement of the network architecture to a state at which individual filaments carry load, while other filaments are less strained. This reminds to the concept of *floppy modes* which have been suggested by Heussinger and Frey [93]. Floppy modes are localized low energy excitations of the network which not only involve displacements of filaments, but also crosslink deflections. A floppy mode is constructed by displacing a filament axially by δz and subsequently displacing all crosslinks on that filament transversally in order to restore segment lengths on the crossing fibers. As a result all segment lengths remain unchanged in first order in δz, see Fig. 10.11. Stretching of filaments is avoided, instead filaments are bent which costs less energy. Floppy modes could also be an explanation of strain stiffening. It is difficult, to infer from the presented simulation results, if strain stiffening is exhibited by the two example networks. Strain stiffening means that at high strain, the network exhibits a shear modulus which is higher than the linear shear modulus G^0 which describes the network response at low strain. G^0 is given by

$$G^0 = \frac{2\langle \bar{\epsilon}_{\mathrm{tot}}(\Gamma)\rangle}{\Gamma^2} \quad \text{for small } \Gamma, \tag{10.13}$$

where $\langle \bar{\epsilon}_{\mathrm{tot}}(\Gamma)\rangle$ is the sum of stretching and bending energy. The low strain behavior of the networks has not been investigated with our simulations, since thermal fluctuations have been too large to obtain reliable average values for the energies.

Onck et al. state that strain-stiffening happens due to non-affine network rearrangements. Non-affine network structure rearrangements have clearly been observed in our simulations. Further, Onck et al. found in their simulations percolations of stretched filaments that connect the top and bottom of the cell along a $\sim 45°$, see Fig. 10.12. Filaments tilted at an angle of $\sim 45°$ have been found with the simulations presented here, too, at example network 2. Moreover, the transition of example network 2 from bending-dominated response to stretching-dominated response agrees with similar observations by Onck et al. [88].

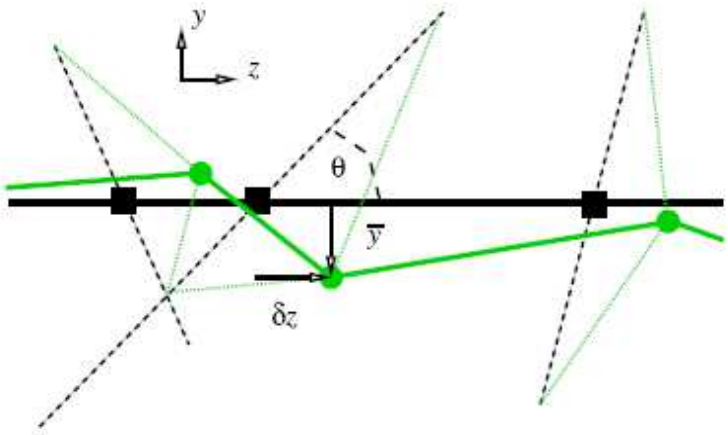

Figure 10.11: Construction of a floppy mode by axial displacement δz of the primary fiber (drawn horizontally) and subsequent transverse deflection $\bar{y} = -\delta z \cot\theta$ of the cross-links to restore the segment lengths on the secondary fibers (dashed lines, possible to first order in δz). Initial cross-link positions are marked as black squares, final configurations as green circles. (Graph taken from Heussinger and Frey, *Physical Review Letters*, 2006, Ref. [93])

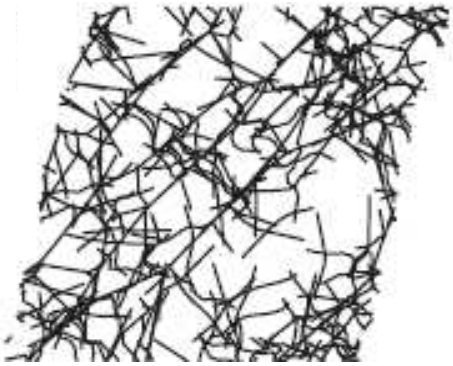

Figure 10.12: Network configuration at strain angle $\Gamma = 0.24$ from a finite element simulation(?). Percolations of stretched filaments appear that connect the top and the bottom of the cell along a $45°$ direction. (Figure taken from Onck et al., *Physical Review Letters*, 2005, Ref. [88]).

10.7.3 Perspectives

With the Monte Carlo simulations, the parameter space can in principle be systematically investigated. From this, phase diagrams can be obtained which separate the bending-dominated from the stretching-dominated regime and the affine from the non-affine deformation regime, in dependence of the shear angle Γ, the filament parameters K, κ, b_0 and the filament and crosslink density. Further interesting quantities to investigate with the Monte Carlo simulation would be

the stretching and bending forces at interfaces within the network. In contrast to purely mechanical approaches, Monte Carlo simulations include thermal effects. This would allow to determine the free energy instead of only the mechanical energy. An idea to obtain the free energy is to include a Monte Carlo trial step at which not individual beads are displaced, but the shear angle Γ of the entire network is changed. From the distribution of shear angles one could infer the free energy. Furthermore, in reality networks could rupture. Rupturing of networks was not included in the presented simulation approach, but could be included.

The Monte Carlo simulation approach suffers from long computing times. It takes long to thermalise systems, i.e., to bring them to equilibrium. After thermalisation it takes again long to calculate thermal averages. Also due to the problem with large computation times, the simulated systems of the shown example networks have been chosen relatively small. Hence finite size effects could be present which would have to be investigated systematically. The differences in the behavior of the two example networks are mainly due to their random architecture. For investigating average properties of random networks, it has to be averaged over a large number of random networks with the same parameters[9]. This would be difficult, again because of the long computation times.

Recently it has come to the author's knowledge that another group is performing similar simulations like these presented here [94].

[9]E.g., in the simulations of Onck et al. it has been averaged over ten realisations of random networks with the same parameters to obtain stress-strain relations. The errors of these relations are still large, see Fig.1 in Ref. [88].

A Appendix

A.1 Re-parameterization of memory integrals

The common notation of memory integrals involving the boundaries $(-\infty, t)$ can be re-parameterized by the substitution $\tau = t - t'$, e.g.,

$$\int_{-\infty}^{t} \gamma_1(t-t')v(t')dt' = \int_{-\infty}^{0} \gamma_1(\tau)v(t-\tau)(-d\tau) = \int_{0}^{\infty} \gamma_1(\tau)v(t-\tau)d\tau. \tag{A.1}$$

A.2 Fourier transform

The Fourier transform of a time-dependent function $x(t)$ is given by

$$\tilde{x}(\omega) = \int_{-\infty}^{\infty} x(t)\exp(-\mathrm{i}\omega t)dt. \tag{A.2}$$

The inverse Fourier transform is given by

$$x(t) = \frac{1}{2\pi}\int_{-\infty}^{\infty} \tilde{x}(\omega)\exp(\mathrm{i}\omega t)d\omega. \tag{A.3}$$

A.3 Fourier transform of the equation of motion

To obtain the Fourier transformed version, Eq. (3.6), of the equation of motion, Eq. (3.5), one Fourier-analyzes $\kappa x(t)$, , $m\ddot{x}(t)$ and $F_{\mathrm{R}}(t)$ according to the inverse Fourier transform, Eq. (A.3). For the velocity memory term one has

$$\begin{aligned} -\int_0^{\infty} \gamma_1(\tau)v(t-\tau)d\tau &= -\int_{-\infty}^{\infty} d\tau \int_{-\infty}^{\infty} d\omega \int_{-\infty}^{\infty} d\omega' \tilde{\gamma}_1(\omega)\tilde{v}(\omega')\exp(\mathrm{i}(\omega-\omega')\tau)\exp(\mathrm{i}(\omega' t)) \\ &= \int_{-\infty}^{\infty} d\omega \tilde{\gamma}_1(\omega)\tilde{v}(\omega)\exp(\mathrm{i}\omega t). \end{aligned} \tag{A.4}$$

One obtains the inverse Fourier transform of the product $\tilde{\gamma}_1(\omega)\tilde{v}(\omega)$. The Fourier transformed $\tilde{v}(\omega)$ of the velocity $v(t) = \dot{x}(t)$ can be written as $\mathrm{i}\omega\tilde{x}(\omega)$, since we assume $\lim_{\pm\infty} x(t) = 0$. Accordingly, the Fourier transformed of the acceleration memory term is given by $-\omega^2\tilde{x}(\omega)\tilde{\gamma}_2(\omega)$.

A.4 Fourier series

When a time-dependent trajectory $x(t)$ is observed over a finite time interval $0 \leq t \leq T_{\rm m}$, $x(t)$ can be expanded in a *Fourier series* as

$$x(t) = \frac{1}{T_{\rm m}} \sum_{k=-\infty}^{\infty} \hat{x}_k \exp(\mathrm{i}\omega_k t), \tag{A.5}$$

with discrete frequencies $\omega_k = 2\pi k/T_{\rm m}$ $(k = 0, \pm 1, \pm 2, ...)$. The Fourier coefficient $\hat{x}_k$ is given by

$$\hat{x}_k = \int_{-\infty}^{\infty} x(t) \exp(-\mathrm{i}\omega_k t) dt. \tag{A.6}$$

B Bibliography

[1] S. M. Block. Real engines of creation. *Nature*, 386:217, 1997.

[2] H. Kress, E. H. K. Stelzer, G. Griffiths, and A. Rohrbach. Control of relative radiation pressure in optical traps: Application to phagocytic membrane binding studies. *Phys. Rev. E*, 71:061927, 2005.

[3] Keir C. Neuman and Steven M. Block. Optical trapping. *Review of Scientific Instruments*, 75(9):2787–2809, 2004.

[4] A. Ashkin, J. M. Dziedzic, J. E. Bjorkholm, and S. Chu. Observation of a single-beam gradient force optical trap for dielectric particles. *Opt. Lett.*, 11:288, 1986.

[5] A. Ashkin. Forces of a single-beam gradient laser trap on a dielectric sphere in the ray optics regime. *Biophys. J.*, 61(2):569–582, 1992.

[6] P. M. Hansen, V. Kjøller Bhatia, N. Harrit, and L. Oddershede. Expanding the optical trapping range of gold nanoparticles. *Nano Lett.*, 5:1937, 2005.

[7] A. Rohrbach. Stiffness of optical traps: Quantitative agreement between experiment and electromagnetic theory. *Phys. Rev. Lett.*, 95:168102, 2005.

[8] S. Hénon, G. Lenormand, A. Richert, and F. Gallet. A new determination of the shear modulus of the human erythrocyte membrane using optical tweezers. *Bioph. J.*, 76:1145, 1999.

[9] E. Helfer, S. Harlepp, L. Bourdieu, J. Robert, F. C. MacKintosh, and D. Chatenay. Microrheology of biopolymer-membrane complexes. *Phys. Rev. Lett.*, 85:457–460, 2000.

[10] B. Schnurr, F. Gittes, F. C. MacKintosh, and C. F. Schmidt. Determining microscopic viscoelasticity in flexible and semiflexible polymer networks from thermal fluctuations. *Macromolecules*, 30:7781–7792, 1997.

[11] F. Gittes, B. Schnurr, P. D. Olmsted, F. C. MacKintosh, and C. F. Schmidt. Microscopic viscoelasticity: Shear moduli of soft materials determined from thermal fluctuations. *Phys. Rev. Lett.*, 79:3286–3289, 1997.

[12] D. Velegol and F. Lannidagger. Cell traction forces on soft biomaterials. i. microrheology of type i collagen gels. *Biophys. J.*, 81:1786, 2001.

[13] K. M. Addas, C. F. Schmidt, and J. X. Tang. Microrheology of solutions of semiflexible biopolymer filaments using laser tweezers interferometry. *Phys. Rev. E*, 70:021503, 2004.

[14] I. M. Tolić-Nørrelykke, E. L. Munteanu, G. Thon, L. B. Oddershede, and K. Berg-Sørensen. Anomalous diffusion in living yeast cells. *Phys. Rev. Lett.*, 93:078102, 2004.

[15] M. Kurachi, M. Hoshi, and H. Tashiro. Buckling of a single microtubule by optical trapping forces: direct measurement of microtubule rigidity. *Cell Motil. Cytoskel.*, 30:221, 1995.

[16] A. Ashkin, K. Schütze, J. M. Dziedzic, U. Euteneuer, and M. Schliwa. Force generation of organelle transport measured in vivo by an infrared laser trap. *Nature*, 348:346, 1990.

[17] A. Ashkin, J. M. Dziedzic, and T. Yamane. Optical trapping and manipulation of single cells using infrared laser beams. *Nature*, 330:769, 1987.

[18] T. Nishizaka, H. Miyata, H. Yoshikawa, S. Ishiwata, and K. Kinosita Jr. Unbinding force of a single motor molecule of muscle measured using optical tweezers. *Nature*, 377:251, 1995.

[19] Michelle D. Wang, Mark J. Schnitzer, Hong Yin, Robert Landick, Jeff Gelles, and Steven M. Block. Force and velocity measured for single molecules of RNA polymerase. *Science*, 282:902–907, 1998.

[20] R. J. Davenport, G. J. L. Wuite, R. Landick, and C. Bustamante. Single-molecule study of transcriptional pausing and arrest by e. coli rna polymerase. *Science*, 287:2497, 2000.

[21] K. Berg-Sørensen, M. Fischer, P. M. Hansen, and L. Oddershede. Cellers nanomekanik. *KVANT*, 1/2007:4, 2007. A translation into English language can be found on www.xscience.info.

[22] J. D. Ferry. *Viscoelastic Properties of Polymers*. John Wiley & Sons, Inc., 1980.

[23] A. R. Khokhlov, A. Y. Grossberg, and V. S. Pande. *Statistical Physics of Macromolecules (Polymers and Complex Materials)*. American Institute of Physics, 2002.

[24] T. G. Mason, H. Gang, and D. A. Weitz. Diffusing-wave-spectroscopy measurements of viscoelasticity of complex fluids. *J. Opt. Soc. Am. A*, 14:139, 1997.

[25] M. Atakhorrami, J. I. Sulkowska, K. M. Addas, G. H. Koenderink, J. X. Tang, A. J. Levine, F. C. MacKintosh, and C. F. Schmidt. Correlated fluctuations of microparticles in viscoelastic solutions: Quantitative measurement of material properties by microrheology in the presence of optical traps. *Phys. Rev. E*, 73:061501, 2006.

[26] See References [10,25]. The response function $\alpha(\omega)$ there corresponds to $1/(\mathrm{i}\omega\tilde{\gamma}(\omega))$.

[27] T. G. Mason and D. A. Weitz. Optical measurements of frequency-dependent linear viscoelastic moduli of complex fluids. *Phys. Rev. Lett.*, 74:1250, 1995.

[28] Andreas R. Bausch, Winfried Möller, and Erich Sackmann. Measurement of local viscoelasticity and forces in living cells by magnetic tweezers. *Biophys. J.*, 76:573–579, 1999.

[29] T. Gisler and D. A. Weitz. Scaling of the microrheology of semidilute f-actin solutions. *Phys. Rev. Lett.*, 82:1606, 1999.

[30] S. Yamada, D. Wirtz, and S. C. Kuo. Mechanics of living cells measured by laser tracking microrheology. *Biophys. J.*, 78:1736–47, 2000.

[31] A. W. C. Lau, B. D. Hoffman, A. Davies, J. C. Crocker, and T. C. Lubensky. Microrheology, stress fluctuations, and active behavior of living cells. *Phys. Rev. Lett.*, 91:198101, 2003.

[32] Y. Tseng, T. P. Kole, and D. Wirtz. Micromechanical mapping of live cells by multiple-particle-tracking microrheology. *Biophys. J.*, 83:3162, 2002.

[33] R. Roscoe. Mechnical models for the representation of visco-elastic properties. *British Journal of Applied Physics*, 1:171, 1950.

[34] J. Alcaraz, L. Buscemi, M. Grabulosa, X. Trepat, B. Fabry, R. Farré, and D. Navajas. Microrheology of human lung epithelial cells measured by atomic force microscopy. *Biophys. J.*, 84:2071, 2003.

[35] P. T. Tran, L. Marsh, V. Doye, S. Inoué, and F. Chang. A mechanism for nuclear positioning in fission yeast based on microtubule pushing. *J. Cell. Biol.*, 153:397–411, 2001.

[36] M. E. Janson, R. Loughlin, I. Loiodice, C. Fu, D. Brunner, F. J. Nédélec, and P. T. Tran. Crosslinkers and motors organize dynamic microtubules to form stable bipolar arrays in fission yeast. *Cell*, 128:357, 2007.

[37] R. Kubo, M. Toda, and N. Hashitsume. *Statistical Physics*, volume 2. Springer-Verlag, Heidelberg, 1985.

[38] K. Berg-Sørensen and H. Flyvbjerg. The colour of thermal noise in classical Brownian motion: a feasibility study of direct experimental observation. *New J. Phys.*, 7:38, 2005.

[39] G. G. Stokes. On the effect of the internal friction of fluids on the motion of pendulums. *Trans. Cambridge Philos. Soc.*, IX:8–106, 1851.

[40] K. Berg-Sørensen and H. Flyvbjerg. Power spectrum analysis for optical tweezers. *Rev. Sci. Ins.*, 75:594, 2004.

[41] A. J. Levine and T. C. Lubensky. Response function of a sphere in a viscoelastic two-fluid medium. *Phys. Rev. E*, 63:041510, 2001.

[42] A. J. Levine and T. C. Lubensky. One- and two particle microrheology. *Phys. Rev. Lett.*, 85:1774, 2000.

[43] J.C. Crocker, M.T. Valentine, E.R. Weeks, T. Gisler, P.D. Kaplan, A.G. Yodh, and D.A. Weitz. Two-point microrheology of inhomogeneous soft materials. *Phys. Rev. Lett.*, 85:888, 2000.

[44] D. T. Chen, E. R. Weeks, J. C. Crocker, M. F. Islam, R. Verma, J. Gruber, A. J. Levine, C. Lubensky, and A. G. Yodh. Rheological microscopy: Local mechanical properties from microrheology. *Phys. Rev. Lett.*, 90:108301, 2003.

[45] M. Buchanan, M. Atakhorrami, J. F. Palierne, F. C. MacKintosh, and C. F. Schmidt. High-frequency microrheology of wormlike micelles. *Phys. Rev. E*, 72:011504, 2005.

[46] M. Atakhorrami and C. F. Schmidt. High-bandwidth one-and two-particle microrheology in solutions of wormlike micelles. *Rheol. Act.*, 45:449, 2006.

[47] AJ Levine and FC MacKintosh. Dynamics of viscoelastic membranes. *Phys. Rev. E*, 66:061606–1–13, 2002.

[48] F. Gittes and F. C. MacKintosh. Dynamic shear modulus of a semiflexible polymer network. *Phys. Rev. E*, 58:R1241–R1244, 1998.

[49] D. Mizuno, C. Tardin, C. F. Schmidt, and F. C. MacKintosh. Nonequilibrium mechanics of active cytoskeletal networks. *Science*, 315:370, 2007.

[50] H. Qian. Single-particle tracking: Brownian dynamics of viscoelastic materials. *Biophys. J.*, 79:137, 2000.

[51] R. Kubo. The fluctuation-dissipation theorem. *Rep. Prog. Phys.*, 29:255, 1966.

[52] D. Bedeaux and P. Mazur. Brownian motion and fluctuating hydrodynamics. *Physica*, 76:247, 1974.

[53] K. Berg-Sørensen, E. J. G. Peterman, T. Weber, C. F. Schmidt, and H. Flyvbjerg. Power spectrum analysis for optical tweezers. II: Laser wavelength dependence of parasitic filtering, and how to achieve high bandwidth. *Rev. Sci. Ins.*, 77:063106, 2006.

[54] L. D. Landau and E. M. Lifschitz. *Statistische Physik, Teil I, Lehrbuch der Theoretischen Physik, Band 5.* Akademie-Verlag Berlin, Berlin, 1978.

[55] K. C. Vermeulen, J. van Mameren, G. J. M. Stienen, E. J. G. Peterman, G. J. L. Wuite, and C. F. Schmidt. Calibrating bead displacements in optical tweezers using acousto-optic deflectors. *Rev. Sci. Ins.*, 77:013704, 2006.

[56] S. F. Tolić-Nørrelykke, E. Schaeffer, J. Howard, F. S. Pavone, F. Juelicher, and H. Flyvbjerg. Calibration of optical tweezers with positional detection in the back-focal-plane. *Rev. Sci. Ins.*, 77:103101, 2006.

[57] L. Oddershede, J. K. Dreyer, S. Grego, S. Brown, and K. Berg-Sørensen. The motion of a single molecule, the λ-receptor, in the bacterial outer membrane. *Biophys. J*, 83:3152, 2002.

[58] H. Flyvbjerg K. Berg-Sørensen, L. Oddershede. Optical tweezers as a tool of precision: Single-molecule mobility as case study. *Proceedings of SPIE*, 5322:64, 2004.

[59] C. Bustamante, J. Liphardt, and F. Ritort. The nonequilibrium thermodynamics of small systems. *Physics Today*, 58:43, 2005.

[60] C. Jarzynski. Nonequilibrium equality for free energy differences. *Phys. Rev. Lett.*, 78:2690, 1997.

[61] G. E. Crooks. Nonequilibrium Measurements of Free Energy Differences for Microscopically Reversible Markovian Systems. *Journal of Statistical Physics*, 90:1481, 1998.

[62] X. S. Xie, J. Yu, and W. Y. Yang. Living cells as test tubes. *Sciene*, 312:228, 2006.

[63] M. L. Gardel, M. T. Valentine, Crocker, J. C., Bausch, A. R., and D. A. Weitz. Microrheology of entangled f-actin solutions. *Phys. Rev. Lett.*, 91(15):158302, Oct 2003.

[64] E.-L. Florin, A. Pralle, E. H. K. Stelzer, and J. K. H. Hörber. Photonic force microscope calibration by thermal noise analysis. *Appl. Phys. A*, 66:S75–S78, 1998.

[65] Alexander Rohrbach, Christian Tischer, Dirk Neumayer, Ernst-Ludwig Florin, and Ernst H. K. Stelzer. Trapping and tracking a local probe with a photonic force microscope. *Review of Scientific Instruments*, 75(6):2197–2210, 2004.

[66] Karel Svoboda and Steven M. Block. Biological applications of optical forces. *Ann. Rev. Biophys. Biomol. Struct.*, 23:247–285, 1994.

[67] Robert M. Simmons, Jeffrey T. Finer, Steven Chu, and James A. Spudich. Quantitative measurements of force and displacement using an optical trap. *Biophys. J.*, 70:1813–1822, 1996.

[68] R. P. Ojha, P.-A. Lemieux, P. K. Dixon, A. J. Liu, and D. J. Durian. Statistical mechanics of a gas-fluidized particle. *Nature*, 427:521, 2004.

[69] W. H. Press, B. P. Flannery, S. A. Teukolsky, and W. T. Vetterling. *Numerical Recipes. The Art of Scientific Computing.* Cambrigde University Press, Cambridge, 1986.

[70] J. L. Hutter and J. Bechhoefer. Calibration of atomic-force microscope tips. *Rev. Sci. Ins.*, 64:1868, 1993.

[71] R. J. Clarke, IO. E. Jensen, J. Billingham, A. P. Pearson, and P. M. Williams. Stochastic elastohydrodynamics of a microcantilever oscillating near a wall. *Phys. Rev. Lett.*, 96:050801, 2006.

[72] In our simulations we have not included a volt-meter conversion, i.e., we assume that we measure positions. β_{input} is therefore 1. β_k and $\beta^{(\text{av})}$ have been determined only in the case of laser driving.

[73] S. P. Gross. Application of optical traps in vivo. *Methods enzymol.*, 361:162, 2002.

[74] P. M. Hansen, I. M. Tolić-Nørrelykke, H. Flyvbjerg, and K. Berg-Sørensen. tweezercalib 2.1: Faster version of matlab package for precise calibration of optical tweezers. *Computer Physics Communications*, 175:8, 2006.

[75] E.J.G. Peterman, F. Gittes, and C.F. Schmidt. Laser-induced heating in optical traps. *Biophysical Journal*, 84:1308–1316, 2003.

[76] K. Berg-Sørensen, L. Oddershede, E.-L. Florin, and H. Flyvbjerg. Unintended filtering in a typical photodiode detection system for optical tweezers. *J. Appl. Phys.*, 93:3167–3176, 2003.

[77] M. Fischer. *Optical Tweezers in Viscoelastic Media.* PhD dissertation, Copenhagen University, Niels Bohr Institute, Faculty of Science, Oct 2007.

[78] J. Kierfeld, O. Niamploy, V. Sa-yakanit, and R. Lipowsky. Stretching of semiflexible polymers with elastic bonds. *Eur. Phys. J. E*, 14:17, 2004.

[79] Doi and Edwards. *Theory of Polymer Dynamics.* Clarendon Press, 1986.

[80] J. F. Marko and E. D. Siggia. Stretching dna. *Macromolecules*, 28:8759, 1995.

[81] F. C. MacKintosh, J. Käs, and P. A. Janmey. Elasticity of semiflexible biopolymer networks. *Phys. Rev. Lett.*, 75(24):4425–4428, Dec 1995.

[82] C. Storm, J. J. Pastore, F. C. MacKintosh, T. C. Lubensky, and P. A. Janmey. Nonlinear elasticity in biological gels. *Nature*, 435:191–194, 2005.

[83] Klaus Kroy and Erwin Frey. Force-extension relation and plateau modulus for wormlike chains. *Phys. Rev. Lett.*, 77(2):306–309, Jul 1996.

[84] Jan Wilhelm and Erwin Frey. Elasticity of stiff polymer networks. *Phys. Rev. Lett.*, 91(10):108103, Sep 2003.

[85] David A. Head, Alex J. Levine, and F. C. MacKintosh. Deformation of cross-linked semiflexible polymer networks. *Phys. Rev. Lett.*, 91(10):108102, Sep 2003.

[86] D. A. Head, A. J. Levine, and F. C. MacKintosh. Distinct regimes of elastic response and deformation modes of cross-linked cytoskeletal and semiflexible polymer networks. *Phys. Rev. E*, 68(6):061907, Dec 2003.

[87] D A Head Alex J Levine and F C MacKintosh. The deformation field in semiflexible networks. *Journal of Physics: Condensed Matter*, 16(22):S2079–S2088, 2004.

[88] P. R. Onck, T. Koeman, T. van Dillen, and E. van der Giessen. Alternative explanation of stiffening in cross-linked semiflexible networks. *Physical Review Letters*, 95(17):178102, 2005.

[89] B. A. DiDonna and Alex J. Levine. Filamin cross-linked semiflexible networks: Fragility under strain. *Physical Review Letters*, 97(6):068104, 2006.

[90] B. A. DiDonna and Alex J. Levine. Unfolding cross-linkers as rheology regulators in f-actin networks. *Physical Review E (Statistical, Nonlinear, and Soft Matter Physics)*, 75(4):041909, 2007.

[91] Z. Chen, C. Cohen, and F.A. Escobedo. Monte carlo simulation of the effect of entanglements on the swelling and deformation behavior of end-linked polymeric networks. *Macromolecules*, 35(8):3296–3305, 2002.

[92] D.M. Bhawe, C. Cohen, and F.A. Escobedo. Formation and characterization of semiflexible polymer networks via monte carlo simulations. *Macromolecules*, 37(10):3924–3933, 2004.

[93] Claus Heussinger and Erwin Frey. Floppy modes and nonaffine deformations in random fiber networks. *Physical Review Letters*, 97(10):105501, 2006.

[94] Sander Pronk, Daniel A. Fletcher, and Phillip L. Geissler. Nonlinear elastic behavior in simulated semiflexible polymer networks. In *51st Biophysical Society Annual Meeting, Baltimore*, March 2007. Poster.

C Acknowledgments

The manifoldness of biology is simply intriguing. How is it possible that life emerges from dead matter and creates such an immense number of complex phenomena on many different time and length scales? I studied physics to understand the dead matter, but the fascination by biology which I had felt since my childhood persisted. For my graduate studies, I grasped the opportunity to combine both of my interests. During my studies in biophysics I realized how difficult many experiments are, how tricky the interpretation of the results is, and how fragmentary our knowledge about life still is. My hope is that the calibration method for optical tweezers developed in my Ph.D. project will soon be employed for quantitative force measurements which will lead to a better understanding of the biological cell.

First, I want to thank my supervisors Kirstine Berg-Sørensen and Lene Oddershede for the possibility to work on this interesting project, for the opportunity to realise my own ideas and for great supervision. I thank all members of the optical tweezers group and the other biophysics groups for creating a great working atmosphere at the Niels Bohr Institute. In particular I am grateful to Nader Reihani and Andrew Richardson for many interesting discussions and for making the experimental verification of the novel calibration method possible. Also, I wish to express my gratitude to Björn Nilsson for excellent IT support at the Niels Bohr Institute, so I could concentrate on science.

I want to thank Reinhard Lipowsky and Angelo Valleriani who coordinated the graduate program, which funded my Ph.D. position. The Marie Curie - Early Stage Training on Biomimetic System, a program initiated by the European Commission, enabled me to perform my graduate studies abroad from my home country. Furthermore, the program included regular workshops for the participating students.

I would like to thank Jan Kierfeld for the great supervision of my abroad project in Golm. Jan taught me a lot about polymer physics and simulations and it was a pleasure to work with him. Furthermore, I want to thank Henrik Flyvbjerg, Hans Fogedby, Simon Tolić-Nørrelykke and Scot Kuo for helpful discussions regarding the calibration of optical tweezers.

I would like to say thanks to the people who helped me with proof-reading my thesis, or parts of it, Christine Selhuber-Unkel, Sandeep Krishna and Heiko Seeger. A particularly big thanks goes to Christine who gave me many useful hints regarding how to improve the comprehensibility of my thesis.

Moreover, I want to thank some people from my non-academic life. I thank Heiko and Giovanna for the great time we spent together in Copenhagen. And I thank my family for all their support.

D Articles

1. F. Grossmann, M. Fischer, T. Kunert and R. Schmidt, **Transmission probabilities for periodically driven barriers**, *Chem. Phys.*, vol. 322, 144-150 (2005) (pre-Ph.D. work)
2. M. Fischer and K. Berg-Sørensen, **Calibration of trapping force and response function of optical tweezers in viscoelastic media**, *J. Opt. A: Pure Appl. Opt.*, vol. 9, S239-S250 (2007)
3. K. Berg-Sørensen, M. Fischer, P. M. Hansen and Lene Oddershede, **Cellers nano-mekanik**, Kvant 2007 vol. 1, 5-7
   - original version in Danish language
   - translation into English language, published on www.xscience.info
4. M. Fischer and K. Berg-Sørensen, **Force spectroscopy with optical tweezers in viscoelastic media: Calibration method and experimental concerns**, accepted by SPIE for proceedings (2007), not published